August 2022

Experimental and Numerical Investigation of the Effect of Newly Tested Blades on the Aerodynamic Performance and Power Output of a Horizontal Axis Wind Turbine

Alaa Sayed Mahmoud Hasan
University of Wisconsin-Milwaukee

Recommended Citation

Hasan, Alaa Sayed Mahmoud, "Experimental and Numerical Investigation of the Effect of Newly Tested Blades on the Aerodynamic Performance and Power Output of a Horizontal Axis Wind Turbine" (2022). *Theses and Dissertations*. 2897.
https://dc.uwm.edu/etd/2897

EXPERIMENTAL AND NUMERICAL INVESTIGATION OF THE EFFECT OF NEWLY TESTED BLADES ON THE AERODYNAMIC PERFORMANCE AND POWER OUTPUT OF A HORIZONTAL AXIS WIND TURBINE

by

Alaa Sayed Mahmoud Hasan

A Dissertation Submitted in
Partial Fulfillment of the
Requirements for the Degree of

Doctor of Philosophy
in Engineering

at

The University of Wisconsin-Milwaukee
August 2022

ABSTRACT

EXPERIMENTAL AND NUMERICAL INVESTIGATION OF THE EFFECT OF NEWLY TESTED BLADES ON THE AERODYNAMIC PERFORMANCE AND POWER OUTPUT OF A HORIZONTAL AXIS WIND TURBINE

by

Alaa Sayed Mahmoud Hasan

The University of Wisconsin-Milwaukee, 2022
Under the Supervision of Professor Ryoichi S. Amano

There is no doubt that the effects of global warming are obvious for every human being on the Earth now. Therefore, the need to develop carbon dioxide-free sources of electricity is urgent. Wind Turbines are one of these most essential recently developed sources. For that reason, the University of Wisconsin-Milwaukee founded the wind tunnel lab., equipped with the state-of-the-art research tools, to take part in this procession.

In chapter (3) of this thesis it is desired to investigate in detail the scenario that takes place behind a single wind turbine unit by focusing on three parameters; average axial wind velocity component, velocity deficit, and total turbulence intensity. The testing was done at mainstream velocity, U_∞, of 5.2 m/s, u and v velocity components were captured by x-probe dual-sensor hot wire anemometer. A massive amount of point data was obtained, which then processed by a Matlab script to plot the desired contours through the successive transverse sections along the entire length of the test section. By monitoring the previously mentioned flow parameters, the regions of low velocity and high turbulence can be avoided while the location of the subsequent wind turbine is selected. The estimation of the distance, at which the inlet flow field will restore its original

characteristics after being mixed through the rotor blades, is very important as this is the distance that should separate two successive turbines in an inline configuration wind farm to guarantee the optimum performance and to extract the maximum power out of the subsequent array of turbines. It is found that the hub height axial velocity recovery at six rotor diameters downstream distance is only 82%. This means that the power extraction out of the downstream turbine in an inline configuration wind farm is only 55% of the upstream turbine, if the same free stream velocity and blade design are adopted.

Then, chapter (4) sheds light on wind farm layout design, site evaluation, and power output prediction by performing modeling and the experimental tests of a wind tunnel test section including a single wind turbine model inside was created and validated against present experimental data of the same model. The Large Eddy Simulation (LES) was used as a numerical approach to model the Navier-Stokes equations. The computational domain was divided into two areas; rotational and stationary. The unsteady Rigid Body Motion (RBM) model was adopted to represent the rotor rotation accurately. It is concluded through this investigation, if the rotational speed control is adopted, that the wind velocity increase enhances the axial velocity recovery. Hence, the separation distance between two successive turbines decreases while maintaining the same level of power extraction. This way, we can optimize available site exploitation.

After that, chapter (5) of this work tries to popularize the use of residential-scale wind turbines because the last few decades witnessed a great development for the large-scale wind turbines, while small-scale wind turbines didn’t grab the same amount of interest. On this track, four airfoils (GOE 447, GOE 446, NACA 6412 and NACA 64(3)-618) characterized by their high published lift-to-drag ratios (161.3, 148.7, 142.7 and 136.3 respectively) are used to generate an entire 7 m long blades for three-bladed rotor wind turbine models tested numerically at 12.5 m/s

rated wind speed, with design tip speed ratio of 7. The criterion to judge each model’s performance is the power output. Thus, the blades of the model which produce the highest power are selected to undergo a leading-edge modification (tubercles), and a tip modification (winglet), seeking power improvement. Finally, the best basic model is tested at a spectrum of tip speed ratios (5 to 7.5, with 0.5 step) to find the optimum tip speed ratio.

Moreover, chapter (6) highlights that Most of the available research work of horizontal axis wind turbines is focused on either lab-scale (15-60 cm rotor diameter) or commercial large-scale (80-130 m rotor diameter). There is a lack of published data on residential-scale turbines. The current work fills this gap because residential-scale turbines will be one of the key technologies during the next ten years since the current administration promotes dependence on renewables to cut carbon footprint. Therefore, the current work runs wind tunnel experimentation and performs 48 numerical simulations to evaluate the performance of a residential scale wind turbine with a blade generated from GOE 447 airfoil at three wind speeds (7.5, 12.5, and 17.5 m/s). Three different vortex generator designs were tested numerically when added on the suction side of a 7 m blade. Two of those designs produced more power than a baseline rotor does (7.2% and 10.9% more power than the baseline rotor were achieved at 12.5 m/s wind speed). Furthermore, three winglet designs were added to the baseline design to investigate their effect on power production. The 90^{o}, $60^{o,}$ and 30^{o} cant angles produce 5.0%,7.9% and 6.9% more power than the baseline design, respectively. It was very important to investigate the effect of combining the most successful vortex generator and winglet design on the performance of a single blade. Combining both techniques impairs the functionality of each other, leading to a deteriorated overall performance and less power (generally 6% to 8% less power than the baseline design).

Furthermore, chapter (7) utilizes wind tunnel experimentation and uses CFD simulations to evaluate the performance of a 14 m-rotor diameter residential scale wind turbine at three wind speeds (7.5, 12.5, and 17.5 m/s). The blades of the rotor baseline design are built using GOE 447 airfoil. Five different tubercle designs were applied to the blade's leading edge. One of those designs produces more power than a baseline rotor, with an optimum power improvement of 5.5% achieved at 12.5 m/s wind speed. Furthermore, three winglet designs were added to the tip of baseline design to investigate their influence on the power production. The 90°, 60° and 30° cant angles produce 5.0%,7.9% and 6.9% more power than the baseline design, respectively, at 12.5 m/s. Moreover, it is vital to investigate the effect of integrating leading-edge tubercles with winglets, then evaluate the influence of the combination on the aerodynamic performance and power output of the turbine model. It is found that when combining both techniques on the same blade, the improvement mechanism associated with each of them interferes with the other, leading to poor overall performance and less power in the majority of the run simulations.

Finally, chapter (8) highlights the topics that have potential for future work.

TABLE OF CONTENTS

LIST OF FIGURES

LIST OF TABLES

LIST OF NOMENCLATURE

Symbols

B	Number of rotor blades
C	Chord length (m)
C_l	Lift coefficient
Cp	Power coefficient
C_T	Thrust coefficient
D	Rotor diameter (m)
I_u	Relative turbulent intensity for axial velocity component
I_v	Relative turbulent intensity for vertical velocity component
I_T	Total turbulence intensity
k	Turbulence kinetic energy (m^2/s^2)
k_{sgs}	Sub grid scale turbulence kinetic energy (m^2/s^2)
k_{res}	Resolved kinetic energy (m^2/s^2)
L	Vortex Generator Length
M	Fraction of turbulence kinetic energy in the resolved motions
r	Rotor radius at any section along the blade span (m)
R	Rotor radius at tip section (m)
Re	Reynold number
S	Vortex Generator Spacing
T	Vortex Generator Thickness
$\overline{U}$	Mean axial wind velocity

$\bar{V}$	Mean vertical wind velocity
u	Axial wind velocity component
u'	Fluctuating axial wind velocity component
u'_{rms}	Root mean square velocity of the fluctuating axial component
v	vertical wind velocity component
v'	Fluctuating vertical wind velocity component
v'_{rms}	Root mean square velocity of the fluctuating vertical component

Vx or Vi	X-component of velocity vector
Vy or Vj	Y-component of velocity vector
Vz or Vk	Z-component of velocity vector

Greek letters

α	Angle of attack (°)
$\mathcal{E}$	Turbulent kinetic energy dissipation rate (m^2/s^3)
ω	Specific turbulence dissipation rate (1/s)
λ	Rotor Tip speed ratio
λ_r	Speed ratio at any section along the blade span
ϕ	Angle of relative wind
θ	Vortex generator installation angle (°)
θ_T	Twist angle (°)
θp	Pitch angle (°)
$\theta p,o$	Pitch angle at the tip (°)

Abbreviations

ADC	Analogue to digital converter
AoA	Angle of Attack
BEM	Blade Element Momentum
CFD	Computational Fluid Dynamics
HAWTs	Horizontal Axis Wind Turbines
HOMER	Hybrid Optimization Model for Electric Renewables
HPC	High-Performance Computing
DNS	Direct numerical simulation
DDES	Delayed-Detached-Eddy Simulation
LES	Large Eddy Simulation
MRF	Moving Reference Frame
MW	Mega Watt
NACA	National Advisory Committee for Aeronautics
NREL	National Renewable Energy Lab.
OPENFOAM	Open-source Field Operation and Manipulation
OPT	Optimum blade
PIV	Particle Image Velocimetry
PV	Photovoltaic
RANS	Reynold Averaged Navier Stokes
RBM	Rigid Body Motion
RSM	Reynolds Stress Model
SGS	Sub Grid Scale

SST	Shear stress transport
TSR	Tip Speed Ratio
UOT	Untampered & optimum twist blade
UUT	Untampered & untwisted blade
VAWTs	Vertical Axis Wind Turbines
UWM	University of Wisconsin-Milwaukee
VFD	Variable Frequency Drive
VG	Vortex Generator
VTC	Vortex Trapping Cavity
WALE	Wall-Adapting-Local-Eddy viscosity
WTs	Wind Turbines

Chapter 1 : Introduction

1.1 Renewable Energy

Energy consumption has increased dramatically over the last decades due to the increase in the population. Fossil fuels (coal, natural gas, and oil) are the primary energy sources in most of the world due to their availability and high calorific value. However, there are limiting factors on the fossil fuels leading the world to seek for new energy resources that are abundant and can be a reliable substitute for fossil fuels. Some of these limiting factors are: fossil fuels are non-renewable, their consumption rate is much higher than their production rate thus expecting to deplete, and such resources are not clean energy sources since their extraction and energy production lead to a high carbon footprint [1]. Due to these reasons, the necessity to rely on and develop new technologies to harvest energy from renewable and clean resources like wind, hydro, and solar becomes a driving factor in the industry to fulfill the demand on electricity.

Currently, renewable energy plays a significant role in new power generation worldwide. Hydropower, wind, biomass and photovoltaic are the leading renewable energy streams with 99% of total renewable sources. These streams add up to hundreds of gigawatts in global energy generation. Further, these mitigate tons of greenhouse gases emissions [2] [3].

Renewable power generation can help countries meet their sustainable development goals through the provision of access to clean, secure, reliable and affordable energy. Renewable energy has gone mainstream, accounting for the majority of capacity additions in power generation today. Tens of gigawatts of wind, hydropower and solar photovoltaic capacity are installed worldwide every year in a renewable energy market that is worth more than a hundred billion USD annually.

Based on Renewables Global Status Report[1] 2019 [4], an evaluation of the world's total energy consumption by source was done by the end of 2017 shows that the majority of the world's total energy consumption still relies on fossil fuels (79.7%), while the modern renewable energy sources constitute only 10.6% of the world's total energy consumption (see **Figure** 1-1).

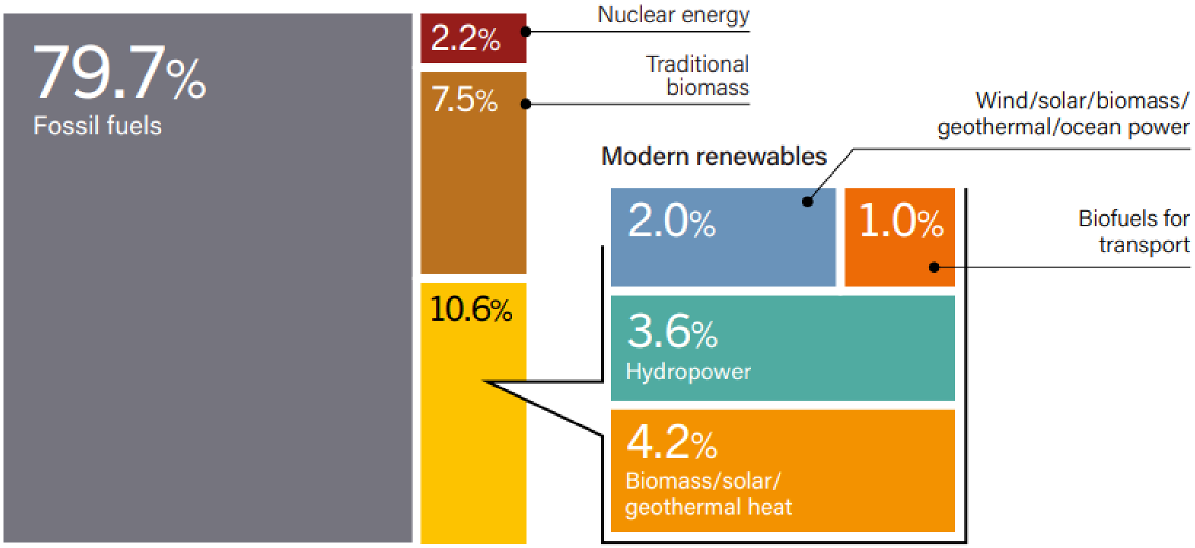

Figure 1-1: Estimated Renewable Share of Total Final Energy Consumption [4]

Meanwhile, within the last ten years, the share of renewables in the net annual additions of power generating capacities increases on yearly basis from 42% in 2008 to 65% in 2018. This fact is represented in **Figure** 1-2.

---

[1] REN21: Renewable Energy Policy Network for the 21st Century; a global renewable energy policy network that provides international leadership for the rapid transition to renewable energy.

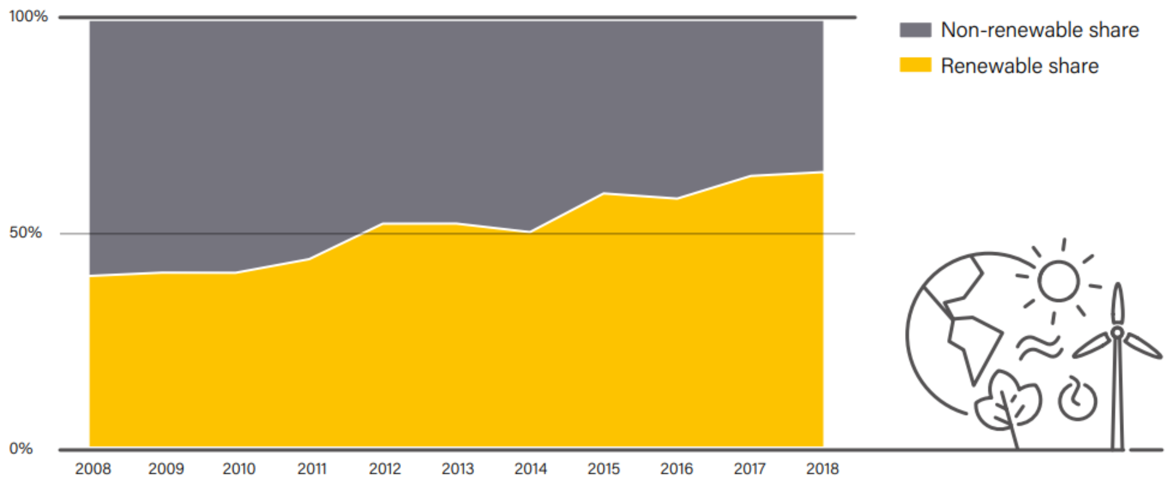

Figure 1-2: Annual Additions of Renewable Power Capacity, by Technology and Total [4]

Figure 1-3 shows the increase in global power capacity within 10 years, 2008 through 2018. The total world's installed capacity in 2008 was about 4600 Gigawatts, 21.7% of it was the renewables' share. However, the total world's installed capacity in 2018 reached 7100 Gigawatts, with 33.8% of it as the renewables' increasing share. It is worth mentioning that 50% of the renewables' share in this year goes for hydropower.

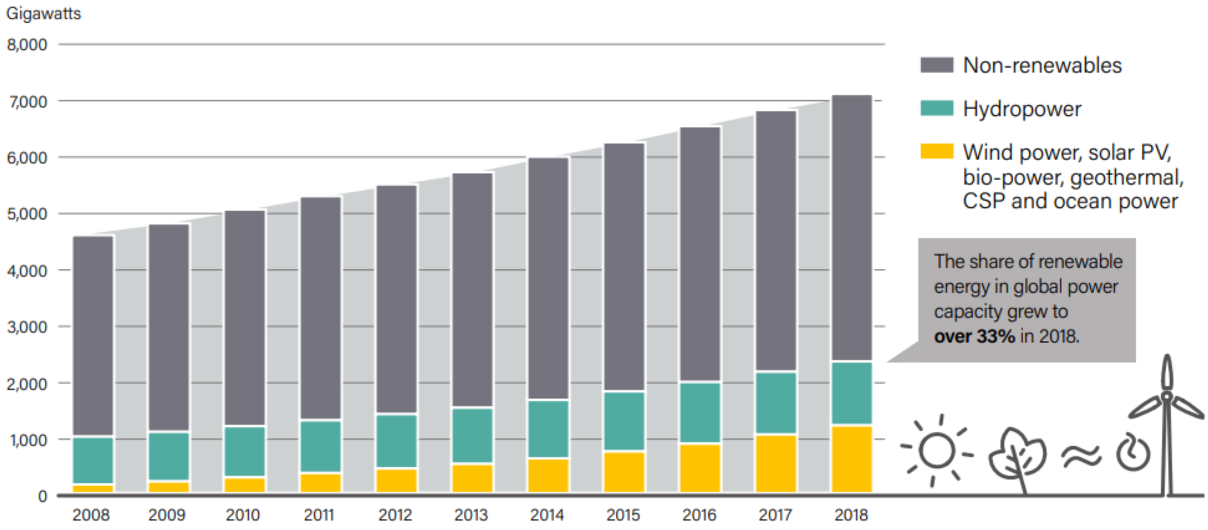

Figure 1-3: Global Power Generating Capacity, by Source [4]

1.2 Wind Power

According to the Global Wind Report [5], 2018 was a good year for the global wind industry with 51.3 GW of new wind energy installed, a slight decrease of 4.0 per cent compared to 2017, but a strong year, nonetheless. Since 2014, annual installations have topped 50 GW each year, despite ups and downs in some markets.

According to Renewables Global Status Report 2019 [4], global electricity production by the end of 2018, the world still depends on fossil fuel to generate the majority of its electricity (73.8%), while the renewable electricity share is only 26.2%. The largest share of the renewable electricity goes for hydropower (15.8%), while the wind power comes in the second place with 5.5% of the total global electricity production (see **Figure** 1-4)

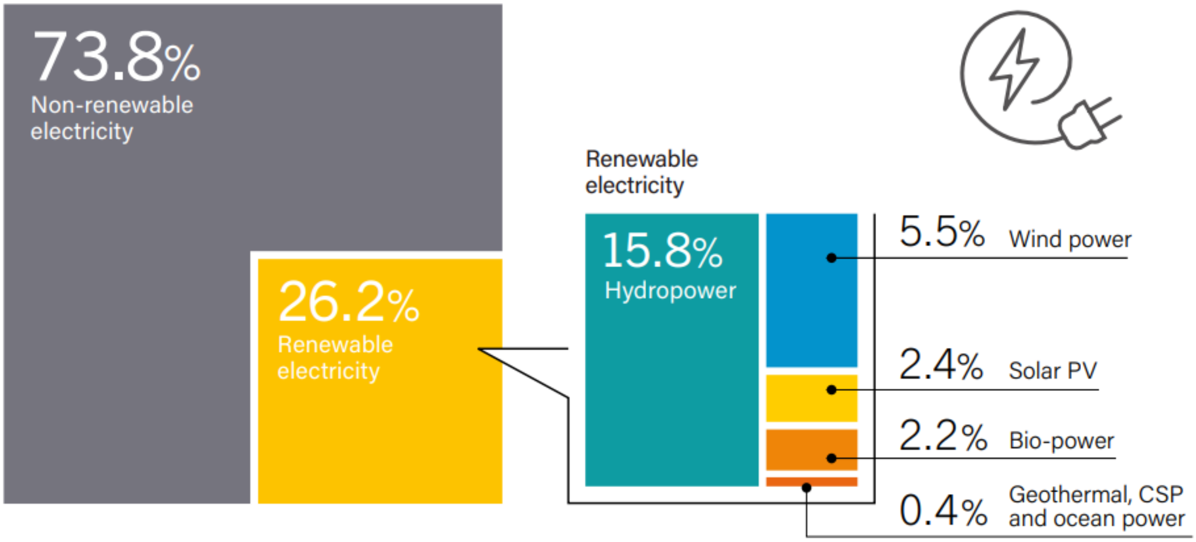

Figure 1-4: Estimated Renewable Energy Share of Global Electricity Production [4]

Figure 1-5 depicts on the annual additions of renewable power capacity categorized based on technology. Within 7 years, 2012 through 2018, the total renewable power installed is increasing. Solar PV panels technology comes as the fastest growing capacity (100 Gigawatts added by the end of 2018), then the wind technology comes in the second place with 51.3 Gigawatts added by the end of 2018.

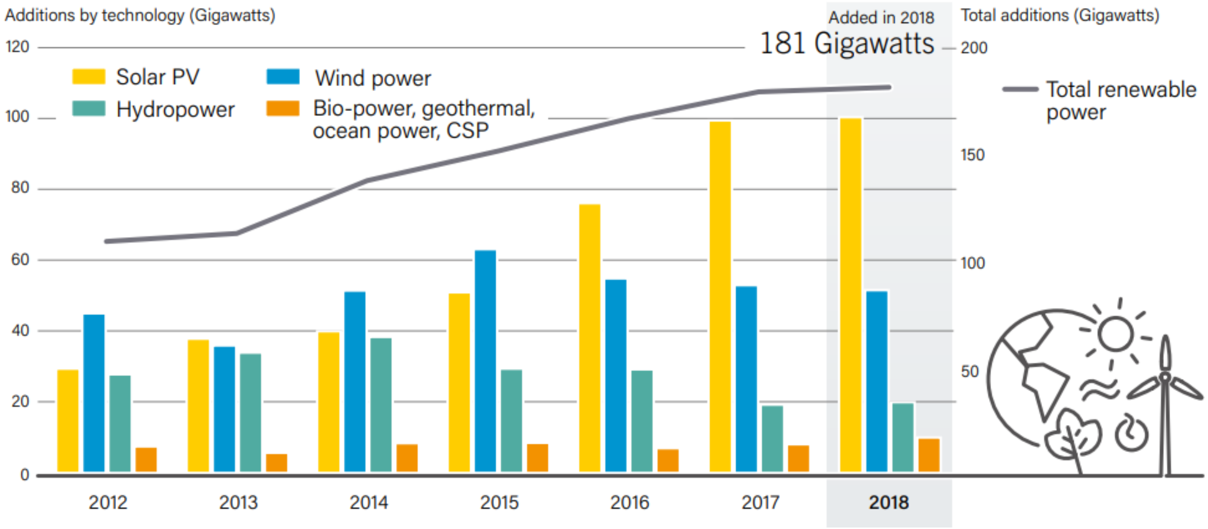

Figure 1-5: Annual Additions of Renewable Power Capacity, by Technology and Total, 2012-2018 [4]

1.3 Modern Wind Turbines

1.3.1 Definition of Wind Turbines

A wind turbine is a machine which converts the power in the wind into electricity. This contrasts with a 'windmill', which is a machine which converts the wind's power into mechanical power. As electricity generators, wind turbines are connected to some electrical network. These networks include battery-charging circuits, residential scale power systems, isolated or island networks, and large utility grids.

1.3.2 Principal of Operation

In modern wind turbines, the actual conversion process uses the basic aerodynamic force of lift to produce a net positive torque on a rotating shaft, resulting first in the production of mechanical power and then in its transformation to electricity in a generator. Wind turbines, unlike most other generators, can produce energy only in response to the resource that is immediately available.

1.3.3 Types of Wind Turbines

Wind turbines are classified into two general types: horizontal axis and vertical axis. A horizontal axis machine has its blades rotating on an axis parallel to the ground. A vertical axis machine has its blades rotating on an axis perpendicular to the ground. There are a number of available designs for both and each type has certain advantages and disadvantages. However, compared with the horizontal axis type, very few vertical axis machines are available commercially.

1.3.3.1 Horizontal Axis Wind Turbines

A Horizontal Axis Wind Turbine (HAWT) is the most common wind turbine design. In addition to being parallel to the ground, the axis of blade rotation is parallel to the wind flow. HAWTs have three designs, some wind turbines are designed to operate in an upwind mode (with the blades upwind of the tower). Large wind turbines use a motor-driven mechanism that turns the machine in response to a wind direction. Smaller wind turbines use a tail vane to keep the blades facing into the wind (see **Figure** 1-6 (a)). Meanwhile, other wind turbines operate in a downwind mode so that the wind passes the tower before striking the blades. Without a tail vane, the machine rotor naturally tracks the wind in a downwind mode, as shown in **Figure** 1-6 (b). Finally, **Figure**

1-6 (c) demonstrates some turbines that have an added structural design feature called an augmentor, a device intended to increase the amount of wind passing through the blades.

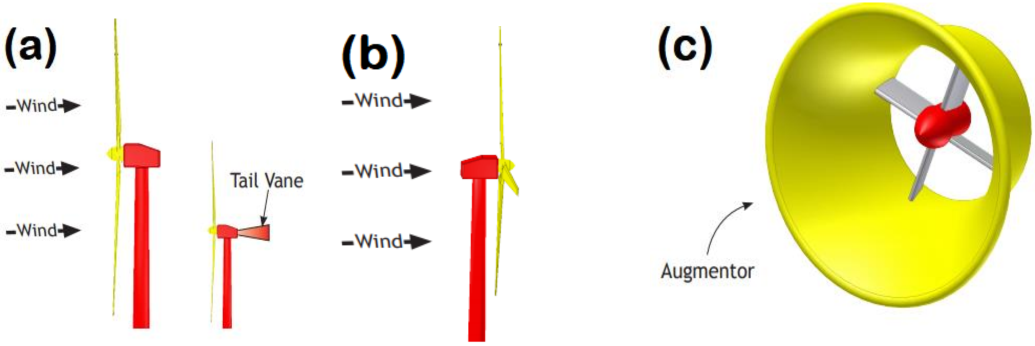

Figure 1-6: HAWTs designs, (a) Upwind, (b) Downwind, (c) Shrouded

HAWT Advantages

- The tall tower base allows access to stronger wind in sites with wind shear. In some wind shear sites, every ten meters up the wind speed can increase by 20% and the power output by 34%.
- High efficiency, since the blades always move perpendicularly to the wind, receiving power through the whole rotation. In contrast, all vertical axis wind turbines, and most proposed airborne wind turbine designs, involve various types of reciprocating actions, requiring airfoil surfaces to backtrack against the wind for part of the cycle. Backtracking against the wind leads to inherently lower efficiency.

HAWT Disadvantages

- Massive tower construction is required to support the heavy blades, gearbox, and generator.

- Components of a horizontal axis wind turbine (gearbox, rotor shaft and brake assembly) being lifted into position.
- Their height makes them obtrusively visible across large areas, disrupting the appearance of the landscape and sometimes creating local opposition.
- Downwind variants suffer from fatigue and structural failure caused by turbulence when a blade passes through the tower's wind shadow (for this reason, the majority of HAWTs use an upwind design, with the rotor facing the wind in front of the tower).
- HAWTs require an additional yaw control mechanism to turn the blades toward the wind.
- HAWTs generally require a braking or yawing device in high winds to stop the turbine from spinning and destroying or damaging itself.
- Cyclic Stresses & Vibration – When the turbine turns to face the wind, the rotating blades act like a gyroscope. As it pivots, gyroscopic precession tries to twist the turbine into a forward or backward somersault. For each blade on a wind generator's turbine, force is at a minimum when the blade is horizontal and at a maximum when the blade is vertical. This cyclic twisting can quickly fatigue and crack the blade roots, hub and axle of the turbines.

1.3.3.2 Vertical Axis Wind Turbines

The Savonius turbine is S-shaped if viewed from above (**Figure** 1-7 (a)). This drag-type Vertical Axis Wind Turbine (VAWT) turns relatively slowly but yields a high torque. It is useful for grinding grain, pumping water, and many other tasks, but its slow rotational speeds make it unsuitable for generating electricity on a large-scale. However, the Darrieus turbine is the most famous VAWT. It is characterized by its C-shaped rotor blades which give it its eggbeater appearance (**Figure** 1-7 (b)). It is normally built with two or three blades. Finally, the giromill is typically powered by two or three vertical airfoils attached to the central mast by horizontal supports (**Figure** 1-7 (c)). Giromill turbines work well in turbulent wind conditions and are an affordable option where a standard horizontal axis windmill type turbine is unsuitable.

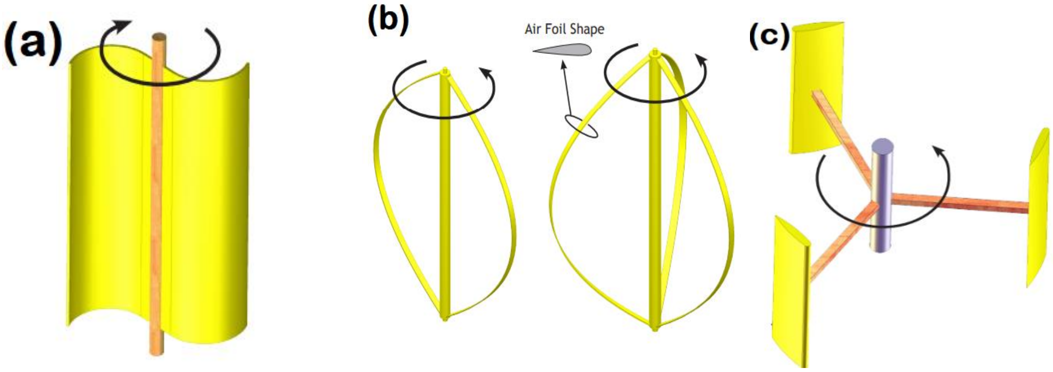

Figure 1-7: VAWTs designs, (a) Savonius, (b) Darrius, (c) Giromill

Traditional VAWT Advantages

- They can produce electricity in any wind direction.
- Strong supporting tower in not needed because generator, gearbox and other components are placed on the ground.
- Low production cost as compared to horizontal axis wind turbines.
- As there is no need of pointing turbine in wind direction to be efficient so yaw drive and pitch mechanism is not needed.
- Easy installation as compared to other wind turbine.
- Easy to transport from one place to other.
- Low maintenance costs.

- They can be installed in urban areas.
- Low risk for human and birds because blades moves at relatively low speeds.
- They are particularly suitable for areas with extreme weather conditions, like in the mountains where they can supply electricity to mountain huts.

Traditional VAWT Disadvantages

- As only one blade of the wind turbine works at a time, efficiency is very low compared to HAWTS.
- They need an initial push to start; this initial push that to make the blades start spinning on their own must be started by a small motor.
- When compared to HAWTs, they are very less efficient because of the additional drag created when their blades rotate.
- They have relative high vibration because the air flow near the ground creates turbulent flow.
- Because of vibration, bearing wear increases which results in the increase of maintenance costs.
- They can create noise pollution.
- VAWTs may need guy wires to hold it up (guy wires are impractical and heavy in farm areas).

1.4 Modern Horizontal Axis Wind Turbines Design

Today, the most common design of wind turbine, and the type, which is the primary focus of this research, is the HAWT. **Figure** 1-8 shows that the main advantage of HAWTs is having high power coefficient among other turbines which reach 49% at tip speed ratio (**λ**) = 7. All turbines VAWTs have low power coefficient and the smallest power coefficient is Savonius turbine having maximum power coefficient 0.15 at λ = 0.8.

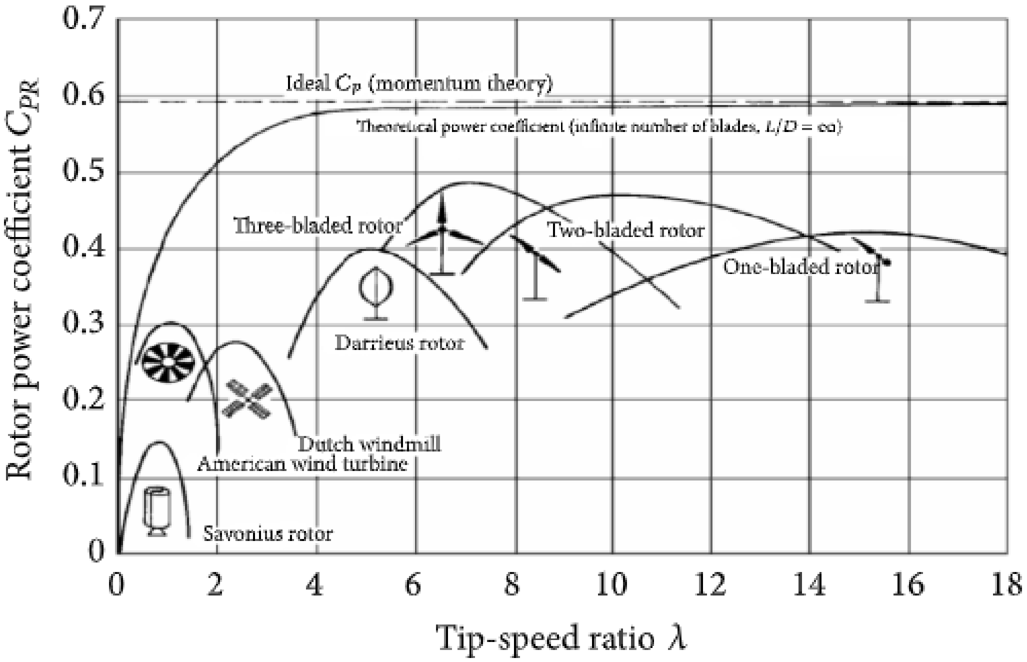

Figure 1-8: Typical performance of wind power machines [6]

HAWT rotors are usually classified according to the rotor orientation (upwind or downwind of the tower), hub design (rigid or teetering), rotor control (pitch vs. stall), number of blades (usually two or three blades), and how they are aligned with the wind (free yaw or active yaw).

The principal subsystems of a typical, land-based HAWT are shown in **Figure** 1-9. These include:

- The rotor, consisting of the blades and the supporting hub.

- The drive train, which includes the rotating parts of the wind turbine (exclusive of the rotor); it usually consists of shafts, gearbox, coupling, a mechanical brake, and the generator.
- The nacelle and main frame, including wind turbine housing, bedplate, and the yaw system.
- The tower and the foundation.
- The machine controls.
- The balance of the electrical system, including cables, switchgear, transformers, and possibly electronic power converters.

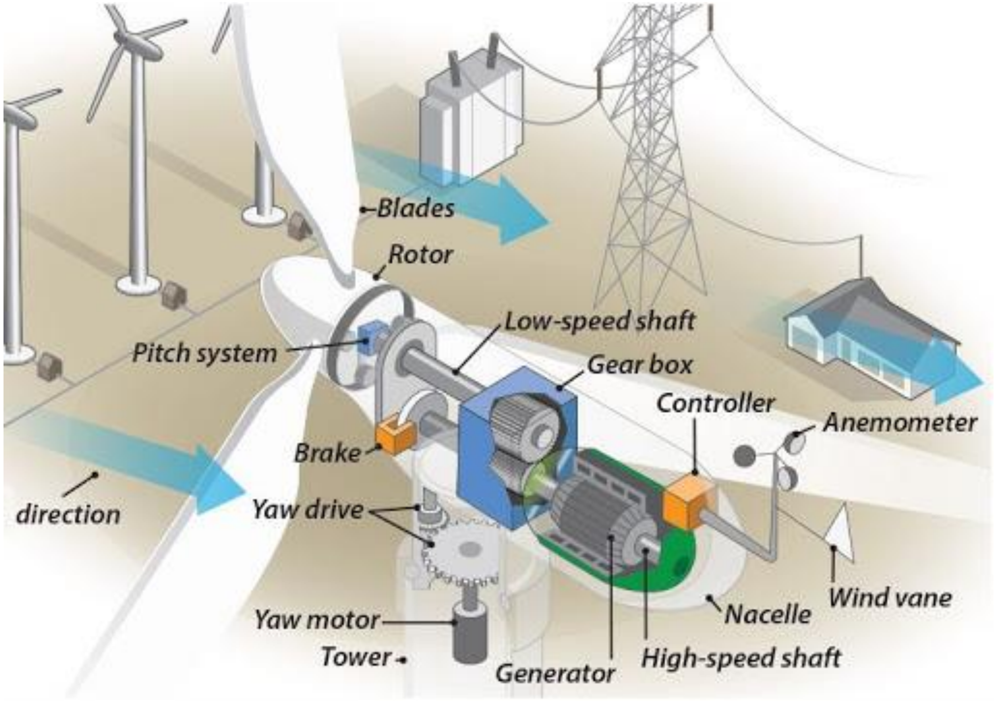

Figure 1-9: The principal subsystems of a typical, land-based HAWT

The main options in wind turbine design and construction include:

- number of blades (commonly two or three)
- rotor orientation: downwind or upwind of tower

- blade material, construction method, and profile
- hub design: rigid, teetering, or hinged
- power control via aerodynamic control (stall control) or variable-pitch blades
- fixed or variable rotor speed
- orientation by self-aligning action (free yaw), or direct control (active yaw);
- synchronous or induction generator (squirrel cage or doubly fed);

Chapter 2 : Literature Review

2.1 Introduction

As the world proceeds on both residential and industrial tracks, the energy demand increases on a daily basis accordingly. Nowadays, the entire world witnesses the drastic effects of global warming. Besides, the world's reserves of oil and fossil fuels come to an end one day soon. The two reasons mentioned above drive the world in the path of developing carbon-free and renewable energy resources. No doubt that wind turbines are one of these technologies which utilize the kinetic energy in the wind, then convert it into mechanical energy, eventually electrical energy. Therefore, the University of Wisconsin-Milwaukee founded the wind tunnel lab., equipped with the state-of-the-art research tools, to take part in this procession.

As a quick review of the wake aerodynamics of a horizontal axis wind turbine. The wake is divided into two regions; near wake and far wake, which is represented in **Figure** 2-1. In the near wake region, the free stream energy extraction by the rotor blades leads to pressure and velocity gradients which dominates the shape of the flow in that region of the wake. By transition to the far wake region, it is characterized by its minimum velocity deficit; since the wake velocity starts to recover its original value approaching free stream velocity, the velocity profile sounds axisymmetric and Gaussian in shape.

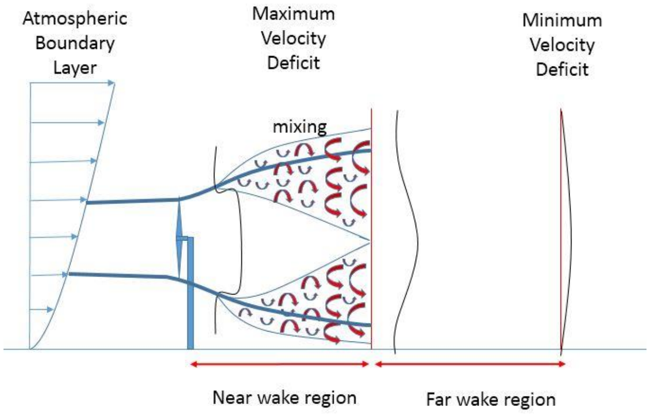

Figure 2-1: Wake profiles of a horizontal-axis wind turbine

2.2 Wake prediction and wind farm optimization models

Studies that quantify the extent to which the wind turbines can be built close to each other is of great importance to save, as much as possible, the cost of land and civil works related to wind farms, while maintaining the maximum power extraction. Therefore, the introduction of current work highlights the different approaches through which the wake region in wind farms was studied in the recent years, with the aim of either turbine blade optimization or wind farm optimization or both. The target approaches are the experimental approach, the Computational Fluid Dynamics (CFD) approach and any combination of them.

Crespo et al. [6] issued a multi-disciplinary study that comprised five sections. Their work is one of the earliest works in the field that had this comprehensive nature.

Section one covered some studies that treated turbines as distributed roughness elements. Based on that assumption, some researchers assumed a logarithmic wind profile for the free stream, others assumed the logarithmic profile for below hub height, but above hub height was supposed to have another pattern with a roughness related to turbine drag (due to power extraction). By this modified profile they obtained the wind velocity attacking each turbine then calculated the extracted power. Although models depend on this assumption to study the wake are now replaced by more accurate ones, it still can predict overall changes in wind characteristics due to passing over large wind farms.

Section two was devoted to discussing models for individual wakes. It started with a detailed description of the wake behavior to be simulated with kinematic and field models. The main factor that derive the wake behavior is the vortex sheets, formed due to variation in circulation along the blades, which results in tip vortices in the form of helical trajectories. These helical trajectories act as a cylindrical shear layer that separate the decelerated flow inside the wake from the ambient outside flow. As we go downstream, due to turbulent diffusion, the outer diameter of the cylindrical shear layer expands. However, that expansion length is limited to one rotor diameter. As we go further downstream, the shear layer thickness increases due to turbulence diffusion till it reaches the wake axis at about two to five rotor diameters, which ends the near wake region. By transition to the far wake region, it is found completely developed without any ambient shear perturbation.

Section three was dedicated to discussing the wake effects in wind farms, starting from studying the interaction of several wakes. The simplest approach was adding the velocity deficits and turbulence kinetic energy of each single turbine to come up with the wind farm wake characteristics. A more accurate approach was to solve the flow equations for the whole wind farm, but the feasibility of this approach depended on the parabolic approximation as a simplifying assumption. One of the essential experimental outcomes presented in this section is that the turbulence intensity had a peak at the second row of turbines, then it settled down to an equilibrium value at the third to the fourth row of turbines. Moreover, this section focused on the topographic effect, turned to the simultaneous study of both the previously mentioned parameters, ended up with shedding light on the offshore wind farms.

Section four showed a brief idea about an alternative tool for wind farm designers, which is the quasi-analytical and semi-empirical expressions that describe the tendencies of the dominant parameters that drive wake evolution, while section five discussed some measurements of structural loads (i.e., dynamic and fatigue loads) affecting the turbine under wake conditions. However, both sections are out of the current work's focus.

Sanderse et al. [7] studied the state-of-the-art numerical calculation of wind turbine wake aerodynamics. Their study included different CFD techniques to model both the rotor and the wake. Their work comprised two approaches for rotor modeling, the generalized actuator disc approach, in which the rotor is represented by forces, and the direct approach. The generalized actuator disc approach can be represented by one of the following methods: actuator disk, actuator line or actuator surface. They discussed the applicability and limitations of the two most essential methodologies in turbulence modeling for wind turbine wakes, RANS and LES. The parabolic, elliptic and linearized models were included when studying RANS.

For rotor modeling, they concluded that the direct approach is not yet appropriate to neither optimizing turbine blades nor optimizing farm layout. They justified the use of actuator approach because the differences between it and the direct approach in the far wake were minimal. Although the actuator line and actuator surface are more accurate, they preferred the use of the actuator disk method because it is sufficient and requires lower computational efforts.

For wake modeling, they found that LES showed more agreement with the experimental data compared with RANS. However, they recommended the use of RANS because LES requires more computational effort, two orders of magnitude, which limits its use in farm applications.

Sumner et al. [8] performed a comprehensive study that covered CFD applications in the field of wind energy starting from the flow around 2D airfoils to the flow through an entire wind farm. Their work can be divided into three main sections. The first section dealt with the application of CFD on 2D airfoil to predict its characteristics to use it in the design of wind turbine blade. Then, the second section showed the great effort done in recent years to develop the numerical techniques used to solve the 3D flow field around an operating turbine. Finally, the third section presented alternative techniques to full 3D CFD studies, like actuator disk or surface techniques, which appeared promising to study the rotor aerodynamics, particularly when it is needed to model the wake effect in a wind farm. Besides, flow over original topography was represented.

Sumner et al. concluded their work with that both the CFD analysis and wind tunnel experiment may be compared to each other in cost. However, CFD has the advantage of providing field data not only points. Moreover, in the short term, RANS approach will be the base of CFD applications by the wind energy sector. In the long term, LES – based methods will eventually supersede the RANS techniques to be able to solve the flow field over complex terrain and to determine the sitting of turbines in a wind farm accurately.

Miller et al. [9] shed light on the trends in techniques, technology, and application of numerical simulation on the wind energy sector. Their work reviewed new numerical simulation techniques for analysis and optimization of flow over complex terrain, cost optimization models and wind farm layout optimization models. Such studies and models were not possible before.

They also reviewed some papers that used the Atmospheric Boundary Layer (ABL) simulation models to select the proper location for a wind farm or to evaluate the current site of previously set up wind farm by simulating wind velocity through the site.

They concluded their work by confirming that replacing and supplement experiments with numerical simulations. For example, CFD analysis of a turbine's wake proved to be better than the wind tunnel analysis. They also presented a study that optimized the dual wind turbine design using CFD instead of depending only on the wind tunnel testing. Also, they included some reviews that were able to capture some phenomena using CFD which were difficult or impossible to observe by experimental measurements. For instance, it was possible to research the 3P pulsation due to wind shear by CFD. As well as finite element analysis (FEA) was able to predict and minimize damage due to vibration in turbine support structures.

Xiaoxia et al. [10] reviewed in their literature some works that quantified the power output loss and increased fatigue load due to the grouping of multiple wind turbines in a wind farm. These works handled the problem of how to arrange the wind turbines in a wind farm. They reviewed some other works focused on the detailed knowledge of the flow and its turbulence structure within the wake region because such practices are essential for the wind farm turbines layout optimization and overall power output prediction.

They developed and validated a newly proposed a 2D analytical wind turbine wake model that adopted Jensen’s wake model [11] as it is the most widely used model for the wind farm layout optimization studies, coupled with Gaussian function, to come up with Jensen-Gaussian wake model to predict the velocity deficit inside the wake region. Then, the new model was combined with the multiple population's genetic algorithm (MPGA) optimization method to optimize the wind farm layout. The performance of the new model was validated against the classic Jensen’s wake model, the cosine shape wake model, and also against real wind tunnel measurement data.

They found that the new model prediction of the velocity deficit is in an excellent agreement to the experimental measurements at different downstream distances. The unique model considered the turbulence inside the wake beside the ambient turbulence. Therefore, the new model ability of wind farm efficiency and power output prediction was more realistic when a comparison held between its performance and the performance of some previous layout studies.

2.3 HAWTs performance and power optimization

Studies that serve projects like wind farm design layout and power generation optimization are of critical importance because the global installed wind energy capacity by the end of 2018 exceeded 591 GW and expected to soar to reach 700 GW by the end of 2020. The previous expectation is based on an increasing percentage of installed capacity ranging from 9.6% to 17.1% in the past five years. [5]

During the last decade, most of the Computational Fluid Dynamics (CFD)-based research works aimed at two main objectives; the first one is HAWT blade optimization. The second one is the wind farm layout optimization. Therefore, the next two sub-sections shed light on 23 previous works; the first 20 of them focus on the first objective, the last three focus on the second objective.

2.3.1 HAWTs blade design optimization

2.3.1.1 Testing different airfoils, blade tapering and twist rates

Amano et al. [12] presented a comparison between the straight and swept edged blades regarding wake sizes and shapes at different wind velocities. At that time, the Blade Element Momentum (BEM) based methods were widely used in industry and research to predict blade performance. The BEM could specify the chord length and angle of twist based on three inputs: rotation rate, wind speed, and spanwise position. The disadvantage of the BEM was that it dealt with each blade cross-section independently. Thus, the complex 3D flow effects were not taken into consideration. For that reason, they used CFD in their work since it solves the governing fluid flow equations instead of depending on predetermined airfoil data to predict blade performance as in BEM. They investigated the swept-edged blade in addition to the straight blade because the swept-edged blade includes the effect of spanwise velocity component and the delay of the stall point of the rotor.

Amano, et al. performed wind tunnel experiments on a full HAWT blade and generated a CFD model of the turbine blade using a 120^o wedge-shaped domain taken lengthwise along the horizontal axis. They used the structured mesh near the blade as this is the area of interest and the unstructured mesh away from the blade. They used the Shear-Stress Transport (SST) k-ω turbulence model along with the moving reference frame function available in FLUENT to include the effect of rotation in fluid flow.

They discovered that for both straight and swept-edged blades, full flow separation occurred at 15 m/s, with power stall at higher speeds. In addition, they found that the wake length increased for both blades up to 15 m/s; at higher speeds, the wake length for the swept edged blade was larger than the straight blade due to the formation of higher spanwise flow along the swept blade.

Shen et al. [13] used the lift surface model as a performance prediction model coupled with a genetic algorithm to describe an optimization method for the design of HAWTs. The two objectives of the proposed optimization method were obtaining the maximum annual energy production and minimum blade loads; hence the minimum cost of the turbine. They applied the method proceeds to the National Renewable Energy Laboratory (NREL) Phase VI rotor to show that the optimization model would result in a more efficient design.

To verify the numerical simulation model, they adopted two ways of comparison. They compared the predicted power to the measurement and achieved 98% agreement in the attached flow region up to 9 m/s wind speed of, but a deviation of 10% was detected beyond that speed limit due to blade stall. In addition, they compared the predicted normal and tangential force coefficients to the measured coefficients at 7 m/s and found 99% agreement along the entire blade span.

Shen proposed two optimized designs to apply to the NREL phase VI rotor blades, the swept-curved and optimized swept-curved blades. Both designs led to performance improvement. The amount of improvement was clearer at higher wind speed (7 & 9 m/s). For instance, for 9 m/s, at mid-span of the blade, the tangential force was 10% higher, and the normal force is 6% higher than their counterparts of the original blade. Besides, rotor thrust coefficient of the optimized designs was less by 3%. Hence, it was discerned that the annual energy production increases and blade root flap wise momentum decreases due to the optimization.

Unlike BEM, CFD considers the 3-D and rotational flows as a result of solving the Navier-Stokes equations for each cell in the domain. De Bellis et al. [14] used the ANSYS Fluent package with the Spalart-Allmaras (SA) turbulence model, integrated that into the single and multi-objective optimization models provided by the modFrontier software to propose a certain twist and chord distribution for a new blade profile, which was shown to give higher torque when compared to the NREL phase VI blade, under both attached (7 m/s) and stalled (20 m/s) flow conditions.

Beyhaghi and Amano did great efforts to improve the aerodynamic performance of cambered airfoils using leading-edge slots. They investigated the effect of five design variables (slot's length, slot's thickness, inlet angle, exit angle, and vertical position) on two objective functions (lift and lift over drag ratio). They discovered that slot's length, inlet angle and vertical position are more influential in controlling the objective functions [15]. Besides, they evaluated the capability of creating narrow channels near the leading edge of NACA 4412 airfoil in increasing lift and decreasing drag. By slightly lowering the slot position with respect to the original design, and tilting up the first leg a few degrees, they could get 8% improvement for lift coefficient over the entire range of angles of attack, without drag penalty [16].

Since maximizing the amount of wind energy converted into electrical energy is essential, several studies were conducted to study the different parameters affect the wind turbine performance, to obtain the maximum energy available in the wind. One of the most essential perspectives is the aerodynamics analysis of different blade profiles, which was performed by Kurtulmus et al [17]. They studied the aerodynamics of different NACA blade profiles (NACA 0012, 4412, 4415, 23012) to get the most optimum angle of attack (at the maximum sliding rate) using Snack 2.0. It was found that for Re less than 3,000,000 the optimum angle of attack was from 3^o to 9^o. However, for Re higher than 3,000,000, the range was from 3^o to 7^o.

Three different Horizontal Axis Wind Turbine (HAWT) blade geometries with the same diameter of 0.72 m using the same NACA 4418 airfoil have been investigated both experimentally and numerically by Hsiao et al. [18]. The first is an optimum (OPT) blade shape, obtained using improved Blade Element Momentum (BEM) theory. The second is an untapered & optimum twist (UOT) blade with the same twist distributions as the OPT blade. The third blade is untapered & untwisted (UUT). All the wind tunnel experiments were performed at constant wind speed (10 m/s), while the different tip speed ratios (λ) were obtained by adjusting the wind turbine's rotational speed. The mechanical torque, which is used to compute the power coefficient (C_P), was measured by averaging the values of the torque transducer.

They concluded that the OPT and UOT blades performed with the same maximum power coefficient, $Cp = 0.428$, but at different tip speed ratios; $\lambda = 4.92$ for the OPT blade and $\lambda = 4.32$ for the UOT blade. Meanwhile, OPT is considered better than UOT since it gives high Cp (higher than 0.420) at wider range of tip speed ratios (4 to 5.5). The UUT blade had a maximum power coefficient of $Cp = 0.210$ at $\lambda = 3.86$, which is less than the first two blades.

2.3.1.2 Testing different winglet designs

Regarding winglets, Tobin et al. [19] used a Particle Image Velocimetry (PIV) system to investigate two similar turbine models, one with the standard rotor design, the other with downstream-facing winglets. It is wanted to see the effect of the winglets on the wake aerodynamics, power and thrust coefficients of the model. They opted for the downstream-facing winglet design since it was proven in their literature that this design was the most effective in power increase. Turbine power was obtained from DC generator terminals.

They obtained an improvement of 8.2% and 15.0% for the power and thrust coefficients of the winglet model. They justified the power increase with the induced drag reduction happened in the winglet model case due to decrease in tip-vortex strength.

Khaled et al. [20] investigated the influences of winglets on the aerodynamic performance of a small horizontal axis wind turbine, particularly on power and thrust coefficients. Firstly, they investigated the effect of winglet length variation (changed from 1% to 7% of the turbine rotor radius), while the cant angle is fixed at 90°, and Tip Speed Ratio (TSR) changed from 2.5 to 9.6. They found that for all cases, the power maximized at the design TSR of 5 then drops, while the thrust coefficient (C_T) continued increasing till TSR is 8.4 then started to fall.

Secondly, for each winglet length, the cant angle changed from 15° to 90°, while the TSR is maintained at its optimum value (5). They found that Cp range increased by the increase of winglet length. Moreover, at each length, Cp is maximum at a cant angle of 50°, while C_T is maximum at 30°.

Farhan et al. [21] numerically tested two different winglet planforms, rectangular and elliptical, using CFD. They applied the two planforms to two different airfoils, S809 and PSU 94-097. For each case of the four cases, two cant angles were tested (45° and 90°), with winglet length changed from 5 cm to 15 cm, and wind speed changed from 5 m/s to 25 m/s. They performed 144 simulations to investigate the effect of the winglet parameters mentioned above on the wind turbine's power output, compared to a baseline design (the NREL phase VI rotor). They found that the optimum winglet design is the rectangular planform when applied to the S809 airfoil with 45° cant angle and 15 cm length at a wind speed of 10 m/s.

Khalafallah et al. [22] investigated the capability of a winglet to increase the turbine power of a horizontal axis wind turbine. In particular, they studied the effects of winglet direction, cant angle, and twist angle for two winglet orientations: upstream and downstream directions.

For each winglet direction, the twist angles are –2°, 2°, and 10° were studied at each of cant angles 20°, 40°, and 60°. To focus on the effect of winglet parameters on the turbine performance, the computations have been performed at the design TSR of 6. In general, they concluded that the winglet pointing to the downstream side showed a more increase in power than those pointing to the upstream side. They claimed that a general increase of the power coefficient occurred except for the three cases of a cant angle of 60° at which the winglet was on the upstream side. A maximum increase in Cp of 1.75% (more than baseline design mentioned in their literature) was observed where winglet pointing to downstream side and has a cant angle of 60° and a twist angle of 2°.

Johansen et. al [23] studied the effect of winglets on wind turbine blades using CFD, they studied different winglet configurations with different heights (1-4% of the rotor radius), different curvature radius (12.5 – 100% of the winglet height), different sweep angles (0° and 30°) and different twist angles (0°-8°). The maximum increase in power was 2.77% with a 3.55% increase in thrust when using 1% of the rotor radius as the winglet height and 50% of the winglet height as the curvature radius along with a twist angle of 4°. Generally, they claimed that mechanical power and thrust increases as the curvature radius decreases. Also, mechanical power and thrust increases as winglet height increases. The power and thrust dependency on the winglet tip twist are very minor.

Muhle et al. [24] performed a pure experimental study that focused on showing the effect of different wing tip configurations on the tip vortex formation and interaction in the near wake of a two-bladed model wind turbine. They investigated the impact of switching from the straight-cut wing tip to the downstream-facing winglet on several parameters. Regarding the mean streamwise velocity, the presence of winglets didn’t significantly affect the mean velocity field. Regarding wake expansion, winglets generated a slightly wider wake than the straight-cut tip. Regarding the phase-averaged vorticity component, an analysis was done between two downstream distances (2.3D and 2.6D) revealed an instability caused by winglets that stimulated tip vortices interaction with the main wake and caused complete breakup at earlier downstream distance of 3D, whereas the straight-cut tip didn’t show any tip vortices interaction till 3.5D. Finally, considering applying winglets to models used in a wind farm, winglets caused earlier and faster tip vortex breakup, the point that enhanced the recovery of the mean wake kinetic energy, which means more potential power extraction out of a downstream turbine.

Ostovan and Uzol [25] did also a pure experimental work to investigate the effect of installing winglets and some wing extensions on the performance of two identical and interacting horizontal axis wind turbines. The attached the winglets and the wing extensions to the upstream turbine to see how this impacts the Cp of the upstream turbine, downstream turbine, and the two turbines combination. They found the for the upstream turbine, the baseline design (without any tip devices) produced the lowest power. Attaching winglets produced 2.6% more power than the baseline design, while attaching the wing extensions produced 17.1% more power than the baseline design. On the other hand, the downstream turbine produced the highest power when the upstream turbine had no tip devices. Attaching the winglets to the upstream turbine caused the downstream one to generate 4.1% less power, while attaching the wing extensions to the upstream turbine resulted in generating 15.7% less power out of the downstream one. Regarding the overall power of the two turbines combination, it increases by 1.1% when winglets were installed to the upstream turbine, while it increases by 9.6% when wing extensions were installed to the upstream turbine.

2.3.1.3 Testing different tubercle designs

Regarding tubercles, Ibrahim et al. [26] used the typical airfoil for entry level wind turbines, NACA 4412, to generate three blade configurations, straight, leading-edge slots and trailing-edge tubercles. Three models 60 cm rotor diameter each were tested at the University of Wisconsin-Milwaukee wind tunnel at a range of low wind speeds (4.1 to 5.15 m/s), to investigate the effect of the two addition to the straight blades on Cp. They found that the slotted leading-edge design gave the highest range of Cp (0.3 to 0.44), then the straight design with a Cp ranging from 0.2 to 0.4, while the trailing-edge tubercles gave the lowest range of Cp (0.08 to 0.18)

Kumar et al. [27] performed a numerical study to investigate the effect of adding leading-edge tubercles to the basic wind turbine model using NACA 4412 airfoil. It is wanted to investigate the effect of adding tubercles on the velocity at which stall occurs. It was found that the tubercles retarded the stall occurrence up to 15 m/s.

Abate et al. [28] studied the effect of 20 different tubercles configurations on the power production of the basic NREL phase VI wind turbine rotor. They found that a significant power improvement was achieved for the high wind speed cases (tubercles showed a 25% power increase at 20 m/s), while the opposite trend was obtained at lower wind speeds (tubercles showed a 45% less power at 10 m/s). The reason behind the previous finding is that the flow around tubercles was characterized by counter-rotating vortices generation, which counteracts the spanwise flow, resulting in a stall strength reduction.

A study that included the effect of leading-edge slots, tubercles and winglets on the straight design power production was done by Amano el al. [29]. They used a hot wire anemometer to perform velocity measurements in the wake of model wind turbine with straight blade generated using NACA 4412 airfoil. Then, they used the experimental data for a numerical model validation. Slots, winglets and tubercles were tested numerically only, to investigate the effect of those modifications on power generation of the straight design. At a wind speed of 9 m/s for both experiment and simulations, the slotted design gave 19.3% higher power than the straight design, then the winglet design produced a 2.5% higher power than the straight design, while the tubercle design produced 76.8% less than the straight design.

Huang et al. [30] performed an experimental study to investigate the effect of applying leading edge protuberances (tubercles) on the performance of both static 3D airfoil and a three-bladed HAWT model. Four protuberant models were created to be applied on the leading edge of the baseline static airfoil, with an amplitude equals 1.5% and 8.5% of the chord length, and a wavelength equals 15% and 6.5% of the chord length. To fix Re, the lower amplitude protuberances were tested at 9.5 m/s, while the higher amplitude protuberances were tested at 10.5 m/s, whereas the AoA was changed from -10 to 40. They found that the protuberance wavelength had a minor effect on the lift coefficients of those with smaller amplitudes. However, wavelength had a major effect on those protuberances with larger amplitudes. Regarding the rotor models, they applied four sinusoidal protuberance configurations to the leading edge of the baseline rotor. The four configurations come from combining two amplitudes (4% and 12% of the chord length) to two wavelengths (40.4% and 14.5% of the chord). All resultant rotors were tested at wind speeds of 6, 8 and 10 m/s, while the TSR increased from 1 to 8 at each wind speed. All protuberances configurations didn’t improve Cp, except for the smaller- amplitude, larger- wavelength configuration that generated more power than the baseline rotor only at wind speed of 6 m/s.

Zhang and Wu [31] used RANS simulations to investigate the effect of adding sinusoidal waves (tubercles) to the leading edge of a rotor blade on the shaft torque of a wind turbine. They proposed five different configurations of tubercles with wavelengths equal 17%, 25% and 42% of the root chord, and wave heights (half amplitudes of sine wave) equal 1.25%, 2.5% and 3.75% of the root chord. They found that for design condition (wind speed is less than 12 m/s), blade with leading-edge tubercles is unfavorable, since an early boundary-layer separation occurs due to the geometric disturbances of the leading-edge tubercles, hence shaft-torque decreased for the five cases. On contrast, for off-design conditions (wind speeds higher than 15 m/s), shaft-torque increased significantly, particularly for the cases with high wavelength and wave height (for instance, at 15 m/s, the shaft-torque is 85% higher than the torque of the straight blade).

2.3.2 Turbine and wind farm performance optimization

Jackson and Amano [32] carried out a comprehensive study which included experimental and CFD analyses of the wake dynamics behind a small-scale HAWT. The wind tunnel at UWM was used to perform single, double and triple testing at 6.6 m/s wind speed. Hotwire anemometry was used to measure the axial and vertical velocity components. Furthermore, high-speed camera imaging was done to provide only a qualitative description for the blade-generated vortices evolution and the wake turbulence structure.

Regarding CFD, they used the Reynold Stress Model (RSM) with a fully-discretized rotor, the issue that raised the computational cost, but the UWM High-Performance Computing (HPC) cluster made the mission simpler. They implemented the steady state Moving Reference Frame (MRF) model hence used its results as an initial condition for the unsteady Rigid Body Motion simulation. Finally, the experimental results were in a good agreement to the experimental data.

They concluded their work with that the fully-discretized rotor RSM simulations were more accurate than the actuator disc RANS based simulations, the issue that would help wind turbine and wind farm designers for well understanding of wake regions hence build wind farms with less blade vibrations and higher efficiency.

Ma et al. [33] used ANSYS Fluent software to perform coarse-resolution CFD simulations using two different techniques; the first technique was the unsteady Delayed-Detached-Eddy Simulation (DDES) with SA as a turbulence model, while the second technique was the steady Reynolds-Averaged Navier-Stokes (RANS) with the SST k-ω turbulence model. The purpose of these simulations was the performance of a real 5.8-kW HAWT in the form of power coefficient (Cp) comparison at several TSRs. They compared the experimental values of Cp at several TSRs to their predicted counterparts by both turbulence models. They recommended the use of the DDES technique for most of engineering and industrial wind turbine applications due to its reliability, regardless of the more significant computational effort required.

Choi et al. [34] used the commercial multi-purpose CFD solver ANSYS CFX to build a full wind farm model which contained two HAWTs with full-scale dimensions; each turbine provided 2 MW output power. They carried out a steady-state analysis of the problem using the RANS approach with the SST k-ω model. The separation distance between the two turbines was increased from one case study to another; hence, the power output of the downstream turbine increased significantly, which meant an increase in the wind farm annual energy production.

In the light of the importance of testing different airfoils and blade profiles [12-18], and the importance of winglets [19-25] and tubercles [26-31] for HAWTs power output improvement, in addition to the efforts done to optimize a wind farm power generation [32-34], this work decided to conduct experimental studies to understand the wake of a HAWT. Moreover, use a number of newly tested airfoils, and to implement the state-of-art modifications, to optimize power production of residential-scale wind turbines.

Chapter 3 : Experimental Study of the Wake Regions in Wind Farms

This chapter scans the details the wake region that evolves behind a single wind turbine model by focusing on three parameters: average axial wind velocity component, velocity deficit and total turbulence intensity. The testing was done at mainstream velocity, U_∞, of 5 m/s, the u and v velocity components were captured by x-probe dual-sensor hot wire anemometer. A detailed description of the experimental setup is presented including the wind tunnel, the model wind turbine, the traverse system, the hot wire probe, the hot wire anemometer, and the hot wire calibrator.

A huge amount of point data was obtained then processed by a Matlab script to plot the desired contours through the successive transverse sections along the entire length of test section. By monitoring the previously mentioned flow parameters, the regions of low velocity and high turbulence can be avoided while the location of the subsequent wind turbine is selected. The estimation of the distance at which the inlet flow field will restore its original characteristics after being blended through the rotor blades is very important as this is the distance that should separate two successive turbines in an inline configuration wind farm to guarantee the optimum performance and to extract the maximum power out of the subsequent array of turbines.

3.1 Experimental Setup

3.1.1 Wind Tunnel at UWM

The wind tunnel at UWM Lab. has hexagonal shaped cells at inlet section to reduce large scale turbulence. The first section is the contraction section which has an inlet area of about 9.3 m^2 and a contraction ratio of 6.2. Then, the test section comes with dimensions of 1.2m x 1.2m x 2.43m, and cross-section area of 1.4 m^2. It has polycarbonate walls to provide a smooth surface hence eliminate the boundary layer effect as much as possible. The final section is the diffuser section which has an expansion ratio of 2.25. This section ends up with six blades suction fan, which is of 1.83 m rotor diameter attached to 25.4 kW motor controlled by a variable frequency drive (VFD) to obtain different wind speeds through the test section. The wind tunnel with its three sections is shown in **Figure** 3-1.

Figure 3-1: UWM wind tunnel sections

3.1.2 Model Wind Turbine at UWM Lab.

The design of the model used in this work is demonstrated in **Figure** 3-2 .It is a small scale 3-blades model of 20.3 cm rotor diameter made from ABS plastic. Its tower is made from 12.7 mm diameter steel rod with hub height of 30.5 cm. In addition, it has a base in the form of steel plate with dimensions of 30.5 cm x 30.5 cm x 6.4 mm, to guarantee fixing the model in its place when the blowing wind speed is high.

The three-blade model, shown in **Figure** 3-3, was used to create the blades on a 3-D rapid prototyping machine. The turbine blade cross section was built according to NACA 4424 profile drawn in **Figure** 3-4. The reason why NACA 4424 profile was selected is that its design offered a thicker blade profile relative to the chord length to improve the strength and prevent the blades from breaking during testing.

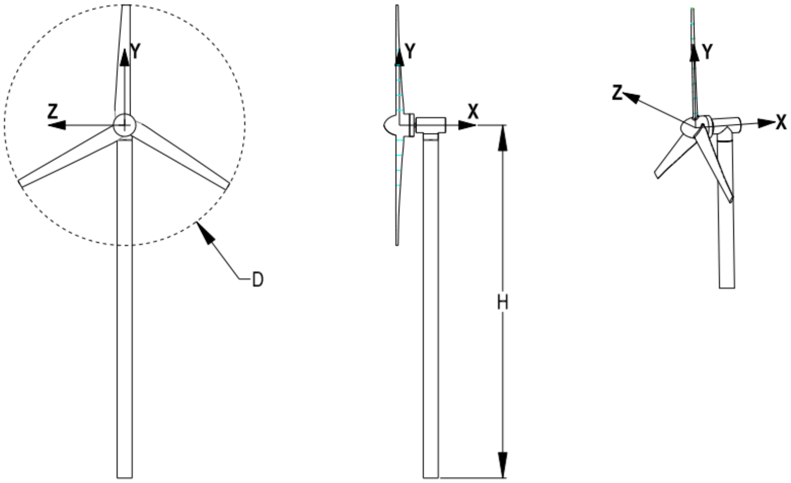

Figure 3-2: Model wind turbine design

Figure 3-3: Design of rotor blades

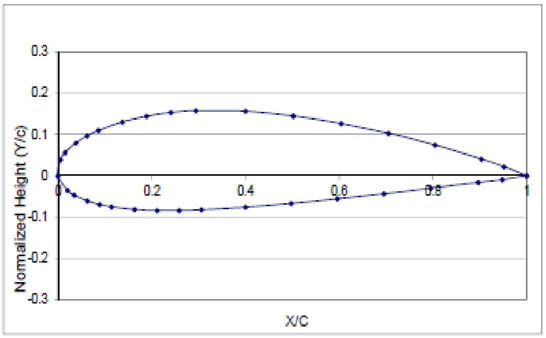

Figure 3-4: NACA4424 blade profile

3.1.3 Traverse System

Inside the wind tunnel test section, a 3-axis traverse system is mounted on the top panel. Stepper motors are attached to each arm to allow the hot wire probe to be positioned accurately upon command. The stepper motors were driven by a Velmex VXM controller which is connected to the data acquisition card DAQ PC. The Velmex VXM controller is mounted on the top surface of the upper wall of the test section, which is shown in **Figure** 3-5.

Figure 3-5: Velmex VXM stepping motors controllers

3.1.4 Hot Wire Probe

The Dantec Model 55P61 miniature wire probe, shown in **Figure** 3-6, is used in this work for velocity measurement. It is a dual sensor, cross-wire (e.g. X-wire) type probe designed to measure u and v components of the velocity vector. The probe wires are aligned such that they are in the same plane of the mean flow, with the sensors plane parallel to probe axis.

The 55P61 has two platinum-plated tungsten, 5 mm diameter, wires welded to the probe at 45° to each other and can measure velocity components within a ± 45° cone. The range of velocity that can be measured by the probe is from 0.05 m/s to 500 m/s. [35]

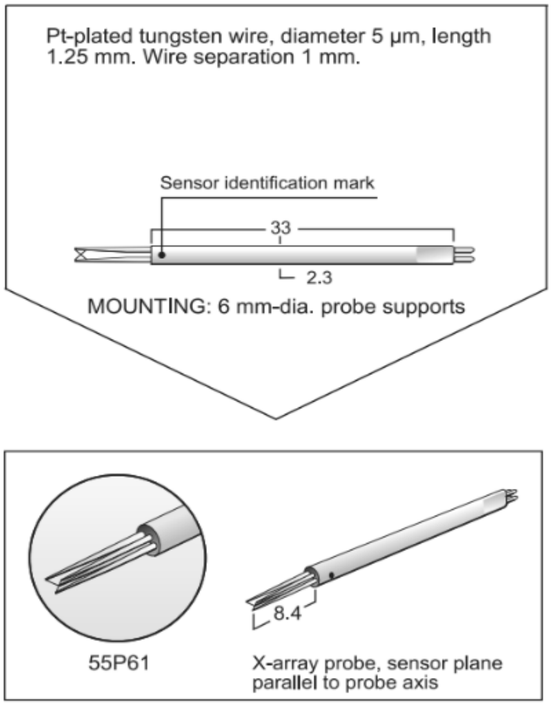

Figure 3-6: Hot wire probe [35]

3.1.5 Hot Wire Anemometry

Two Dantec 54T30 Miniature Constant Temperature Anemometers (CTA's) are used. They can provide a 0-5 V analog output voltage based on the characteristics of the probe. The offset voltage on each wire was approximately 1.3 V at zero velocity. [36]

3.1.5.1 Hot wire overheat adjustment

Setting the desired wire operating temperature is critical for calibration and velocity measurements. The wire temperature setting is determined based on the probe manufacturer's recommendations to prevent the wire from burning out while maintaining optimum sensitivity to velocity changes. If the wire temperature is set too high, the wires could burn out prematurely. Setting the wire temperature too low could result in a loss of sensitivity for turbulence measurements. Failure to account for differences in temperature between calibration and experimentation can lead to significant error in the measurements.

The wire operating temperature is set through a process called overheat adjustment where the decade resistance is calculated from values of the wire temperature coefficient of resistance (TCR), sensor resistance, sensor lead resistance, support resistance, flow temperature, and desired operating wire temperature. All wire temperatures were set to 242^{o}C based on the manufacturer's recommendation. All the previous parameters are included in MS Excel spreadsheet provided by Dantec. In case of dual sensor probe, each wire has to be adjusted individually. **Figure** 3-7 and **Figure** 3-8 show a couple of screenshots representing the overheat adjustment of each wire. The outcome of the spreadsheet is how to adjust the dip switches inside each CTA.

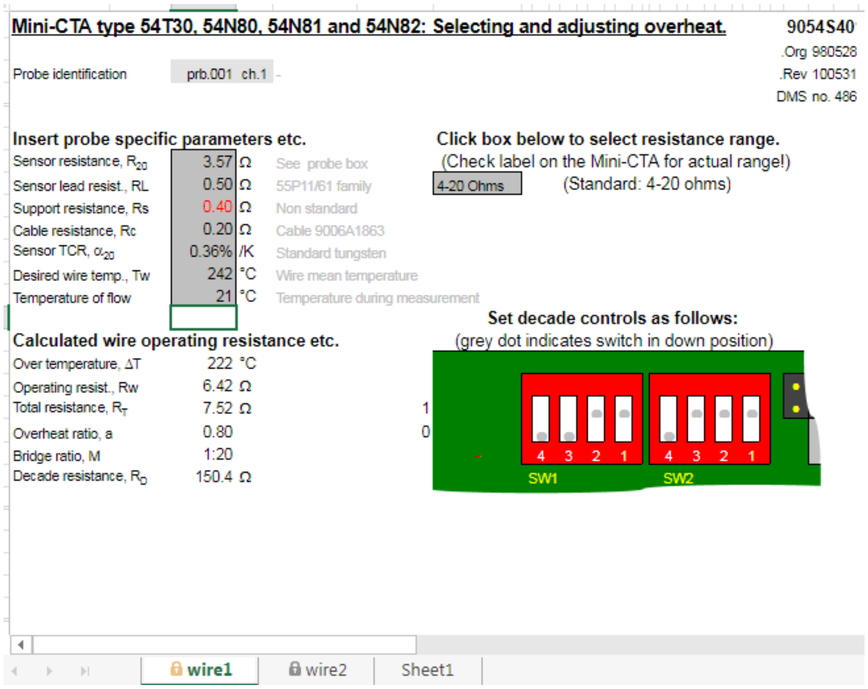

Mini-CTA type 54T30, 54N80, 54N81 and 54N82: Selecting and adjusting overheat. 9054S40

.Org 980528
.Rev 100531
DMS no. 486

Probe identification prb.001 ch.1 -

Insert probe specific parameters etc.

Sensor resistance, R_{20}	3.57	Ω	See probe box
Sensor lead resist., RL	0.50	Ω	55P11/61 family
Support resistance, Rs	0.40	Ω	Non standard
Cable resistance, Rc	0.20	Ω	Cable 9006A1863
Sensor TCR, α_{20}	0.36%	/K	Standard tungsten
Desired wire temp., Tw	242	°C	Wire mean temperature
Temperature of flow	21	°C	Temperature during measurement

Click box below to select resistance range.
(Check label on the Mini-CTA for actual range!)
4-20 Ohms (Standard: 4-20 ohms)

Calculated wire operating resistance etc.

Over temperature, ΔT	222	°C
Operating resist., Rw	6.42	Ω
Total resistance, R_T	7.52	Ω
Overheat ratio, a	0.80	
Bridge ratio, M	1:20	
Decade resistance, R_D	150.4	Ω

Set decade controls as follows:
(grey dot indicates switch in down position)

Figure 3-7: Overheat adjustment spreadsheet for wire1.

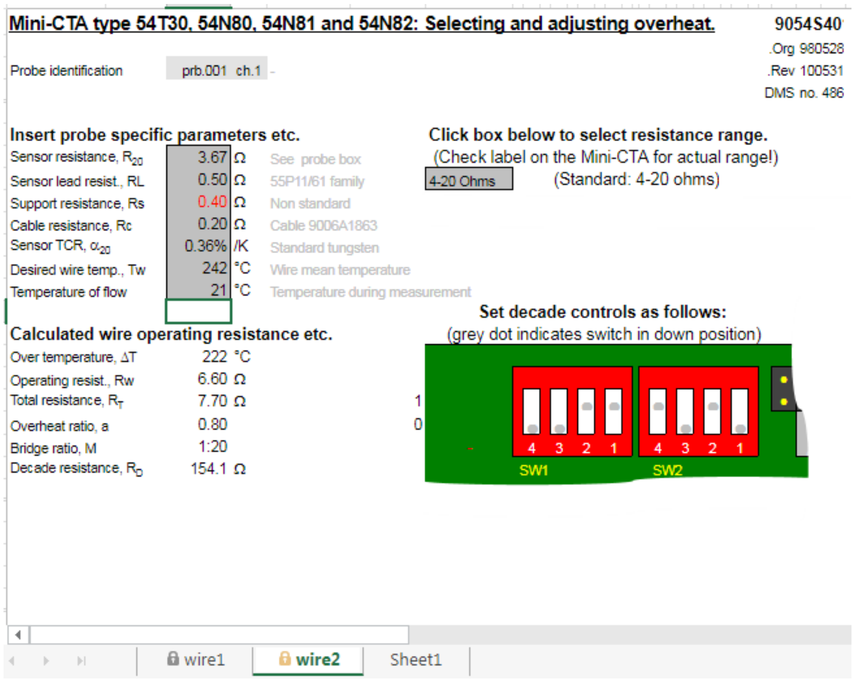

Mini-CTA type 54T30, 54N80, 54N81 and 54N82: Selecting and adjusting overheat. 9054S40

.Org 980528
.Rev 100531
DMS no. 486

Probe identification prb.001 ch.1 -

Insert probe specific parameters etc.

Sensor resistance, R_{20}	3.67	Ω	See probe box
Sensor lead resist., RL	0.50	Ω	55P11/61 family
Support resistance, Rs	0.40	Ω	Non standard
Cable resistance, Rc	0.20	Ω	Cable 9006A1863
Sensor TCR, α_{20}	0.36%	/K	Standard tungsten
Desired wire temp., Tw	242	°C	Wire mean temperature
Temperature of flow	21	°C	Temperature during measurement

Click box below to select resistance range.
(Check label on the Mini-CTA for actual range!)
4-20 Ohms (Standard: 4-20 ohms)

Calculated wire operating resistance etc.

Over temperature, ΔT	222	°C
Operating resist., Rw	6.60	Ω
Total resistance, R_T	7.70	Ω
Overheat ratio, a	0.80	
Bridge ratio, M	1:20	
Decade resistance, R_D	154.1	Ω

Set decade controls as follows:
(grey dot indicates switch in down position)

Figure 3-8: Overheat adjustment spreadsheet for wire2.

3.1.5.2 Hot wire calibration

A Model 54H10 Hot-Wire Calibrator from Dantec Dynamics [37] was used to provide a uniform free jet to the hot-wire probe. The calibration velocity was based on isentropic relations and known geometry of an internal, low turbulence, nozzle. **Figure** 3-9 contains five parts that represent the entire equipment used for hot wire calibration process. Part 1 denotes the 54H10 calibrator with a 2-axis rotation probe support holder for measurements at different yaw angles, which is represented by part 5. The 54H10 was modified, according to Dantec's instructions, to use in continuous mode where the differential pressure across the exit nozzle could be adjusted to vary the calibration velocity. Part 2 indicates the Fluke Model 922 Airflow Meter/Micro manometer which was used to measure the differential pressure across the internal nozzle of the hot-wire calibrator. The micro manometer has a published 4000 Pascal (Pa) differential pressure range with 1 Pa resolution and ± 1% of reading +1 Pa accuracy. The Airflow Meter/Micro manometer was purchased as a kit that also included a 30.5 cm long pitot tube for air velocity measurement. With the pitot tube attached to the micro manometer, the air velocity measurement range was published as 1-80 m/s with 0.001 m/s resolution and 2.5% of reading accuracy.

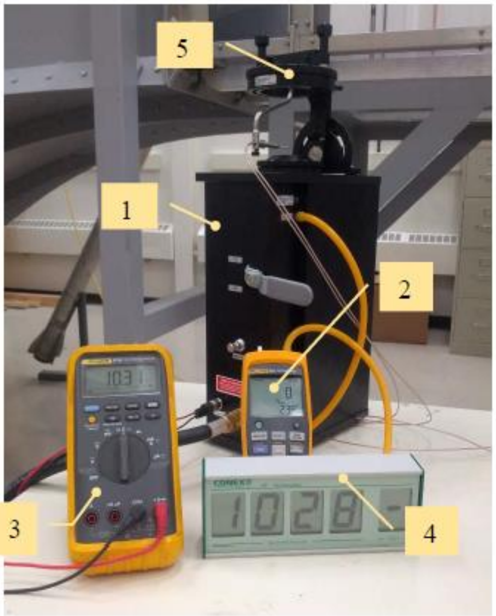

Figure 3-9: Equipment used for hot wire calibration

The 54H10 has an internal thermistor to measure the air temperature within the calibrator. The resistance of the thermistor was measured using a Fluke Model 87 Multimeter, which is demonstrated by part 3. The multimeter has a published accuracy of 0.05%+2 Ω in the range of resistances of the thermistor. Barometric pressure (nozzle exit pressure) was measured using a Conex Electro Systems Model JDB1 digital barometer, shown as part 4. The JDB1 barometer has an accuracy of ±0.05 inHg and a resolution of 0.01 inHg. **Figure** 3-10 depicts the entire calibration setup while it is inside the wind tunnel test section to emulate the circumstances of the actual measurements.

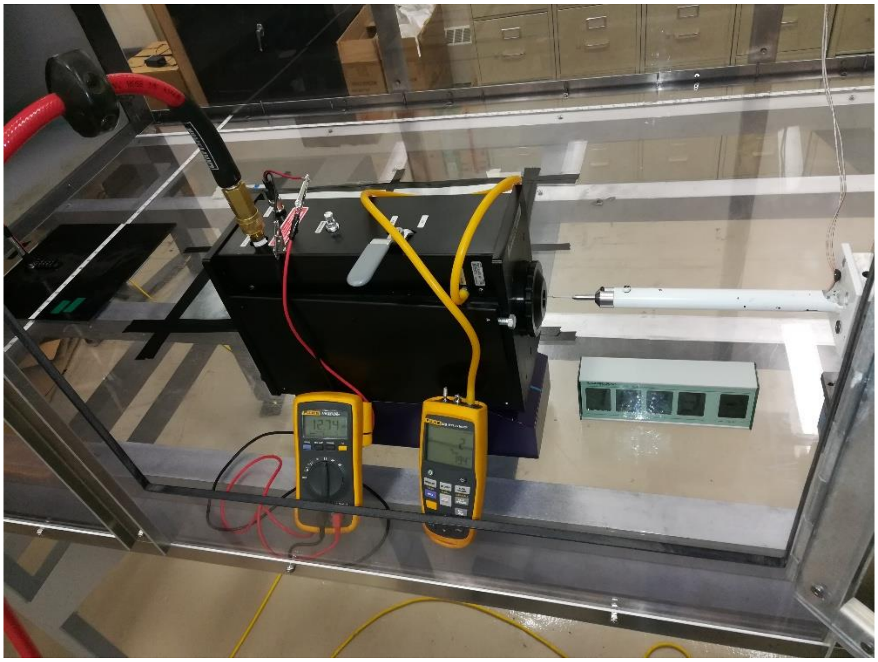

Figure 3-10: In-situ calibration of hot wire anemometer

Dantec provided an Excel spreadsheet to use with the 54H10 calibrator where the calibration velocity is determined from user input for the barometric pressure, thermistor resistance, nozzle differential pressure, and measured wire voltages at various differential pressure settings. The spreadsheet calculates the coefficients of a 4th order polynomial curve fit for converting wire voltage to velocity. However, to reduce the time required for calibration, we used a LabVIEW instrument was created by Jackson [38] to read the hot wire voltages with user input for the thermistor resistance, nozzle differential pressure, barometric pressure, and ambient temperature. The data was stored in a text file with each measurement appended to the file. A MATLAB script was developed to read the table of calibration data and compute the calibration velocity based on acquired average wire voltages and user input for barometric pressure, thermistor resistance, nozzle differential pressure and ambient temperature. **Figure** 3-11 depicts a sample of the generated calibration curves.

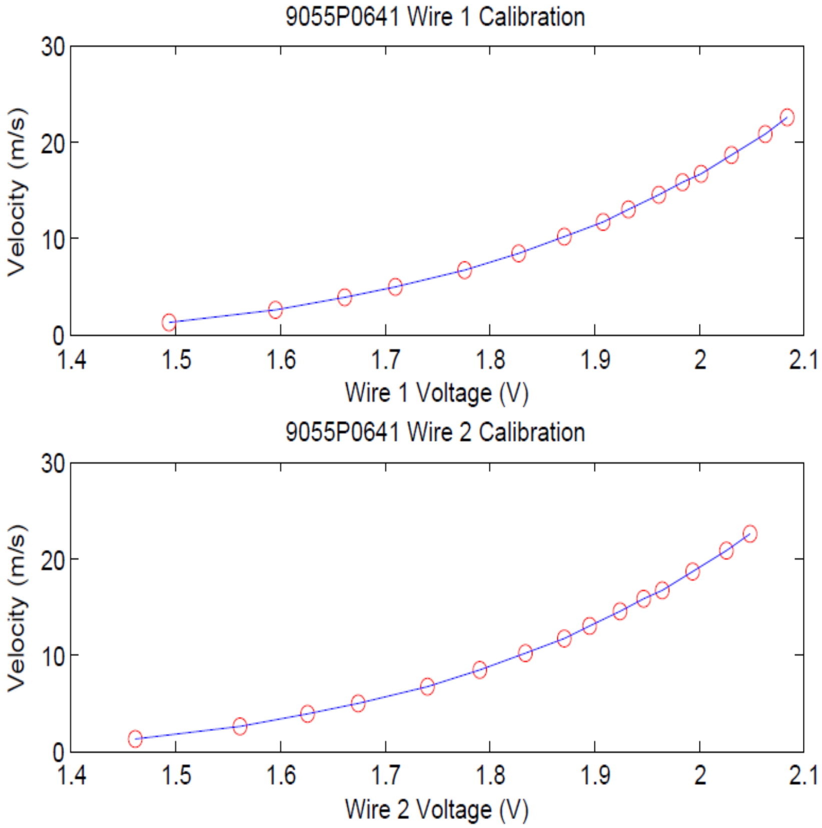

Figure 3-11: Sample of obtained calibration curves

3.2 Equations of the studied parameters

A statistical analysis of the velocity yielded quantities used to assess turbulence in the flow. The equations listed below consider the axial velocity to be a discrete time series composed of a mean, $\overline{U}$, and a fluctuating component, *u'*.

$$u = \overline{U} + u' \tag{1}$$

A similar equation can be written for the vertical component, v.

$$v = \bar{V} + v' \tag{2}$$

Mean velocities are determined from

$$\bar{U} = \frac{1}{N}\sum_{1}^{N} Ui \tag{3}$$

$$\bar{V} = \frac{1}{N}\sum_{1}^{N} Vi \tag{4}$$

The root mean square (RMS) velocities of the fluctuating component are defined as

$$u'_{rms} = \sqrt{\tfrac{1}{N-1}\textstyle\sum_{1}^{N}(Ui-\bar{U})^2} \tag{5}$$

$$v'_{rms} = \sqrt{\tfrac{1}{N-1}\textstyle\sum_{1}^{N}(Vi-\bar{V})^2} \tag{6}$$

The turbulent intensity, which indicates the fraction of the total energy of the flow that resides in the turbulent regime, can be estimated as relative turbulence intensity and total turbulence intensity. The relative turbulent intensity for each velocity component is

$$I_u = 100 \times \frac{u'_{rms}}{\bar{U}} \tag{7}$$

$$I_v = 100 \times \frac{v'_{rms}}{\bar{V}} \tag{8}$$

and the total turbulence intensity is computed from

$$I_T = 100 \times \sqrt{\frac{\frac{1}{2}\left({u'_{rms}}^2 + {v'_{rms}}^2\right)}{\bar{U}^2 + \bar{V}^2}} \qquad (9)$$

Finally, velocity deficit can be calculated from the following equation,

$$Velocity\ Deficit = 1 - \frac{\bar{U}}{U_\infty} \qquad (10)$$

3.3 Results and discussion

The entire setup in the test section during the experiment including the traverse system, probe holder, dual-sensor probe and the wind turbine model is depicted in **Figure** 3-12. Meanwhile, **Figure** 3-13 shows a description of both the numbers and locations of the trasverse planes array selected to scan the details of both near and far wake regions, along with a clarification of coordinate system position.

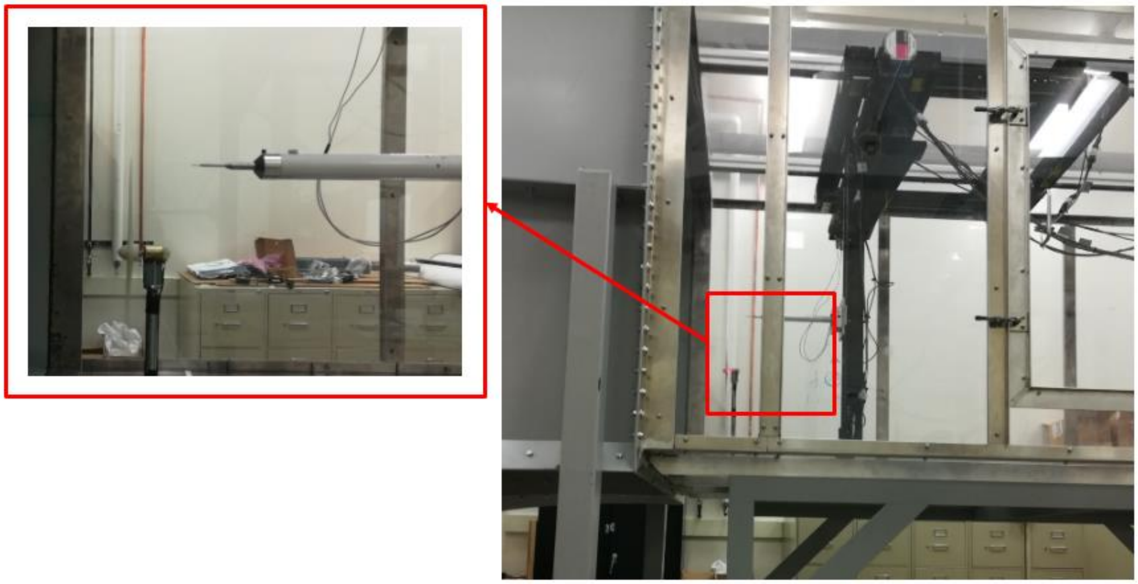

Figure 3-12: The entire setup in the test section during the experiment

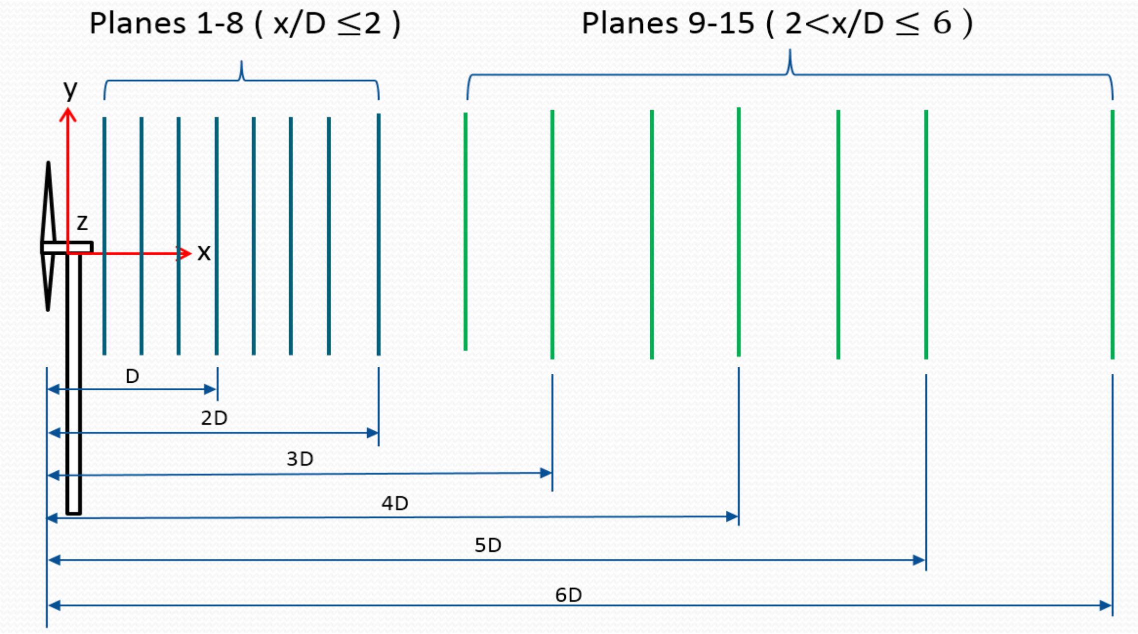

Figure 3-13: locations of the transverse planes array.

It is worth mentioning to define at this stage a term called blockage ratio, which is the ratio of rotor swept area to the test section inlet area. In this study, the blockage ratio is 2.25 %, much less than the range of 6-7.5% recommended by Howell et al. [39]. The blockage ratio must be less than the range above to guarantee a negligible wall effect on the flow.

The downstream distance between the model turbine and the test section entrance is 0.305 m (1.5 D). It is safe to put the turbine model at this downstream distance because the distance between the test section floor and the lowest position of rotor blade tip is 0.2035 m, which is larger than the boundary layer thickness at 0.305 m, which is 5.16 mm only. Hence, the boundary layer effect is away from the turbune model.

The rotor blades speed of rotation was measured using a Monarch Model PLT200 laser tachometer mounted on a tripod. The tachometer has an LCD display for a direct reading in RPM. The accuracy of the tachometer is listed at 0.01% of reading. The rotor blades rotational speed corresponds to 5.2 m/s free stream velocity was found ranging from 1270 to 1280 RPM, which is equivalent to a tip speed ratio of

2.6. Generally, the optimum tip speed ratio for wind turbines, which gives the maximum power output, ranges from 7 to 8. The tip speed ratio of the current model is less than the optimum value because the rotor hub is coupled to small DC motor, which acts as a constant decelerating load. Unfortunately, the measurement of the motor output power and control of blade speed was given up because the efficiency of the motor is not known and the motor output voltage signal was very noisy and the current too small due to the low blade torque. It was fine to continue with this low tip speed ratio because the power extraction is not the current work's focus, but the wake region investigation.

Figure 3-14 shows the grid details of the measurement planes. Each plane covers a square area of 11 inches x 11 inches (i.e., 1.375 D x 1.375 D). The velocity measurements were carried out along 23 Z-columns by 23 Y-rows with an increment of 0.5 inches in both Z and Y directions to make the grid resolution fine enough to capture the changes in velocity and turbulent intensity at every single point of the 529 points that form each plane.

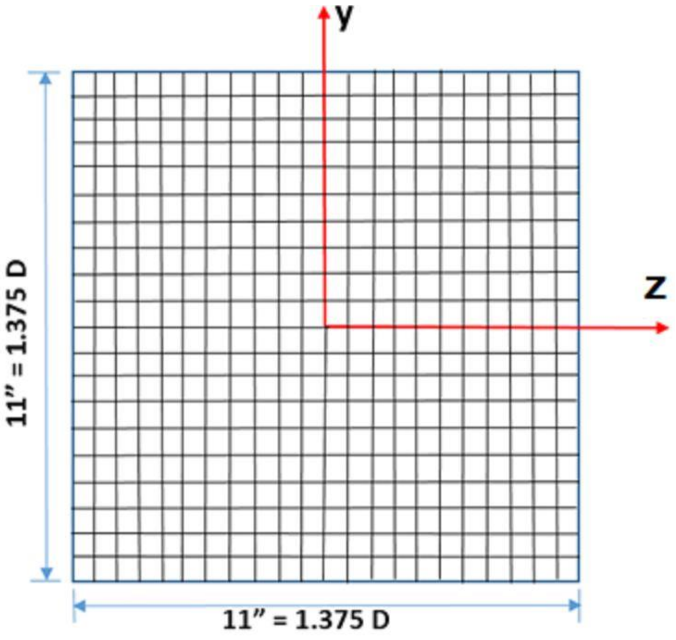

Figure 3-14: Grid details of the measurement planes

The wake region behind a turbine rotor is characterized by high-frequency eddies. Therefore, the velocity measurements were done with high frequency as well, and for a relatively extended period. The measurements were taken 10,000 times at each point, the sensor stayed at each point for 10 seconds, resulting in a measurement frequency of 1000 Hz. **Table** 3-1 shows measurement planes downstream distance in inches versus multiples of rotor diameter representation to give an impression of how far each plane is away from the rotor plane.

Table 3-1: Planes downstream distance in inches versus multiples of rotor diameter representation

Plane No.	Downstream distance (inches)	Downstream distance (m)	Multiples of rotor diameter
1	2	0.0508	¼ D
2	4	0.1016	½ D
3	6	0.1524	¾ D
4	8	0.2032	D
5	10	0.2540	1 ¼ D
6	12	0.3048	1 ½ D
7	14	0.3556	1 ¾ D
8	16	0.4064	2 D
9	20	0.5080	2 ½ D
10	24	0.6096	3 D
11	28	0.7112	3 ½ D
12	32	0.8128	4 D
13	36	0.9144	4 ½ D
14	40	1.0160	5 D
15	48	1.2192	6 D

Figure 3-15 shows a scan for average axial velocity $\overline{U}$ through nine planes. These planes cover the downstream distance between ¼ D and 4 D. Rotor and hub diameters are represented by two red circles for clarification. The z and y dimensions of the planes are trimmed to 1.25 rotor diameters for better axes representation. $\overline{U}$ is determined from Eq. (3). Generally, $\overline{U}$ is reduced lower than free stream axial velocity U_∞ directly behind the rotor as the inlet flow field is blended by the rotating blades.

Figure 3-15, in part(a), it is evident that the minimum $\overline{U}$ is about 2.8 m/s which is obtained directly behind the nacelle, as the nacelle blocks the flow. Average value of $\overline{U}$ in the upper half-plane is 5.2 m/s, which is the axial free stream velocity, as the effect of the shear layer expansion explained by Crespo [2] is negligible directly behind the rotor. This shear layer is formed by the vortex sheets generated by different circulation along blades. These vortices leave the blades at its trailing edge, then start rolling up and expansion downstream till it converges at a certain downstream distance. The length of this expansion region is evaluated by Crespo to be one turbine diameter. The maximum value of $\overline{U}$ over this plane is 5.7 m/s which is reached at the center of the lower-half plane. This value is higher than free stream velocity U_∞, and is obtained due to the Venturi effect which forces the velocity of fluid particles to accelerate. This Venturi effect is caused by the narrow flow area formed between the rotating blades at its lowest position and the wind tunnel test section floor, which chokes the streamlines within this particular zone. Figure 3-15: Average axial velocity of nine planes. (a) plane 1 at downstream distance = ¼ D. (b) plane 2 at downstream distance = ½ D. (c) plane 3 at downstream distance = ¾ D. (d) plane 4 at downstream distance = D. (e) plane 5 at downstream distance = 1 ¼ D. (f) plane 6 at downstream distance = 1 ½ D. (g) plane 8 at downstream distance = 2 D. (h) plane 10 at downstream distance = 3 D. (i) plane 12 at downstream distance = 4 D.

Figure 3-15, part (b) shows a scan for average axial velocity $\overline{U}$ over plane 2 at downstream distance = ½ D. the hub height $\overline{U}$ the value behind nacelle starts to jump, reaching about 3 m/s. Average value of $\overline{U}$ in the upper half-plane again is 5.2 m/s, while its value in the lower half-plane is about 5.3 m/s which is still higher than an upper-half plane, but uniform to an extent which means that the Venturi effect starts to fade away.

In parts (c), (d), (e) and (f) of **Figure** 3-15, as we go further downstream, the rate of hub height $\overline{U}$ value recovery is relatively high. The reason why the recovery rate is relatively high at that downstream distance is that the increase in shear layer thickness still doesn’t reach the axis of the wake (i.e., the thickness of the shear layer doesn’t converge to reach the wake axis yet), which allows the axial velocity to recover with a relatively high rate without suppression. An axial velocity of 4 m/s is reached at the hub height in part (f) of **Figure** 3-15.

In parts (g) and (h) of **Figure** 3-15, the hub height axial velocity continues its increase almost with the same high rate, where an axial velocity of 4.3 m/s is reached at the hub height in part (h). However, in part (i), of the same figure, the hub height axial velocity rate of increase becomes lower, where an axial velocity of only 4.4 m/s is reached at the hub height. Hence, the axial velocity recovery is suppressed to 4.4 m/s, and its value fluctuates between 4.3 to 4.4 m/s till the last measurement plane at a downstream distance of six rotor diameters.

The reason why this axial velocity recovery suppression occurs at about 2.5 rotor diameters is that, regardless of the shear layer outer diameter expansion, the shear layer thickness increase inward as we go downstream till it reaches the wake axis at about 2.5 rotor diameters, so this convergence hinders more velocity recovery starting from the aforementioned downstream distance. This finding agrees with Crespo’s finding who told in his work that the shear layer convergence occurs between two and five rotor diameters.

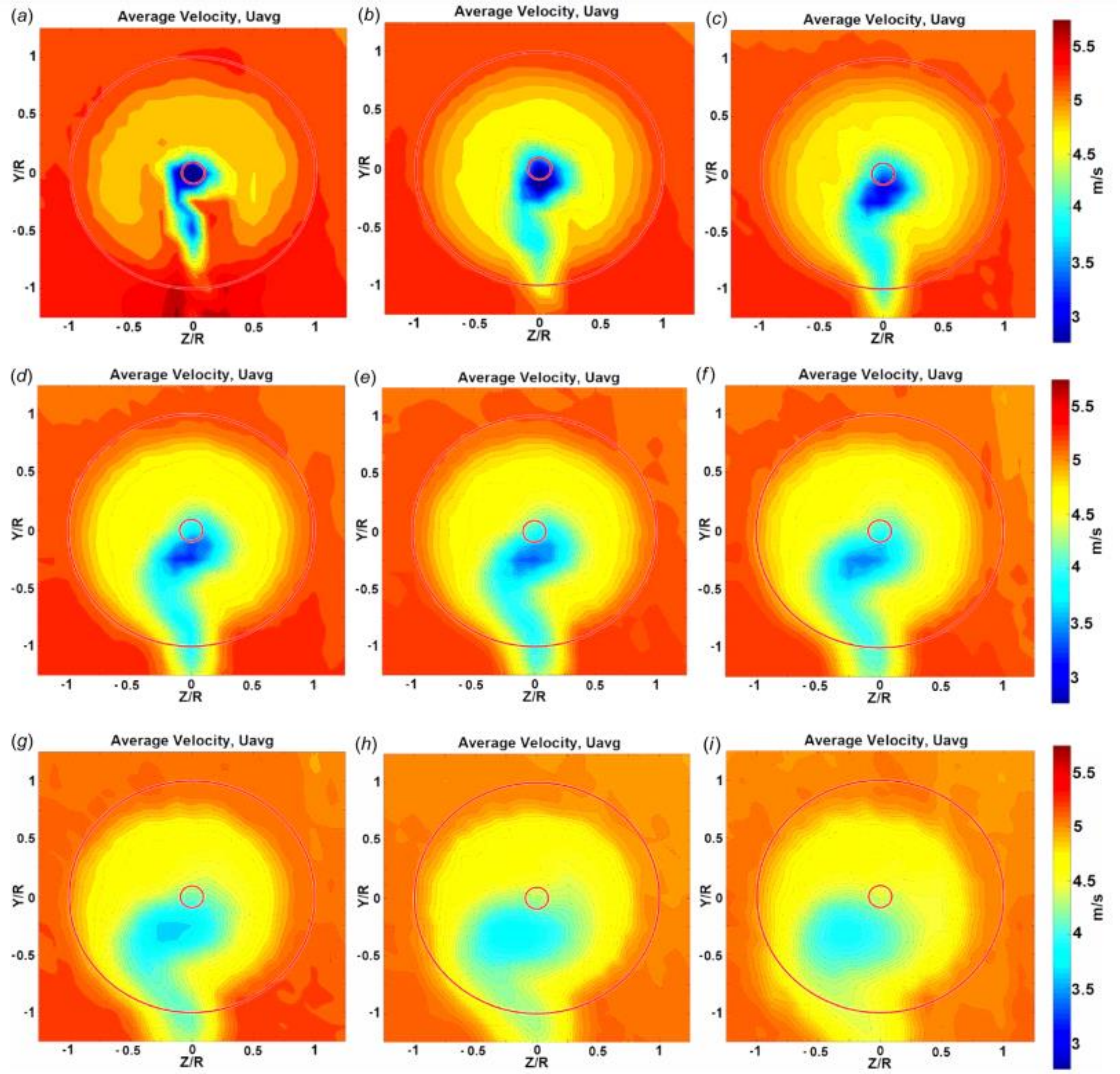

Figure 3-15: Average axial velocity of nine planes. (a) plane 1 at downstream distance = ¼ D. (b) plane 2 at downstream distance = ½ D. (c) plane 3 at downstream distance = ¾ D. (d) plane 4 at downstream distance = D. (e) plane 5 at downstream distance = 1 ¼ D. (f) plane 6 at downstream distance = 1 ½ D. (g) plane 8 at downstream distance = 2 D. (h) plane 10 at downstream distance = 3 D. (i) plane 12 at downstream distance = 4 D.

Figure 3-16 shows a scan for the average vertical velocity $\bar{V}$ through the same nine planes which cover the downstream distance between ¼ D and 4 D. In all parts of **Figure** 3-16 the average vertical velocity on the right half of the red circle that represents the rotor swept area is negative, while in the left half is positive, this is because the rotor blades are rotating counter clock wise when the rotor is observed from the back side. So, fluid particles in the right half are forced to move downward (negative vertical velocity), while the other particles in the left half are forced to move upward (positive velocity value). As we go downstream, both right and left rotation-affected areas to expand, but the rotation effect itself erodes due to turbulence diffusion and interaction with the free stream.

As defined in Eq. (10), velocity deficit is a way to monitor the reduction that happens to the axial wind velocity after mainstream momentum transfer to the rotor. A positive value of velocity deficit means that average axial velocity $\bar{U}$ is less than main stream velocity U_∞. A negative value of velocity deficit means that $\bar{U}$ is larger than U_∞.**Error! Reference source not found.**

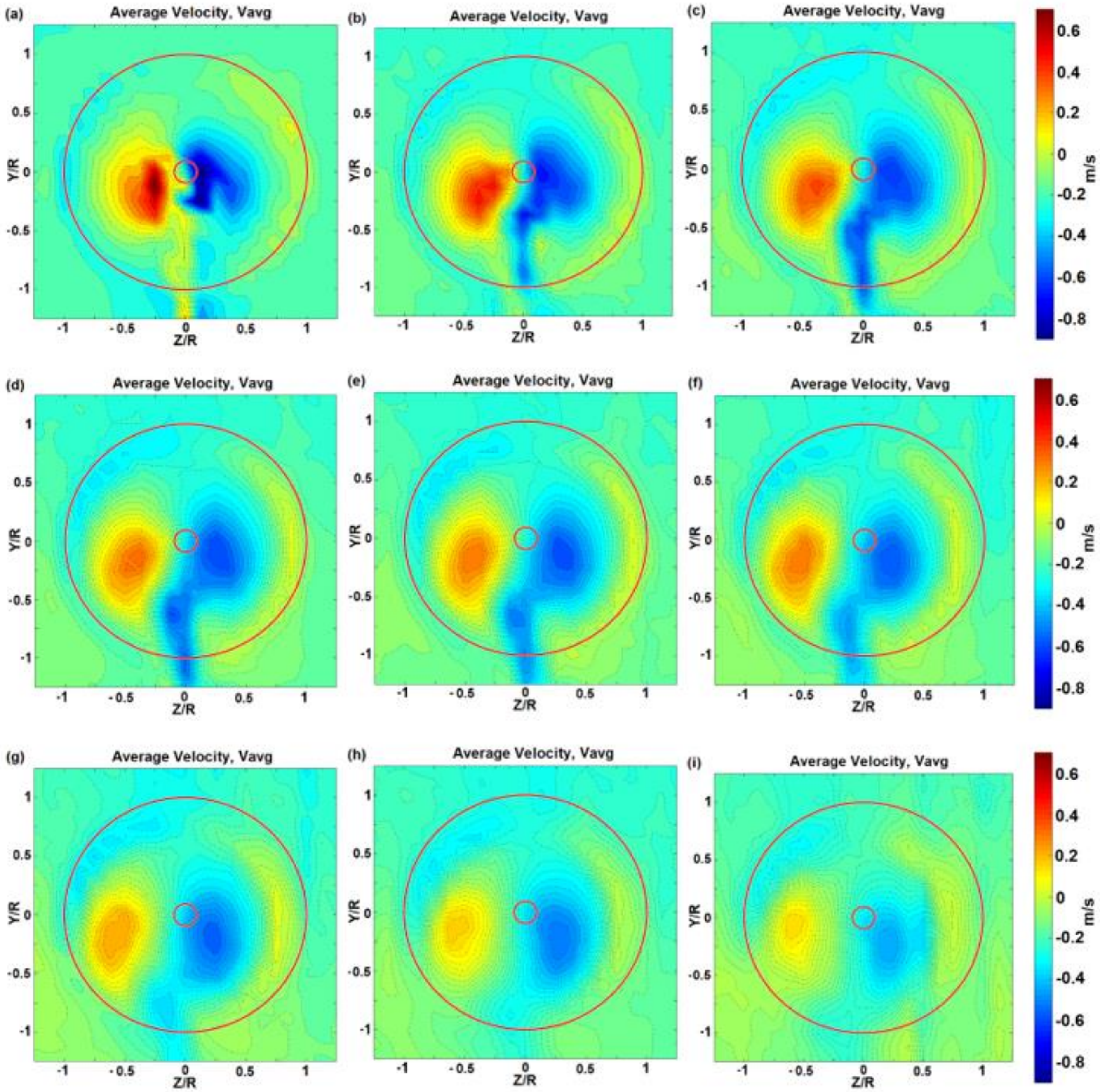

Figure 3-16: Average vertical velocity of nine planes. (a) plane 1 at downstream distance = ¼ D. (b) plane 2 at downstream distance = ½ D. (c) plane 3 at downstream distance = ¾ D. (d) plane 4 at downstream distance = D. (e) plane 5 at downstream distance = 1 ¼ D. (f) plane 6 at downstream distance = 1 ½ D. (g) plane 8 at downstream distance = 2 D. (h) plane 10 at downstream distance = 3 D. (i) plane 12 at downstream distance = 4 D

In **Figure** 3-17, it is desired to show images of the velocity deficit as measurement planes go downstream, covering the same downstream distance that extends from ¼ D to 4 D. Parts from (a) to (f) of this figure comprises the first 1 ½ D, where the drastic velocity deficit change occurs. The hub height deficit decreases from 0.6 in part (a) to 0.2 in part (f). Parts (g) to (h) cover the downstream distance from 2 D to 4 D, where the hub height deficit comes to an almost stable condition. The hub height velocity deficit decreases from 0.2 in part (g) to 0.1 in part (i).

Figure 3-18 shows the total turbulent intensity through the same selected nine transverse planes extending from ¼ D to 4 D. Total turbulence intensity is computed from Eq. (9). In part (a) of this figure, the total turbulence intensity has a value of zero everywhere in the plane outside the rotor swept area, as the shear layer expansion effect is still negligible at this downstream distance. Then, its value ranges from 10% to 15% within the rotor swept area. Moreover, its maximum value is around 45% which is reached directly behind the nacelle. Finally, the turbulence caused by the tower justifies the reason for the relatively high turbulent intensity region ranges from 25% to 35% just behind it. It is worth mentioning that the gradual expansion of the cylindrical shear layer diameter expansion is well-represented through parts (a) to (f) of the figure. Most of the expansion is obtained at 1.5 rotor diameters, then the rate of expansion is significantly decelerated.

Parts (g), (h) and (i) of **Figure** 3-18 shows a scan for the turbulence intensity through planes 8 to 12 in the far wake region. These planes cover the downstream distance between 2 D and 4 D. The scale upper limit is set to 25% instead of 45%, particularly for the far wake region planes, to increase the ability of colors contrast to represent the turbulence intensity difference through a single plane well. As we go downstream, the turbulence caused by nacelle vanishes gradually. In part (g) (plane 8), the hub height turbulence intensity significantly erodes till it reaches about 8%, and it continues declining till it reaches

5% in part (i) (plane 12). Moreover, the parts of this figure emphasize the decelerated expansion rate of the shear layer and shows the eccentricity of the wake towards the bottom-left.

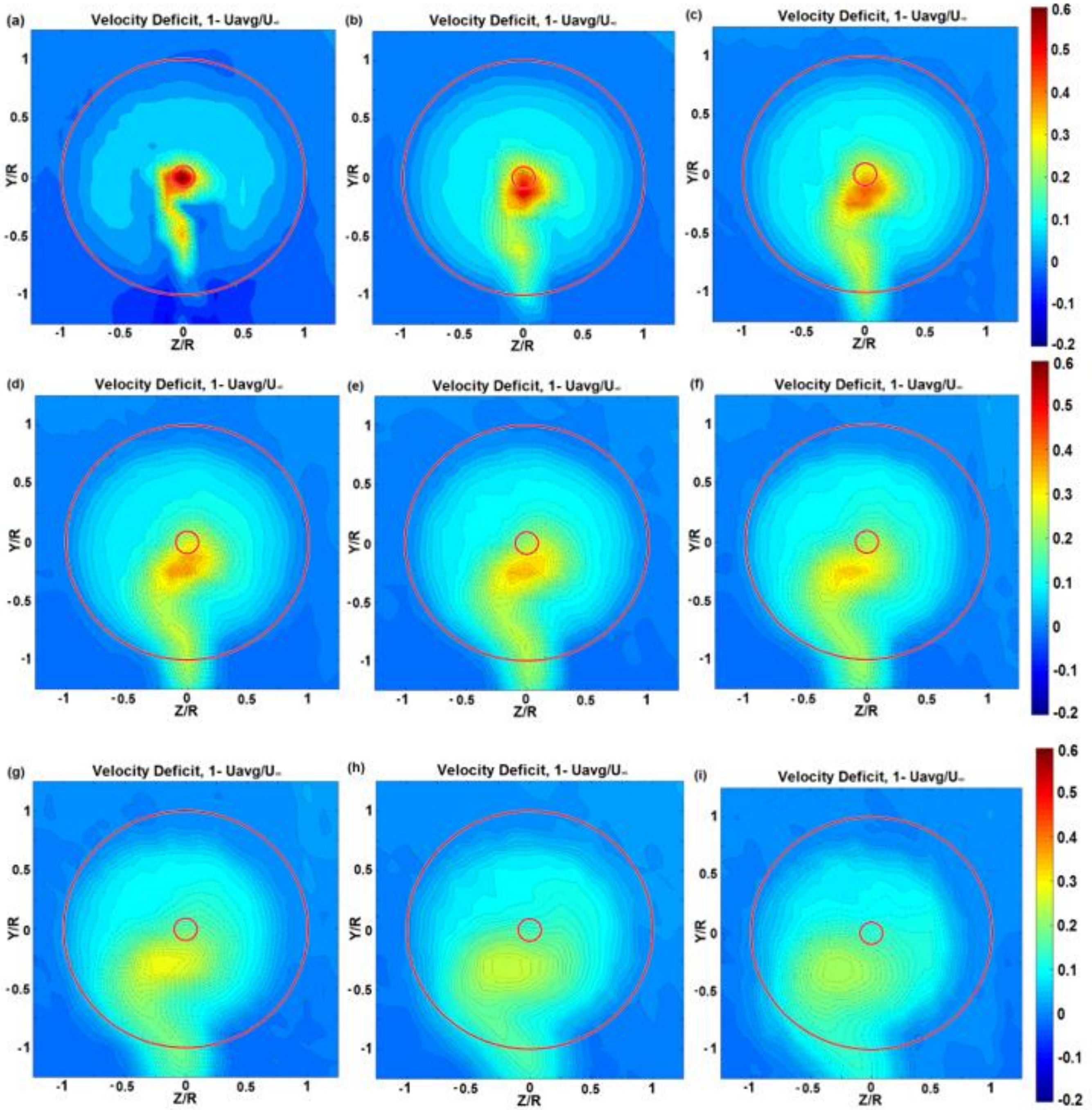

Figure 3-17: Velocity deficit of nine planes. (a) plane 1 at downstream distance = ¼ D. (b) plane 2 at downstream distance = ½ D. (c) plane 3 at downstream distance = ¾ D. (d) plane 4 at downstream distance = D. (e) plane 5 at downstream distance = 1 ¼ D. (f) plane 6 at downstream distance = 1 ½ D. (g) plane 8 at downstream distance = 2 D. (h) plane 10 at downstream distance = 3 D. (i) plane 12 at downstream distance = 4 D.

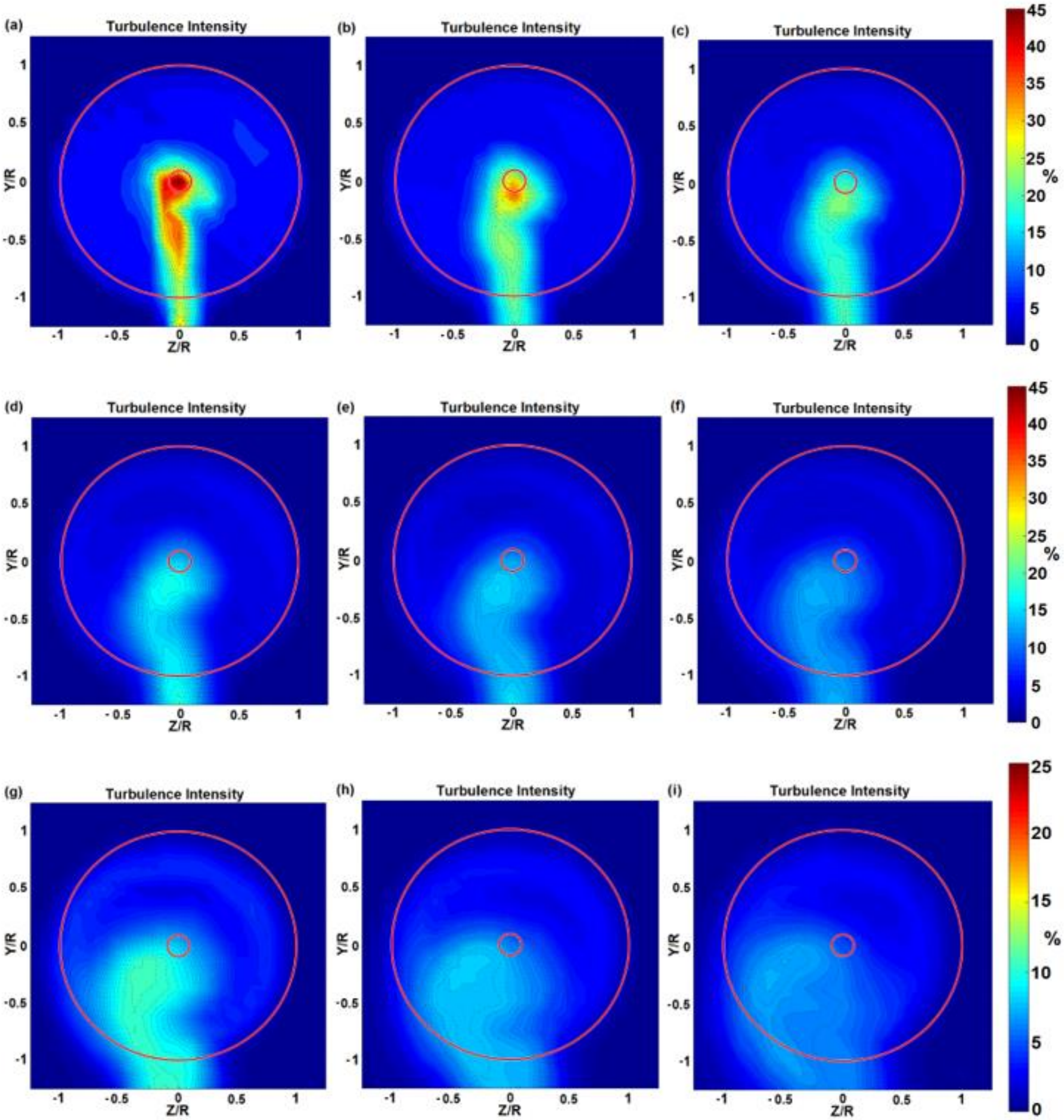

Figure 3-18: Turbulence intensity of nine planes. (a) plane 1 at downstream distance = ¼ D. (b) plane 2 at downstream distance = ½ D. (c) plane 3 at downstream distance = ¾ D. (d) plane 4 at downstream distance = D. (e) plane 5 at downstream distance = 1 ¼ D. (f) plane 6 at downstream distance = 1 ½ D. (g) plane 8 at downstream distance = 2 D. (h) plane 10 at downstream distance = 3 D. (i) plane 12 at downstream distance = 4 D.

A different perspective to look at the behavior of axial velocity recovery that happens behind the rotor is to trace the horizontal centerlines axial velocity deficit at different downstream distances along the entire length of the test section. This array is represented by **Figure** 3-19. It is evident that the deficit values for all line graphs are symmetric about z/R=0. In addition, the hub height deficit value reaches a maximum of 0.65 at a downstream distance of x/D=0.25; then it decays as we go downstream till it reaches a minimum of 0.15 at x/D=6.

An analogous perspective is adopted in **Figure** 3-20 which depicts the vertical centerlines axial velocity deficit at different downstream distances along the entire length of the test section. Although the decay behavior is still present, however, the symmetry about y/R=0 is lost because of the turbulence caused by the tower and the interaction with the test section bottom side.

Figure 3-21 represents horizontal centerlines turbulence intensity at normalized different downstream distances along the entire test section length. Typically, outside the rotor swept area, the turbulence intensity is 0 %. Touching blade tips lead to a significant jump in turbulence intensity percentage, the turbulence intensity increases dramatically till it reaches its maximum value along each line graph at z/R = 0. It seems that the line graphs are perfectly symmetric about z/R = 0. On the other hand, **Figure** 3-22 represents vertical centerlines turbulence intensity at normalized different downstream distances along the entire test section length. Similarly, to the deficit behavior, the symmetry about y/R = 0 is lost as the effect of tower and nacelle is significant while tracing the vertical centerlines.

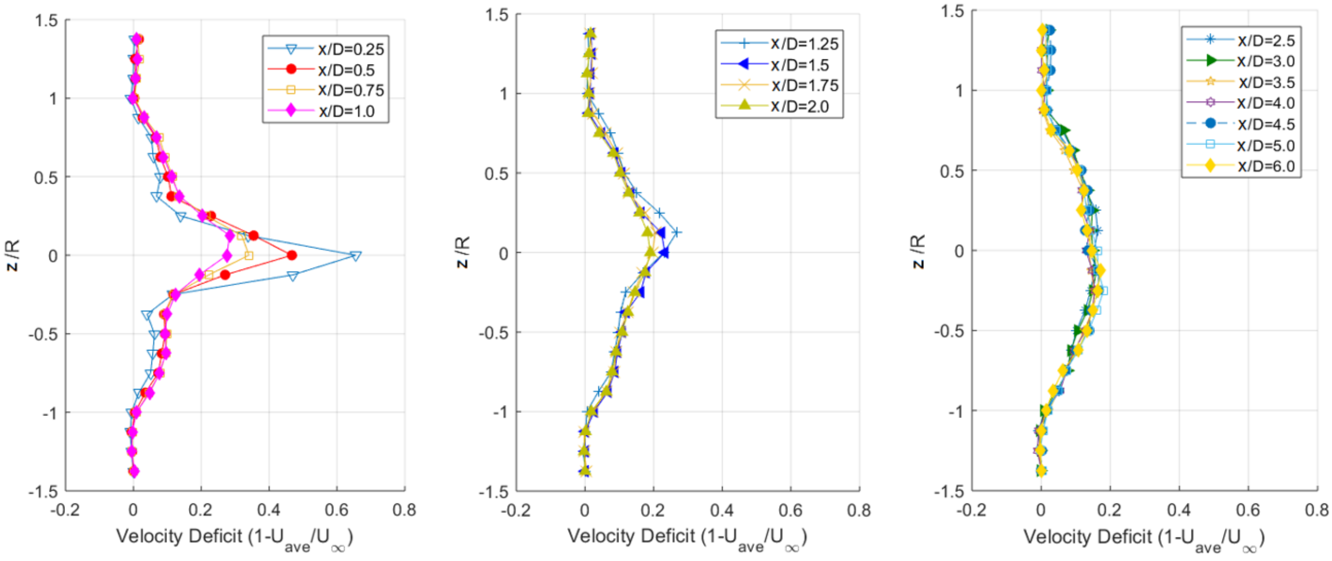

Figure 3-19: Horizontal centerlines axial velocity deficit at normalized different downstream distances

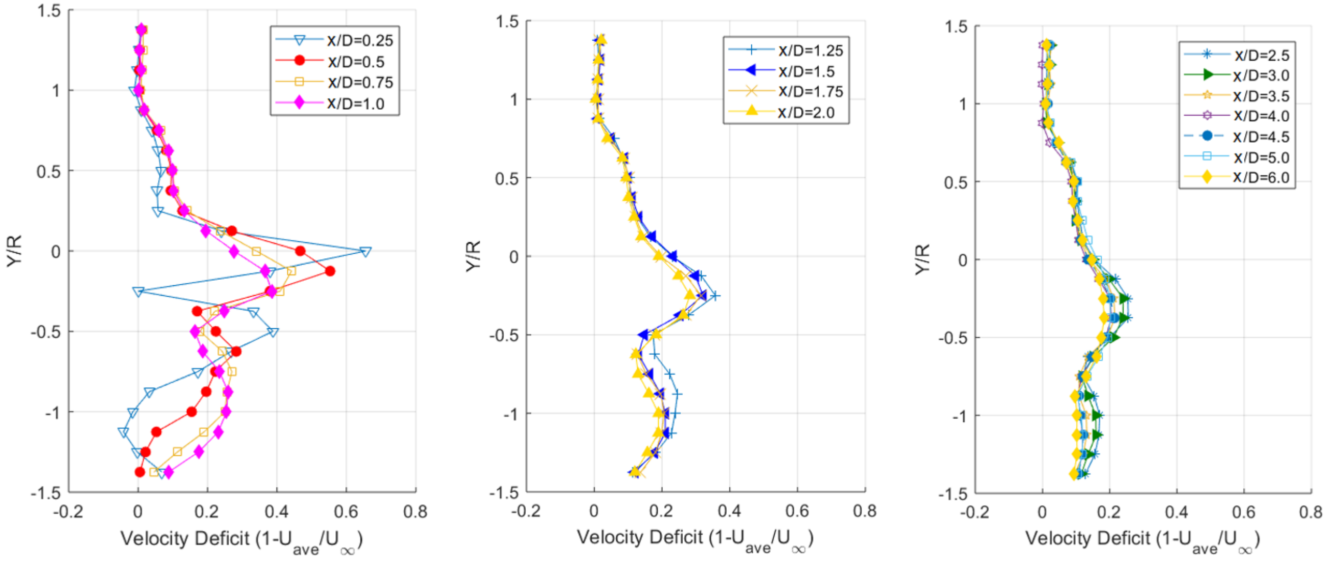

Figure 3-20: Vertical centerlines axial velocity deficit at normalized different downstream distances.

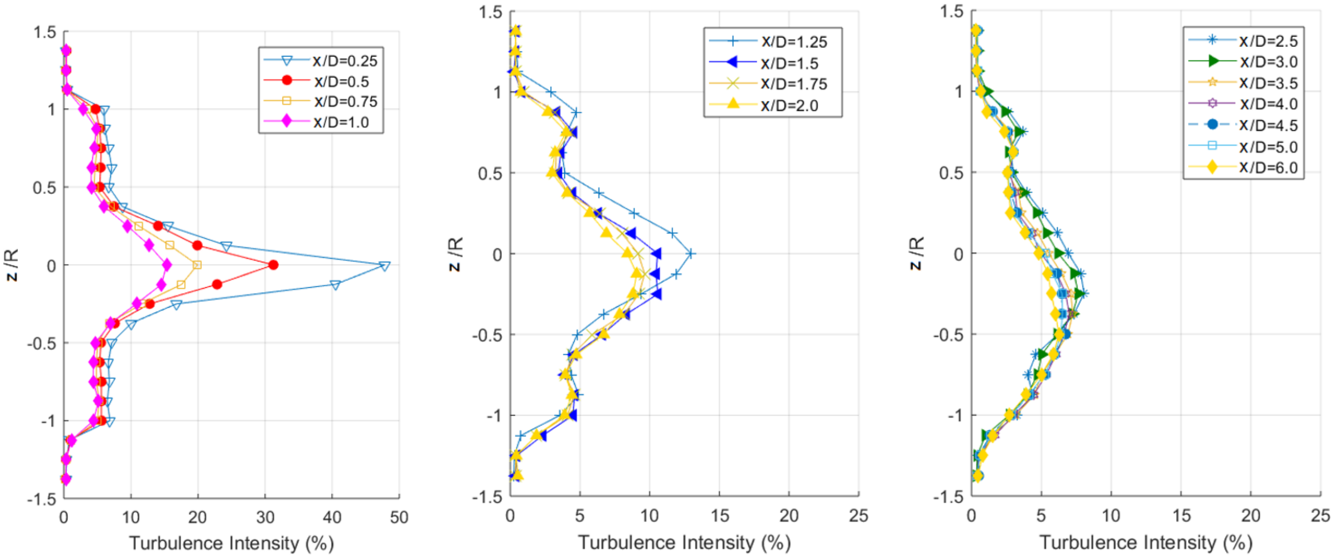

Figure 3-21: Horizontal centerlines turbulence intensity at normalized different downstream distances

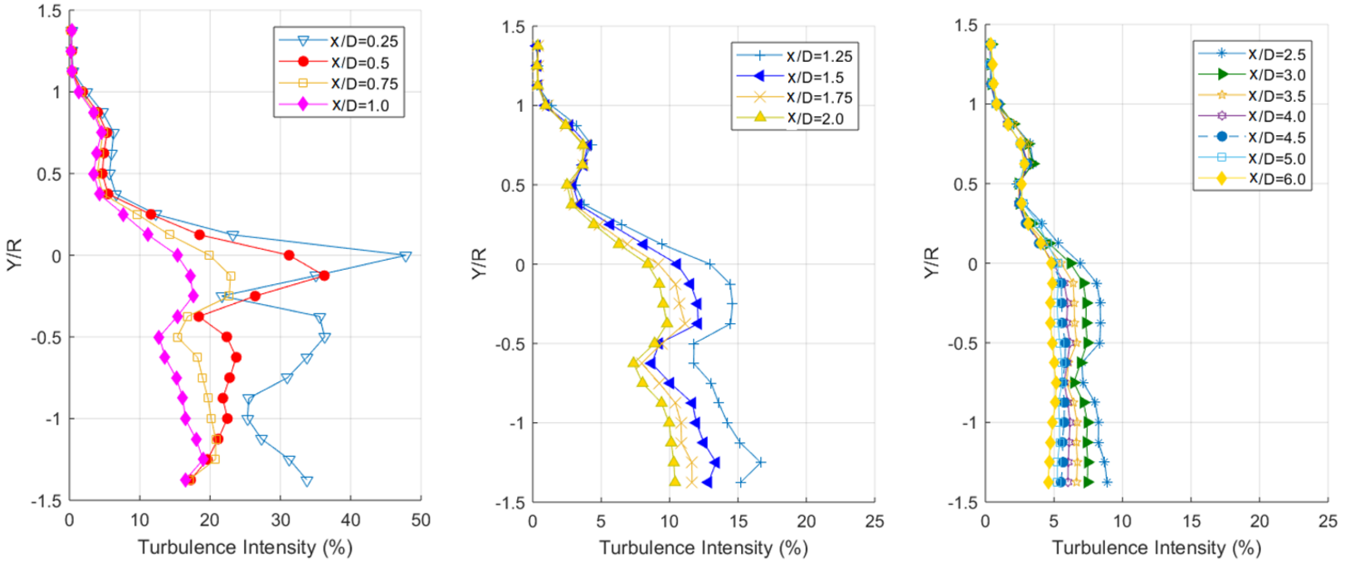

Figure 3-22: Vertical centerlines turbulence intensity at normalized different downstream distances

Figure 3-23 represents wake characteristics along the axial direction at hub height for free stream velocity of 5.2 m/s. The $\bar{U}/U\infty$ value increases till it maintains an average value of 0.82 along the wake centerline from a downstream distance of x/D = 3 to x/D = 6, which represents the length limit of the test section. It is known that the turbine power output is directly proportional to the wind velocity. So, the obtained 0.82 velocity recovery corresponds only 0.55 of the power that would be generated if the axial velocity recovery was 1.

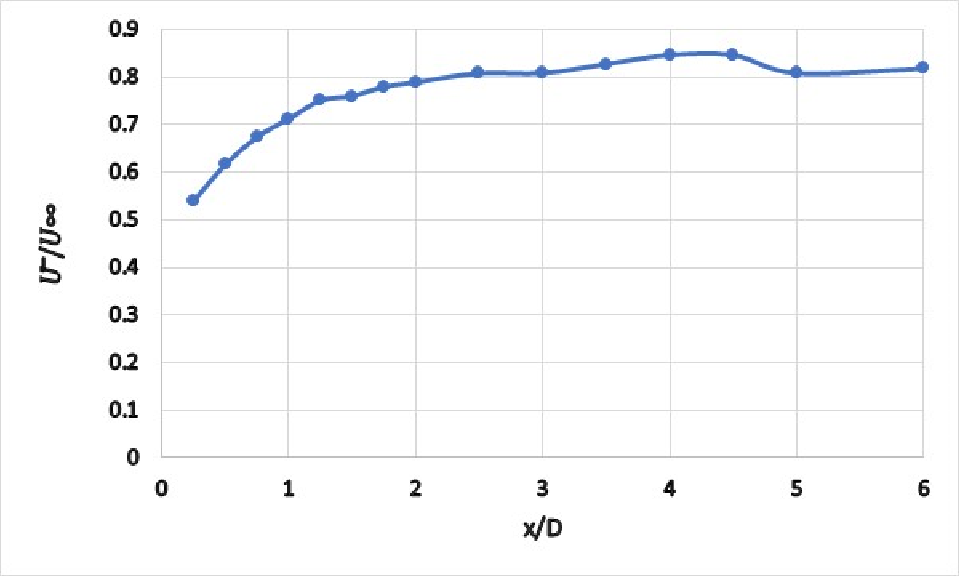

Figure 3-23: Wake characteristics along the axial direction at hub height for free stream velocity of 5.2 m/s.

3.4 Conclusions

Through this investigation, the following conclusions emerged:

- The data obtained from this work is an excellent base to validate computational fluid dynamics (CFD) models by comparing the CFD results to these experimental outcomes.

- This work can be considered as a strong pillar to support projects like wind farm layout design, site evaluation, and power output prediction.
- The investigation on the wake region characteristics provided by this study, can experimentally, strengthen our grasp of blade-formed vortices shedding downstream of a single wind turbine, the behavior of the resultant shear layer expansion, and its thickness increase till it reaches the wake axis, particularly for low inflow wind speed (5.2 m/s)
- Finally, sites with low wind speeds do not enhance the axial velocity recovery, in contrast, it has slower velocity recovery compared to sites with higher wind speeds. Therefore, while selecting the distance between two successive wind turbines in an inline configuration wind farm, for low inflow wind speed (5.2 m/s), six-rotor diameters are very short to obtain an appropriate velocity recovery, since it does not exceed 82 %.

Chapter 4 : Comparative Study of the Inline Configuration Wind Farm

Studies that serve projects like wind farm design layout and power generation optimization are of critical importance because the global installed wind energy capacity by the end of 2018 exceeded 591 GW and expected to soar to reach 700 GW by the end of 2020. The previous expectation is based on an increasing percentage of installed capacity ranging from 9.6% to 17.1% in the past five years. [5] Therefore this chapter provides an in-depth analysis of the flow around the rotor and in the wake of a single Horizontal Axis Wind Turbine (HAWT) model at different free stream velocities and Tip Speed Ratios (TSRs). Moreover, it extracts some recommendations that might be beneficial for large scale projects such as wind farm layout design and power output prediction. For this purpose, a modeling and experimental testing of a wind tunnel test section, including a single wind turbine model inside were created and validated against present experimental data of the same model. The Large Eddy Simulation (LES) was used as a numerical approach to model the Navier-Stokes equations. The computational domain was divided into two areas: rotational and stationary. The unsteady Rigid Body Motion (RBM) model was adopted to represent the rotor rotation accurately.

4. 1 Numerical Simulations

4.1.1 Validation Model

For this work, the commercial software STAR CCM+ was used to build a 3D model, including the turbine model inside the wind tunnel test section. The length of the wind tunnel test section is about 12D. Therefore, an upstream distance of 1.5D and a downstream distance of 10.5D were left as spacing to do the experiment and build the numerical model used for validation. The inlet section was set to be velocity inlet with 5.2 m/s as incoming wind speed. The exit section was configured to be a pressure outlet. While the top, bottom, and both sides were set to be walls.

The computational domain of this model is divided into two sub-domains: (a) the cylindrical rotating sub-domain surrounding the rotor which is represented by the unsteady RBM model and (b) the rectangular stationary sub-domain that describes the flow through the rest of the test section. In **Figure** 4-1 (a), the rotating sub-domain is represented by the circle that bounds the rotor, which is characterized by the fine meshing that can capture the extreme velocity and pressure gradients caused by rotor blades. The rectangle outside the previously mentioned circle represents the stationary sub-domain, which is characterized by its less fine meshing. In **Figure** 4-1 (b), there is a volumetric control in the form of cuboid which enables setting the mesh inside the wake region to a finer size than the rest of mesh domain outside, since the wake region is the part of the computational domain which is more essential to focus. Moreover, prism layers are of high importance to be able to simulate the viscous sublayer well and to predict the change in velocity near the solid boundaries accurately.

Therefore, **Figure** 4-2 highlights the 12 prism layers that were generated to enclose all this model's solid boundaries, including tower, nacelle, and blades. The red square at the top-right corner of the figure represents a blade cross-section at its mid-span length. A higher-resolution grid was generated at blade leading edge since it is the locus where the blade-generated vortices detach and go downstream forming the wake cylindrical shear layer [40].

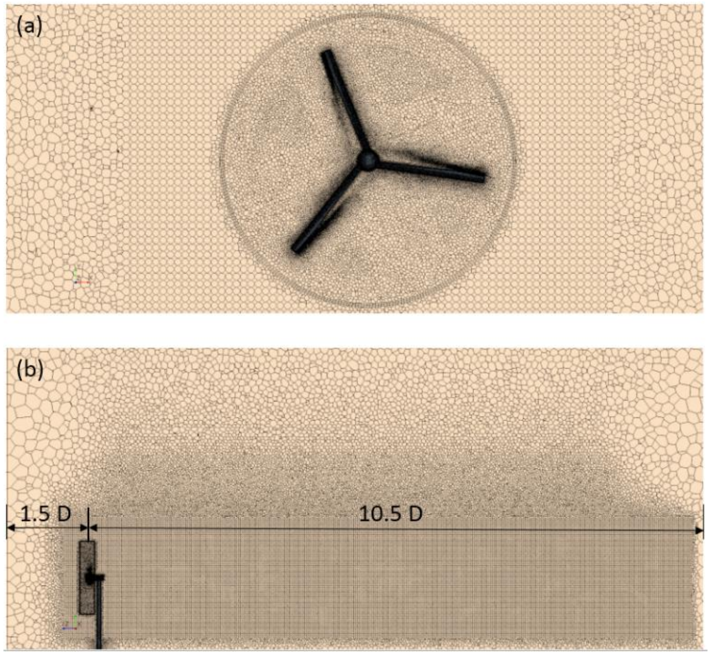

Figure 4-1: Computational domain (a) transverse sectional plane at 1.5D (b) longitudinal vertical sectional plane at wake centerline.

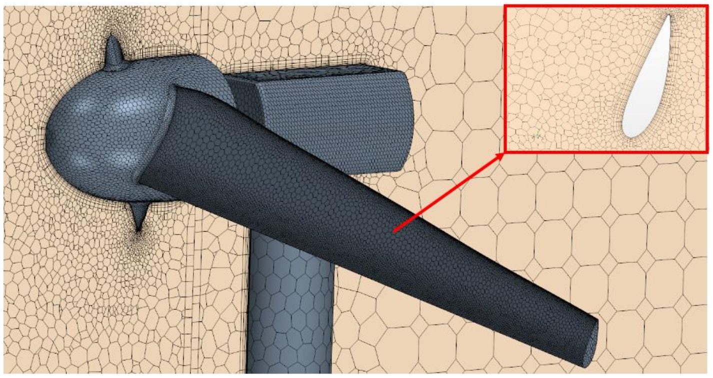

Figure 4-2: Prism layers around solid boundaries.

Although the unstructured mesh takes longer convergence time, the polyhedral unstructured mesh was embraced in this work for both rotating and stationary sub-domains. That is because the eddies, separation and wake regions around blades, tower, and a nacelle, as well as vortices shedding behind the rotor, are expected to be more accurate and well represented. It is worth mentioning that the cell base size for the stationary sub-domain is 0.0425 m, while it is 0.0275 m for the rotational sub-domain, it is intended to be finer to be able to capture the abrupt changes in velocity, pressure, turbulence, and shear stresses caused by the rotor blades.

LES deals with the different-scale eddies using two techniques. For large-scale eddies, they are solved by Navier-Stokes equations. For small-scale eddies, they are shaped by the Wall-Adapting-Local-Eddy viscosity (WALE) Sub-Grid Scale (SGS) model. WALE outperforms the Smagorinsky SGS in formulating the turbulent eddy viscosity and the accurate scaling near the wall without damping effects [41]. Regarding the unsteady conditions, the total simulation time is 0.54 seconds, which represents 12 rotor revolutions, with a time step of 0.12 milliseconds.

4.1.2 Model Assessment & Grid Independency Check

Four different grid counts were used to discretize this model domain. A comparison between the numerical axial velocity values and its experimental counterparts was held along central horizontal line probes at different downstream distances. **Table** 4-1 shows a comparison of the average error percentage which was investigated for each grid count.

Table 4-1: Axial velocity error percentage at different grid counts.

Case No.	Grid Count (Millions)	Average Error % at x/D=0.25	Average Error % at x/D=0.5
1	2.8	7.82	8.46
2	4.7	7.51	8.26
3	6.5	4.77	5.03
4	7.8	4.72	4.79

Figure 4-3 plots a graphical axial velocity comparison between the experimental and numerically-obtained values from different cell counts at x/D= 0.25. **Figure** 4-4 plots the same comparison but for x/D= 0.5. Although for both line probes, the error percentage decreases as the cell count increases, however, the simulations of the current work will adopt grid size 3 to compromise between the results accuracy and the simulation time cost. It is worth mentioning that each simulation of the present work was completed in 3 days, using the UWM computation clusters with 320 cores.

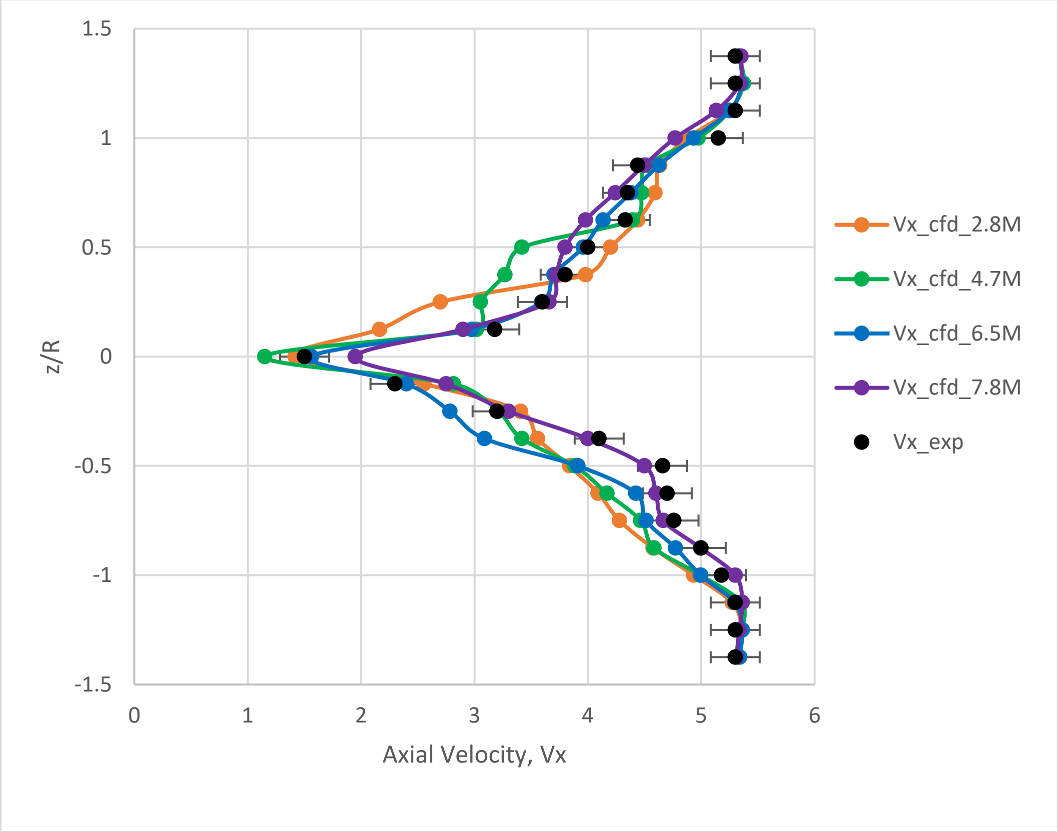

Figure 4-3: Axial velocity comparison at different cell counts, where x/D=0.25

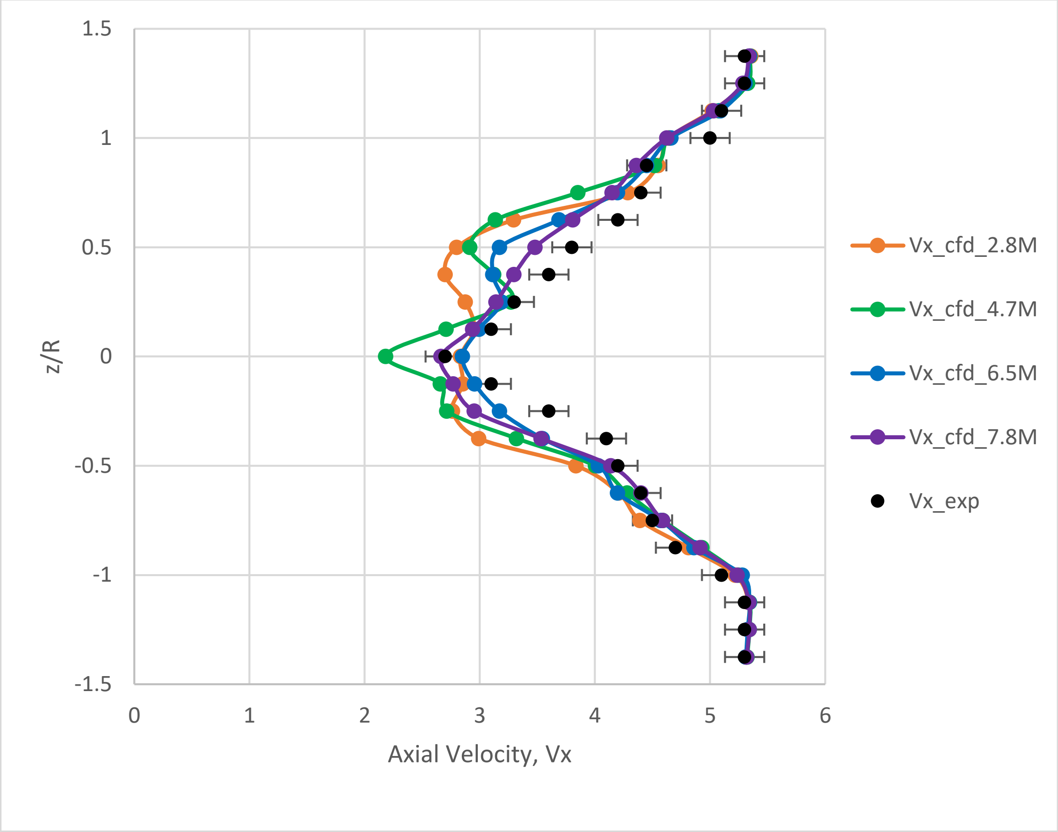

Figure 4-4: Axial velocity comparison at different cell counts, where x/D=0.5

Compromising between the minimized error and the total computational time was the main criterion in the independence test. While the change in the error between the different grid sizes significantly diminished between the grid size 3 and 4 (0.05% and 0.24% respectively), the time consumption was 1.5 times. Additional to such test, an assessment for the time-averaged y+ on the turbine blades was checked to be found in the viscous sublayer zone (y+ < 5) as shown in **Figure** 4-5. Finally, and though using unconditionally-stable implicit time marching, the convective Courant number was below 5 (seen in **Figure** 4-6) as recommended to keep excellent stability for the LES computation.

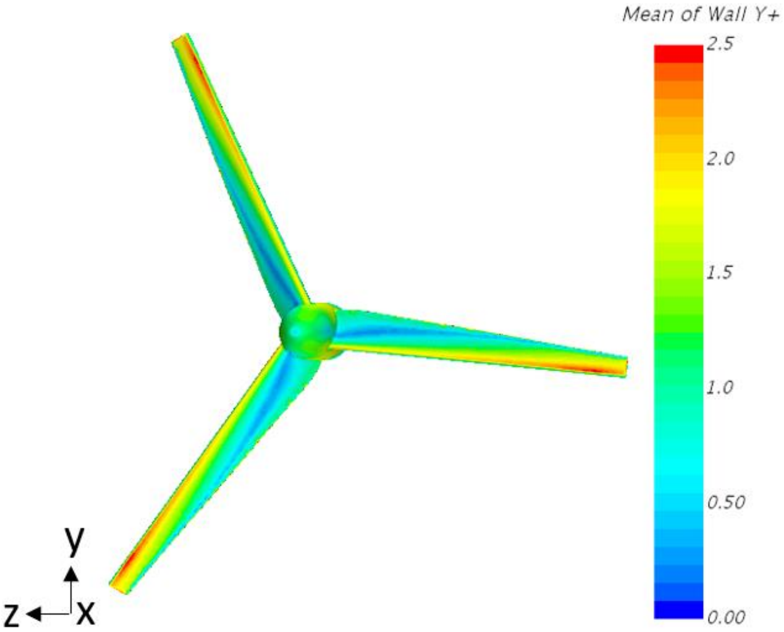

Figure 4-5: Mean of wall Y+ over the upstream surface of rotor blades

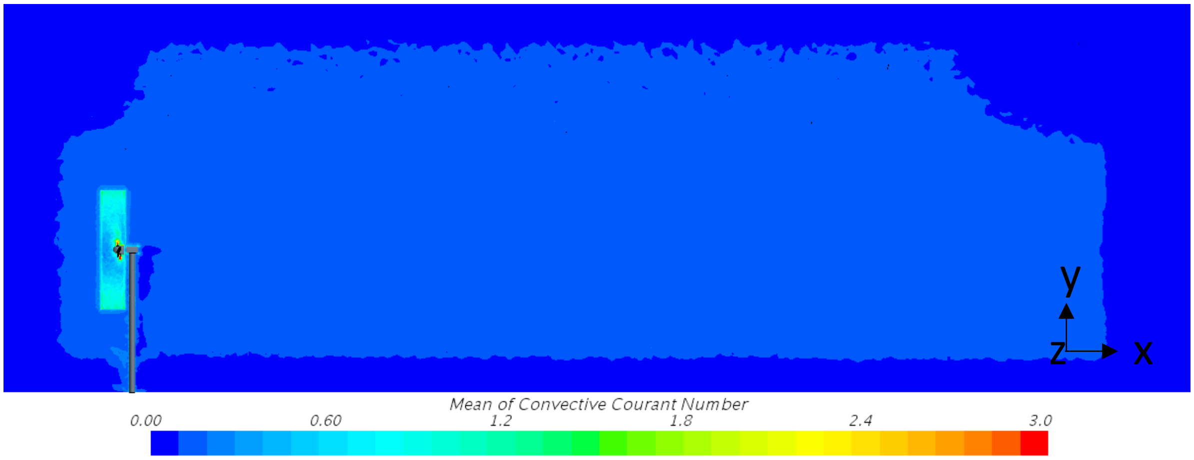

Figure 4-6: Mean of Convective Courant Number over a longitudinal plane at the centerline of the domain.

Large Eddy Simulation (LES) is used as the turbulence model to be able to deal successfully with the various scale eddies resulting from the rotor blades and its interactions with the surrounding flow. The advantage of LES is that it can deal with both large-scale and small-scale eddies. It can compute the large-scale eddies directly, and models only the sub-grid scale motions. [42]

Since it is an incompressible flow, the segregated flow model is used with the SIMPLE-type algorithm for pressure-velocity coupling. Moreover, the transient rigid body motion was used to model the rotor since it considers the periodic interactions of the rotating blades with the nacelle, tower, and even the wake. Although it is time-consuming but more accurate than steady-state approximations. For highly skewed cells at rotating interfaces, second-order upwind spatial discretization is used with LES since it reduces the spectral magnitudes at higher frequencies.

In the meantime, the discretization error in the LES, like any other numerical method, is a function of the grid size. Finer resolutions in the space and time help in achieving better accuracy to the real case data; especially with modeling the Kolmogorov scale eddies.

4.1.3 Case Studies

In this work, it is desired to shed light on the effect of two factors on the wake region length and power generation of a single wind turbine model. These two factors are:

- The variation of free stream velocity, while the Tip Speed Ratio (TSR) is kept constant.
- The variation of TSR, while the free stream velocity is kept constant.

Three different free stream velocities were adopted in the CFD simulations; 7, 10 and 13 m/s, to consider the entire range from low wind speed to high wind speed. Simulations with stream velocities more than 13 m/s are avoided since the HAWTs starts to stall at 15 m/s, then lose power. At every single velocity, four different TSR values were simulated 2.5, 4, 5.5, and 7, since it is desired to capture the TSR at which the power production is optimized. The domain downstream distance is extended to 17D, instead of 10.5D in case of validation model, so that the complete axial velocity recovery distance would be contained within the extension for high wind speeds.

4.2 Results

4.2.1. The effect of TSR variation (free stream velocity is constant)

4.2.1.1 Low wind speed (free stream velocity = 7 m/s)

Figure 4-7 represents the axial velocity decay downstream of the turbine model through a longitudinal sectional plane cutting through the entire length of the simulation domain at the wake centerline. This decay is caused by the streamlines blending due to interaction with the rotating blades. The common condition among the four cases enclosed in this figure is that the free stream velocity is 7 m/s, but the TSR is increased from one case to the next. Part (a) represents the case of TSR=2.5, where the complete axial velocity recovery occurs at a downstream distance of 14.5 rotor diameters (14.5 D). The complete velocity recovery is retarded because of the poor mixing between the wake region and surrounding environment, since the rotational speed, hence TSR, is still relatively low. In part (b), the TSR is increased to 4, then the interaction between the turbine wake and the surrounding environment is enhanced, resulting in a shorter downstream distance of 9.5 rotor diameters (9.5 D) to reach complete velocity recovery. Similarly, in part (c), the downstream distance of complete velocity recovery is shortened more when the TSR is increased to 5.5 to be 7.5 D. In part (d) a complete velocity recovery is reached at 6.5 D.

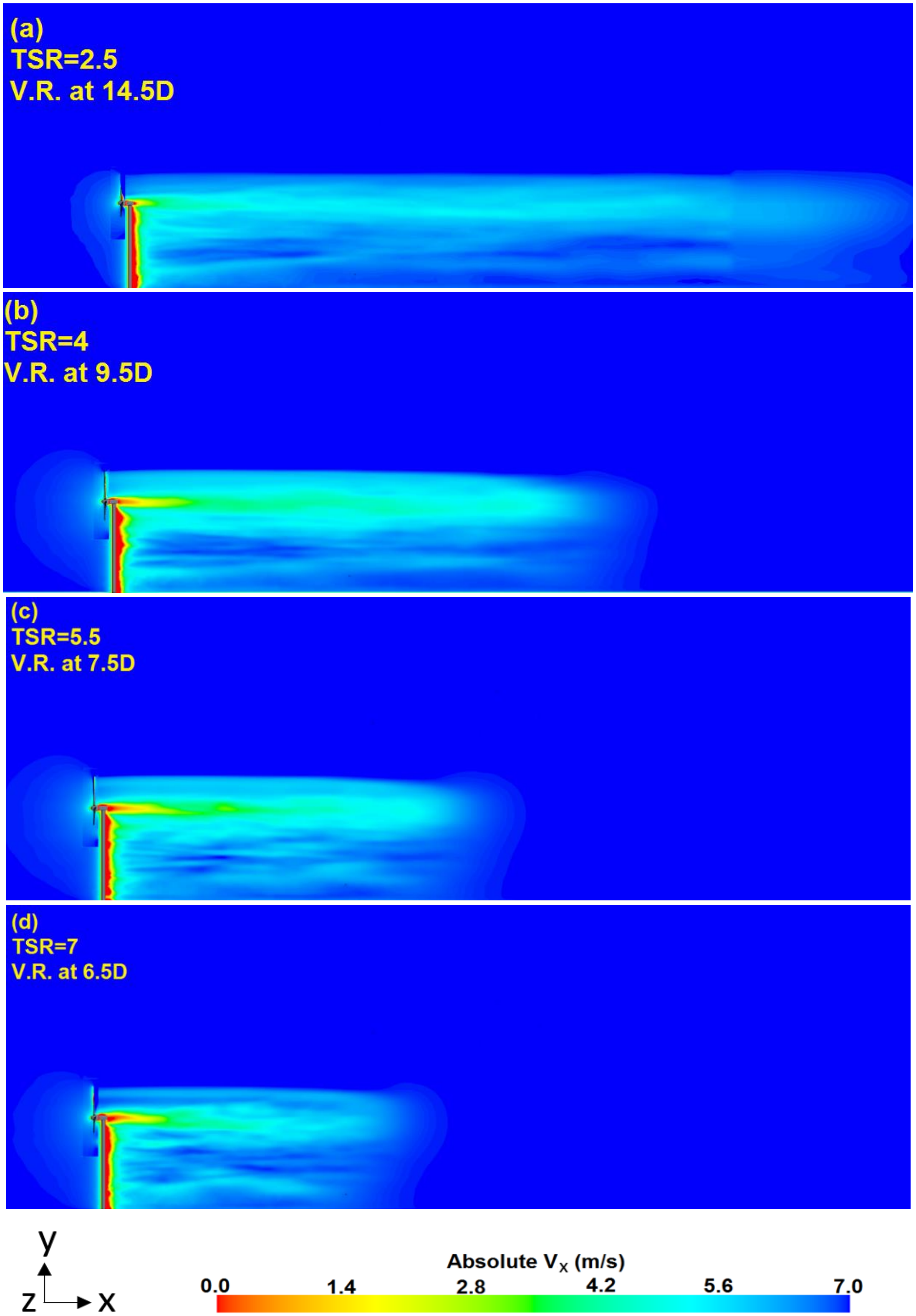

Figure 4-7: Longitudinal section for axial velocity Vx (m/s) for free stream velocity of 7 m/s, (a) TSR=2.5, (b) TSR=4, (c) TSR=5.5, TSR= 7

Figure 4-8 shows a graphical comparison of the hub height axial velocity recovery, which is defined as the ratio of the hub height axial velocity to the free stream velocity, for different TSRs while the free stream velocity is kept constant at 7 m/s. It is evident that as the TSR is increased, the complete velocity recovery is attained earlier. In addition to that, the graph indicates another finding, the rate of velocity recovery is enhanced as the TSR is increased. For example, the 80% velocity recovery is obtained at 7.5 D for TSR=2.5, while the same velocity recovery is obtained at 7 D for TSR=4, in the meantime, the same velocity recovery is obtained at 5.5 D for TSR=5.5. Finally, it is obtained at 2.5 D for TSR=7.

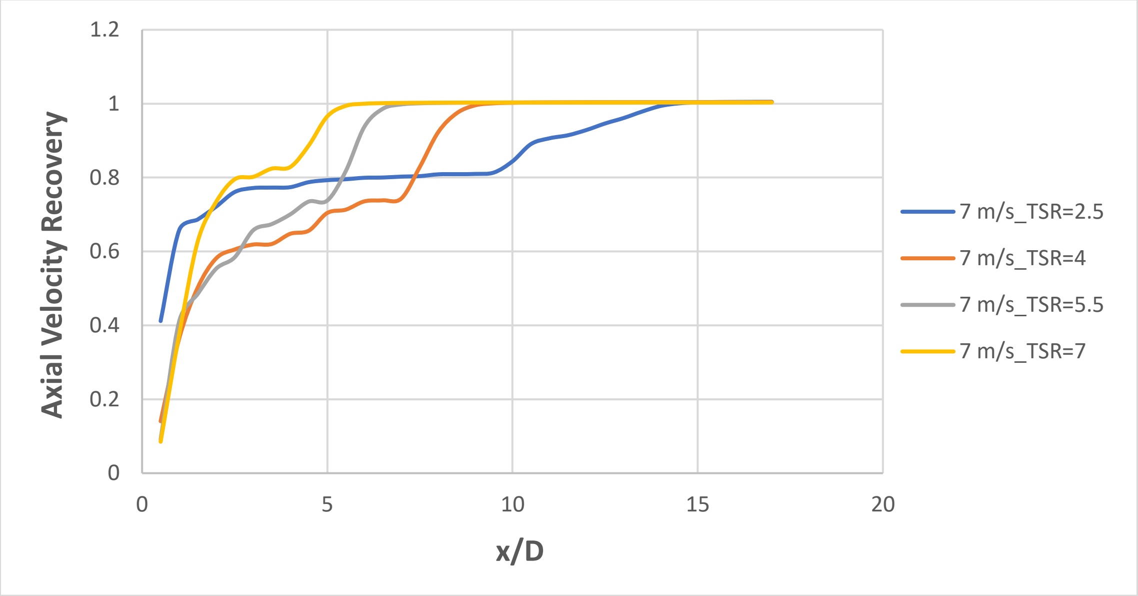

Figure 4-8: Hub height axial velocity recovery with free stream velocity of 7 m/s for different TSRs.

If it is wanted to highlight the close details of the wake region within the first three rotor diameters downstream of the rotor, **Figure** 4-9 is the best scene to investigate these details. The wake details in case of free stream velocity of 7 m/s with TSR=4 are shown in such figure. In the upstream region of the rotating blades and tower, the velocity is decelerated to 6 m/s, while the air particles are forced to a complete stop at the hub nose. Furthermore, the fluid particles adjacent to the pressure side of the blades is decelerated to 1 m/s, but the flow at the blade tip is accelerated to 9 m/s. Moreover, there is a recirculation zone directly downstream of the tower, where the velocity is -2 m/s (reversed direction). All of these velocity variances are considered while calculating the vibrational loads affecting the rotor and tower.

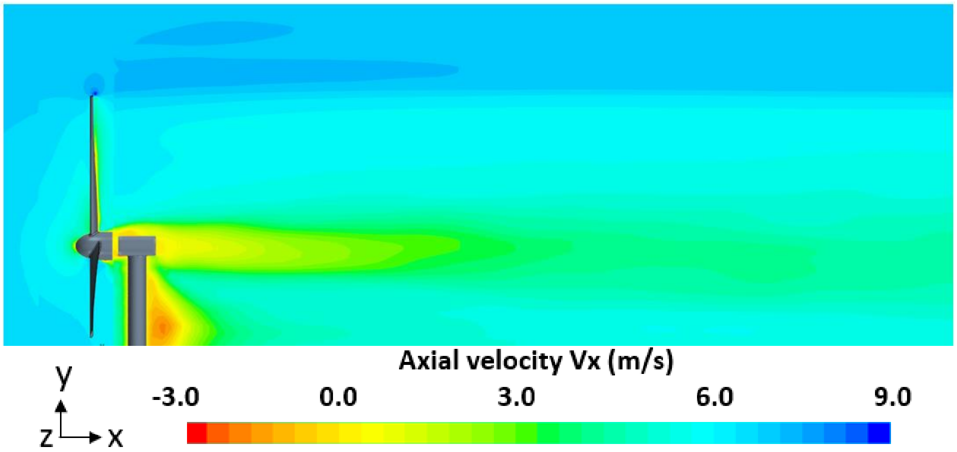

Figure 4-9: Wake region close details for free stream velocity of 7 m/s with TSR=4.

Finally, the lowest axial velocity is obtained directly behind the nacelle, and the width of the generated shear layer doesn't show a remarkable expansion, neither in the near wake region represented in this figure nor in the far wake region represented in part (b) of **Figure** 4-7.

4.2.1.2 Medium wind speed (free stream velocity = 10 m/s)

Figure 4-10 represents the axial velocity decay downstream of the turbine model through a longitudinal sectional plane. The common free stream velocity among the four cases enclosed in this figure is 10 m/s, which is the only difference from what is provided in **Figure** 4-7. Fortunately, the distance of complete velocity recovery at different TSRs is identical for both free stream velocities (7 & 10 m/s). There is just one shift in case of TSR=7; the complete velocity recovery is obtained at 6.5D for 7 m/s, while obtained at 6.2D for 10 m/s.

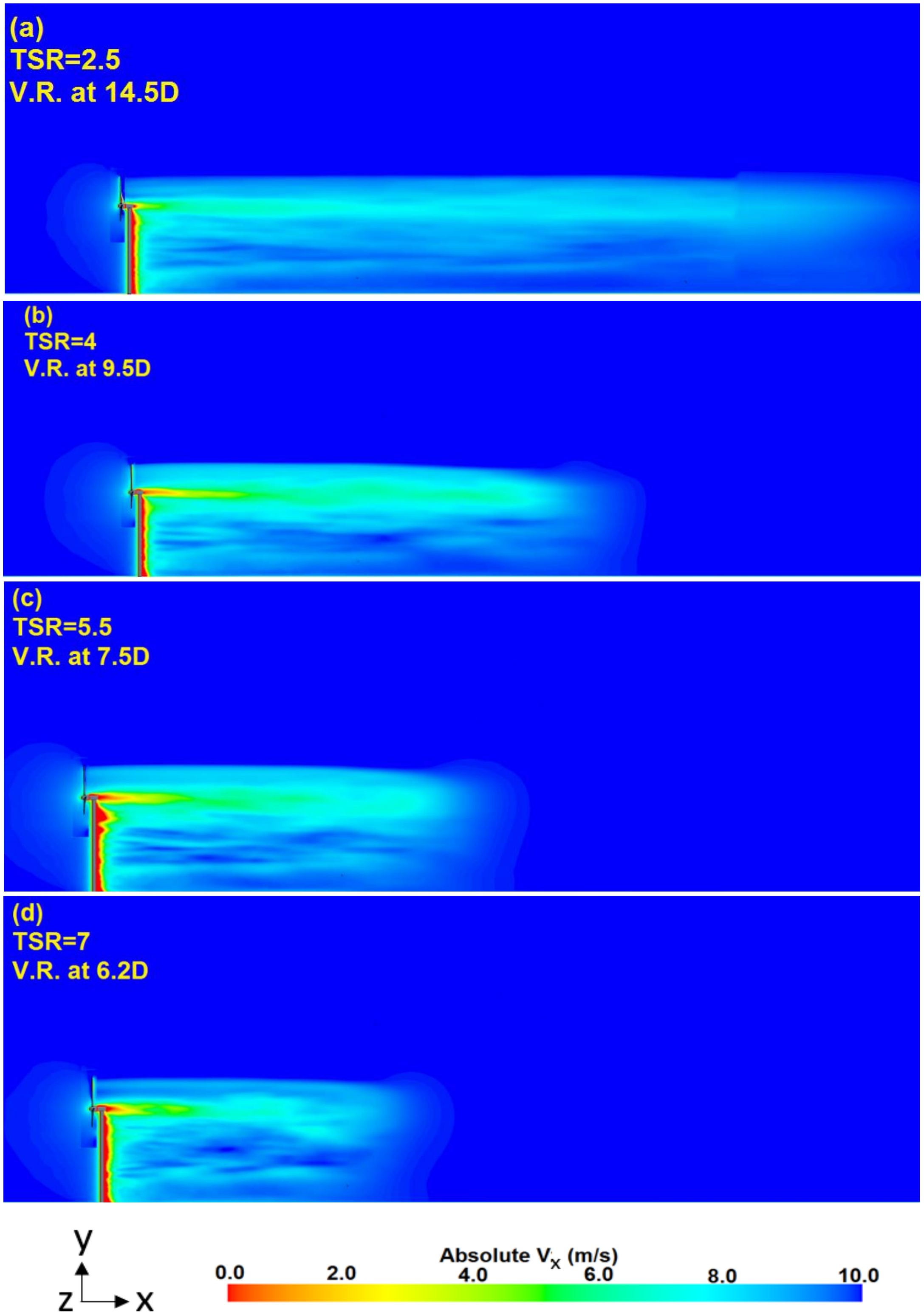

Figure 4-10: Longitudinal section for axial velocity Vx (m/s) for free stream velocity of 10 m/s, (a) TSR=2.5, (b) TSR=4, (c) TSR=5.5, TSR= 7.

Figure 4-11 presents identical trends to what is presented in **Figure** 4-8, in terms of earlier velocity recovery for higher TSR. Even the rates of velocity recovery are almost similar to the rates of the 7 m/s case.

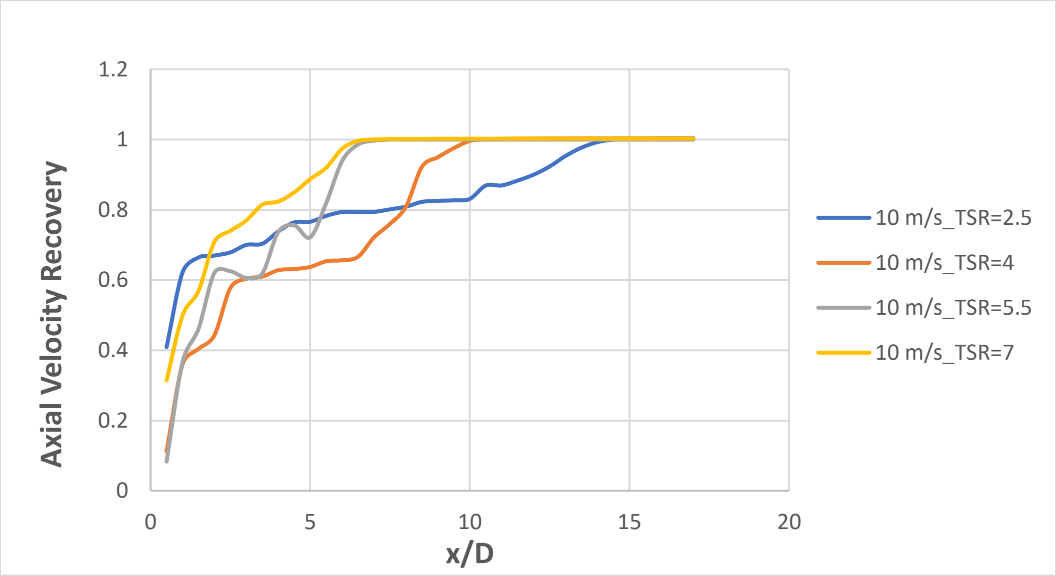

Figure 4-11: Hub height axial velocity recovery with free stream velocity of 10 m/s for different TSRs

Figure 4-12 shows the wake region close details for free stream velocity of 10 m/s with TSR=4. It provides similar features to what is obtained in **Figure** 4-9. We still have a decelerated flow upstream of the rotor, stagnation point at the hub nose, accelerated flow at the blade tip, and a recirculation zone behind the tower.

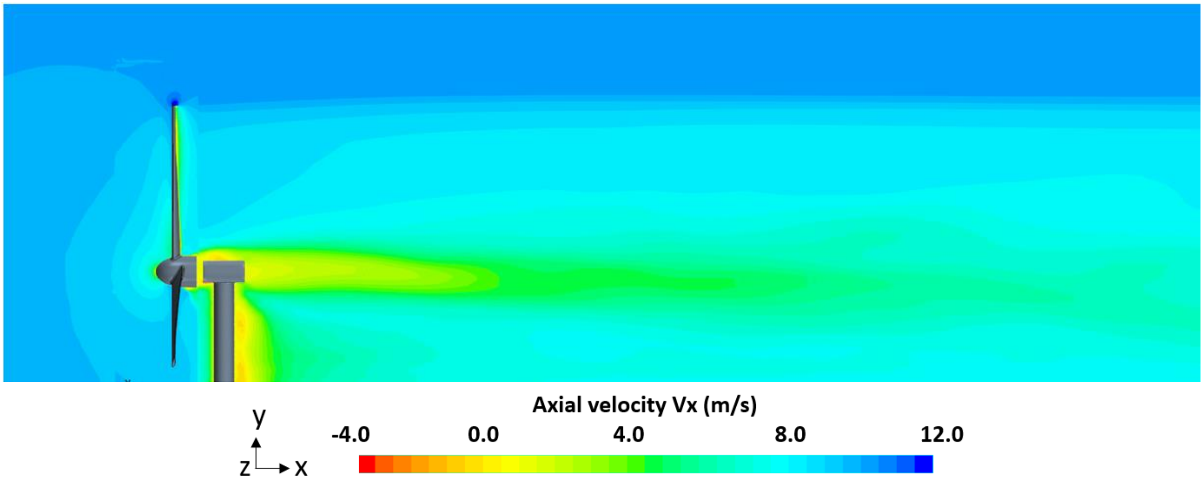

Figure 4-12: Wake region close details for free stream velocity of 10 m/s with TSR=4.

4.2.1.3 High wind speed (free stream velocity = 13 m/s)

Figure 4-13 represents the axial velocity decay downstream of the turbine model through a longitudinal sectional plane with a free stream velocity of 13 m/s. The distance at which the complete velocity recovery is accomplished with TSR increase is identical to the two previous cases (7 & 10 m/s).

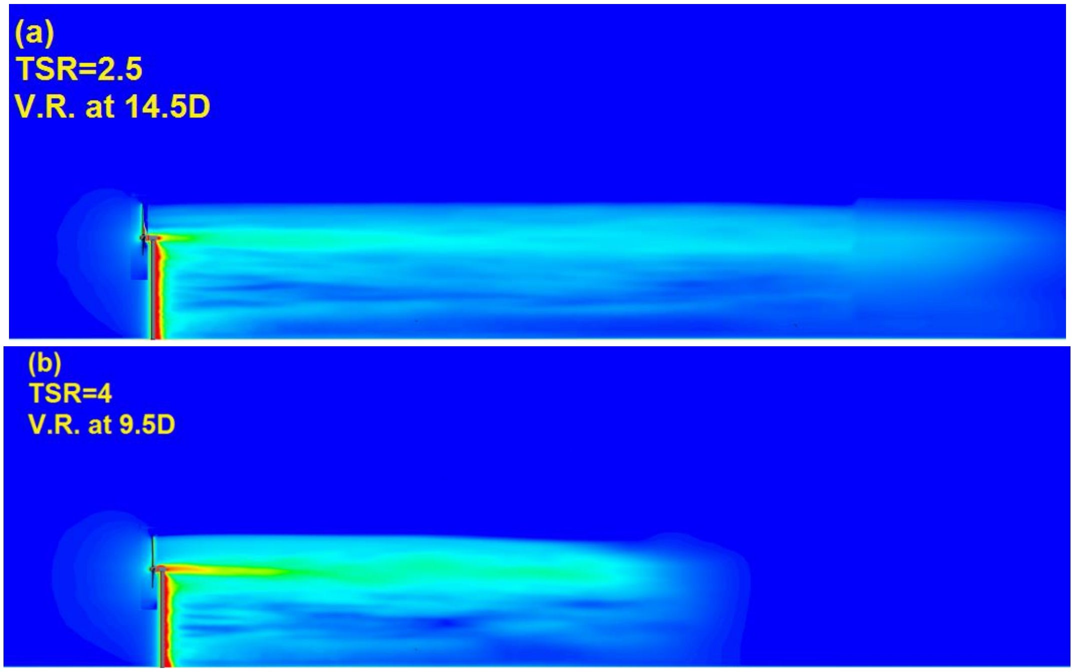

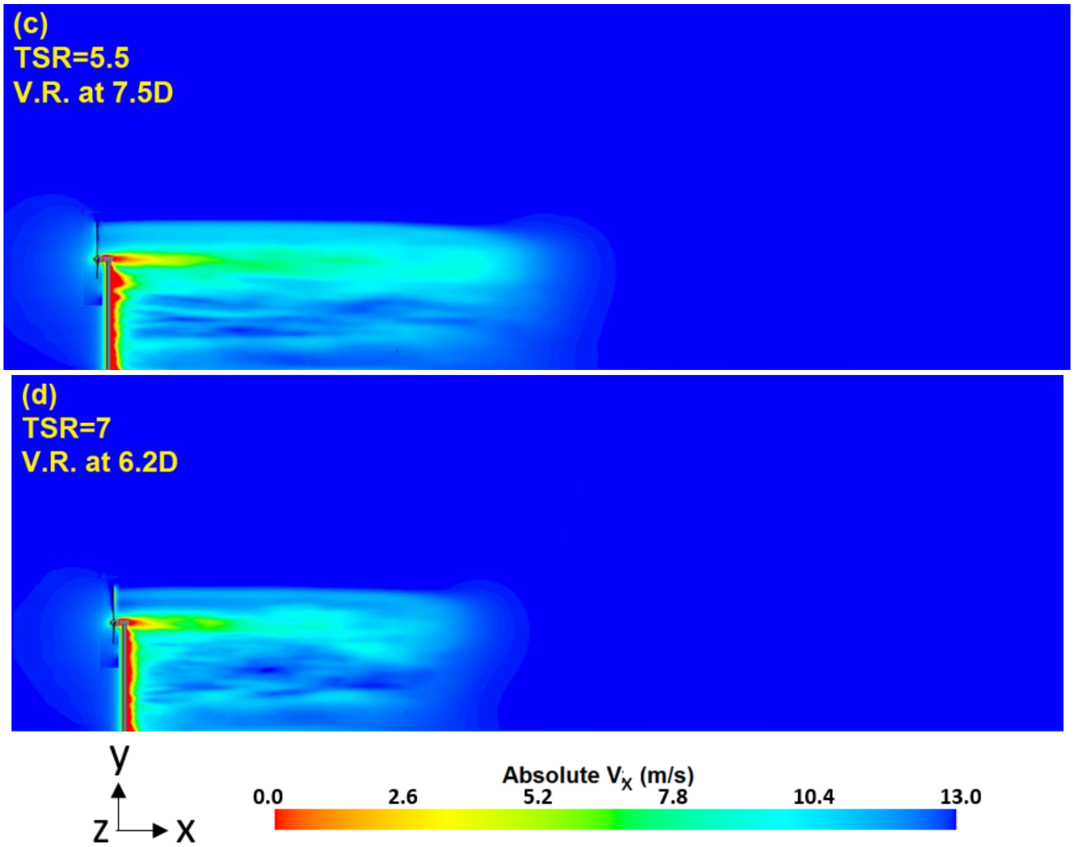

Figure 4-13: Longitudinal section for axial velocity Vx (m/s) for free stream velocity of 13 m/s, (a) TSR=2.5, (b) TSR=4, (c) TSR=5.5, TSR= 7.

Figure 4-14 indicates earlier complete velocity recovery with the increased TSR. Generally, the velocity recovery rate is increased as the TSR is increased, but with little differences from the cases of 7 & 10 m/s. For example, the 80% velocity recovery for TSR=2.5 is attained at 9D, while it was 7.5D for 7 &10 m/s. Another example, the 80% velocity recovery for TSR=4 is attained at 7.5D, while it was 7D for 7 &10 m/s.

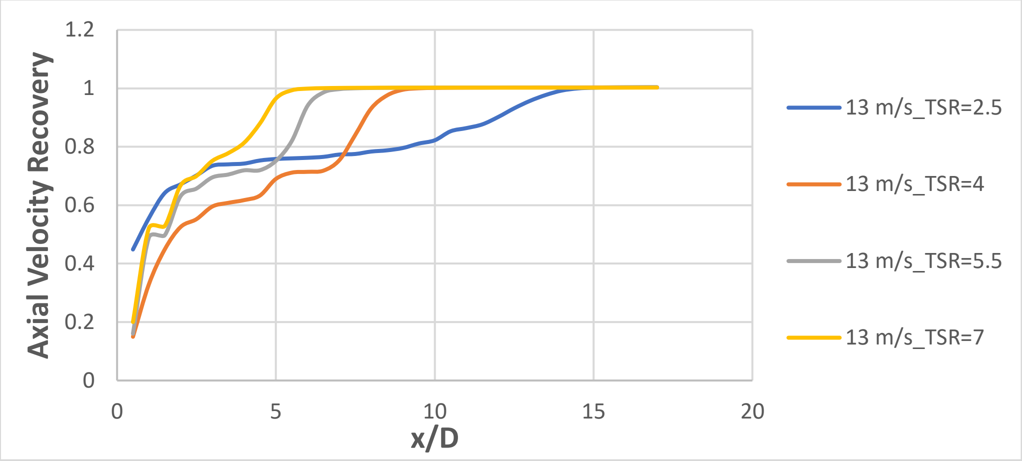

Figure 4-14: Hub height axial velocity recovery with free stream velocity of 13 m/s for different TSRs

The general flow features provided by **Figure** 4-15 for 13 m/s free stream velocity are so similar to the two previous two cases (7 & 10 m/s), except for little differences; the decelerated flow region upstream of the rotor is larger, the recirculation downstream of the tower is suppressed, and the volume of the wake affected by the nacelle extends further downstream through the turbine wake.

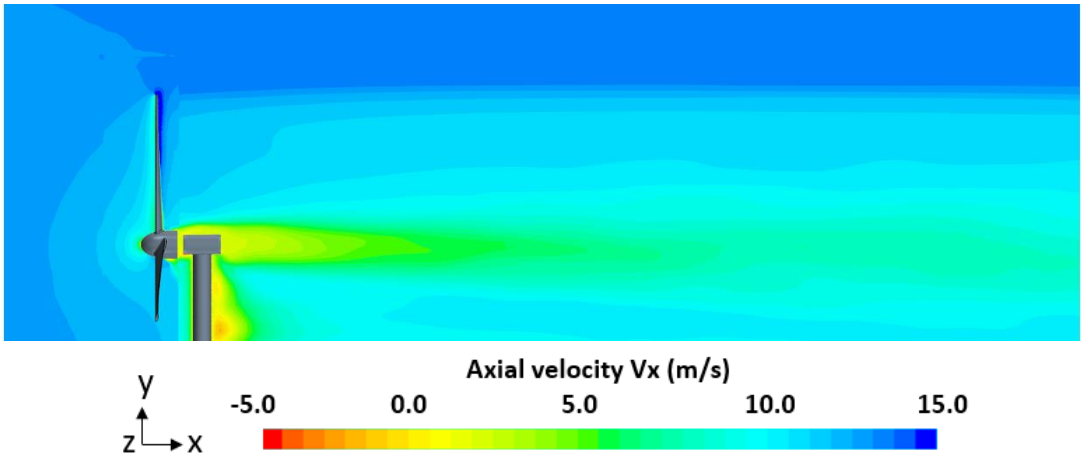

Figure 4-15: Wake region close details for free stream velocity of 13 m/s with TSR=4

Figure 4-16 provides a qualitative description of the axial velocity change captured on four transverse planes at different downstream distances within the first rotor diameter of the wake. The free stream velocity is 13 m/s with TSR=4. Part (a), where x/D=0, the planes cut through the rotor blades, it shows that the flow is decelerated upstream of the tower and blades to 11 m/s, particularly at the root of the blades where the velocity is 7 m/s. Part (b) is at x/D=0.25, it shows how the wake starts to evolve downstream of the rotor and tower. The velocity behind the tower is decreased to 10 m/s, while the flow behind the nacelle is more decelerated to 7 m/s. For parts (c) and (d), where x/D equals 0.5 and 1 respectively, flow features are similar to (a), besides, the core of the wake starts to meander to the right.

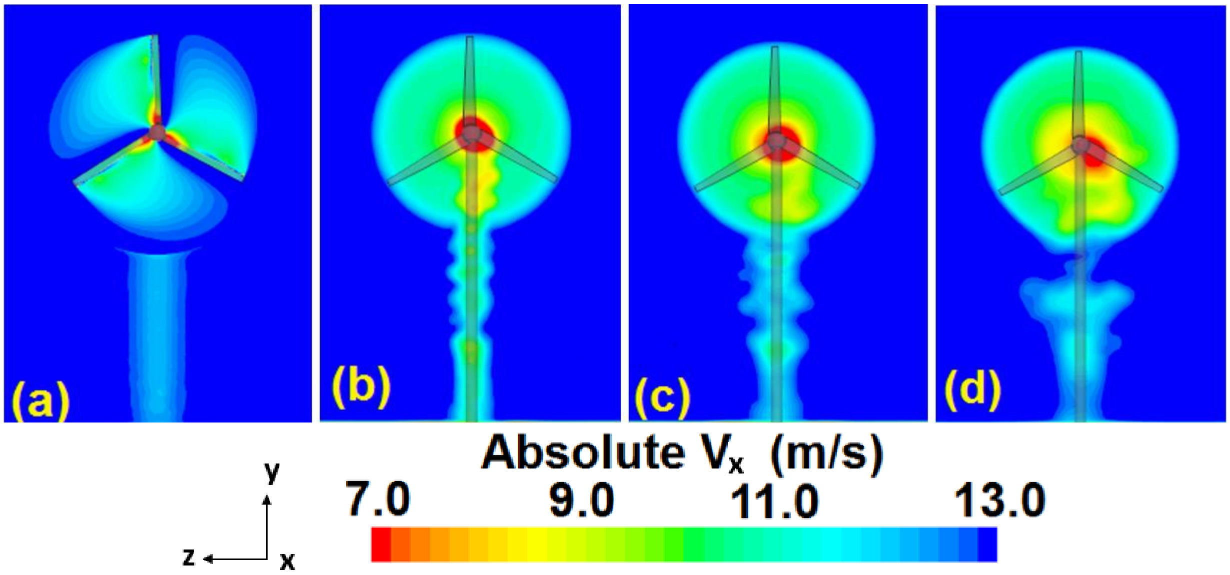

Figure 4-16: Axial velocity change captured on four transverse planes at different downstream distances; (a) x/D=0, (b) x/D=0.25, (c) x/D=0.5 and (d) x/D=1.

4.2.2 The effect of free-stream velocity variation (TSR is constant)

Figure 4-17 and **Figure** 4-18 are created to examine this factor, so the two figures show a graphical comparison of the hub height axial velocity recovery of the three different free stream velocities (7, 10 and 13 m/s), while the TSR is constant and equal to 4 and 5 respectively. It is found that whatever the free stream velocity is, the TSR dictates the distance of complete velocity recovery. Furthermore, the rates of velocity recovery increase are almost the same for constant TSR.

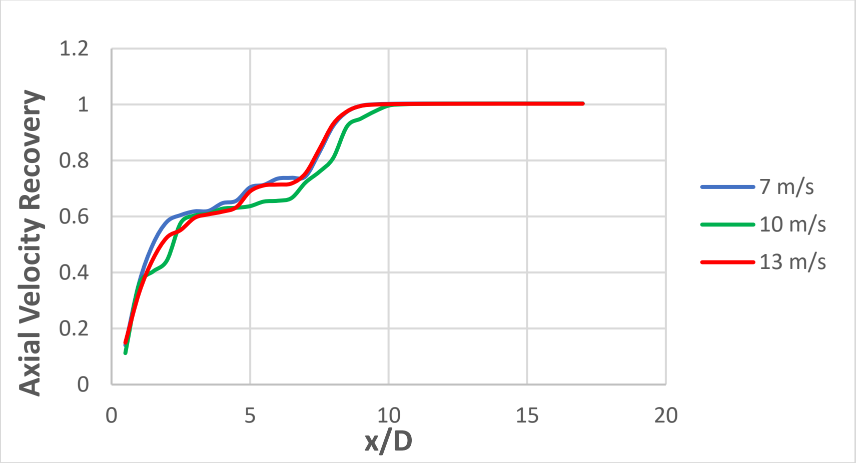

Figure 4-17: Hub height axial velocity recovery of the three different free stream velocities (7, 10 and 13 m/s), while the TSR is constant and equal to 4.

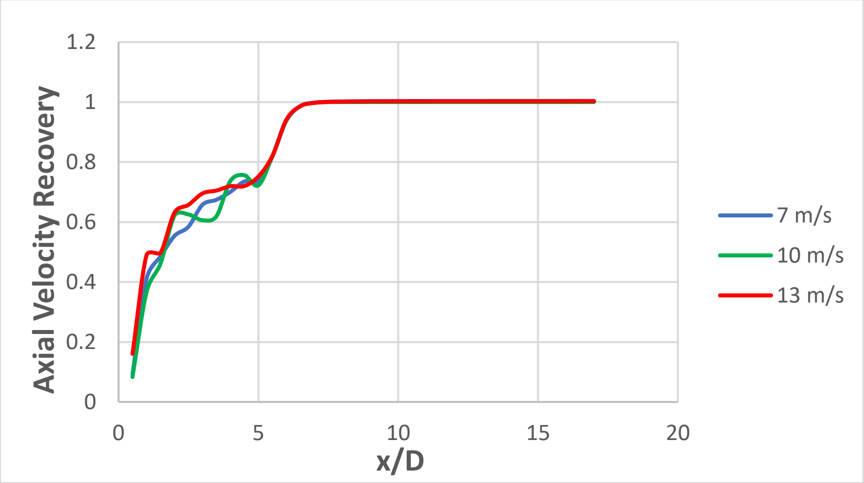

Figure 4-18: Hub height axial velocity recovery of the three different free stream velocities (7, 10 and 13 m/s), while the TSR is constant and equal to 5.5.

4.2.3 The effect of TSR variation on power production

Table 4-2 highlights the most important findings of the current chapter. For fixed free stream, increasing the TSR increases the numerically predicted power production, hence the Power Coefficient (Cp), to an optimum value then the power falls. For instance, the free stream velocity of 13 m/s generates 33.4 W power for TSR=2.5. the generated power jumps to an optimum of 87 W at TSR=4. Then the power falls again to 50 W at TSR=5.5. Finally, it becomes –33 W at the TSR=7. The negative power means that the turbine can't respond to this high TSR, it no longer produces power at this high rotation, it needs some power from an external source to rotate at this high TSR. Therefore, it is an impossible case. It is obvious that the TSR range of 4 to 5.5 is the optimum TSR for all free stream velocities.

Table 4-2: Calculated CFD power output (W) and its corresponding power coefficient for each case study

TSR	**7 m/s**		**10 m/s**		**13 m/s**	
	P(W)	**Cp**	**P(W)**	**Cp**	**P(W)**	**Cp**
2.5	3.8	0.06	13.7	0.08	33.4	0.09
4	12	0.2	38.2	0.22	87	0.23
5.5	6	0.1	20	0.11	50	0.13
7	-9	-0.15	-18	-0.1	-33	-0.08

For running at constant TSR, the generated power slightly increases, hence the Cp, as the free stream velocity increases. For example, the TSR=4 generates 12 W power (Cp=0.2) for 7 m/s as free stream velocity, while it generates 38.2 W power (Cp=0.22) for 10 m/s as a free stream velocity. Finally, the power is 87 W (Cp=0.23) for 13 m/s as a free stream velocity. The reason why the current work's optimum TSR, hence optimum Cp, is less than the optimum TSR for modern turbines is the limitation of the blade design. The NACA 4424 profile was selected, regardless of its poor power generation, because it offered a thicker blade profile relative to the chord length to improve the strength and prevent the blades from breaking during experimental testing.

4.3 Conclusions

For fixed free stream velocity (whatever its low or medium or high wind speed), increasing the TSR (between 4 and 5.5 for this particular blade design) reduces the distance of complete velocity recovery, hence the separation distance between two turbines in a wind farm, while both the generated power and associated Cp increases to a maximum value (0.2 to 0.23) then falls.

For fixed TSR, increasing the free stream velocity almost does not affect the distance of complete velocity recovery (the separation distance), but the generated power increases significantly (transition to medium wind speed generates 3.25 times the power generated by low wind speed, in addition, transition to high wind speed generates 2.5 times the power generated by medium wind speed)

For fixed TSR, increasing the free stream velocity results in an increase for the associated Cp (transition from a wind speed value to a higher one leads to 5 to 15% increase in Cp).

Chapter 5 : Study of Aerodynamic Performance and Power Output for Residential-Scale Wind Turbines

This chapter presents the rotor blade airfoil analysis of residential-scale wind turbines. On this track, four new airfoils (GOE 447, GOE 446, NACA 6412, and NACA 64(3)-618) characterized by their high lift-to-drag ratios (161.3, 148.7, 142.7, and 136.3, respectively). Those new airfoils are used to generate an entire 7 m long blades for three-bladed rotor horizontal axis wind turbine models tested numerically at low, medium, and rated wind speeds of 7.5, 10 and 12.5 m/s, respectively, with a design tip speed ratio of 7. The criterion to judge each model's performance is power output. Thus, the blades of the model which produce the highest power are selected to undergo a tip modification (winglet) and leading-edge modification (tubercles), seeking power improvement. It is found that the GOE 447 airfoil outperformed the other three airfoils at all tested wind speeds. Thus, it is opted for adding winglets and tubercles. At 12.5 m/s, winglet design produced 5% more power, while tubercles produced 5.5% more power than the GOE 447 baseline design. Furthermore, the computational domain is divided into two regions; rotating (the disc that encloses the rotor) and stationary (the rest of the flow domain). Meanwhile, the numerical model is validated against the experimental velocity measurements. Since Reynolds-Averaged Navier-Stokes (RANS) with k-ω SST turbulence model can capture the laminar-to-turbulent boundary layer transition, it is used in the 18 simulations of the current work. However, Large Eddy Simulation (LES) can deal successfully with the various scale eddies resulting from the rotor blades and its interactions with the surrounding flow. Thus, the LES was used in the six simulations done at the rated wind speed. LES power output calculation is 7.9% to 11.9% higher than the RANS power output calculation.

5.1 Model Geometry

Figure 5-1, **Figure** 5-2, **Figure** 5-3 and **Figure** 5-4 show the profiles of the three airfoils opted for the current study. The reason behind this selection is the high lift-to-drag ratios that characterize the three air foils. The data obtained from NACA Airfoil Tool website is concluded in **Table** 5-1. It is worth mentioning that airfoil NACA 6412 will be my focused part in the results analysis, since it is wanted to provide three individual reports.

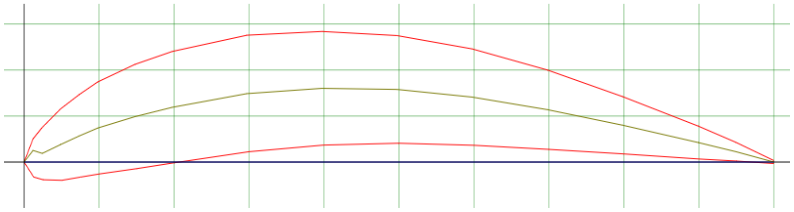

Figure 5-1: Airfoil GOE 447

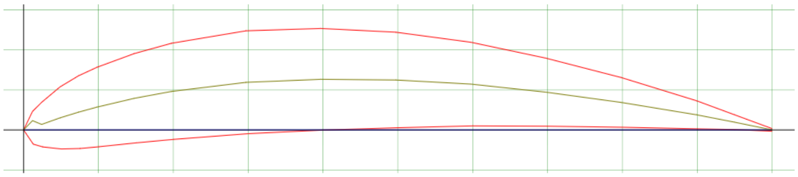

Figure 5-2: Airfoil GOE 446.

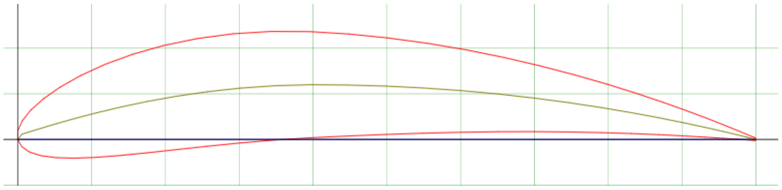

Figure 5-3: Airfoil NACA 6412.

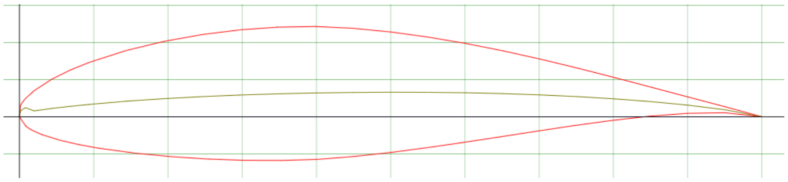

Figure 5-4: Airfoil NACA 64(3)618

Table 5-1: Aerodynamic properties of the opted airfoils.

Airfoil type	Lift-to-drag ratio	α	Max. thickness (% of chord)	Max. camber (% of chord)
NACA 64(3)618	136.3	6.5°	17.9	3.3
NACA 6412	142.7	5.75°	12	6
GOE 446	148.7	2.75°	12.9	6.3
GOE 447	161.3	4°	12.7	8

As shown in **Table** 5-2, **Table** 5-3, and **Table** 5-4**, t**he following set of equations [43] are used to generate the design parameters of each blade at various cross section along the span from root to tip:

$$r = \left(\frac{r}{R}\right) R \tag{1}$$

$$\lambda r = (\frac{r}{R})\lambda \tag{2}$$

$$\phi = tan^{-1}(2/(3\,\lambda r)) \tag{3}$$

$$C = 8\pi r \, sin\,\phi/(3BC_l \;\lambda r) \tag{4}$$

$$\theta_p = \phi - \alpha \tag{5}$$

$$\theta_T = \theta_p - \theta_{p,o} \tag{6}$$

Where

R : Rotor radius at tip section

r : Rotor radius at any section along the blade span

λ : Rotor Tip speed ratio

λr : Speed ratio at any section along the blade span

ϕ : Angle of relative wind

C : Chord length

Cl : Lift coefficient

B : Number of rotor blades

θ_T : Twist angle

θp : Pitch angle

θp,o : Pitch angle at the tip

Table 5-2: Geometry parameters of various sections of the blade (GOE 446)

r/R	r(m)	λr	ϕ(rad)	ϕ(deg)	θp (deg)	θ_T (deg)	C (m)
1	7	7	0.094951706	5.4403	2.6903	0.0000	0.2648
0.9	6.3	6.3	0.105427751	6.0406	3.2906	0.6003	0.2939
0.8	5.6	5.6	0.118489959	6.7890	4.0390	1.3487	0.3301
0.7	4.9	4.9	0.135224132	7.7478	4.9978	2.3075	0.3765
0.6	4.2	4.2	0.157416873	9.0193	6.2693	3.5790	0.4378
0.5	3.5	3.5	0.188221505	10.7843	8.0343	5.3440	0.5225
0.4	2.8	2.8	0.233743181	13.3925	10.6425	7.9522	0.6468
0.3	2.1	2.1	0.307397473	17.6126	14.8626	12.1723	0.8450
0.2	1.4	1.4	0.44441921	25.4633	22.7133	20.0230	1.2006

Table 5-3: Geometry parameters of various sections of the blade (NACA 6412)

r/R	r(m)	λ_r	ϕ(rad)	ϕ(deg)	θ_p (deg)	θ_T (deg)	C (m)
1	7	7	0.094951706	5.4403	-0.3097	0.0000	0.2648
0.9	6.3	6.3	0.105427751	6.0406	0.2906	0.6003	0.2939
0.8	5.6	5.6	0.118489959	6.7890	1.0390	1.3487	0.3301
0.7	4.9	4.9	0.135224132	7.7478	1.9978	2.3075	0.3765
0.6	4.2	4.2	0.157416873	9.0193	3.2693	3.5790	0.4378
0.5	3.5	3.5	0.188221505	10.7843	5.0343	5.3440	0.5225
0.4	2.8	2.8	0.233743181	13.3925	7.6425	7.9522	0.6468
0.3	2.1	2.1	0.307397473	17.6126	11.8626	12.1723	0.8450
0.2	1.4	1.4	0.44441921	25.4633	19.7133	20.0230	1.2006

Table 5-4: Geometry parameters of various sections of the blade (NACA 64(3)618)

r/R	r(m)	λr	ϕ(rad)	ϕ(deg)	θp (deg)	θ_T (deg)	C (m)
1	7	7	0.094951706	5.4403	-1.0597	0.0000	0.2648
0.9	6.3	6.3	0.105427751	6.0406	-0.4594	0.6003	0.2939
0.8	5.6	5.6	0.118489959	6.7890	0.2890	1.3487	0.3301
0.7	4.9	4.9	0.135224132	7.7478	1.2478	2.3075	0.3765
0.6	4.2	4.2	0.157416873	9.0193	2.5193	3.5790	0.4378
0.5	3.5	3.5	0.188221505	10.7843	4.2843	5.3440	0.5225
0.4	2.8	2.8	0.233743181	13.3925	6.8925	7.9522	0.6468
0.3	2.1	2.1	0.307397473	17.6126	11.1126	12.1723	0.8450
0.2	1.4	1.4	0.44441921	25.4633	18.9633	20.0230	1.2006

The current wind turbine model geometry was generated using SoildWorks, then exported into Star CCM+ to generate mesh and solve the fluid flow of the wake region. The Following simulation includes a model of 14 m rotor diameter, with a hub height of 21 m. It is subtracted from the block that represents the fluid domain. The fluid block cross section dimensions are 42 m x 42 m while its total length is 310 m. Turbine model is located 30 m downstream of the entrance, while the distance allowed downstream of it is 280 m. According to previous research works in this field, the current work's 9% blockage ratio is small enough to avoid the fluid domain's solid boundary effect. In addition, the 20 rotor diameters left behind the rotor to study the wake is reasonable. The current work's geometry and domain are shown in **Figure** 5-5.

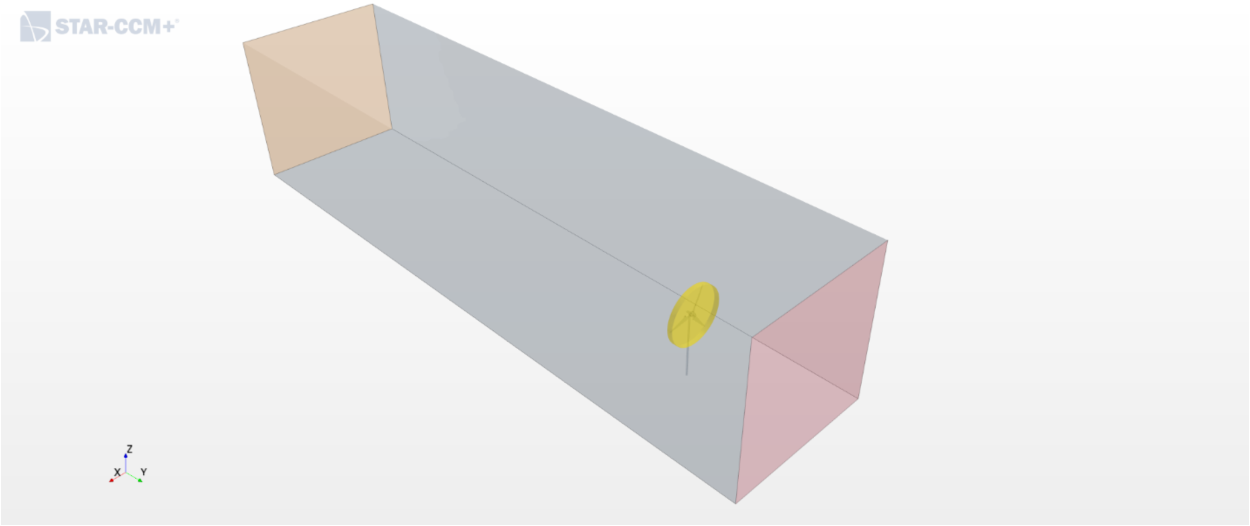

Figure 5-5: Model geometry.

For the tubercles, it is designed as a sine wave with a constant amplitude of 4.5% of the cord at the root section and a constant wavelength of 15.8% of the cord at the root section. This design was inspired by the work of Abate et al. [28]. Whereas, for the winglets, its orientation is selected to be downstream facing since this is the orientation found to be most effective in power increase [19]. The winglet height is designed to be 2.0% of the blade radius (R), while the radius of curvature is designed as 25.0% of the winglet height, and the cant angle is 90°. The previous design was tested with different blades by Johansen et al. [23] and found to give higher power production. The basic, tubercle, and winglet blades generated using the GOE 447 airfoil are shown in **Figure** 5-6 (a), (b), and (c), respectively.

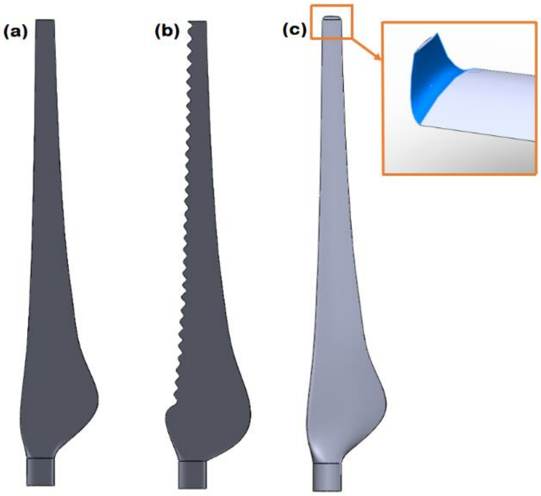

Figure 5-6: Basic, tubercle and winglet blades made with the GOE 447 airfoil.

To reach the maximum accuracy obtained through validation, the fluid domain of NACA 64(3)618 model is discretized to 6.5M cells. However, the new airfoils are thinner and more curved (NACA 6412, GOE 446, and GOE 447), besides having some designs with winglets and tubercles.

For each LES simulation, it took about three days using 200 cores of the University of Wisconsin-Milwaukee high-performance computational clusters. The time step is set to 6.9×10^-4 seconds, which covers only half a degree of rotor rotation. The maximum Courant-Friedrichs-Lewy (CFL) number of 3 appears at a very low number of cells at the tip of the blade leading edge, as presented in **Figure** 5-7. Although using unconditionally stable implicit time marching, the convective CFL number should be below five as recommended to keep excellent stability for the LES computation. [42]

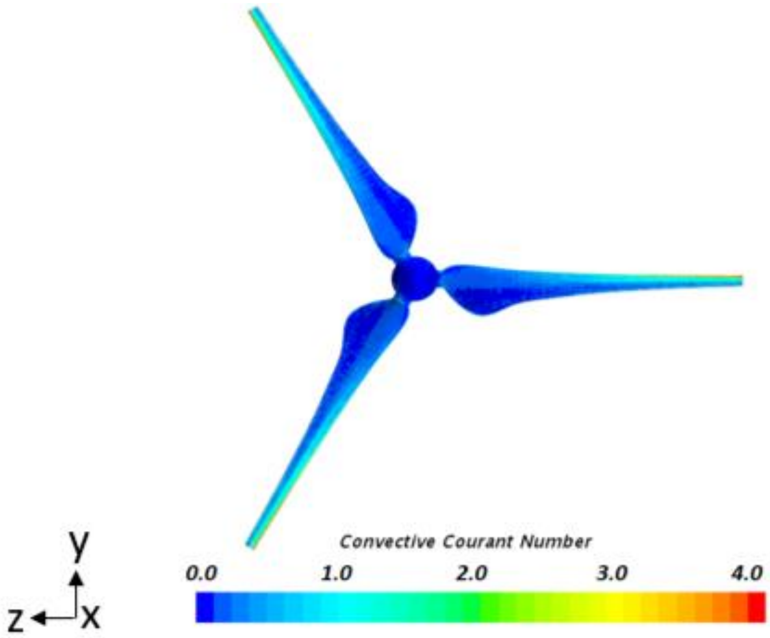

Figure 5-7: Convective Courant Number over the blades generated using NACA 64(3)618 airfoil.

The minimum cell size for the validation CFD model was selected after several trials and errors until the 5% error in axial velocity along the line probes was obtained. Then, for the scaled-up CFD model, the ratio of the minimum cell size to the chord length and the growth rate is kept equal for both the small and scaled models. Moreover, because the new airfoils are thinner and more curved, besides having some designs with winglets and tubercles, the minimum cell size in the rotational domain is reduced to 0.02 m (cell count inside the rotational domain only is about three million), to capture the vortices generated by these small geometrical features accurately. Therefore, the LES simulations have a cell count of about nine million.

Large-eddy simulation (LES) requires a much finer mesh than that required for standard RANS simulations. If the local grid size is insufficient, the LES subgrid-scale (SGS) model is employed for inappropriate length scales, and the results will be inaccurate. Guidelines such as the ratio of turbulence kinetic energy to modeled turbulence kinetic energy are useful to determine if a grid size is appropriate for LES simulation or not.

Reasonable local cell sizes should be larger than Kolmogorov Length Scale, and less than Taylor Micro Scale at the same time, where the Kolmogorov scale represents an expensive over-refinement of mesh more appropriate to direct numerical simulation, and values above the Taylor scale indicate an inappropriate cell size for the SGS model to contribute substantially. The minimum cell size of the current work' LES simulations is selected according to the Taylor scale, to maintain the results accurately and keep the computational cost reasonable at the same time.

In LES computations, one of the ways to determine the quality of a coarse mesh and to see how well the flow is resolved is by calculating, based on time averaged LES results, the ratio of SGS turbulence kinetic energy to total turbulence kinetic energy. The ratio which gives the fraction of turbulence kinetic energy in the resolved motions, M, is given as:

$$M=k_{sgs}/(k_{sgs}+k_{res}) \qquad (7)$$

where k_{sgs} is SGS turbulence kinetic energy, and k_{res} is resolved kinetic energy.

It is worth mentioning that M = 0 corresponds to direct numerical simulation (DNS) and indicates that the flow is very well resolved, while M = 1 corresponds to RANS and indicates poor resolution for a coarse mesh. It is recommended to get 80% or higher of the large scales resolved for an accurate LES simulation. Otherwise, the mesh should be refined. **Figure** 5-8 shows that the surface average of M over the central longitudinal plane is 0.039, which means that 96.1% of the large scales were resolved, and the grid size is fine enough.

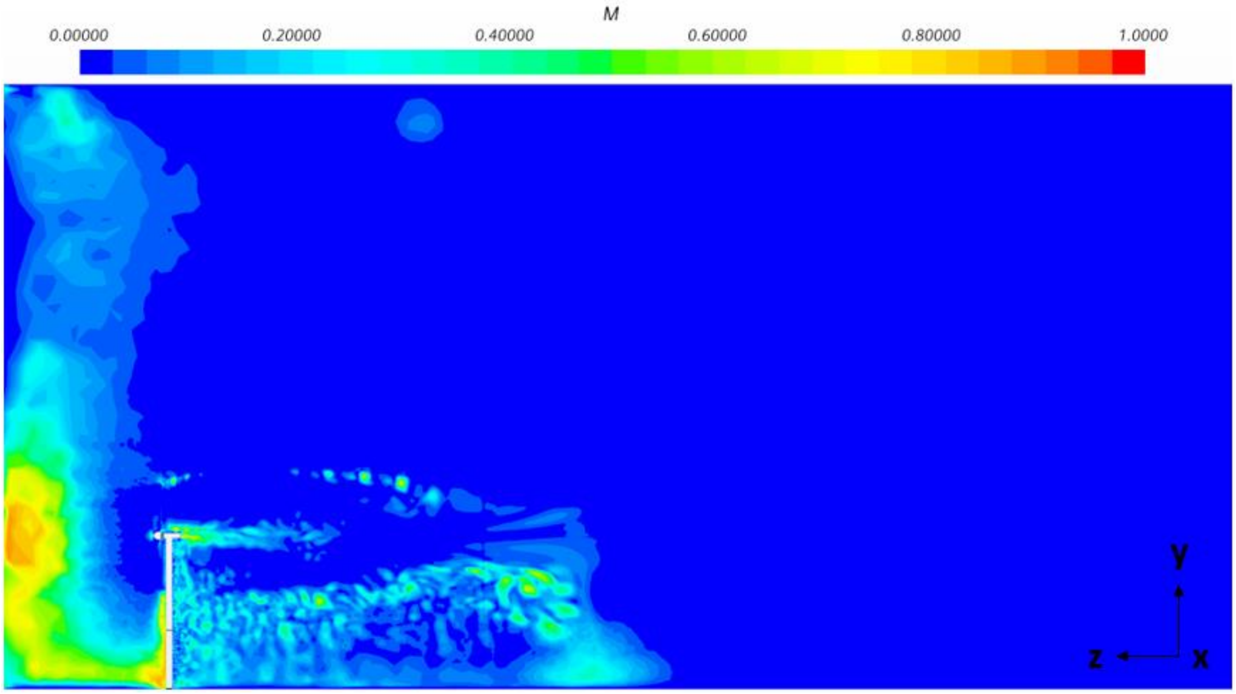

Figure 5-8: Fraction of turbulence kinetic energy in the resolved motions, M, over a central longitudinal plane for NACA 64(3)618 LES simulation

5.2 Results

In total, 18 simulations were performed for the current chapter; all of them are done at TSR equal to 7. RANS equations with the k-ω SST turbulence model can capture the laminar-to-turbulent boundary layer transition, particularly when combined with fine enough, near-wall prism layer meshing with low Y+ value [44], [45]. In addition, the whole aerodynamic performance of wind turbine blades was proven to be insignificantly affected by the unsteady behavior of localized vortices [31]. Therefore, RANS equations have acceptable accuracy and more time-efficient (compared to LES). Thus, it is used for the 18 simulations of the current chapter.

Moreover, LES is used only in the six simulations done at the rated wind speed (12.5 m/s) to promote the RANS results by performing the six simulations using both RANS and LES and showing how close the power outputs are. It was not time-efficient to use LES for the 18 simulations since each LES simulation took three days of running on 200 cores, while each RANS simulation took only four to five hours. In short, the general aerodynamic performance is found to be very similar using RANS and LES. However, LES outperforms RANS in describing the unsteady behavior of localized vortices, that's why LES was opted for performing the six rated wind simulations.

A detailed description of the simulations performed, TSR, wind velocity, power output, and power coefficient for each model can be found in **Table** 5-5. For all tested wind speeds, GOE 447 showed the best performance in terms of generating high power output, that is why it is selected to implement further blade modifications. Tubercles outperform the GOE 447 baseline design and the one with winglets at all wind speeds. The power output of the LES simulations is 7.9% to 11.9% higher than the power obtained using the k-ω SST model.

In the following discussion, pressure distribution around airfoils, axial velocity, and vorticity scenes of the LES simulations that were done at rated wind speed (12.5 m/s) are presented.

The absolute pressure distribution around both root (r/R=0.2) and tip (r/R=0.9) sections of the blades generated using NACA 64(3)618, NACA 6412, and GOE 447, respectively, are shown in **Figure** 5-9. The counterclockwise direction of rotation is evident since, in the six parts of the figure, the high-pressure side of the blade is to the left of the airfoils, while the low-pressure side to the right of the airfoils. In addition, higher pitch angles at the root are well-demonstrated in parts (a), (c), and (e), while the pitch angle is almost zero at blade tip in parts (b), (d), and (f).

Moreover, at the root sections, in parts (a), (c), and (e), the average pressure differential between the pressure- and suction- sides of the blade is 400, 500, and 550 Pa, respectively. On the other hand, at the tip sections, in parts (b), (d), and (f), the average pressure differential between the pressure- and suction-sides of the blade is 2000, 3500, and 4500 Pa, respectively. The increase in pressure differential between the pressure- and suction-sides explains why the power output increases from the model with NACA 643(3)618 to the model with GOE 447. Power output is discussed in detail later (see **Table** 5-5).

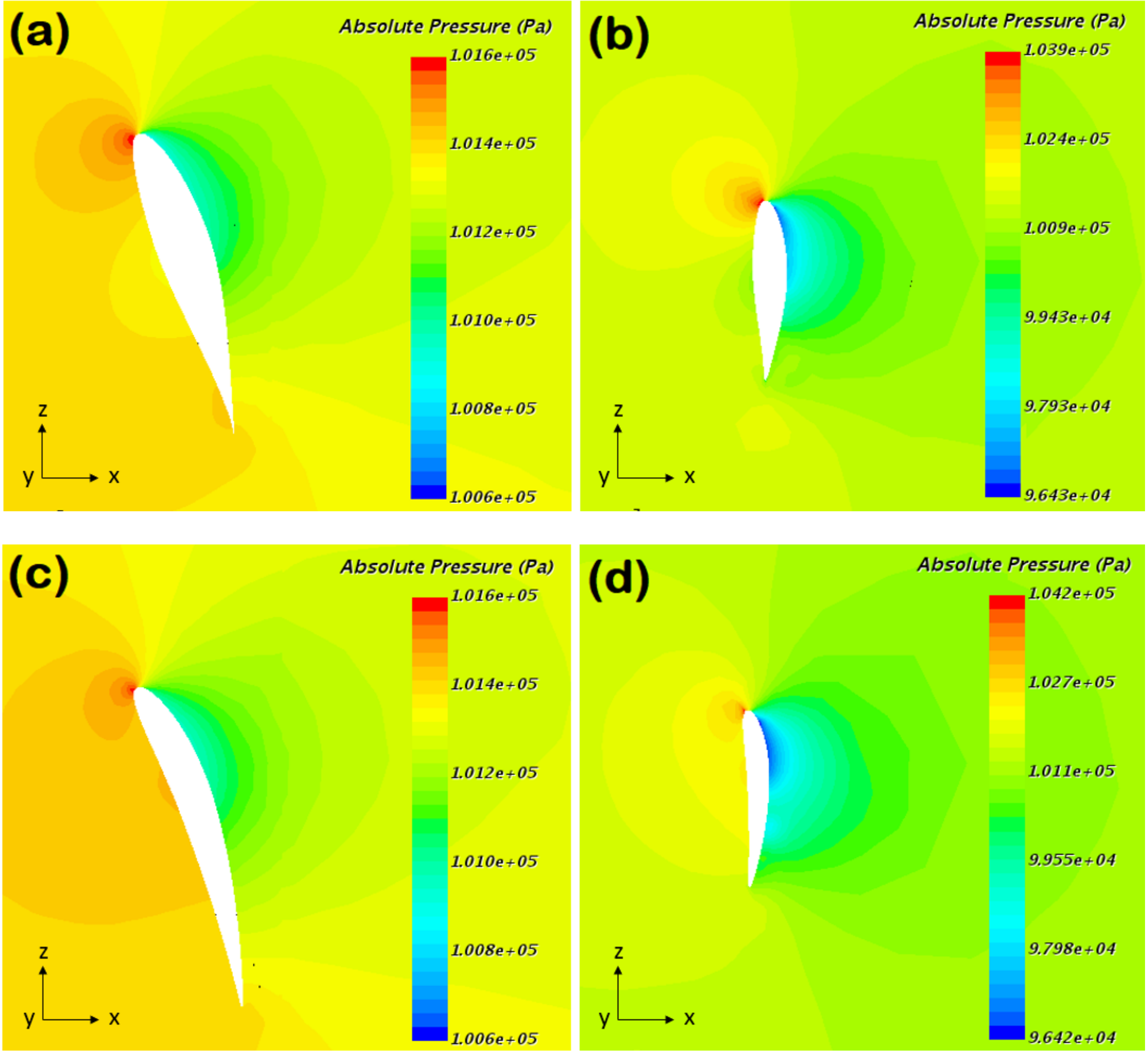

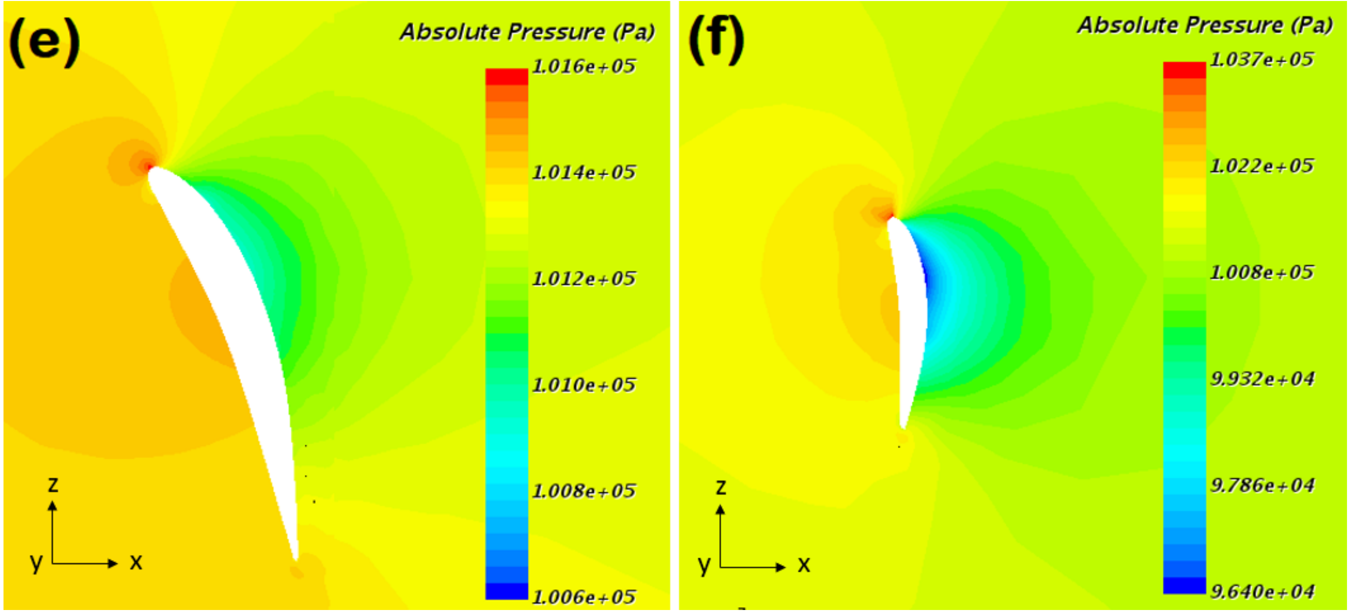

Figure 5-9: Absolute pressure distribution around blades at wind speed of 12.5 m/s:(a)Airfoil NACA 64(3)618 at r/R=0.2, (b)Airfoil NACA 64(3)618 at r/R=0.9,(c)Airfoil NACA 6412 at r/R=0.2, (d)Airfoil NACA 6412 at r/R=0.9,(e) Airfoil GOE 447 at r/R=0.2, (f)Airfoil GOE 447 at r/R=0.9

To investigate the evolution of the wake region, the hub height axial velocity recovery for various models at a wind speed of 12.5 m/s is traced in **Figure** 5-10. All models included in the figure produce a wake that reaches 100% velocity recovery at a downstream distance of 7.5D. However, the difference can be seen in the level of maximum velocity deficit and the level of velocity fluctuations within each model's wake. Hence, the basic and winglet GOE 447 models are characterized by reaching the highest level of velocity deficit (axial velocity drops to 0 m/s at 3.1D). Meanwhile, the NACA 6412 and the tubercle GOE 447 models have a lower velocity deficit (1.2 m/s at 3.1D and 3.5D, respectively). Finally, the wake of the NACA 64(3)618 model reached 3.2 m/s at 2.4D, which is the least hub height velocity deficit among the five models shown in the graph. So, thicker and less curved airfoil (NACA 64(3)618) generates less and earlier maximum velocity drop than the thinner and more curved airfoils (NACA 6412 and GOE 447).

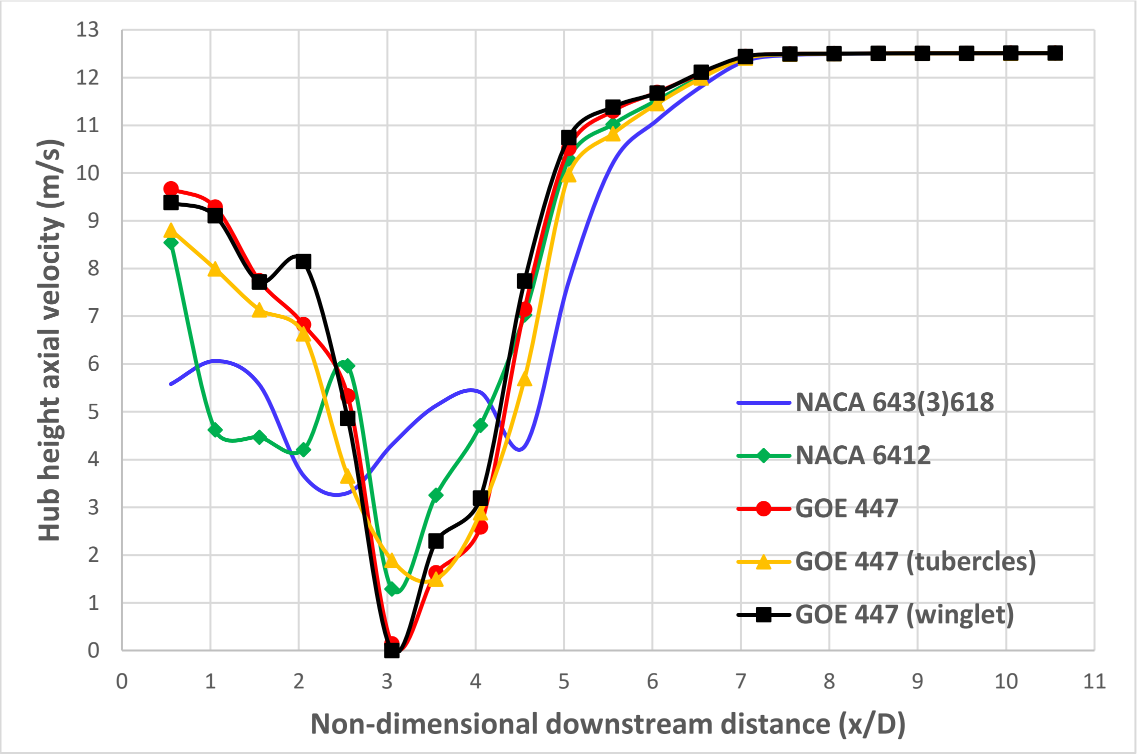

Figure 5-10: Hub height axial velocity recovery for various models at wind speed of 12.5 m/s.

The absolute axial velocity (Vx) distribution over a horizontal plane cuts through the wake region at each model's hub height is shown in **Figure** 5-11. For all models, the axial velocity component is decelerated ahead of the rotor from the 12.5 m/s incoming wind speed to 9.5 m/s. After that, the wake behind the rotor is a stream tube that expands to a specific larger diameter downstream, then contracts until dissipates. Therefore, the relative flow area around the wake stream tube is getting narrower as we go further downstream. Thus, the axial velocity is higher than the surrounding environment within this annulus. Therefore, the stream tube expansion explains the reason behind the emergence of the sub-envelope region of accelerated flow around the wake. It then follows that momentum transport from the rotor weakens, while mixing with the surrounding environment is enhanced. Therefore, the wake region disappears at almost 7.5D for all models.

Moreover, also in, the high-velocity spots generated near the blade tip is a good indication of the tip-generated vortices. These vortices are shedding and losing strength by going downstream. The strength of these tip vortices is relatively low for the NACA 64(3)618 (high-velocity spots are absent), compared to the NACA 6412 and the basic GOE 447 models. On the other hand, considering the basic GOE 447 as a baseline, the leading-edge tubercles mitigate the strength of the tip vortices, but they do not lose coherence and disperse earlier than the baseline design. At the same time, the winglets generate higher levels of turbulence and stronger tip-vortices in the near wake. Also, winglets force the tip-vortices layer to lose its coherence at a far wake and made the tip vortices sheet to break at an earlier downstream distance. That is, tip vortices disperse at 3.4D for the basic GOE 447 design while they disperse at 3.0D for the winglet blade model.

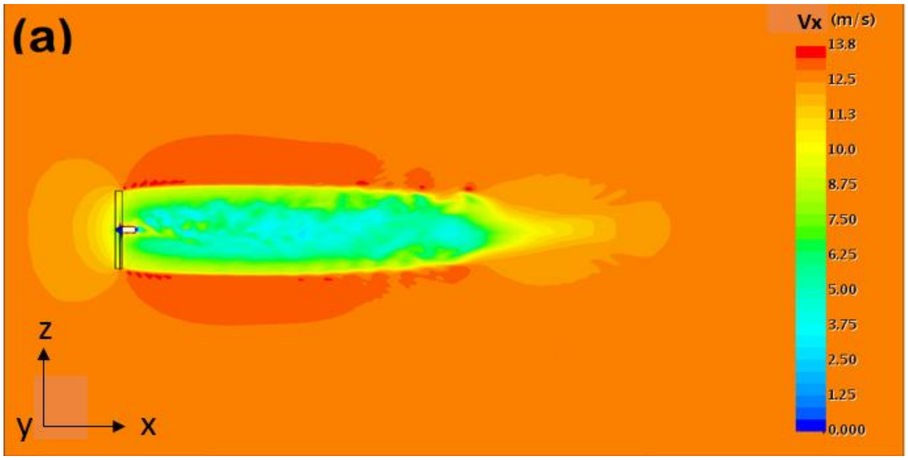

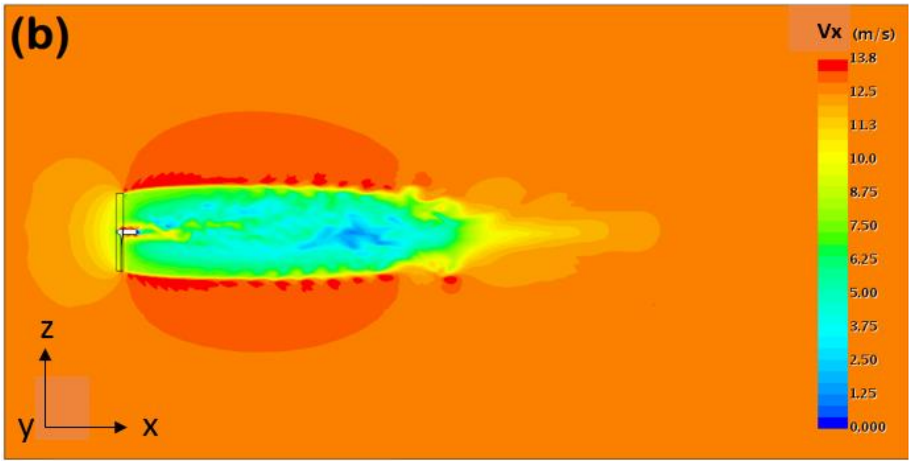

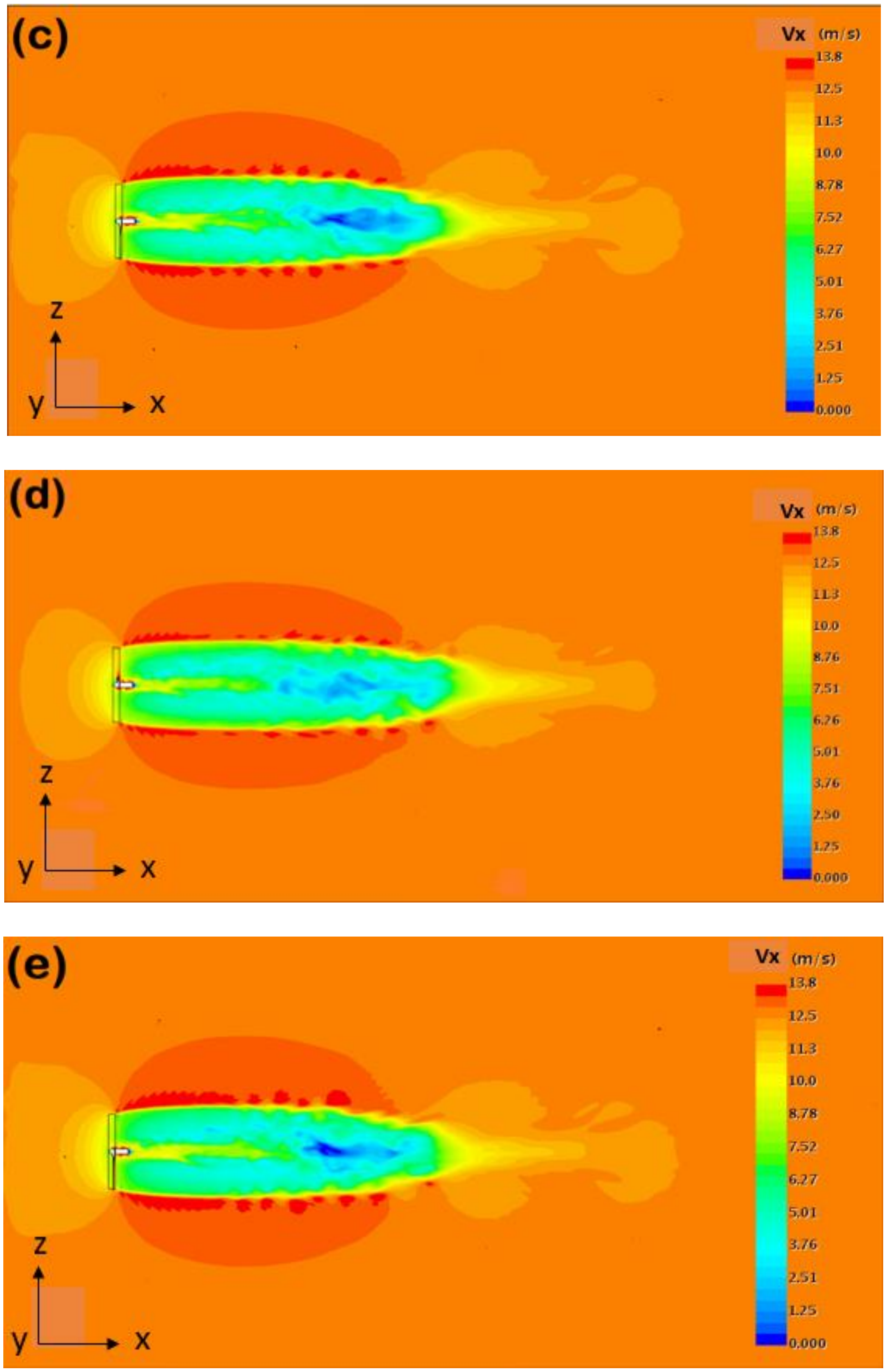

Figure 5-11: Absolute axial velocity (Vx) distribution over a horizontal plane cuts through the wake body at each model's hub height at wind speed of 12.5 m/s:(a) model with blades generated using NACA 64(3)618, (b) model with blades generated using NACA 6412, (c) model with blades generated using GOE 447, (d) model with blades generated using GOE 447 with leading-edge tubercles, (e) model with blades generated using GOE 447 with downstream-facing winglet

Vorticity is the tendency of a fluid particle to rotate upon itself. Turbulence is rotational, three dimensional, and characterized by high levels of fluctuating vorticity. Therefore, vorticity dynamics are essential for turbulent flows description [46]. **Figure** 5-12 shows the vorticity magnitude contours for the same five models represented in **Figure** 5-11. For all models, a core, high vorticity region is generated because of the turbulence created by the hub and nacelle (11Hz), this high vorticity flow region loses its vorticity strength by mixing with the outer wake flow and expands as we go downstream (3.5Hz). Moreover, the wake region is bounded by a circumferential layer characterized by higher vorticity than the inside of the wake tube. This high vorticity layer is a good demonstration of the tip-generated vortices.

In **Figure** 5-12 (a) that represents the thicker airfoil NACA 64(3)618, the magnitude of the vorticity in the circumferential layer is relatively low (5Hz) compared to the thinner airfoils. In addition, the circumferential layer keeps its form until the end of the wake region. **Figure** 5-12 (b) and (c) represent airfoils NACA 6412 and GOE 447, which are thinner and more curved than NACA 64(3)618. The vorticity magnitude in the circumferential layers of both airfoils is higher (9 and 10 Hz, respectively), which means that both airfoils create more energetic tip vortices than NACA 64(3)618. Besides, the circumferential layer starts to lose coherence, tip vortices-breakup takes place, and localized vortices begin to exist individually.

Figure 5-12 (d) and (e) confirm the fact that considering the basic GOE 447 as a baseline, the leading-edge tubercles mitigate the strength of the tip vortices (7.5 Hz). In comparison, the winglets generate higher levels of turbulence and stronger tip-vortices in the near wake (10.5 Hz). In addition, winglets force the tip-vortices layer to lose its coherence at a far wake and made the tip vortices sheet to break at an earlier downstream distance.

Comparing **Figure** 5-12(d) that represents GOE 447 with tubercles to **Figure** 5-12(c) that represents the baseline, and by focusing on the vorticity in the region between the nacelle and blade tip, relatively high-intensity streaklines can be noticed with tubercles (2 Hz). At the same time, they do not exist with the baseline design (1Hz). This is an indication of the ability of the tubercles to counteract the spanwise flow and guiding the flow across the span. This action enhances flow attachment to the blade, reducing stall, hence increases the power output.

Comparing **Figure** 5-12(e) that represents GOE 447 with winglets to **Figure** 5-12 (c) that represents the baseline, and by focusing on the vorticity in the region between the nacelle and blade tip, it can be noticed that winglets reduce vorticity magnitude behind blade root to 0 Hz and to 0.5 Hz behind blades span. At the same time, it is 1Hz in the baseline design. The vorticity reduction associated with the winglets indicates the ability of the winglets to reduce the spanwise flow and move the tip vortex away from the rotor plane, reducing both downwash and rotor induced drag, hence increasing power output.

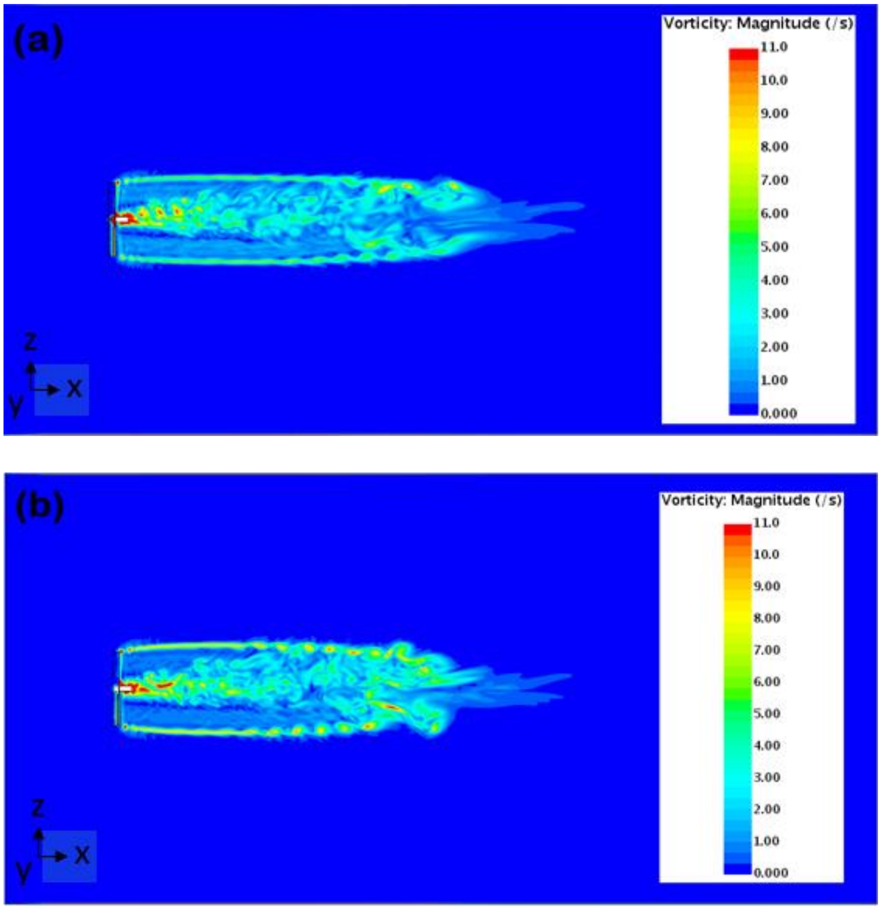

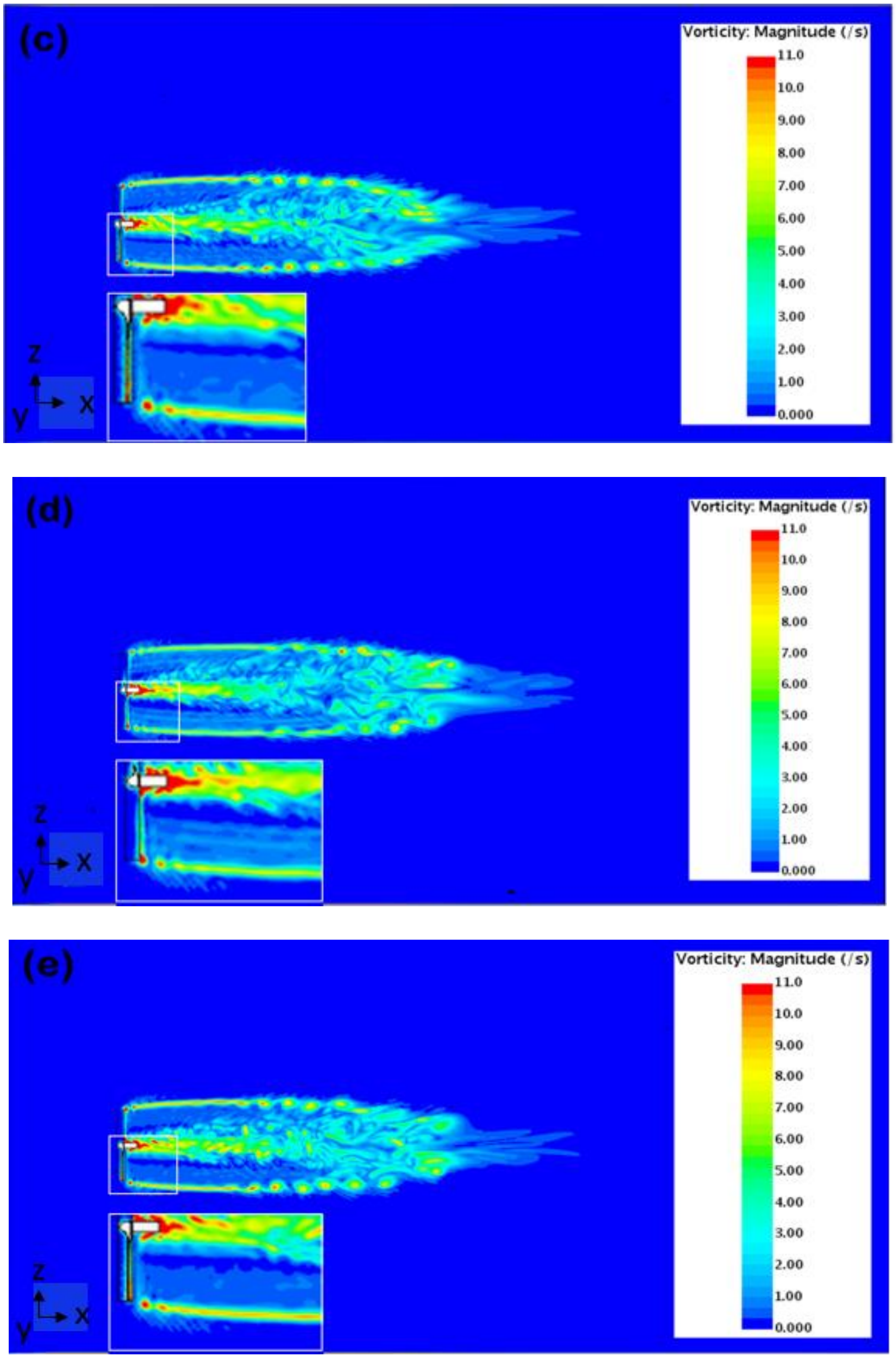

Figure 5-12: Vorticity magnitude distribution over a horizontal plane cuts through the wake body at each model's hub height at wind speed of 12.5 m/s:(a) model with blades generated using NACA 64(3)618, (b) model with blades generated using NACA 6412, (c) model with blades generated using GOE 447, (d) model with blades generated using GOE 447 with leading-edge tubercles, (e) model with blades generated using GOE 447 with downstream-facing winglet.

Table 5-5: Power output and associated power coefficient for all simulated models.

Model	**TSR**	**Wind speed (m/s)**	**Power output (kW)**		**Power coefficient (Cp)**	
			k-ω SST	LES	k-ω SST	LES
NACA 64(3)618	7	12.5	47.1	51.8	0.261	0.287
GOE 446	7	12.5	56.3	60.8	0.312	0.337
NACA 6412	7	12.5	58.2	64.6	0.323	0.358
GOE 447	7	12.5	60.3	67.5	0.334	0.374
GOE 447 (winglet)	7	12.5	63.3	69.6	0.351	0.386
GOE 447 (tubercles)	7	12.5	63.6	70.0	0.353	0.388
NACA 64(3)618	7	10	23.8	-	0.258	-
GOE 446	7	10	28.6	-	0.310	-
NACA 6412	7	10	29.3	-	0.317	-
GOE 447	7	10	30.7	-	0.333	-
GOE 447 (winglet)	7	10	32.1	-	0.347	-
GOE 447 (tubercles)	7	10	32.2	-	0.348	-
NACA 64(3)618	7	7.5	9.7	-	0.249	-
GOE 446	7	7.5	11.9	-	0.306	-
NACA 6412	7	7.5	12.2	-	0.313	-
GOE 447	7	7.5	12.8	-	0.328	-
GOE 447 (winglet)	7	7.5	13.3	-	0.342	-
GOE 447 (tubercles)	7	7.5	13.3	-	0.342	-

5.3 Conclusions

Different rotor blade airfoils used to generate a wind turbine blade has a minor effect on the wake of each model as long as having the same hub height axial velocity recovery, a small variance in the maximum velocity deficit achieved, close rates of axial velocity recovery, and close wake expansions. However, the type of airfoil has a significant effect on pressure distributions around the blades, and the rate of the tip-vortices generation, hence the airfoil design strongly impacts on power outputs and associated power coefficients.

Given that TSR is fixed at seven for all simulations of this work, at all wind speeds, thinner and more curved airfoils (NACA 6412 and GOE 447) produce more power than thicker and less curved ones (NACA 64(3)618).

GOE 447 outperforms the other three airfoils at all wind speeds. Moreover, adding tubercles and winglets to the baseline GOE 447 generates more power. At 12.5 m/s, winglet design produces 5% more power, while tubercles produce 5.5% more power than the GOE 447 baseline design. With the wind speed of 10 m/s, winglet design provides 4.4% more power, while tubercle blades produce 4.7% more power than the GOE 447 baseline design. With the wind speed of 7.5 m/s, both winglet and tubercle blade designs generate almost equal power, which is 4.2% higher than the baseline output power. Moreover, at the rated wind speed, the LES power output calculation is 7.9% to 11.9% higher than the RANS power output calculation.

It is interesting for future experimental and numerical work to investigate the effect of different winglet configurations (different cant angles and lengths), different tubercles configurations (different amplitudes and wavelengths), and a combination of them on the blade aerodynamic performance and power production. In addition, a study of the vortex generators used for aviation technology will be interesting too.

Numerical limitations restricted the total cell count to a maximum of 9M, the issue that will be handled at UWM soon by adding more computational power. This added power can enable increasing the cell count so that the minimum cell size gets closer to the Kolmogorov scale. Hence more accurate LES results can be obtained.

Chapter 6 : Experimental and Numerical Investigation of Vortex Generators and Winglets in Horizontal Axis Wind Turbine Blade Design

6.1 Introduction

Energy consumption has increased dramatically over the last decades due to the increase in the population. Fossil fuels are the primary energy source in most of the world due to their availability and high calorific value. However, there are limiting factors on the fossil fuels leading the world to seeking new energy resources that are abundant and can be a reliable substitute for fossil fuels [1]. According to Renewables Global Status Report [4], the world still depends on fossil fuel to generate most of its electricity (73.8%), while the renewable electricity share is only 26.2%. The largest share of renewable electricity goes for hydropower (15.8%), while wind power comes in second place with 5.5% of the total global electricity production. Within the last decade, the total installed renewable power capacity has been increasing. Solar photovoltaic (PV) panels technology comes as the fastest growing capacity, then the wind technology comes in the second place (by the end of 2018, 100 Gigawatts were added as PV, while 51.3 Gigawatts were added as wind power).

Because of the integral role wind power plays in shaping the future of the world’s energy, many studies integrated wind power with the rest of renewable energy technologies in a single system to achieve a net-zero energy model in different applications [47], [48], [49], [50], [51]. Anwar et al. [52] used HOMER software to perform feasibility and sensitivity analysis of a system that integrated PV panels, wind, biogas, fuel-cell, diesel, and batteries for electrification of rural, off-grid areas. Qandil et al. [53] used the same software to investigate the possibility of combining energy efficiency opportunities with a system of renewables (PV, wind, digester gas, and aeration tanks' microturbines) to achieve a net-zero energy model in small size wastewater treatment plants.

Although vertical-axis wind turbines (VAWTs) have lower efficiency than horizontal-axis counterparts, they are receiving a lot of interest from researchers because they can produce electricity in any wind direction. Therefore, neither yaw drive nor pitch mechanism is needed [47]. Moreover, VAWTs do not need a strong support structure to carry power generation components off the ground. Therefore, Laws, et al. [54] have used OpenFOAM to introduce a simple design modification to the blade of a Savonius wind turbine. The design modification improved the power efficiency by 10-28%. Hassanzadeh et al. [55] tested experimentally four different blade profiles of two-blade Savonius wind turbine under different wind speeds to get the maximum power coefficient among all tested cases. Alom and Saha have examined newly developed elliptical-bladed Savonius rotor [56].

On the other hand, horizontal axis wind turbines (HAWTs) are the most commercially used wind turbines due to their high efficiency. Therefore, many studies have been performed, experimentally and numerically, to improve the performance of both the individual wind turbine and the whole wind farm [47].

Regarding wind farms' output improvement, Hasan et al. [57] tested the wake region of a small-scale HAWT inside a wind tunnel using hot-wire anemometry to show axial and vertical velocity components, besides turbulence intensity, over many transverse sectional planes along the wake. Then, the previous study was expanded to include computational fluid dynamics (CFD) simulations of the same turbine model under different operating conditions. By tracking the hub-height axial velocity recovery at different wind speeds and tip speed ratios (TSRs), the separation distance between two successive units in a wind farm was determined [58]. Moreover, Jackson and Amano [32] investigated, experimentally and numerically, the velocity deficit in case of having single, double, and triple wind turbine models in an inline configuration inside a wind tunnel. Choi et al. [34] used the commercial multi-purpose CFD solver ANSYS CFX to build a full wind farm model which contained two HAWTs with full-scale dimensions; each turbine provided 2 MW output power. They carried out a steady-state analysis of the problem using the Reynold Averaged Navier Stokes (RANS) approach with the Shear Stress Transport (SST) k-ω model. The separation distance between the two turbines was increased from one case study to another; hence, the power output of the downstream turbine increased significantly, which yielded an increase in the wind farm annual energy production.

Regarding individual wind turbines, many researchers utilized various techniques seeking optimizing the performance of a wind turbine model. Addamane et al. [59] studied the effect of pitch angle on the performance of HAWTs under three wind velocities. They found that increasing the pitch angle decreases the thrust. Furthermore, they found that for each velocity, there is a pitch angle that maximizes the generated power where the optimum pitch angle tends to increase with wind velocity. At the optimum pitch angle, the angle of attack (AoA) is close to stall angle. Muheisen et al. [60] studied the effect of equipping the HAWT blades with multi-cross sections with fences. They found that using-multi section blades enhances the power coefficient by eight percent for the studied case. Moreover, they found that introducing fences to multi-cross section blades enhances the rotor’s performance and stability. Eltayesh et al. [61] investigated the solidity effect on the thrust, power and flow field generated from HAWTs. They showed that using a 3-bladed rotor maximizes the power coefficient among all studied configurations, on the other hand, they yield stronger vortices and flow separation. Besides, Mohammadi and Maghrebi [62] investigated reducing boundary layer separation by blowing a different number of air jets on the suction side of HAWT blades. They found that the generated torque was doubled compared to the baseline blade in the best case. They also proved that the torque increases with the number of blown air jets. Besides, they showed that placing air jets near the blades' tips enhances the performance more than placing them in the middle or inner portions of blades.

Since most of the research and development in the field of HAWTs focuses on large, utility-scale wind turbines, more attention should be paid to the small wind turbines for residential and urban applications. Therefore, Hasan et al. [63] performed a numerical study that investigated the effect of using four newly introduced airfoils for blades generation of residential scale turbines. Airfoils are NACA 64(3)618, GOE 446, NACA 6412, and GOE 447. Since GOE 447 was proven to generate the highest power, it was selected to add leading edge tubercles and winglets, which achieved an increase in the power output at all tested wind speeds (4.2-5.5% power increase than the GOE 447 baseline design). Furthermore, Hays and Treuren [64] focused on utilizing small wind turbines in urban environment. Having the turbines working near the end user makes the optimization process not only limited to power maximization, but also noise suppression. Therefore, they studied two rotors designed with NREL S823 and Eppler 216 airfoils. They found that the thinner profile and increased camber of the Eppler 216 improved the turbine aerodynamic performance, increased power, and reduced the noise significantly.

Other works adopted winglets as a tip modification to improve the turbine's aerodynamic performance, hence power maximization. Khaled et al. [20] investigated the influences of winglets on power and thrust coefficients. Firstly, they investigated the effect of winglet length variation (changed from 1% to 7% of the turbine rotor radius), while the cant angle is fixed at 90°, and TSR changed from 2.5 to 9.6. They found that for all cases, the power maximized at the design TSR of 5 then drops, while the thrust coefficient (C_T) continued increasing till TSR is 8.4 then started to fall. Secondly, for each winglet length, the cant angle changed from 15° to 90°, while the TSR is maintained at its optimum value (5). They found that Cp range increased by the increase of winglet length. Moreover, at each length, Cp is maximum at a cant angle of 50°, while C_T is maximum at 30°.

Khalafallah et al. [22] investigated the effects of winglet direction, cant angle, and twist angle for two winglet orientations: upstream and downstream directions. For each winglet direction, –2°, 2°, and 10° twist angles were studied at 20°, 40°, and 60° cant angles, with fixed TSR of 6 in all simulations. They concluded that the winglet pointing to the downstream side showed a more increase in power than those pointing to the upstream side. They claimed that a general increase of the Cp occurred except for the three cases of a cant angle of 60° at which the winglet was on the upstream side. Compared to the baseline design mentioned in their literature, maximum increase in Cp of 1.75% was observed where winglet pointing to downstream side and has a cant angle of 60° and a twist angle of 2°.

Muhle et al. [24] performed a pure experimental study that showed the effect of different wingtip configurations on the tip vortex formation and interaction in the near wake of a two-bladed model wind turbine. They investigated the impact of switching from the straight-cut wing tip to the downstream-facing winglet on several parameters. Regarding the mean streamwise velocity, the presence of winglets didn't significantly affect the mean velocity field. Regarding wake expansion, winglets generated a slightly wider wake than the straight-cut tip. Regarding the phase-averaged vorticity component, an analysis was done between the two downstream distances 2.3D and 2.6D, revealing an instability caused by winglets that stimulated tip vortices interaction with the main wake and caused complete breakup at an earlier downstream distance of 3D, whereas the straight-cut tip didn't show any tip vortices interaction till 3.5D. Then, considering applying winglets to models used in a wind farm, winglets caused earlier and faster tip vortex breakup, the point that enhanced the recovery of the mean wake kinetic energy, which means more potential power extraction out of a downstream turbine.

Ostovan and Uzol [25] also did pure experimental work to investigate the effect of installing winglets and some wing extensions on the performance of two identical and interacting HAWTs. They attached the winglets and wing extensions to the upstream turbine to see how this impacts the Cp of the upstream, downstream, and the two turbines combination. They found that for the upstream turbine, the baseline design (without any tip devices) produced the lowest power. Attaching winglets produced 2.6% more power than the baseline design while attaching the wing extensions produced 17.1% more power than the baseline design. Besides, the downstream turbine produced the highest power when the upstream turbine had no tip devices. Attaching the winglets to the upstream turbine caused the downstream one to generate 4.1% less power, while attaching the wing extensions to the upstream turbine resulted in generating 15.7% less power out of the downstream one. Regarding the overall power of the two turbines combination, it increased by 1.1% when winglets were installed to the upstream turbine, while it increased by 9.6% when wing extensions were installed to the upstream turbine.

Qaissi et al. [65] investigated the effect of integrating a vortex trapping cavity (VTC) in the critical region of a highly twisted span blade for 2-D and 3-D models in terms of lift coefficient and torque, respectively. Their 2-D case analysis results showed that integrating the VTC enhanced the generated lift force with a smaller wake region, while their 3-D case analysis results showed that integrating the VTC enhances the generated torque by trapping separated eddies inside the cavity.

Regarding vortex generators (VGs) which are flow-guiding devices known for their ability to increase turbine efficiency and hence annual energy production via energizing the flow around the blade root section [66]. VGs are typically attached to the suction side of a turbine blade, where they cause local mixing in the boundary layer [67]. The high kinetic energy flow outside the boundary layer is induced to mix with the low momentum fluid within the boundary layer. The mixing action promotes both the energy and momentum of the fluid within the boundary layer. Consequently, delaying (or preventing) the undesired flow separation. [68], [69], [70]

Early studies were performed to determine the optimum geometry parameters of a VG (chordwise location, length, thickness, height, opening, spacing, and the angle a VG makes with the chordwise flow).

It was a hot research interest back in the days to determine the optimum values of those parameters that can achieve the optimum turbine power improvement [71]. Recently, some other studies shed light on the evaluation of utilizing VGs to upgrade power values of both lab-scale [72] and multi-megawatt wind turbines [73].

This work is an extension of a previous work of the principal author [63] that numerically proposed the GOE 447 airfoil as an excellent candidate for building turbine blades of residential-scale HAWTs. This work aims to investigate two modern blade modifications (VGs and winglets) when added individually to a turbine blade and study the cases of combining these two modifications at the same time to a single blade. It is desired to determine the effect of the mentioned scenarios on the turbine's power output for such thin and curved airfoils as GOE 447.

Most of the available research work of HAWTS is focused on either lab-scale (15-60 cm rotor diameter) or commercial large-scale (80-130 m rotor diameter). There is a lack of published data on residential-scale wind turbines. The current work fills this gap since it is going to be counted on during the next 10 years since the current US administration promotes dependence on renewables to cut carbon footprint [74]. In the windy Midwest, residential-scale WTs will be a good alternative for the less efficient solar panels in the region.

Earlier blades were built using thin airfoils, but they were susceptible to fracture. That's why recent blades are built using thick airfoils, but it comes with an early separation problem. Nowadays with the recent advances in composites manufacturing, thinner blades can be manufactured without the fear of fracture [75]. Very rare data are available for thin airfoil blades. All previously published work discusses modifications applied to thick airfoils blades. However, it is essential to provide data to study the effect of modern blade modifications on thinner airfoils.

6.2 Experimental Setup

The details of the experimental setup are shown in **Figure** 6-1. Briefly, the wind tunnel at the University of Wisconsin-Milwaukee was used to perform velocity measurements at several transverse planes in the wake region of a single wind turbine model. The test section has a 1.2m×1.2m×2.4m window. The entire tunnel as 3m×3m inlet section with multi-layered honey-combed converging to the test section. The total length of the tunnel is 18 m. Its suction fan is equipped with a Variable Frequency Drive (VFD) motor to control the incoming wind speed at the test section entrance, which was set to 5.2 m/s for the experiment.

The axial and vertical velocity components were measured at 529 points in each measurement plane using a dual sensor, cross-wire type hot wire anemometer (HWA) probe. It has two platinum-plated tungsten, 5 micrometers diameter, and wires welded to the probe at 45^o to each other. The tested model is a small-scale 3-blades model of 20.3 cm rotor diameter made from ABS plastic. Its tower is made from a 12.7 mm diameter steel rod with a hub height of 30.5 cm. The turbine blade cross-section was built using the NACA 4424 airfoil.

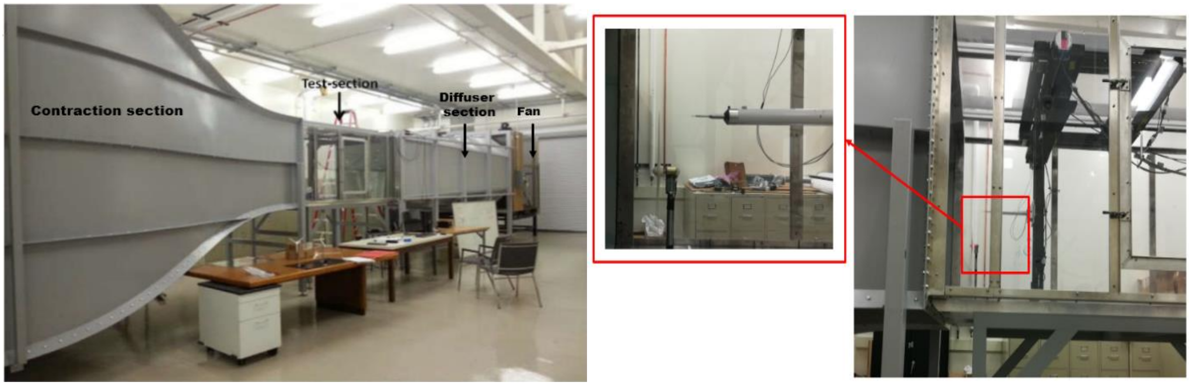

Figure 6-1: Experimental setup, (left) UWM wind tunnel, (right) measurement setup inside the test section

6.3 Numerical Model Validation

The validation model mesh details are shown in **Figure** 6-2. There are two meshing domains: the rotating domain for the disc that encloses the rotor (35% of the total number of cells is devoted to discretizing the rotational domain) and the stationary domain for the rest of the fluid domain. **Figure** 6-3 plots a graphical axial velocity comparison between the experimental and numerically obtained values from different cell counts at y/D= 0.25, where the incoming wind speed is 5.2 m/s. **Figure** 6-4 plots the same comparison but for y/D= 0.5. For both line probes, the error percentage decreases as the cell count increases. Four different grid counts were used to discretize this model domain. **Table** 6-1 compares the average error percentage, which was investigated for each grid cells count. A cell count of 8.8M is considered for the subsequent simulations to obtain a tradeoff between the accuracy of the results (less than 5% average error in axial velocity measurements) and the simulation time cost, noting that the maximum deviation between 8.8M and 10.2M is about 0.25%

Meanwhile, there is a cylinder generated around the rotor and a block along the wake centerline to increase cell density locally at these regions since they are the critical regions of the fluid flow where streamlines are blended; the velocity components change drastically (Figure 6-2). Moreover, local mesh at the blade surface and tip is finer than the rest of the rotational domain, since these are the locations where velocity gradient is initiated, and wake vortices are evolved. Furthermore, the mesher tessellates all the model's solid boundaries with 12 prism layers for good near-wall representation. **Figure** 6-5 shows the Y+ value over the upstream surface of the rotor blades. The Y+ is equal to one everywhere on the surface, except for limited region at blade's leading edge where Y+ reaches its maximum value of 2.3, which is low enough to capture the laminar-to-turbulent transition.

In total, 48 simulations were performed for the current work; all of them were done at TSR equal to 7. RANS equations with the k-ω SST turbulence model can capture the laminar-to-turbulent boundary layer transition, particularly when combined fine enough, near-wall prism layer meshing with low Y+ value [44], [45]. In addition, the whole aerodynamic performance of wind turbine blades was proven to be insignificantly affected by the unsteady behavior of localized vortices [76]. Therefore, RANS equations have acceptable accuracy and more time-efficient (compared to LES). Thus, the previous physics were used for the 48 simulations of the current work.

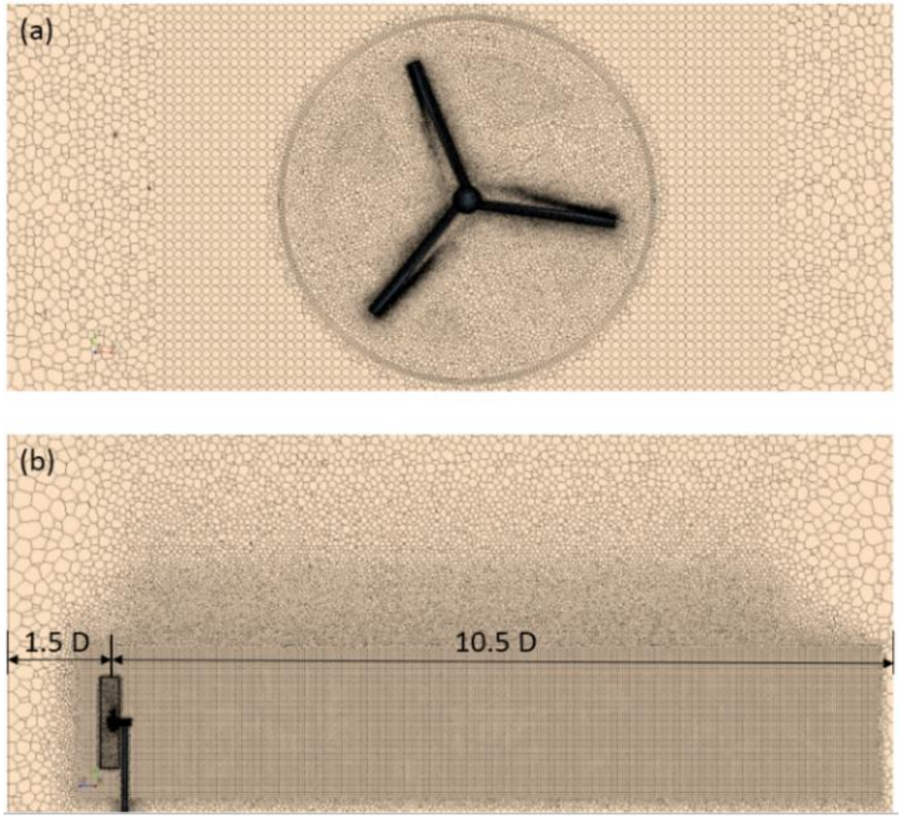

Figure 6-2: Mesh details of the computational domain (a) transverse sectional plane cuts through rotor blades, (b) longitudinal vertical sectional plane at wake centerline

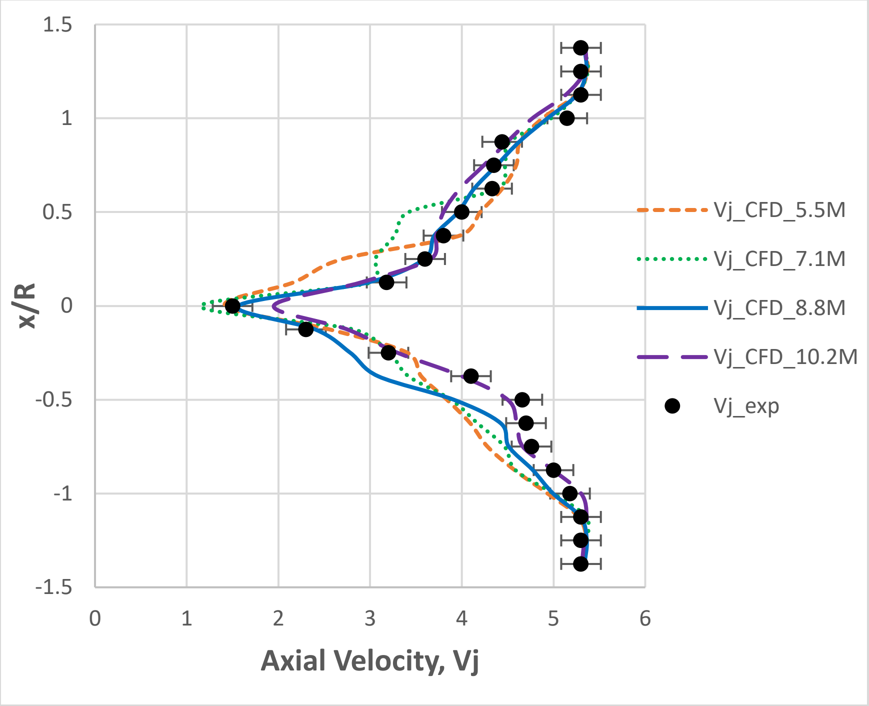

Figure 6-3: Axial velocity comparison at different cell counts, where z/D=0.25, at wind speed of 5.2 m/s

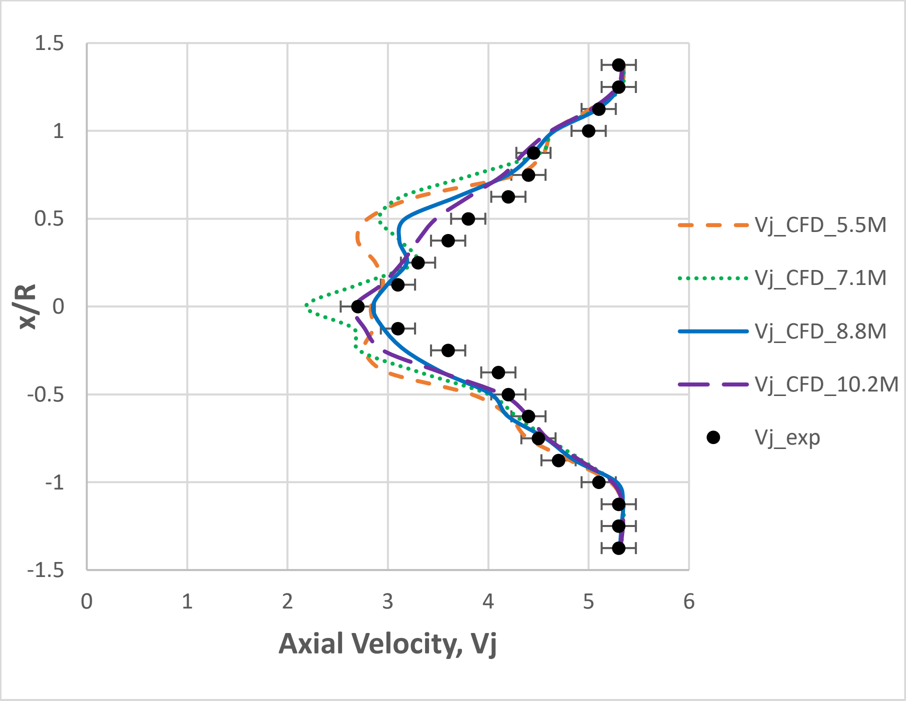

Figure 6-4: Axial velocity comparison at different cell counts, where z/D=0.5, at wind speed of 5.2 m/s

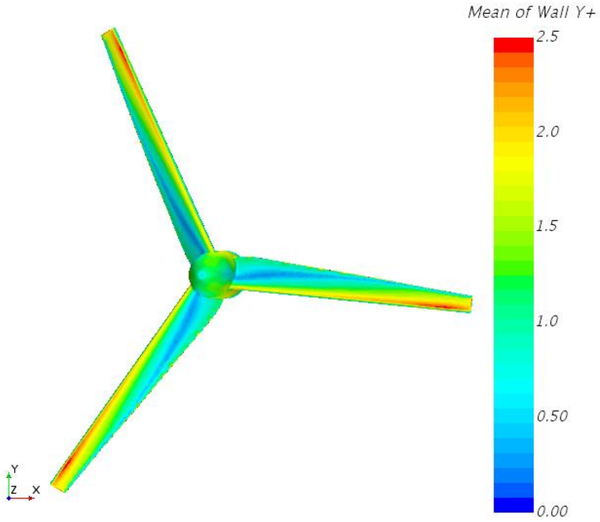

Figure 6-5: Mean of wall Y+ over the upstream surface of the rotor blades, at a wind speed of 5.2 m/s

Table 6-1: Axial velocity error percentages for different grid counts

Case No.	Grid Count (Millions)	Average Error % at y/D=0.25	Average Error % at y/D=0.5
1	5.5	6.86	6.48
2	7.1	5.72	5.76
3	8.8	4.55	4.53
4	10.2	4.51	4.50

6.4 Geometry Models

SolidWorks was used to generate the geometry models for the upcoming CFD work. It is worth mentioning that the blade length of all upcoming simulations is 7 m. **Figure** 6-6 shows very small objects on the backside of the blades, the suction side VGs. **Figure** 6-7 demonstrates the downstream side of the rotor highlighting the winglets (tip modifications). In this figure, the reader can notice that the winglets point towards the downstream direction.

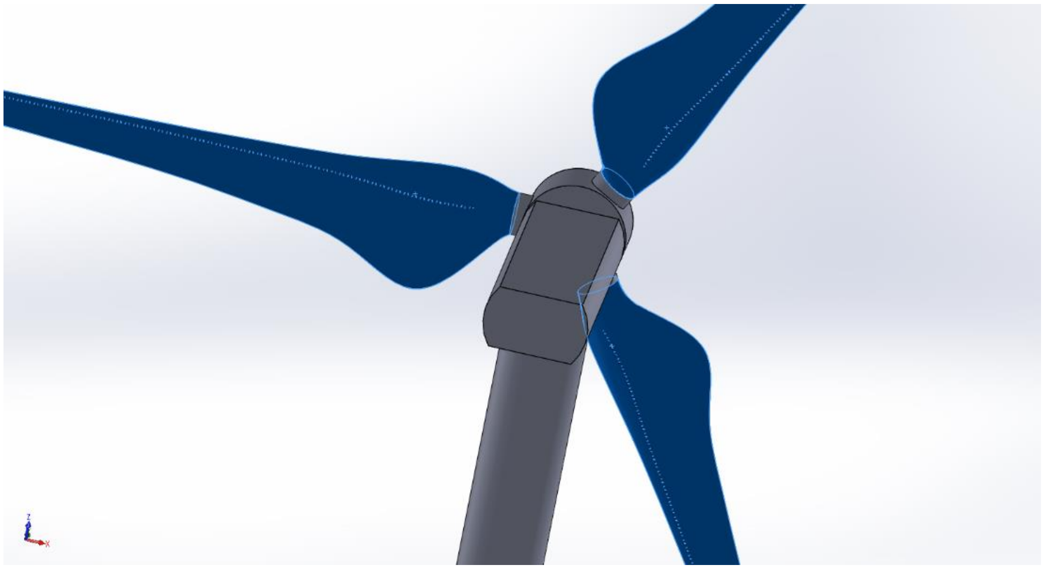

Figure 6-6: GOE 447 blades with suction-side vortex generators

Figure 6-7: GOE 447 blades with downstream-facing winglets

6.4.1 Vortex Generators

Figure 6-8 focuses on a turbine blade suction side leading edge to show the design parameters of the VGs. The figure represents Θ, the installation angle on the suction side, which is the angle that a VG makes with the chordwise flow direction. The figure also demonstrates S, the spacing between two VGs, H, the VG's height, L, the VG's length, and T, the VG’s thickness. It is worth noting that the proposed design parameters are set in the light of previous research work [77], [78], [79].

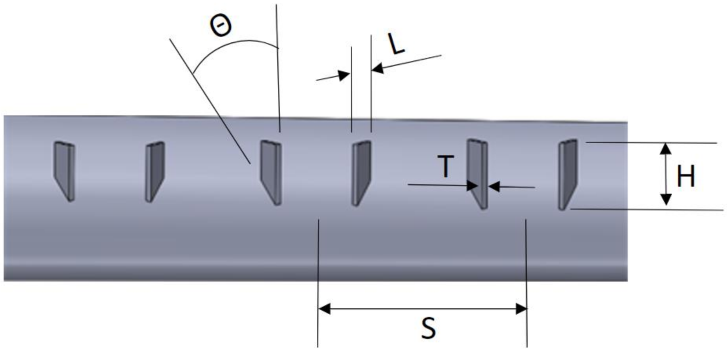

Figure 6-8: Vortex generator design parameters

Table 6-2: Geometry parameters of the vortex generator configurations

Configuration	Θ (degree)	H (m)	S (m)	L (m)	T (m)
VG 1	20	0.026	0.028	0.0154	0.00154
VG 2	20	0.01	0.028	0.0154	0.00154
VG 3	16	0.01	0.028	0.0154	0.00154

Table 6-2 shows the dimensions of each geometry parameter used for the three VGs configurations. The inlet opening for all configurations is one-third of the spacing. It is worth mentioning that these configurations are created as per design considerations of references [79] and [80].

Figure 6-9 focuses on the leading-edge section of the suction surface to highlight the details of configurations 1 and 2.

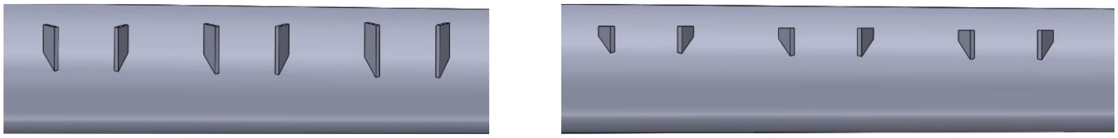

Figure 6-9: Vortex generators:(left) configuration 1, (right) configuration 2, both at a 10%C distance from the leading edge

6.4.2 Winglets

The orientation of all winglets in this work is selected to be downstream facing since this is the orientation found to be most effective in power increase [81]. The winglet height is 2.0% of the blade length (R), while the curvature radius is 25.0% of the winglet height, and the cant angle is 90°. Amano et al. [47], [48], [49], [50], [51]. reported that the cant angle with 45 degrees with 4% tip-to-span ratio gives the best power performance. The previous design was tested with different blades by Johansen et al. [82] and found to give higher power production than the basic design. In addition, Khalafallah et al. [22] showed that the 60° cant angle design has a promising potential towards power improvement. Therefore, it is included in the current work, besides the 30° cant angle design, to investigate the effect of adding a wide range of winglet designs on the proposed GOE 447 blade's aerodynamic performance. The three designs of winglets are shown in **Figure** 6-10.

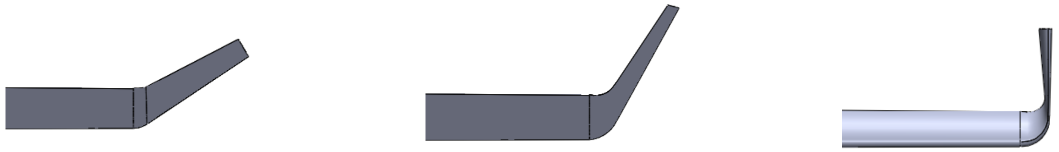

Figure 6-10: Blade with winglet: (left) cant angle 30, (middle) cant angle 60, (right) cant angle 90

6.5 Results

6.5.1 Vortex Generators Analysis

When the flow passes the blade, VGs create a pair of contra-rotating vortices, which transport momentum from the upper part of the boundary layer to the lower part of the boundary layer thereby increasing the mixing closer to the wall.

It is worth noting that VGs are installed on the suction side downstream of the leading edge at 10% of the chord length. Essential perspectives to look at the effect of VGs can be horizontal planes that cut through the computational domain longitudinally and cut through the one of the blades in the spanwise direction at 10%, 12% and 25% of the chord (see **Figure** 6-11). It is essential to highlight that wind speed is 12.5 m/s blowing in the negative-y direction for all VG analysis results shown in this section.

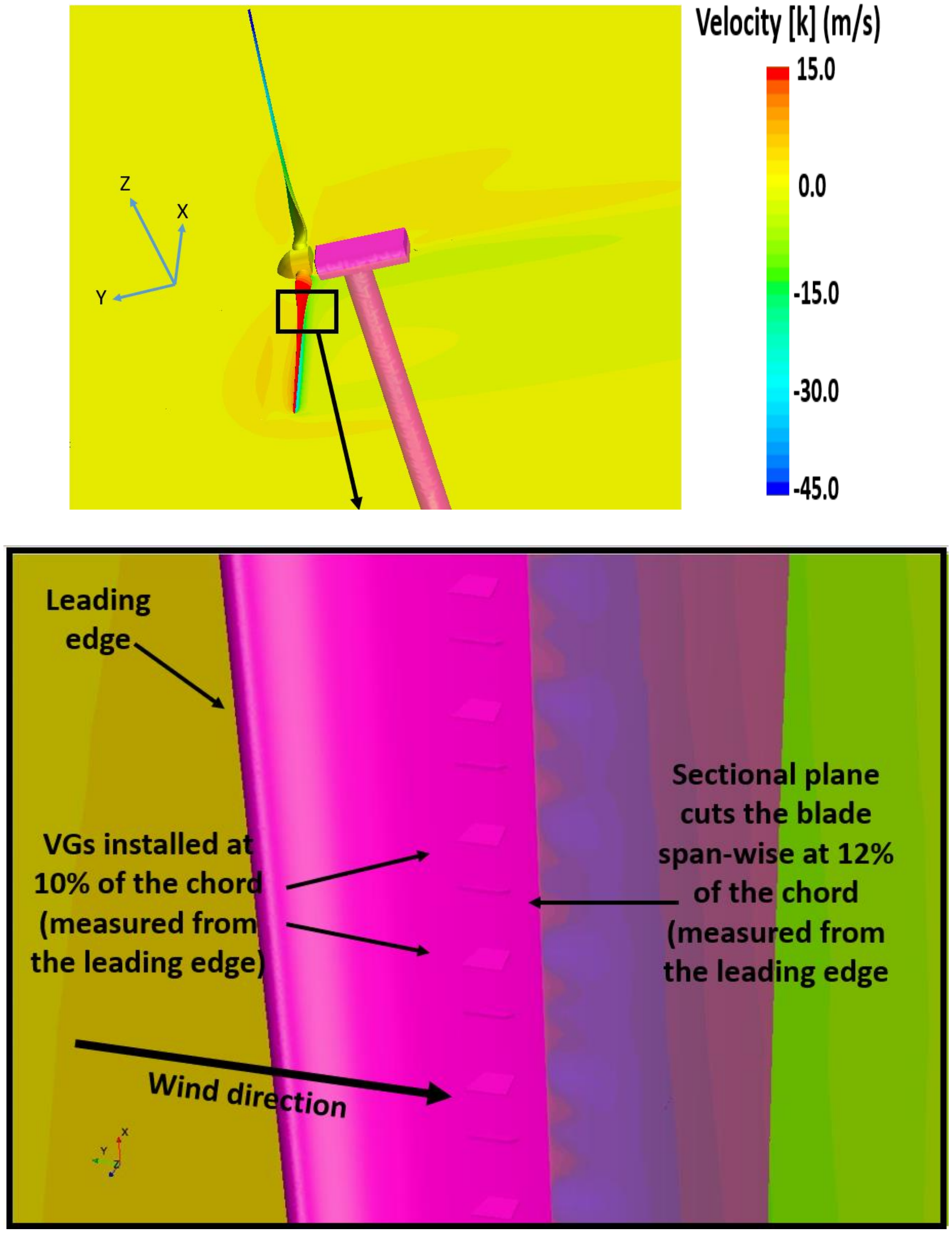

Figure 6-11: Demonstration of the horizontal x-y plane that cuts the blade in the spanwise (negative x) direction

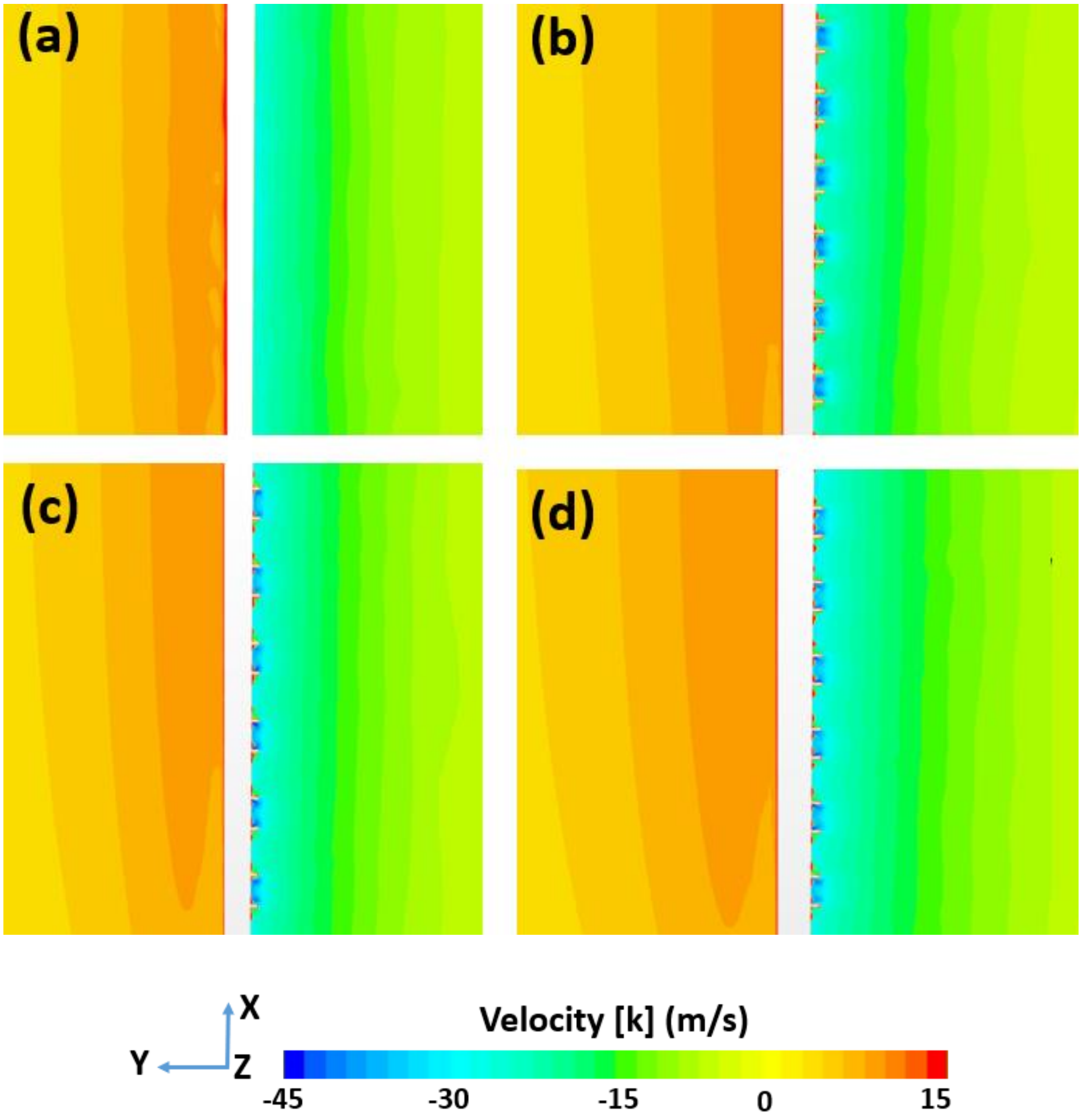

Figure 6-12: Vz contours along a horizontal plane that cuts a blade in a spanwise direction at 10%C (across vortex generators: (a) GOE 447 base design, (b) vortex generator configuration 1, (c) vortex generator configuration 2, (d) vortex generator configuration 3

Figure 6-12 shows the Vz contours along a horizontal x-y plane that cuts through VGs. Only a portion of the blade with seven VGs is shown. The white bar in the middle of each figure part is the blade's section. It is worth noting that the main relative flow is in the negative z direction (into the paper). On the suction side (right hand side of each figure part), Vz takes a negative value, which means the flow moves into the paper. This scene is selected since it shows the dominant velocity component of the flow. In

Figure 6-12 part (a), where there are no VGs, the average Vz in the vicinity of the suction side is -25 m/s. Moreover, for the three VG configurations, two darker spots are seen inside every VG, an excellent representation of the pair of contra-vortices described in reference [79]. Furthermore, the size of the vortices generated by configurations 2 (**Figure** 6-12 (c)) and 3 (**Figure** 6-12 (d)) is less than configuration 1 (**Figure** 6-12(b)) because the height of VG 2 and 3 is less than 1.

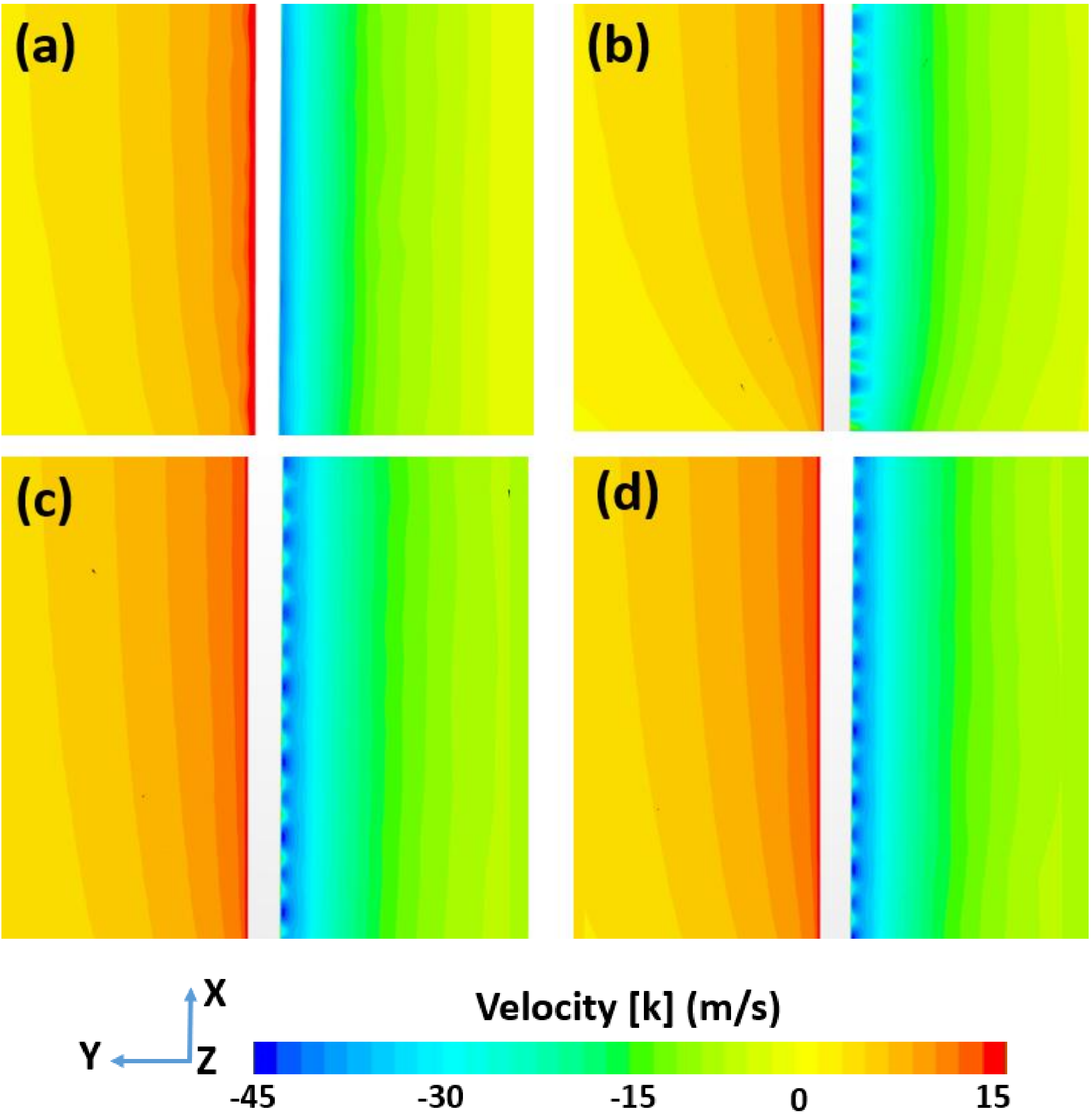

Figure 6-13: Vz contours along a horizontal plane that cuts a blade in a spanwise direction at 25%C (downstream of vortex generators: (a) GOE 447 base design, (b) vortex generator configuration 1, (c) vortex generator

In **Figure** 6-13, downstream of the VGs themselves, mixing zones are created because of the VGs. It is also obvious that VG 2 and 3 (characterized by less heights) produce more homogeneous mixing than VG 1. VG 1 tends to create more disturbance in the near-wall flow than VG 2 and 3. In contrast, VG 2 and 3 make effective and less chaotic mixing.

Again, **Figure** 6-14 emphasizes the ability of VGs to generate a pair of vortices in the middle of each adjacent VGs. This can be demonstrated by the high vorticity spots introduced by VGs. Also, it can be noticed that the size of high vorticity spots caused by VG 1 is slightly amplified than VG 2 and 3.

Figure 6-15 demonstrates the position of the plane that cuts through the blade at 30% of the span measured from the hub. The plane is used to show the contours of the z-component of the velocity, velocity magnitude, absolute pressure, and turbulent viscosity around the root section of the blade in the subsequent few figures in Figs. 16 thru 19 since the tip and root sections are where the off-design conditions are likely to happen.

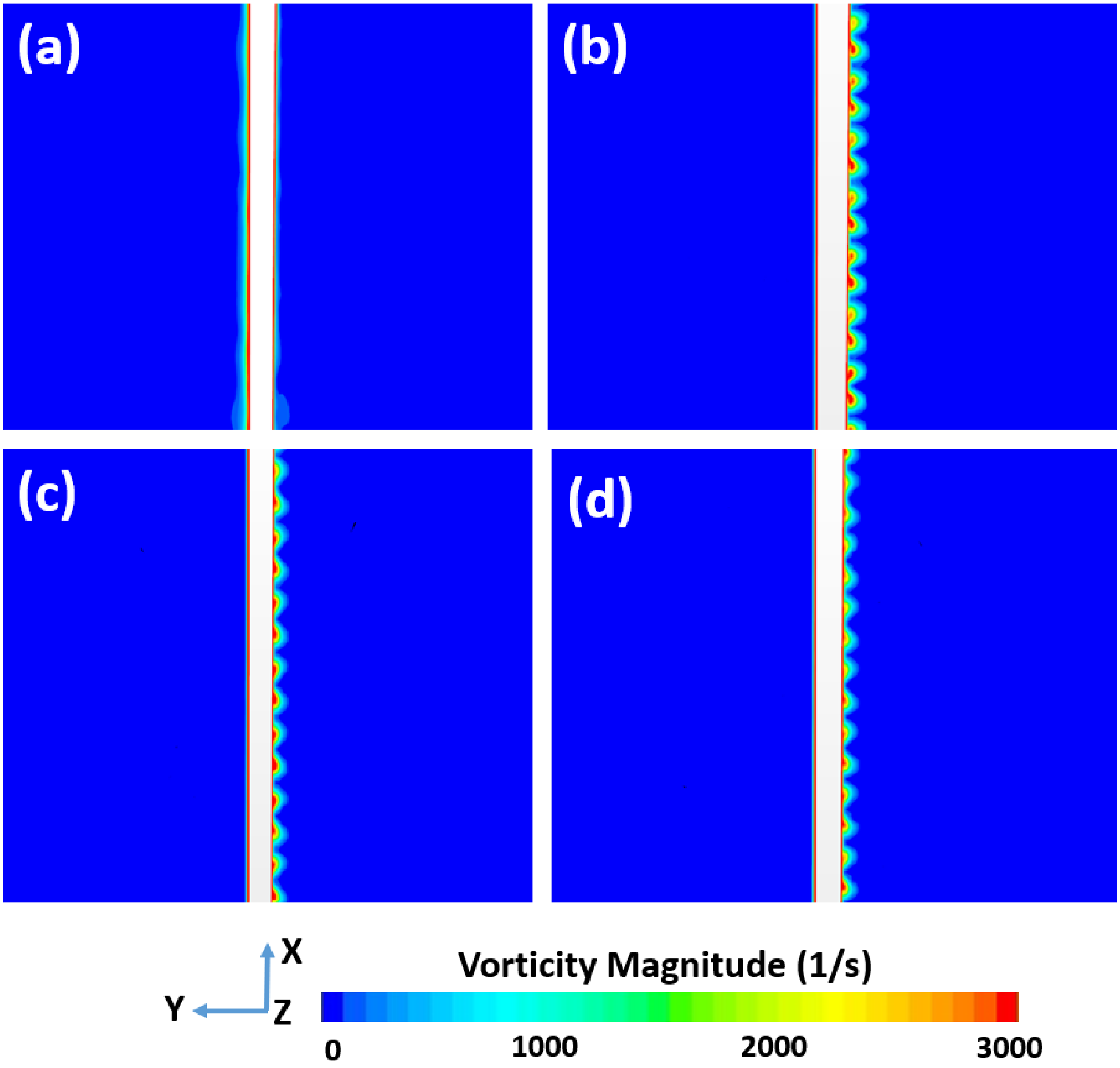

Figure 6-14: Vorticity contours along a horizontal plane that cuts a blade in a spanwise direction at 25%C (downstream of vortex generators: (a) GOE 447 base design, (b) vortex generator configuration 1, (c) vortex generator configuration 2, (d) vortex generator configuration 3

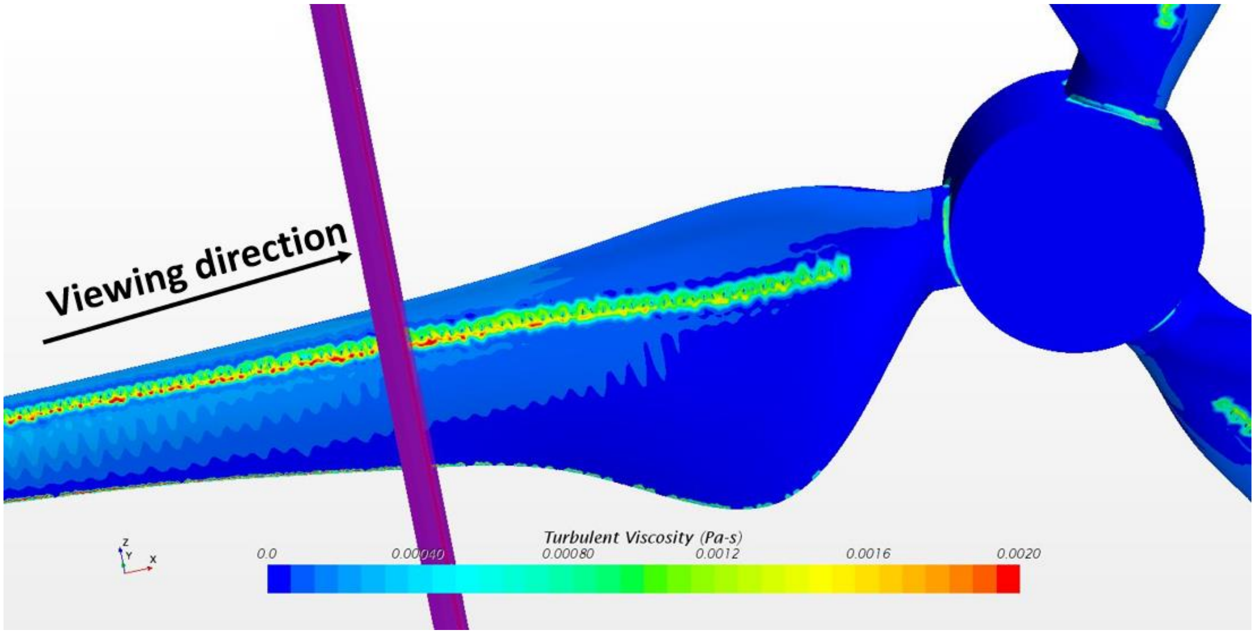

Figure 6-15: Demonstration of the plane that cuts the blade at 30% of the span

In **Figure** 6-16, it is essential to point out that the blade rotates to the left (positive z-direction). The dominant relative flow is in the negative z direction. It is obvious that the disturbance that VG 1 introduces is intense so that it causes earlier separation when compared to the baseline design and the other two VG configurations. VG 1 forces the negative z velocity component that generates lift away from the airfoil suction side earlier than VG 2 and 3. In contrast, VG 2 and 3 guide the flow to stay attached slightly longer than the baseline design, and VG 1, leads to power improvement. Moreover, at the trailing edge, Vz contours show that VG 1 creates a more intense region of reversed flow, in positive z direction, than the baseline and the other two VG configurations. Therefore, VG 1 causes power deterioration.

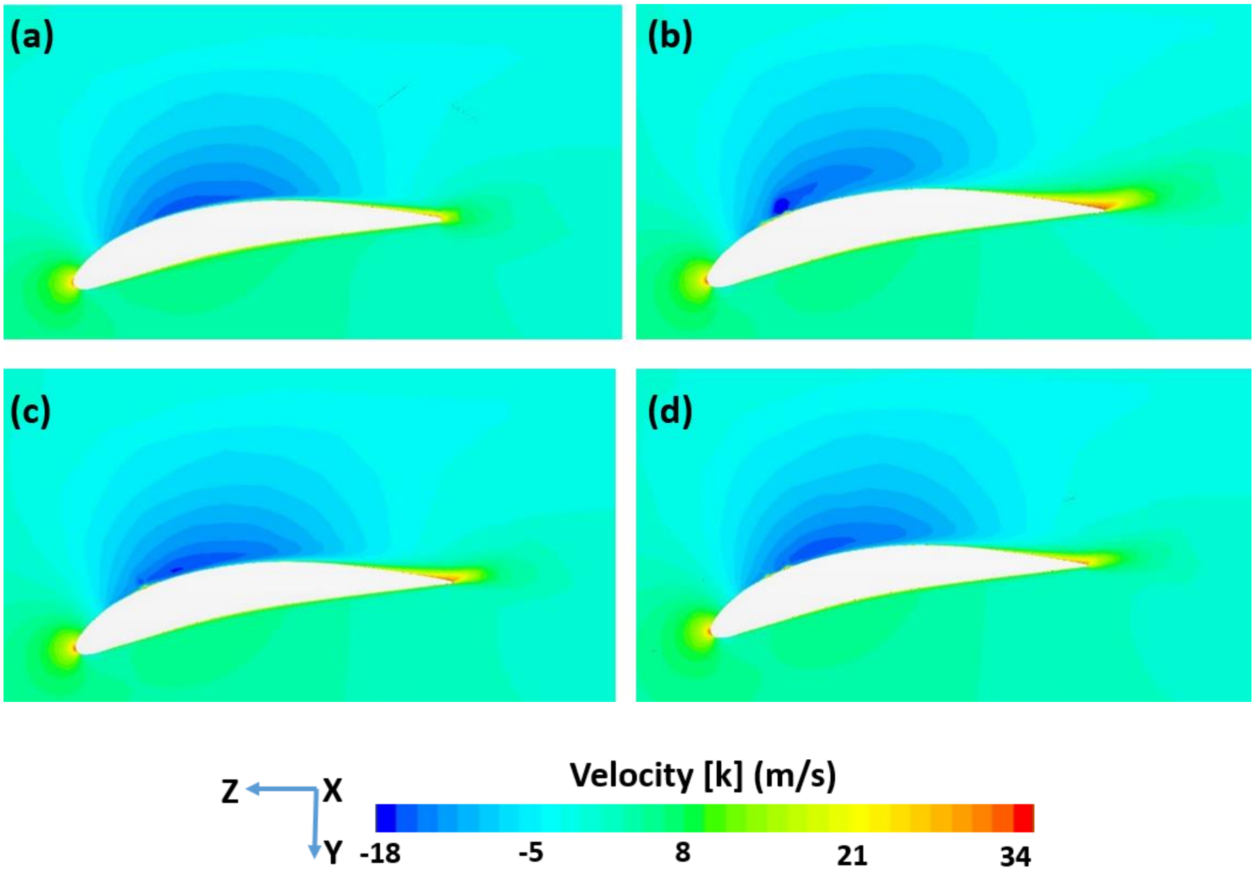

Figure 6-16: Contours of Vz around the root section at 30% of the span: (a) GOE 447 baseline design, (b) VG configuration 1, (c) VG configuration 2, (d) VG configuration 3

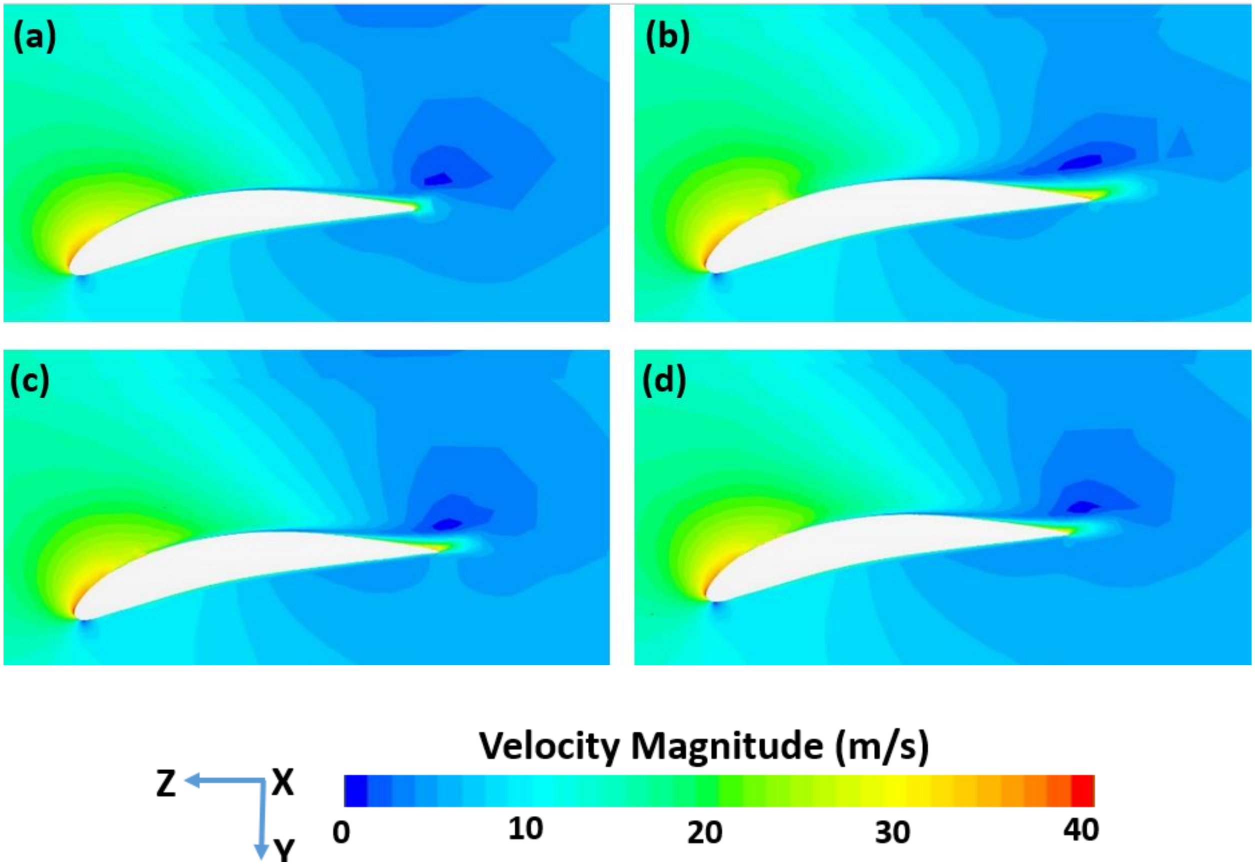

Figure 6-17 Contours of velocity magnitude around the root section at 30% of the span: (a) GOE 447 baseline design, (b) VG configuration 1, (c) VG configuration 2, (d) VG configuration 3

Figure 6-17 confirms what have been discovered from the previous figure. It is obvious that VG 2 and 3 support boundary layer attachment for a longer distance than VG 1 and the baseline design. That is why VG configurations 2 and 3 sustains lift, hence increases power.

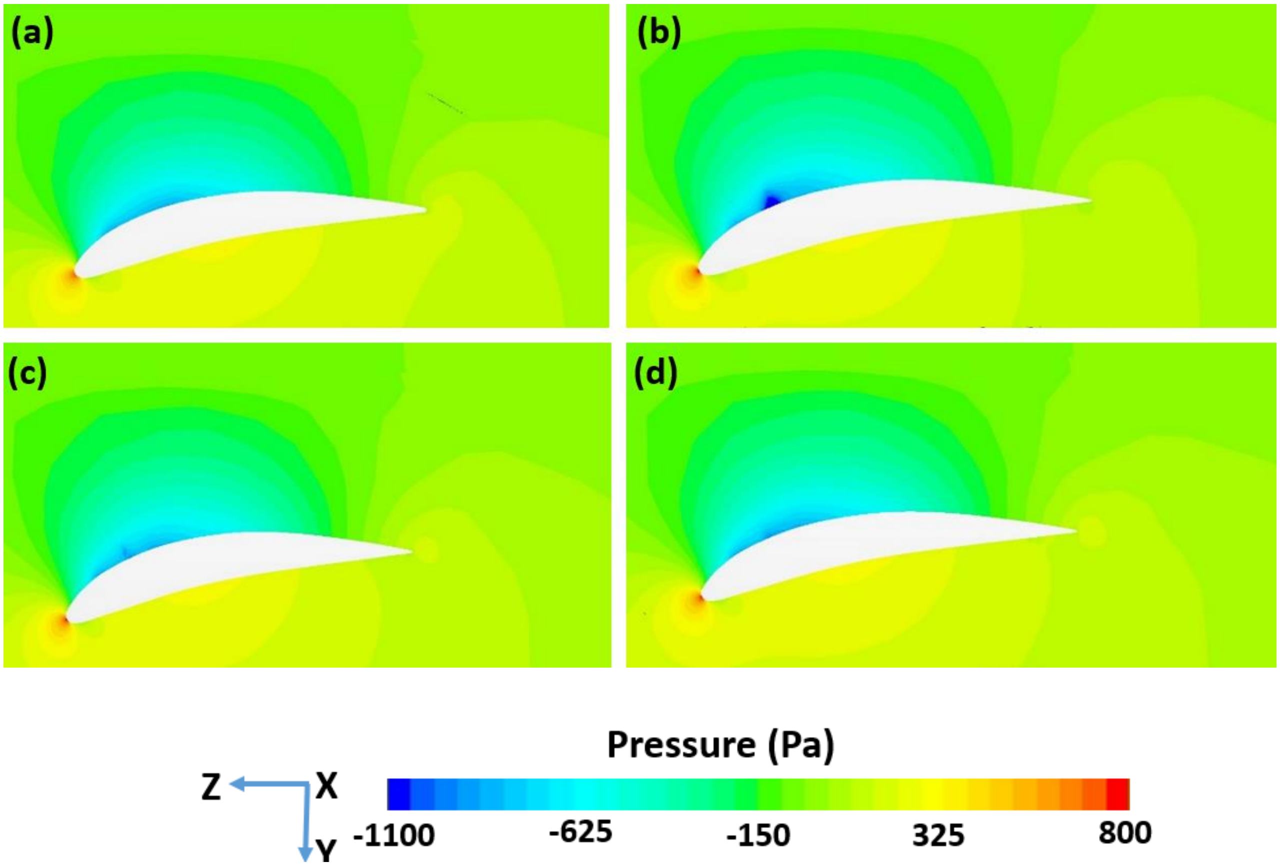

Figure 6-18: Contours of pressure distribution around the root section at 30% of the span: (a) GOE 447 baseline design, (b) VG configuration 1, (c) VG configuration 2, (d) VG configuration 3

The most important thing about **Figure** 6-18 is that it demonstrates the ability of VGs to generate high negative pressure (-1100 Pa) on the suction side of the blade than the baseline design does (only -900 Pa). Although VG 1 generates high negative pressure, the area on the suction side of VG 1 blade that keeps this low pressure is less than VG 2 and 3. Subsequently, VG 2 and 3 can generate higher net pressure than VG 1 and the baseline design, ensuring that higher lift is generated too.

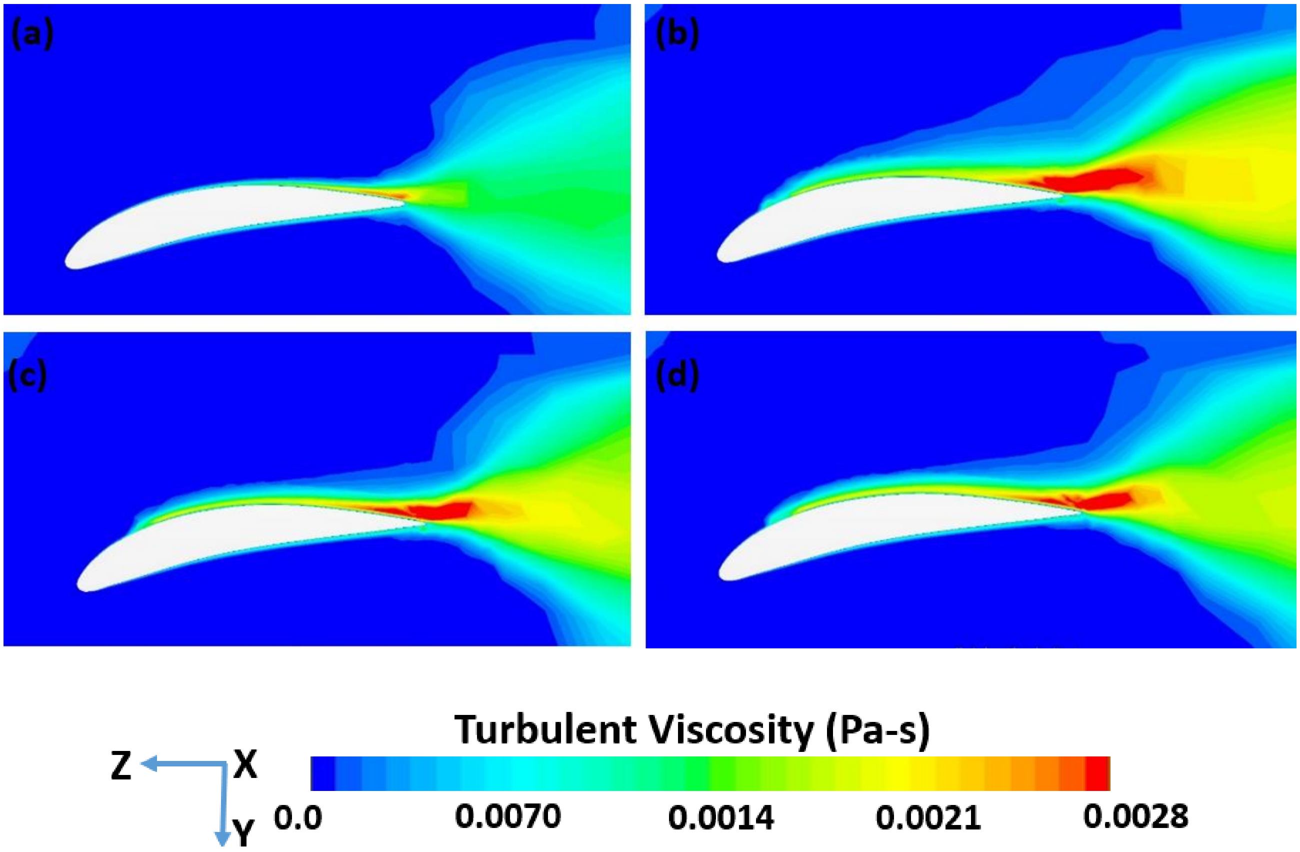

Figure 6-19: Contours of turbulent viscosity around the root section at 30% of the span: (a) GOE 447 baseline design, (b) VG configuration 1, (c) VG configuration 2, (d) VG configuration 3

VGs generate eddies on the suction side of the blade that rolls over towards the trailing edge. The turbulent viscosity is a measure of the turbulent transfer of energy due to the mentioned moving eddies. In **Figure** 6-19, the excited mixing that VGs cause is well-demonstrated for all VG configurations. The amount of turbulence induced by VG 2 and 3 is just enough to energize the near boundary layer flow, hence sustaining flow attachment and increasing power. Besides, VG 1 over-energizes the flow and causes the separation to happen earlier. Thus, losing lift and decreasing power.

6.5.2 Winglets Analysis

Due to pressure differences on both sides of an operating turbine blade, an outward spanwise flow on the pressure side and an inward spanwise flow on the suction side are incurred through the tip. This action creates tip vortex flow that leads to lift force reduction and an additional induced drag. The main purpose of a winglet is to reduce the spanwise flow by diffusing and moving the tip vortex away from the rotor plane towards the wake’s downstream direction. Hence reducing the induced drag on the blade. Consequently, increasing the aerodynamic efficiency of the turbine.

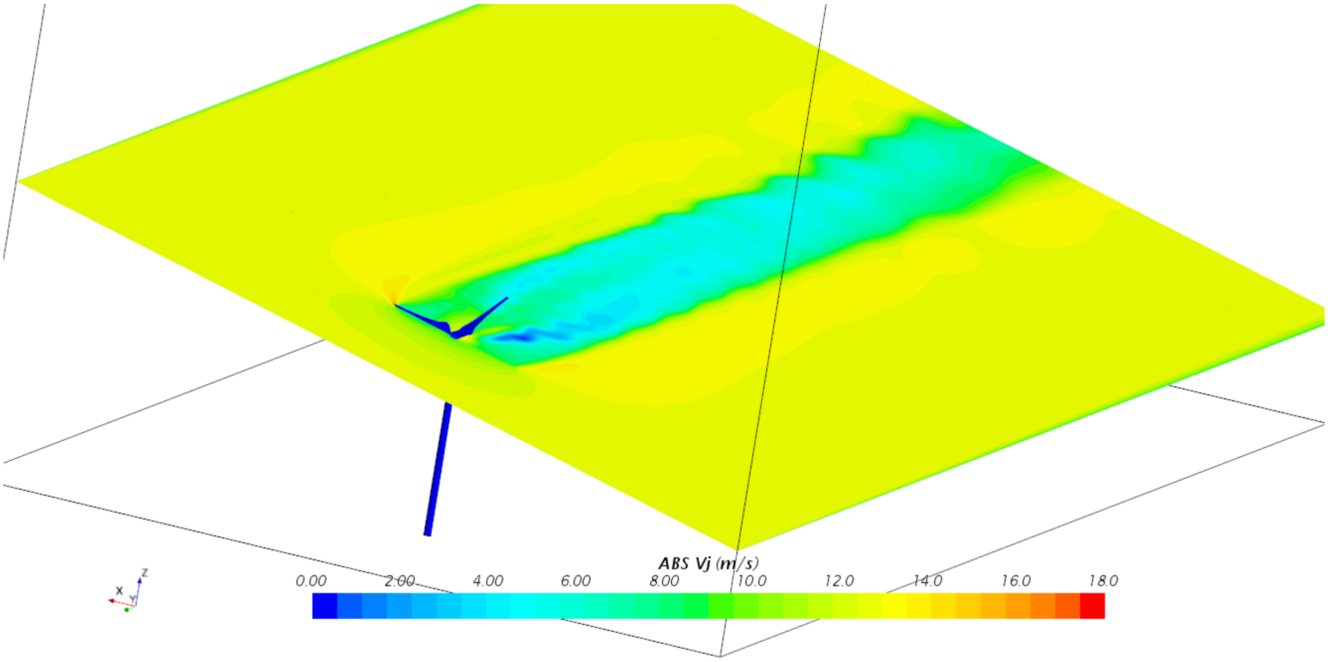

Figure 6-20: Representation of the tilted plane that cuts through one of the blades

For the purpose of understanding the aerodynamic performance of winglet blades, the tilted plane shown in **Figure** 6-20 has been selected so that it cuts one of the blades at the tip.

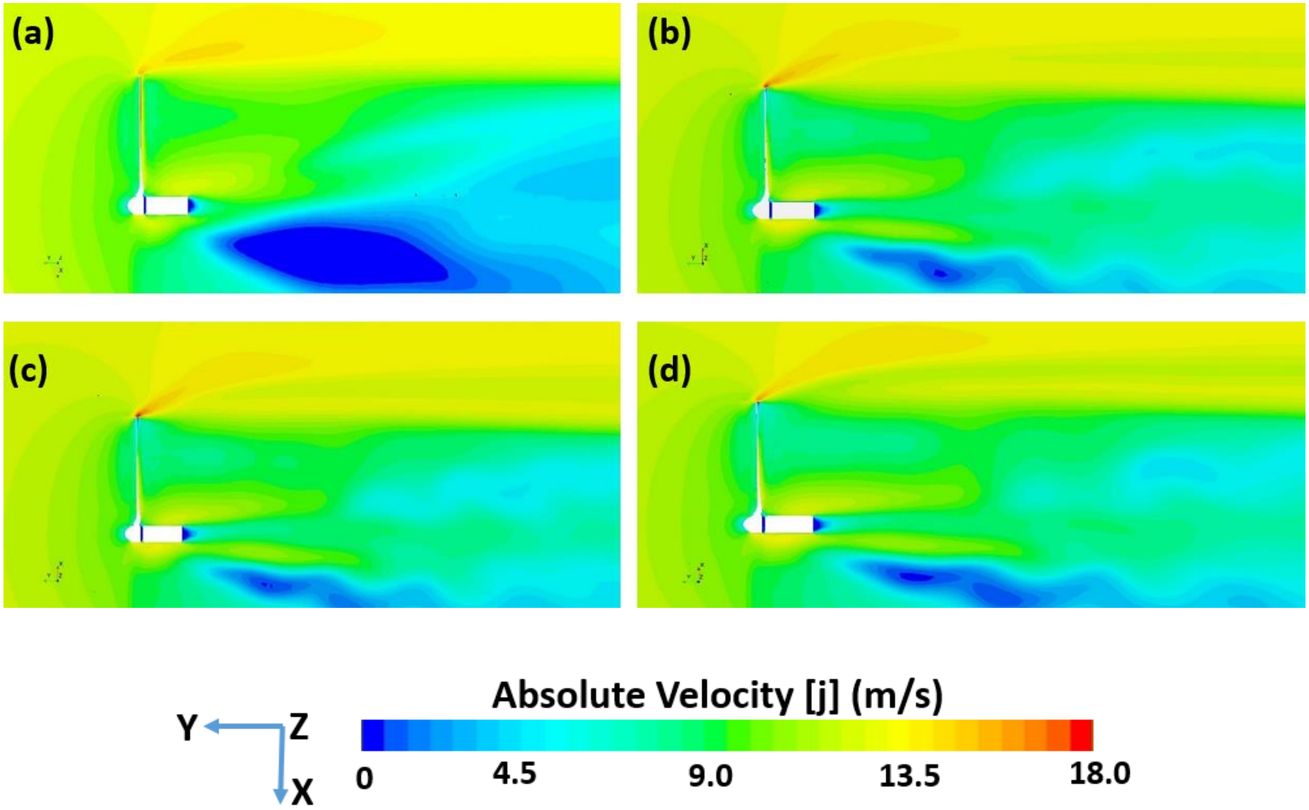

Figure 6-21: Absolute axial velocity contours over a tilted plane that cuts through one of the blades: (a) GOE 447 base design, (b) 30 degrees cant angle winglet, (c) 60 degrees cant angle winglet, (d) 90 degrees cant angle winglet

Figure 6-21 compares the three winglet designs to the GOE 447 baseline design by portraying the absolute axial velocity contours. It is evident that the axial velocity component is maximized at the blade tip in the four parts of the figure. However, the axial velocity maximization is greater for the winglet blades than in the GOE447, baseline blade. Axial velocity maximization is the greatest at the tip of the 60^{o} cant angle winglet (part c) which indicates the ability of this design to better diverge the tip vortex flow, hence allowing higher turbine efficiency. Moreover, by comparing the axial velocity value in the near wake of the rotational plane, it can be seen that the axial velocity in the near wake of the baseline design drops from 12.5 m/s to only 10 m/s. However, the axial velocity in the near wake of the winglet rotors decreases to 6 m/s. The greater the axial velocity drop, the increased rotor ability to extract more momentum from the upstream flow. The previous phenomenon is a good indication of the ability of winglets to reduce induced drag, increasing lift force, hence increasing the turbine efficiency.

Table 6-3 shows a conclusive comparison that highlights the entire outcomes of the current work. It is obvious that all winglet configurations lead to higher power production, particularly the 60° cant angle design. Moreover, VGs configuration (1) seems to induce earlier separation rather than enhancing flow attachment. However, VGs configurations (2) and (3) successfully promote flow attachment at all wind speeds, hence leading to higher power production.

Table 6-3: Quantitative comparison of power output and power coefficient values for the GOE 447 baseline blade and all proposed blades

Model	7.5 m/s			12.5 m/s			17.5 m/s		
	P	Cp	Improvement %	P	Cp	Improvement %	P	Cp	Improvement %
447 baseline design	12.75	0.3274		60.30	0.3344		163.43	0.3303	
VG_1	11.87	0.3048	-6.9	57.71	0.3201	-4.3	162.23	0.3279	-0.7
VG_2	13.69	0.3517	7.4	65.39	0.3627	8.4	182.23	0.3683	11.5
VG_3	14.05	0.3608	10.2	66.87	0.3709	10.9	185.67	0.3753	13.6
winglet 30	13.66	0.3508	7.1	64.45	0.3575	6.9	178.56	0.3609	9.3
winglet 60	13.78	0.3539	8.1	65.09	0.3610	7.9	180.65	0.3651	10.5
winglet 90	13.33	0.3423	4.6	63.34	0.3513	5.0	179.56	0.3629	9.9
VG_2& winglet 30	11.93	0.3064	-6.4	56.36	0.3126	-6.5	156.1	0.3155	-4.5
VG_2& winglet 60	11.96	0.3071	-6.2	56.7	0.3145	-6.0	157.19	0.3177	-3.8
VG_2& winglet 90	11.68	0.2999	-8.4	55.24	0.3064	-8.4	153.57	0.3104	-6.0
VG_3& winglet 30	12.01	0.3084	-5.8	56.56	0.3137	-6.2	157.18	0.3177	-3.8
VG_3& winglet 60	12.09	0.3105	-5.2	57.25	0.3175	-5.1	159.13	0.3216	-2.6
VG_3& winglet 90	11.73	0.3012	-8.0	55.33	0.3069	-8.2	154.27	0.3118	-5.6

6.5.3 Combining VGs and winglet on a single blade

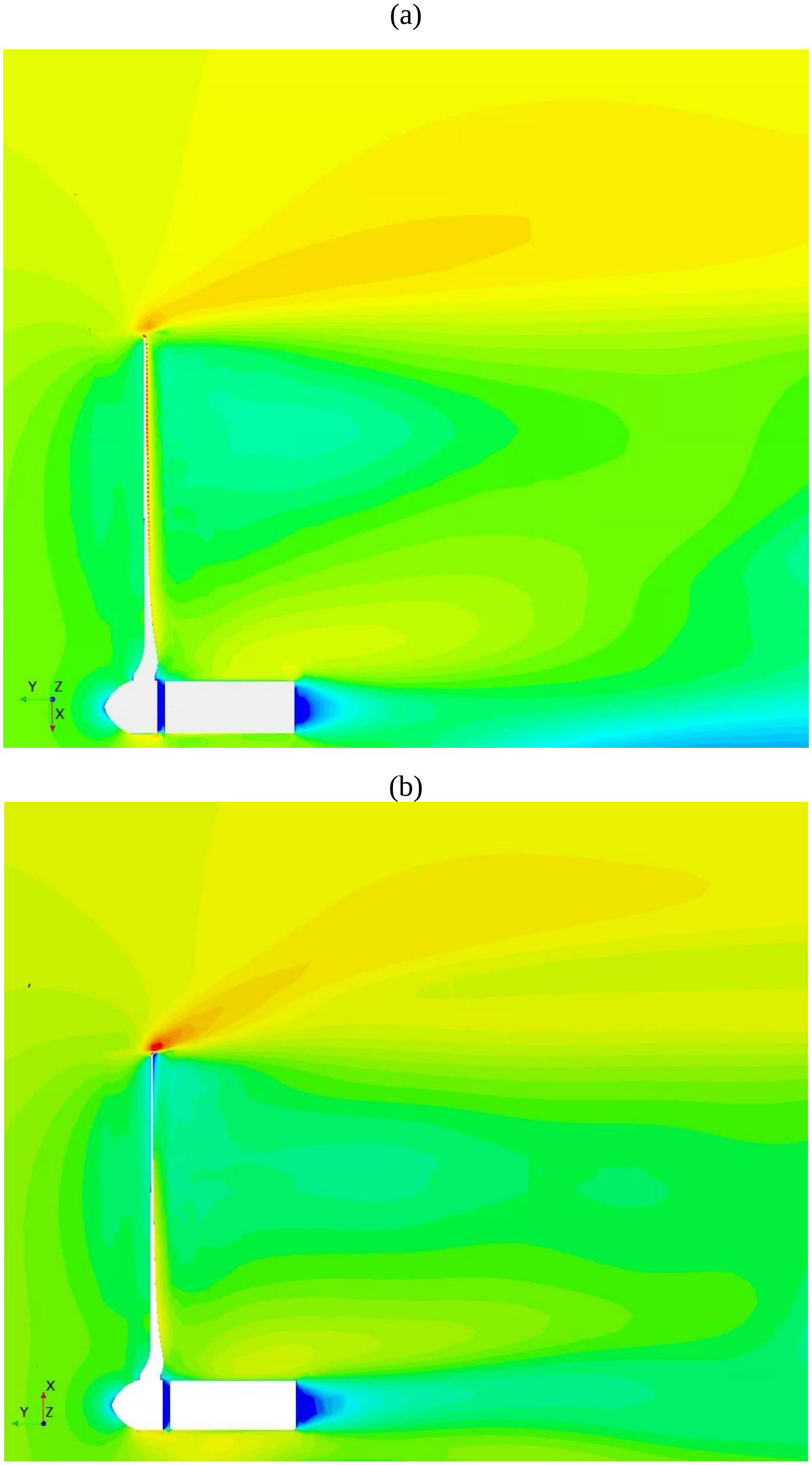

(c)

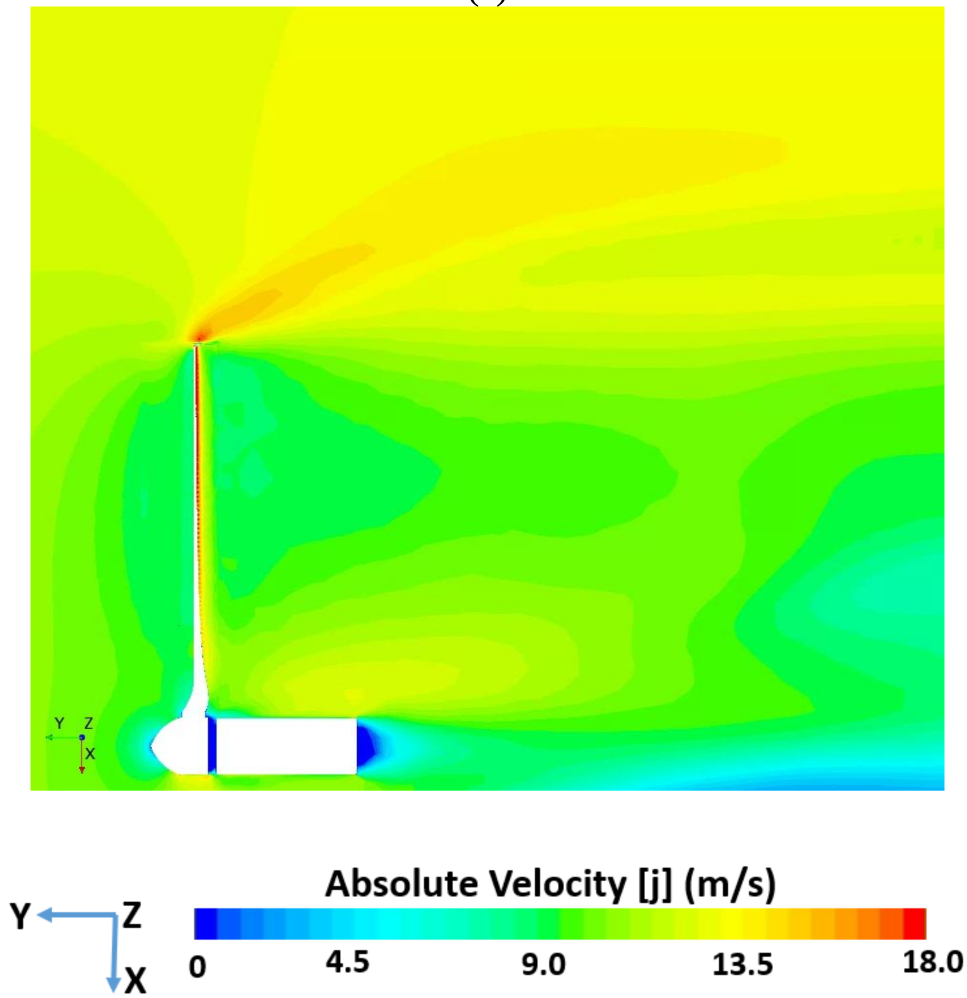

Figure 6-22: Absolute axial velocity contours over a tilted plane that cuts through one of the blades: (a) Blade with VG 3 only, (b) Blade with winglet 60 only, (c) Blade with both VG 3 & winglet 60.

Table 6-3 shows that combining the most efficient VGs designs with the most efficient winglet design leads to, unexpectedly, a reduction in power production (an average of 6.5% less power than the baseline design at rated wind speed). The reason behind this observation can be explain by **Figure** 6-22**.** In part (a), VG 3 is used alone, where there is no significant change on the tip axial velocity compared to the baseline design. However, VG allows the axial velocity to drop from 12.5 m/s upstream to 5 m/s downstream. This great axial velocity drop reflects the ability of VGs to enhance flow attachment to the blade and allows for greater momentum extraction by the rotor, hence higher power than the baseline. In part (b), where the 60-degrees winglet is used alone, the change in the tip axial flow is significant. The significant increase in tip flow velocity reflects the ability of winglets to diverging tip vortex away from the rotor, thus reducing induced drag, allowing great momentum extraction and higher power than the baseline. In contrast, part (c) shows the blade when both techniques combined. VGs dictates the chordwise flow structure. Consequently, the spanwise floe structure is affected. Hence, the winglet function is impaired by the change in the spanwise flow structure. So, the generated power is less than the baseline. It can be noticed in part (c) that the axial flow velocity behind rotor only drop to 10 m/s.

6.6 Conclusions

Geometry parameters of VGs play a key role in dictating the chordwise flow, hence the turbine's flow attachment and power production. Less height and incidence angle of a VG lead to more effective mixing on the suction side. Consequently, greater acceleration for the flow attached to the suction side results in higher net pressure, generating more lift and higher power production. Average power improvement increases with the increase in wind speed. The power improvement percentage increases with the increase of wind speed. For instance, maximum power improvement is achieved with the VG 3 attached to the baseline blade. 13.6% power improvement is achieved at 17.5 m/s wind speed.

Winglets’ ability to diverge tip vortex flow away from the rotor to reduce induced drag and produce more power are excellent for thin airfoils. The power improvement drops slightly at the rated wind speed for winglets with cant angles 30^{o} and 60^{o} However, power improvement gets higher as the wind speed goes higher for the wiglet with 90^{o} cant angle. For instance, a maximum of 10.5% power improvement is achieved by the 60^{o} winglet blade at 17.5 m/s wind speed.

Chapter 7 : Experimental and Numerical Investigation of Tubercles and Winglets in Horizontal Axis Wind Turbine Blade Design

7.1 Introduction

Due to their availability and high calorific value, fossil fuels are still the main energy sources in most of the world to facing the soaring energy demand [1]. According to Renewables Global Status Report [4], the world still depends on fossil fuel to generate most of its electricity (73.8%), while the renewable electricity share is only 26.2%. The worldwide endeavors towards decarbonization are in the transition from incentivizing buildings and facilities that participate in cutting carbon footprint to applying fines on the entities that exceeds certain amount of CO2 emissions. Many countries around the world are working hard to prevent fossil fuel infrastructure build-out. Other countries passed local laws, decarbonization legislation and executive orders to transform to low-carbon economy. Even some countries announced banning the sales of internal combustion engines vehicles and replacing that with electric vehicles by 2035. [83], [84], [85], [86]

Wind turbine technology plays a key role in shaping the future of world's energy [47], [48], [49], [50], [51]. Therefore, many studies incorporated wind power with other renewables to achieve a net zero energy model in different applications. Anwar et al. [52] used HOMER software to perform feasibility and sensitivity analysis of a system that integrated PV panels, wind, biogas, fuel-cell, diesel, and batteries for electrification of rural, off-grid areas. Qandil et al. [53] used the same software to investigate the possibility of combining the application of energy efficiency opportunities with a system of renewables (PV, wind, digester gas, and aeration tanks' microturbines) to achieve a net zero energy model in small size wastewater treatment plants.

Since vertical axis wind turbines (VAWTs) can produce electricity in any wind direction, and they need neither yaw drive nor pitch mechanism, they catch the attention of many researchers [87], [88], [89], despite having lower efficiency than horizontal axis counterparts. Moreover, VAWTs do not need strong support structure to carry power generation components off the ground. So, Laws et al. [54] have used OPENFOAM to introduce, numerically, a simple design modification to the blade of a Savonius wind turbine. The design modification improved the power efficiency by 10-28%. Hassanzadeh et al. [55] tested experimentally four different blade profiles of two-blade Savonius wind turbine under different wind speeds to get the maximum power coefficient among all tested cases. Alom and Saha have examined the aerodynamic drag and lift characteristics of a newly developed elliptical-bladed Savonius rotor [56].

On the other hand, horizontal axis wind turbines (HAWTs) are the most commercially used wind turbines due to their high efficiency. That is why HAWTs performance has been investigated by many researchers to improve the performance of both the individual wind turbine, and the whole wind farm. [90]

Regarding individual wind turbines, many researchers utilized various techniques seeking optimizing the performance of a wind turbine model. Eltayesh et al. [61] investigated the solidity influence on the thrust, power and flow field generated from HAWTs. They showed that using a 3-bladed rotor maximizes the power coefficient among all studied configurations, on the other hand, they yield stronger vortices and flow separation. Additionally, Muheisen et al. [60] studied the effect of equipping the HAWT blades with multi-cross sections with fences. They found that using-multi section blades enhances the power coefficient by eight percent for the studied case. Moreover, they found that introducing fences to multi-cross section blades enhances the rotor’s performance and stability. Besides, Mohammadi and Maghrebi [62] investigated reducing boundary layer separation by blowing a different number of air jets on the suction side of HAWT blades. They found that the generated torque was doubled compared to the baseline blade in the best case. They also proved that the torque increases with the number of blown air jets. Besides, they showed that placing air jets near the blades' tips enhances the performance more than placing them in the middle or inner portions of blades.

Regarding wind farms' output improvement, Jackson and Amano [32] investigated, experimentally and numerically, the velocity deficit in case of having single, double, and triple wind turbine models in an in-line configuration inside a wind tunnel. Choi et al. [34] used the commercial multi-purpose CFD solver ANSYS CFX to build a full wind farm model which contained two HAWTs with full-scale dimensions; each turbine provided 2 MW output power. They carried out a steady-state analysis of the problem using the Reynold Averaged Navier Stokes (RANS) approach with the Shear Stress Transport (SST) k-ω model. The separation distance between the two turbines was increased from one case study to another; hence, the power output of the downstream turbine increased significantly, which yielded an increase in the wind farm annual energy production.

Hasan et al. [57] have tested the wake region of a small scale HAWT inside a wind tunnel using hot wire anemometry, to show axial and vertical velocity components, besides turbulence intensity, over many transverse sectional planes along the wake. Then, the previous study was expanded to include computational fluid dynamics (CFD) simulations of the same turbine model under different operating conditions. By tracking the hub-height axial velocity recovery at different wind speeds and tip speed ratios (TSRs), the separation distance between two successive units in a wind farm was determined [58].

Since most of the research and development in the field of HAWTs focuses on large, utility-scale wind turbines, more attention should be paid to the small wind turbines for residential and urban applications. Therefore, Hasan et al. [63] performed a numerical study that investigated the effect of using four newly introduced airfoils for blades generation of residential scale turbines. Airfoils are NACA 64(3)618, GOE 446, NACA 6412, and GOE 447. Since GOE 447 was proven to generate the highest power, it was selected to add leading edge tubercles and winglets, which achieved an increase in the power output at all tested wind speeds (4.2-5.5% power increase than the GOE 447 baseline design). Furthermore, Hays and Treuren [64] focused on utilizing small wind turbines in urban environment. Having the turbines working near the end user makes the optimization process not only limited to power maximization, but also noise suppression. Therefore, they studied two rotors designed with NREL S823 and Eppler 216 airfoils. They found that the thinner profile and increased camber of the Eppler 216 improved the turbine aerodynamic performance, increased power, and reduced the noise significantly.

Many studies proposed the leading-edge **tubercles** for HAWTs power maximization. Abate et al. [28] studied the effect of 20 different tubercles configurations on the power production of the basic NREL phase VI wind turbine rotor. They found that a significant power improvement was achieved for the high wind speed cases (tubercles showed a 25% power increase at 20 m/s), while the opposite trend was obtained at lower wind speeds (tubercles showed a 45% less power at 10 m/s). The reason behind the previous finding is that the flow around tubercles was characterized by counter-rotating vortices generation, which counteracts the spanwise flow, resulting in a stall strength reduction.

Huang et al. [30] performed an experimental study to investigate the effect of applying leading edge protuberances **(tubercles)** on the performance of both static 3D airfoil and a three-bladed HAWT model. Four protuberant models were created to be applied on the leading edge of the baseline static airfoil, with an amplitude equals 1.5% and 8.5% of the chord length, and a wavelength equals 15% and 6.5% of the chord length. To fix Re, the lower amplitude protuberances were tested at 9.5 m/s, while the higher amplitude protuberances were tested at 10.5 m/s, whereas the AoA was changed from -10 ^{o} to 40 ^{o}. They found that the protuberance wavelength had a minor effect on the lift coefficients of those with smaller amplitudes. However, wavelength had a major effect on those protuberances with larger amplitudes. Regarding the rotor models, they applied four sinusoidal protuberance configurations to the leading edge of the baseline rotor. The four configurations come from combining two amplitudes (4% and 12% of the chord length) to two wavelengths (40.4% and 14.5% of the chord). All resultant rotors were tested at wind speeds of 6, 8 and 10 m/s, while the TSR increased from 1 to 8 at each wind speed. All protuberances configurations didn’t improve the power coefficient (Cp), except for the smaller- amplitude, larger- wavelength configuration that generated more power than the baseline rotor only at wind speed of 6 m/s.

Zhang and Wu [76] used RANS simulations to investigate the effect of adding sinusoidal waves **(tubercles)** to the leading edge of a rotor blade on the shaft torque of a wind turbine. They proposed five different configurations of tubercles with wavelengths equal 17%, 25% and 42% of the root chord, and wave heights (half amplitudes of sine wave) equal 1.25%, 2.5% and 3.75% of the root chord. They found that for design condition (wind speed is less than 12 m/s), blade with leading-edge tubercles is unfavorable, since an early boundary-layer separation occurs due to the geometric disturbances of the leading-edge tubercles, hence shaft-torque decreased for the five cases. On contrast, for off-design conditions (wind speeds higher than 15 m/s), shaft-torque increased significantly, particularly for the cases with high wavelength and wave height (for instance, at 15 m/s, the shaft-torque is 85% higher than the torque of the straight blade).

Other works adopted winglets as a tip modification to improve the turbine’s aerodynamic performance, hence power maximization. Khaled et al. [20] investigated the influences of winglets on power and thrust coefficients. Firstly, they investigated the effect of winglet length variation (changed from 1% to 7% of the turbine rotor radius), while the cant angle is fixed at 90°, and TSR changed from 2.5 to 9.6. They found that for all cases, the power maximized at the design TSR of 5 then drops, while the thrust coefficient (C_T) continued increasing till TSR is 8.4 then started to fall. Secondly, for each winglet length, the cant angle changed from 15° to 90°, while the TSR is maintained at its optimum value (5). They found that Cp range increased by the increase of winglet length. Moreover, at each length, Cp is maximum at a cant angle of 50°, while C_T is maximum at 30°.

Khalafallah et al. [22] investigated the effects of winglet direction, cant angle, and twist angle for two winglet orientations: upstream and downstream directions. For each winglet direction, –2°, 2°, and 10° twist angles were studied at 20°, 40°, and 60° cant angles, with fixed TSR of 6 in all simulations. They concluded that the winglet pointing to the downstream side showed a more increase in power than those pointing to the upstream side. They claimed that a general increase of the Cp occurred except for the three cases of a cant angle of 60° at which the winglet was on the upstream side. Compared to the baseline design mentioned in their literature, maximum increase in Cp of 1.75% was observed where winglet pointing to downstream side and has a cant angle of 60° and a twist angle of 2°.

Muhle et al. [24] performed a pure experimental study that focused on showing the effect of different wing tip configurations on the tip vortex formation and interaction in the near wake of a two-bladed model wind turbine. They investigated the impact of switching from the straight-cut wing tip to the downstream-facing winglet on several parameters. Regarding the mean streamwise velocity, the presence of winglets didn't significantly affect the mean velocity field. Regarding wake expansion, winglets generated a slightly wider wake than the straight-cut tip. Regarding the phase-averaged vorticity component, an analysis was done between the two downstream distances 2.3D and 2.6D revealed an instability caused by winglets that stimulated tip vortices interaction with the main wake and caused complete breakup at earlier downstream distance of 3D, whereas the straight-cut tip didn't show any tip vortices interaction till 3.5D. Finally, considering applying winglets to models used in a wind farm, winglets caused earlier and faster tip vortex breakup, the point that enhanced the recovery of the mean wake kinetic energy, which means more potential power extraction out of a downstream turbine.

Ostovan and Uzol [25] also did a pure experimental work to investigate the effect of installing winglets and some wing extensions on the performance of two identical and interacting HAWTs. They attached the winglets and the wing extensions to the upstream turbine to see how this impacts the Cp of the upstream turbine, downstream turbine, and the two turbines combination. They found that for the upstream turbine, the baseline design (without any tip devices) produced the lowest power. Attaching winglets produced 2.6% more power than the baseline design, while attaching the wing extensions produced 17.1% more power than the baseline design. On the other hand, the downstream turbine produced the highest power when the upstream turbine had no tip devices. Attaching the winglets to the upstream turbine caused the downstream one to generate 4.1% less power, while attaching the wing extensions to the upstream turbine resulted in generating 15.7% less power out of the downstream one. Regarding the overall power of the two turbines combination, it increases by 1.1% when winglets were installed to the upstream turbine, while it increases by 9.6% when wing extensions were installed to the upstream turbine.

This work is an extension of a previous work of the main author [63] that numerically proposed the GOE 447 airfoil as an excellent candidate for building turbine blades of residential scale HAWTs. This work is aimed at investigating two modern blade modifications (tubercles and winglets) when added individually to a turbine blade, in addition to studying the cases of combining these two modifications at the same time to a single blade. It is desired to determine the influence of the mentioned modifications on turbine's power output for such thin and curved airfoils as GOE 447.

Most of available research work of HAWTS is focused on either lab-scale (15-60 cm rotor diameter) or commercial large scale (80-130 m rotor diameter). There is a lack of published data of residential-scale wind turbines. The current work fills this gap since it is going to be counted on during the next 10 years, since the current US administration promotes dependence on renewables to cut carbon footprint [74]. In the windy Midwest, residential-scale WTs are going to be a good alternative for the less efficient solar panels in the region.

Earlier blades were build using thin airfoils, but they were susceptible to fracture. That’s why recent blades are built using thick airfoils, but it comes with early separation problem. Nowadays with the recent advances in composites manufacturing, thinner blades can be manufactured without the fear of fracture [75]. Very rare data are available for thin airfoil blades. All previous published work discusses modifications applied to thick airfoils blades. However, it is essential to provide data to study the effect of modern blade modifications on thinner airfoils.

7.2 Geometry Models

Figure 7-1 shows an upstream isometric of the GOE 447 rotor with the tubercles (wavy pattern) at the leading edge. **Figure** 7-2 demonstrates the downstream side of the rotor highlighting the winglets (tip modifications) on two blades. In this figure, the reader can notice that the winglets points towards the downstream direction. **Figure** 7-3 demonstrates GOE 447 blades with combined leading-edge tubercles and downstream facing winglets.

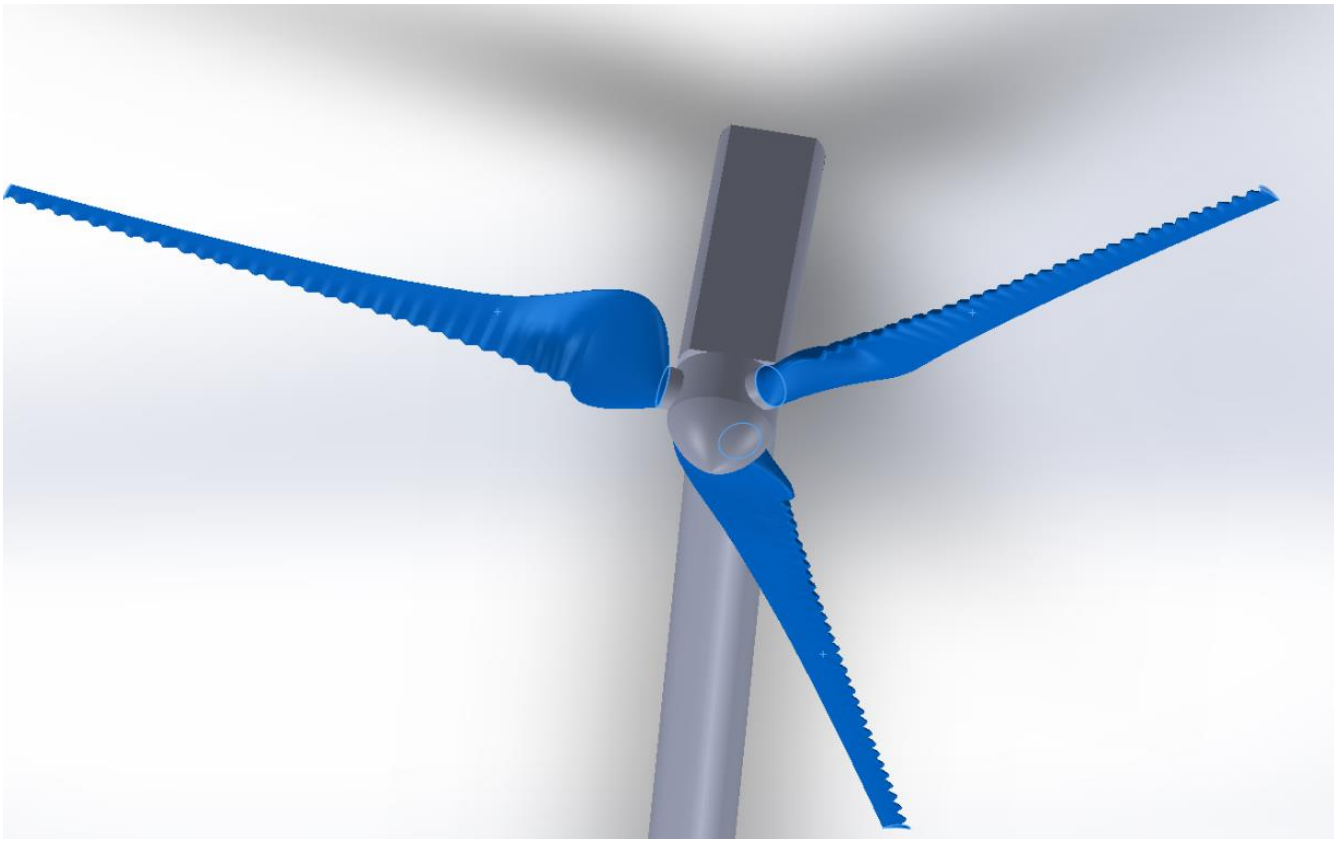

Figure 7-1: GOE 447 blades with leading edge tubercles

Figure 7-2: GOE 447 blades with downstream-facing winglets

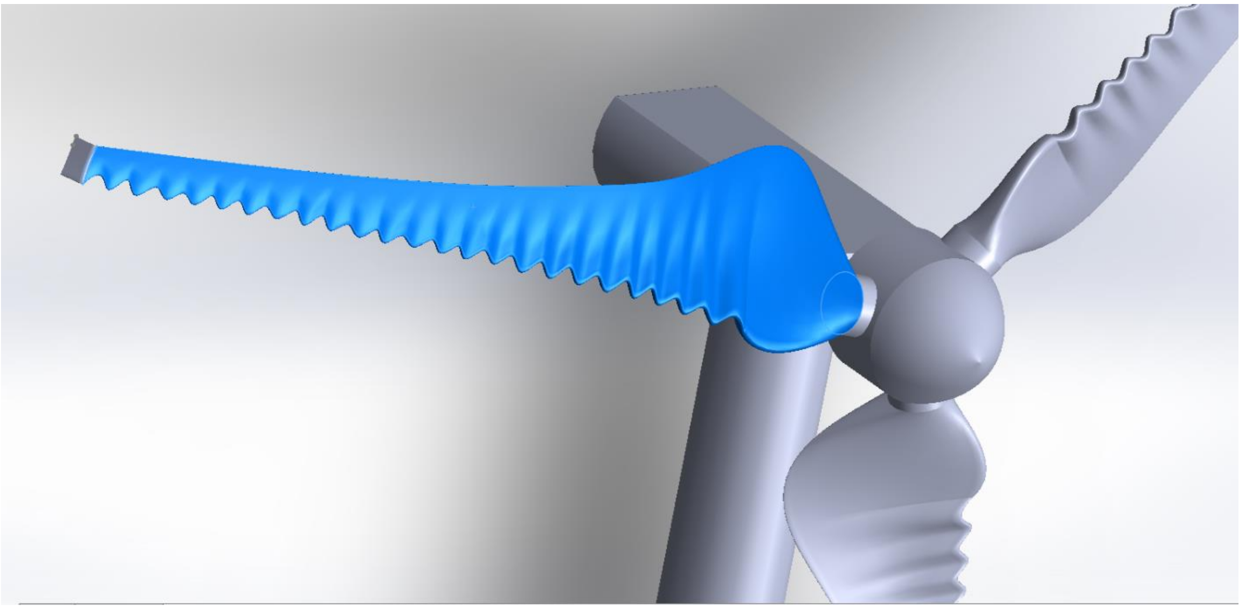

Figure 7-3: GOE 447 blades with combined leading-edge tubercles and downstream facing winglets

7.2.1 Tubercles

Table 7-1 shows the five different configurations adopted in this work. It is desired to cover a wide range of amplitudes of the wavy shape, specifically from 3% to 6.5% of the chord length at the root section (C). Also, it is wanted to investigate a wide range of wavelengths, specifically from 7% of C to 28% of C.

Table 7-1: The five different tubercles configurations

Tubercle configuration	Amplitude (% of C)	Wavelength (% of C)
a	4.5	28
b	3.5	18
c	3	12
d	3.5	7
e	6.5	7

Figure 7-4 illustrates how the parameters in the previous table applied to the leading edge of the baseline GOE 447 blade.

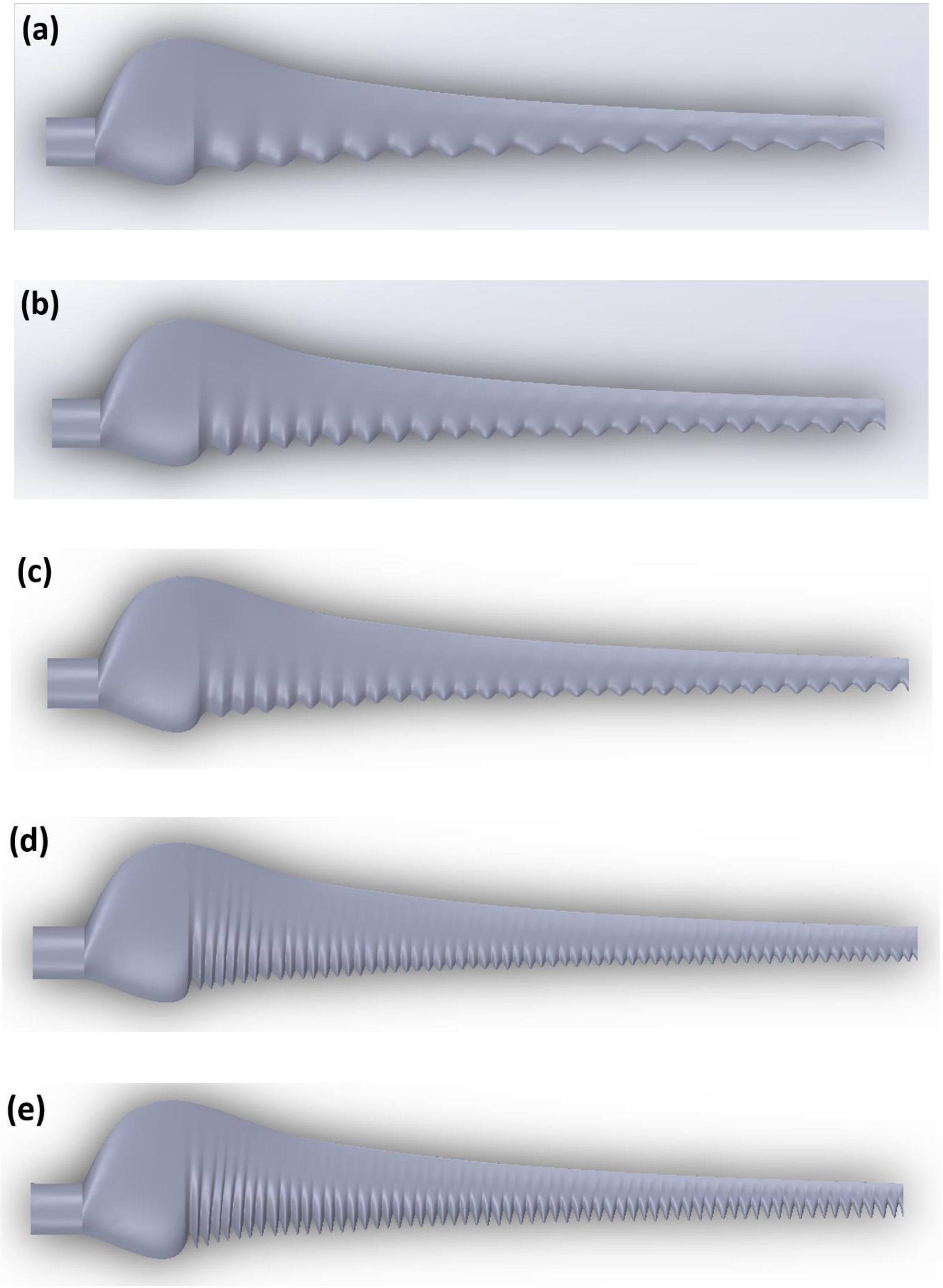

Figure 7-4:Leading edge tubercles, five different configurations

7.2.2 Winglets

The orientation of all winglets in this work is selected to be downstream facing since this is the orientation found to be most effective in power increase [81]. The winglet height is designed to be 2.0% of the blade length (R), while the radius of curvature is designed as 25.0% of the winglet height, and the cant angle is 90°. The previous design was tested with different blades by Johansen et al. [82] and found to give higher power production than basic design. In addition, Khalafallah et al. [22] showed that the 60° cant angle design has a promising potential towards power improvement. Therefore, it is included in the current work, besides the 30° cant angle design, to investigate the effect of adding wide range of winglet designs on the proposed GOE 447 blade's aerodynamic performance. The three designs of winglet are shown in **Figure** 6-10.

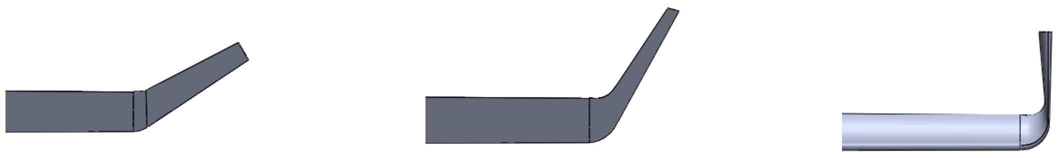

Figure 7-5: Blade with winglet: (left) cant angle 30, (middle) cant angle 60, (right) cant angle 90

7.3 Results

Table 7-2 shows a conclusive comparison that highlight the entire outcomes of the current work. It is obvious that all tubercle configurations lead to poorer aerodynamic performance, compared to the GOE 447 baseline design, except for configuration (d) which is characterized by low values of both amplitude and wavelength. Moreover, all winglet configurations lead to higher power production, particularly the 60^o cant angle design.

The current work also investigates the effect of combining both tubercles and winglets together on a single blade. It is essential to evaluate the influence of the tubercles-winglets combination on the aerodynamic performance and power production of the baseline GOE 447 rotor. The tubercles-winglets combination was solely investigated by running 36 simulations. Four tubercles designed were integrated with the three winglet designs, and each of the 12 resultant rotor was simulated at three different wind speeds (7.5, 12.5 and 17.5 m/s).

It can be noticed that the tubercles-winglets combination results in less power production than the baseline design in all cases, except for four simulations. Three of them are the rotors resultant from integrating tubercle (d) with the three winglet designs at 17.5 m/s, achieving an average of 4% power improvement only. However, this power improvement is not valuable because of two reasons; first the 17.5 m/s wind speed is less likely to happen. Second the power improvement accomplished by integrating one technology at rated wind speed is higher. For instance, tubercle (d) design achieves 5.5% power improvement. Additionally, winglet with cant angle 60^o achieves 7.9% power improvement.

Table 7-2: Quantitative comparison of power output and power coefficient values for the GOE 447 baseline blade and all proposed blades

Model	7.5 m/s			12.5 m/s			17.5 m/s		
	P	Cp	Improvement %	P	Cp	Improvement %	P	Cp	Improvement %
447 baseline design	12.75	0.3274		60.30	0.3344		163.43	0.3303	
Tubercle a	9.41	0.2417	-26.2	46.19	0.2562	-23.4	132.47	0.2678	-18.9
Tubercle b	9.54	0.2450	-25.2	47.83	0.2653	-20.7	137.77	0.2785	-15.7
Tubercle c	10.64	0.2732	-16.5	52.74	0.2925	-12.5	151.41	0.3060	-7.4
Tubercle d	13.34	0.3426	4.6	63.60	0.3527	5.5	167.67	0.3389	2.6
Tubercle e	7.38	0.1895	-42.1	38.76	0.2150	-35.7	113.13	0.2287	-30.8
Winglet 90	13.33	0.3423	4.6	63.34	0.3513	5.0	179.56	0.3629	9.9
Winglet 60	13.78	0.3539	8.1	65.09	0.3610	7.9	180.65	0.3651	10.5
Winglet 30	13.66	0.3508	7.1	64.45	0.3575	6.9	178.56	0.3609	9.3
Tubercle a & Winglet 30	9.46	0.2429	-25.8	47.55	0.2637	-21.1	133.42	0.2697	-18.4
Tubercle a & Winglet 60	9.17	0.2355	-28.1	47.37	0.2627	-21.4	135.32	0.2735	-17.2
Tubercle a & Winglet 90	9.43	0.2422	-26.0	46.91	0.2602	-22.2	133.66	0.2702	-18.2
Tubercle b & Winglet 30	8.82	0.2265	-30.8	44.58	0.2473	-26.1	130.67	0.2641	-20.0
Tubercle b & Winglet 60	8.69	0.2232	-31.8	44.33	0.2459	-26.5	130.1	0.2630	-20.4
Tubercle b & Winglet 90	9.81	0.2519	-23.1	48.4	0.2684	-19.7	134.25	0.2713	-17.9
Tubercle c & Winglet 30	10.51	0.2699	-17.6	51.79	0.2872	-14.1	144.2	0.2915	-11.8
Tubercle c & Winglet 60	10.5	0.2696	-17.6	52.24	0.2897	-13.4	145.32	0.2937	-11.1
Tubercle c & Winglet 90	11.43	0.2935	-10.4	55.48	0.3077	-8.0	152.14	0.3075	-6.9
Tubercle d & Winglet 30	12.37	0.3177	-3.0	60.48	0.3354	0.3	170.94	0.3455	4.6
Tubercle d & Winglet 60	12.35	0.3172	-3.1	59.55	0.3303	-1.2	170.52	0.3447	4.3
Tubercle d & Winglet 90	12.19	0.3130	-4.4	59.29	0.3288	-1.7	167.44	0.3384	2.5

7.3.1 Tubercles Analysis

All the contours shown in the following analyses are captured from the 12.5 m/s wind speed simulations since it represents the rated wind speed.

Figure 7-6 demonstrates the location of the horizontal sectional x-y plane that cuts a blade exactly at its leading edge and cuts the computational domain at hub-height. The selected plane is essential because of its ability to display the interaction between the main flow in the y-direction and the tubercles.

Figure 7-7 represents a visual comparison of the turbulent kinetic energy contours for the baseline design, tubercle (a) and tubercle (d) configurations respectively. Tubercle (a) and (d) configurations are selected since the former leads to the most significant decrease while the later is the only tubercle configuration that leads to power increase. It is obvious that both configurations produce less turbulent wake, compared to the baseline design. The phenomenon is interesting to visualize, but still doesn't explain why configuration (a) reduces power while (d) increases it.

Figure 7-8 shows a comparison of the vorticity magnitude contours for the baseline design, tubercle configuration (a) and (d) respectively. It is observed that configuration (a) slightly increases the vorticity magnitude, while configuration (d) slightly decreases it, compared to the baseline design. The reduced vorticity is an indication of the ability of configuration (d) to drive the flow in the blade chordwise direction with less rotation in the wake. The phenomenon is also an indication of an enhanced attachment of the flow, less separation, hence more power extraction from the wind.

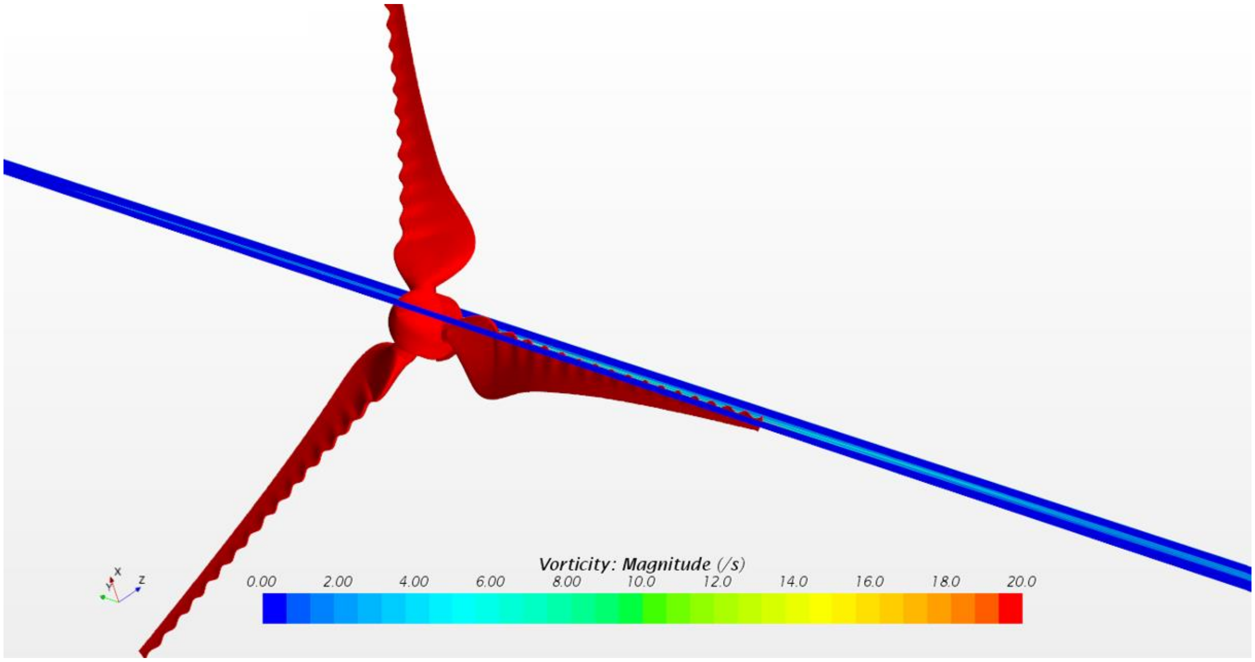

Figure 7-6: Demonstration of the sectional plane location

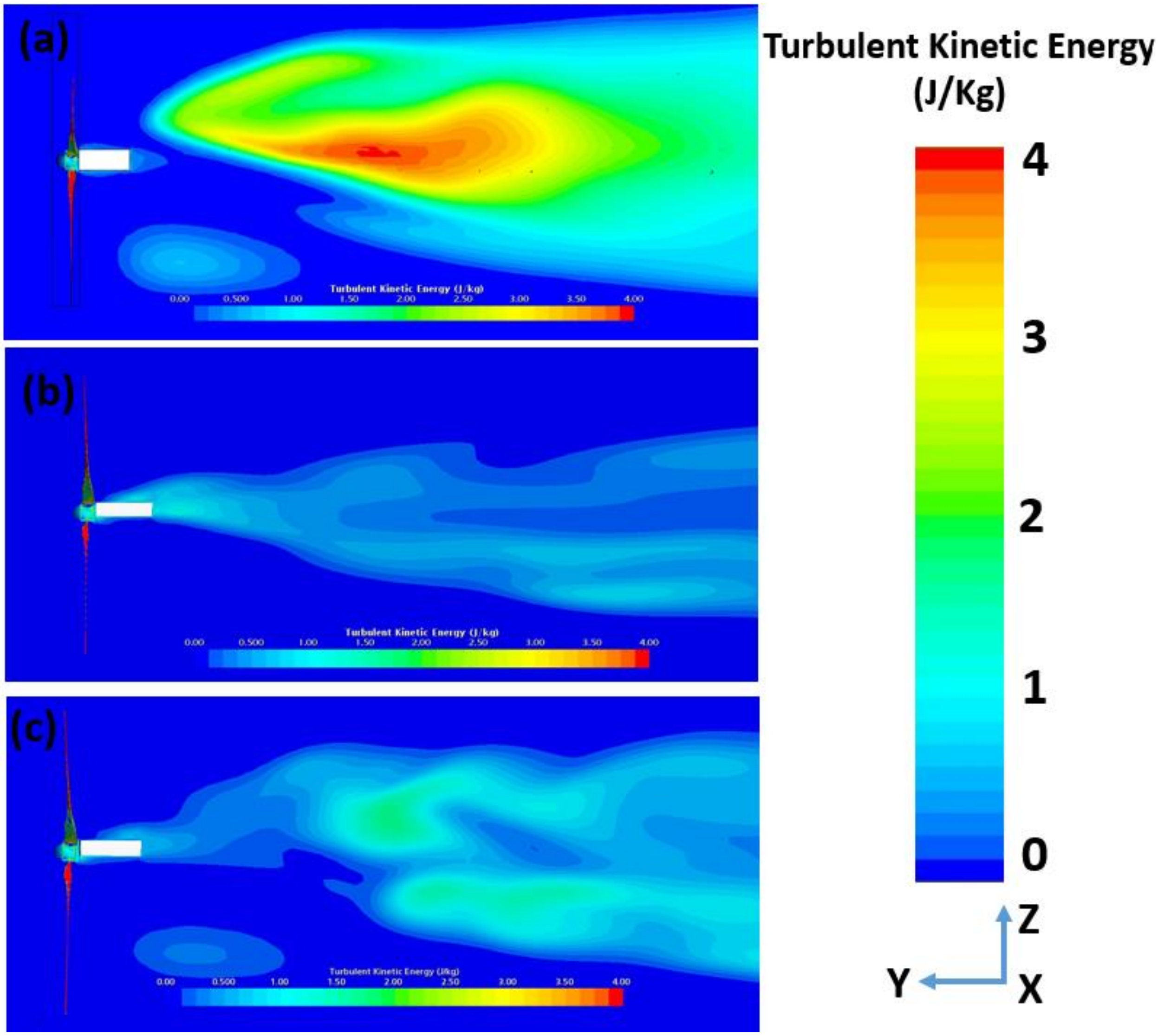

Figure 7-7: Turbulent kinetic energy contours for: (a) baseline GOE 447, (b) tubercle [a], (c) tubercle [d] design over a hub-height horizontal plane

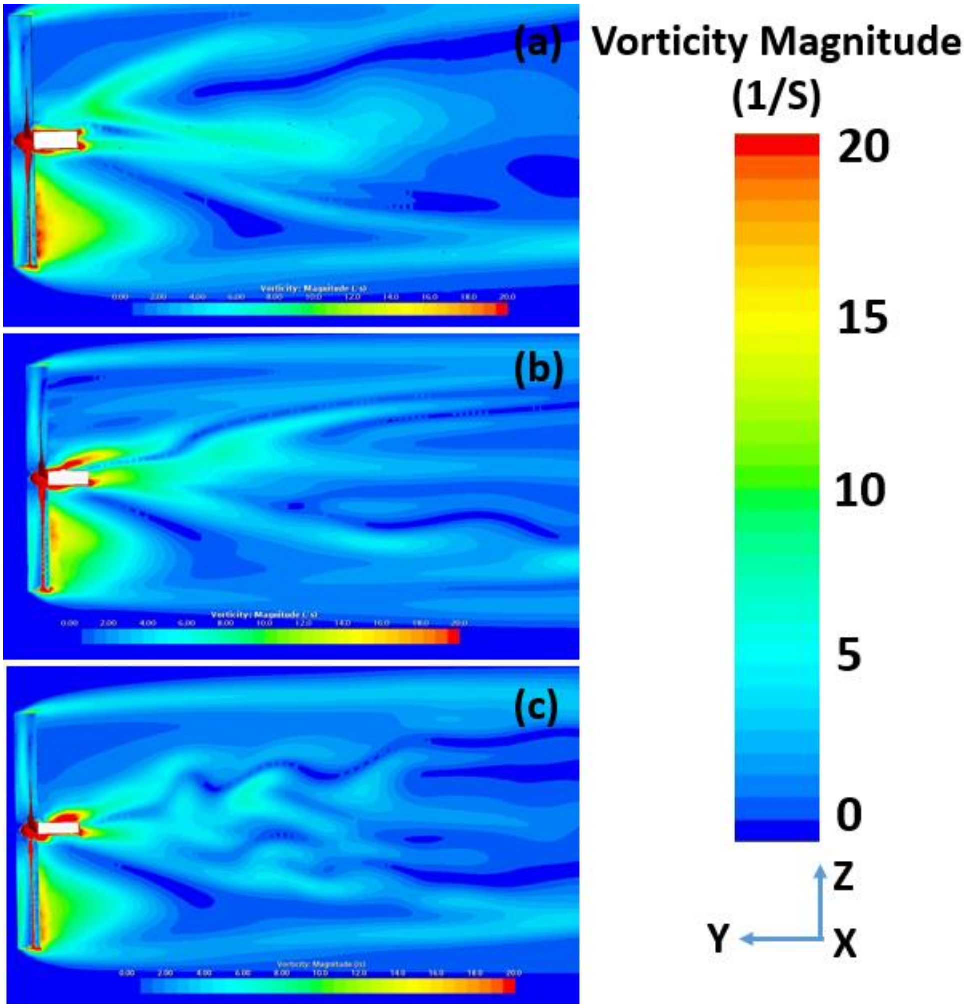

Figure 7-8: Vorticity magnitude contours for: (a) baseline GOE 447, (b) tubercle [a], (c) tubercle [d] design over a hub-height horizontal plane

7.3.2 Winglets Analysis

Due to pressure difference on both sides of an operating turbine blade, an outward spanwise flow on the pressure side and an inward spanwise flow on the suction side are incurred through the tip. This action creates tip vortex flow that leads to lift force reduction and an additional induced drag. The main purpose of a winglet is to reduce the spanwise flow by diffusing and moving the tip vortex away from the rotor plane towards the wake's downstream direction. Hence reducing the induced drag on the blade. Consequently, increasing the aerodynamic efficiency of the turbine.

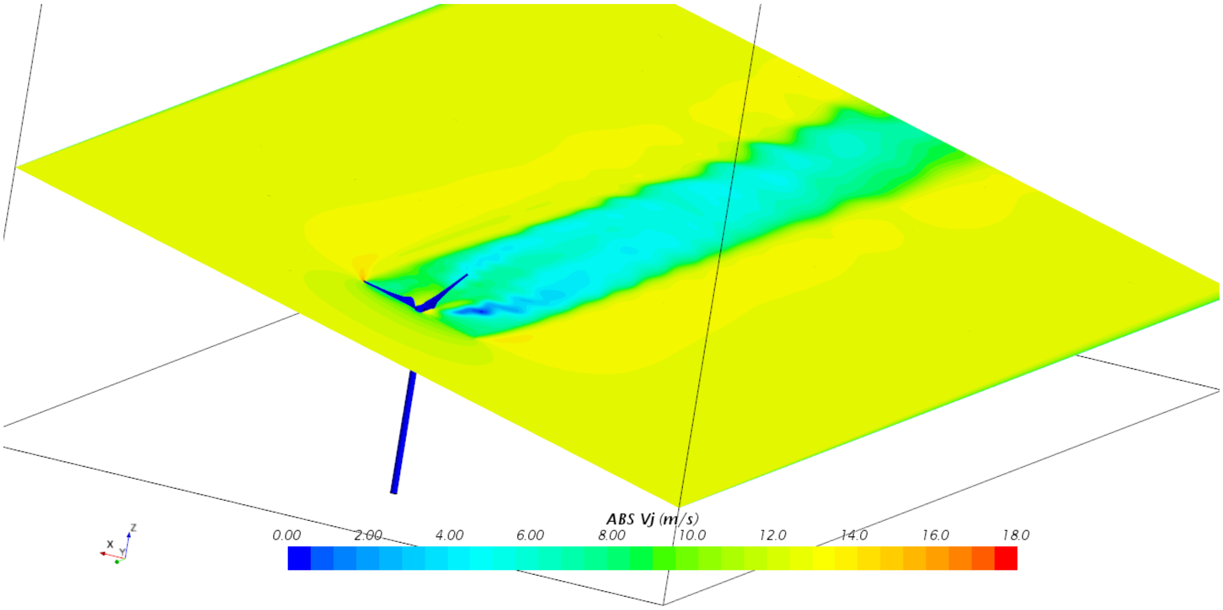

Figure 7-9: Representation of the tilted plane that cuts through one of the blades

It is worth noting that all the scenes for winglets analyses are captured from the 12.5 m/s approaching wind simulations. It is also essential to emphasize that the wind blows in the negative Y direction. For the purpose of understanding the aerodynamic performance of wingletted blades, the tilted plane shown in Figure 7-9 have been selected so that it to cuts one of the blades at the tip.

Figure 7-10 compares the three winglet designs to the GOE 447 baseline design by portraying the axial velocity contours. It is obvious that the axial velocity component is maximized at the blade tip in the four parts of the figure. However, the axial velocity maximization is greater for the wingletted blades than in the baseline blade. Axial velocity maximization is the greatest at the tip of the 60o cant angle winglet (part c) which indicates the ability of this design to better diverge the tip vortex flow, hence allowing higher turbine efficiency. Moreover, be comparing the axial velocity value in the near wake of the rotational plane, it can be seen that the axial velocity in the near wake of the baseline design drops from 12.5 m/s to only 10 m/s. However, the axial velocity in the near wake of the wingletted rotors drops to 6 m/s. The grater the axial velocity drop is an evident sign of the increased rotor ability to extract more momentum from the upstream flow. The previous phenomenon is a good indication of the ability of winglets to reducing induced drag, increasing lift force, hence increasing the turbine efficiency.

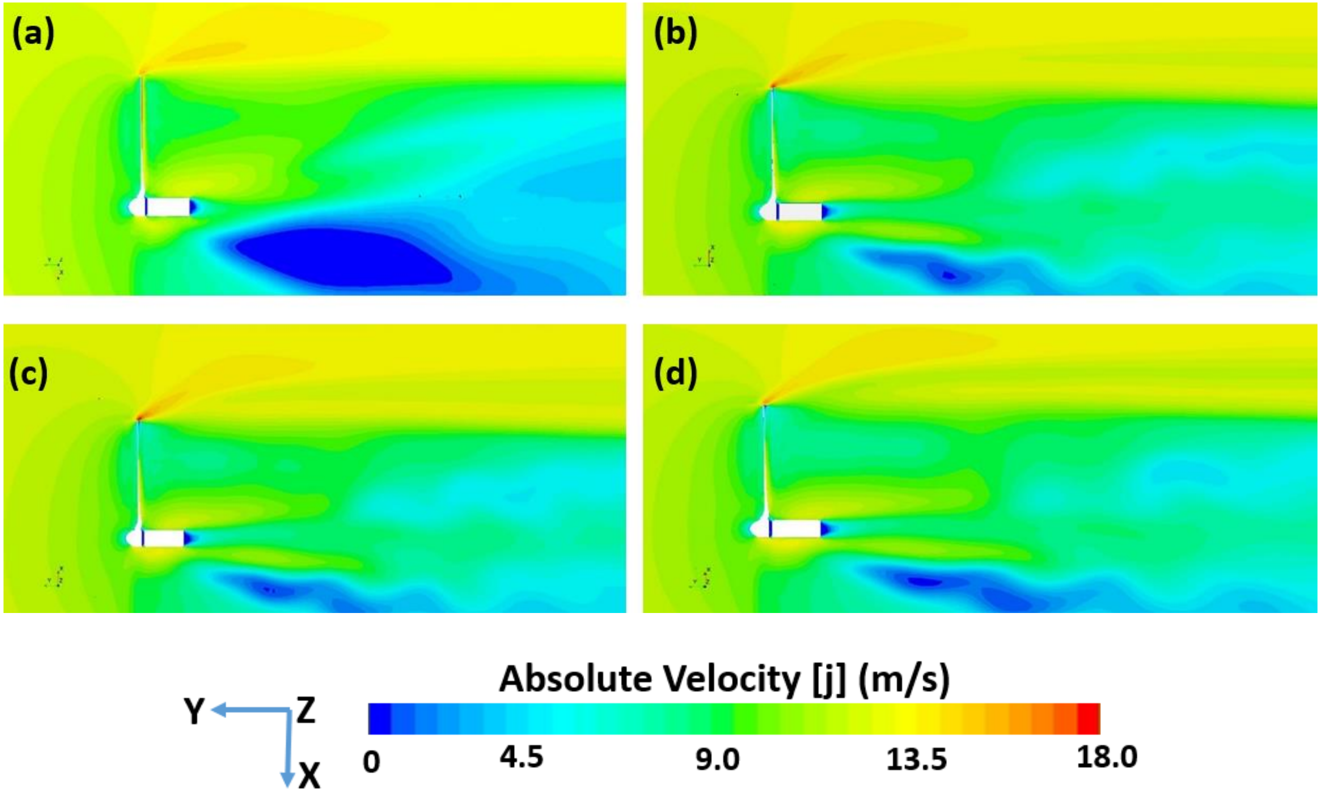

Figure 7-10: Axial velocity contours over a tilted plane that cuts through one of the blades: (a) GOE 447 base design, (b) 30 degrees cant angle winglet, (c) 60 degrees cant angle winglet, (d) 90 degrees cant angle winglet

Figure 7-11 demonstrates a plane that cuts the computational domain at hub height. The plane cuts through no blades. It is used to show vorticity magnitude contours for the baseline design and all winglet configurations.

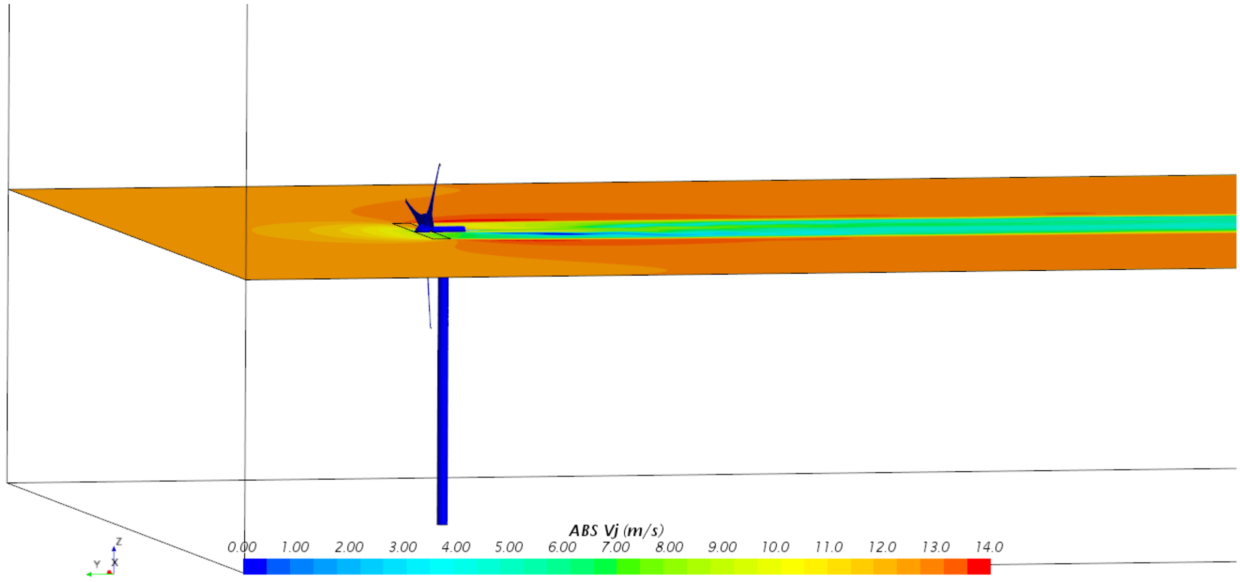

Figure 7-11: Representation of the horizontal plane that cuts the domain at the hub height

Figure 7-12 shows the vorticity magnitude contours over a horizontal plane that cuts the wake at hub height for the baseline and three winglet designs. It is obvious in all parts that tip vortices are guided to shed from the blade's tip and meander downstream. The previous observation is demonstrated by the circumferential sheets of localized high vorticity magnitude that extend downstream of the rotor tips. However, it can be noticed that the strength of the high vorticity circumferential sheet of the winglet designs is higher than its counterpart in the baseline design. For the baseline design, the vorticity magnitude of the vortex sheet in the near wake is 5Hz, while it is 2Hz in the far wake. Whereas the vorticity magnitude of the vortex sheet in the near wake is 7 Hz for the 30^{o} cant angle winglet, 9 Hz for the 60^{o} cant angle, and 8 Hz for the 90^{o} cant angle. Nevertheless, vorticity is 3Hz in the far wake of all winglet designs.

One more feature that characterizes the winglet blade vortex sheet is its coherence and ability to hold its form until the far wake. This observation proves the ability of winglets to a diverging tip generated vortices away from the rotor, reducing induced drag and thus increasing turbine efficiency. Part (c) represents the 60° cant angle winglet has the most coherent vortex sheet. Therefore, this winglet achieves the most drag reduction, hence the most rotor efficiency improvement.

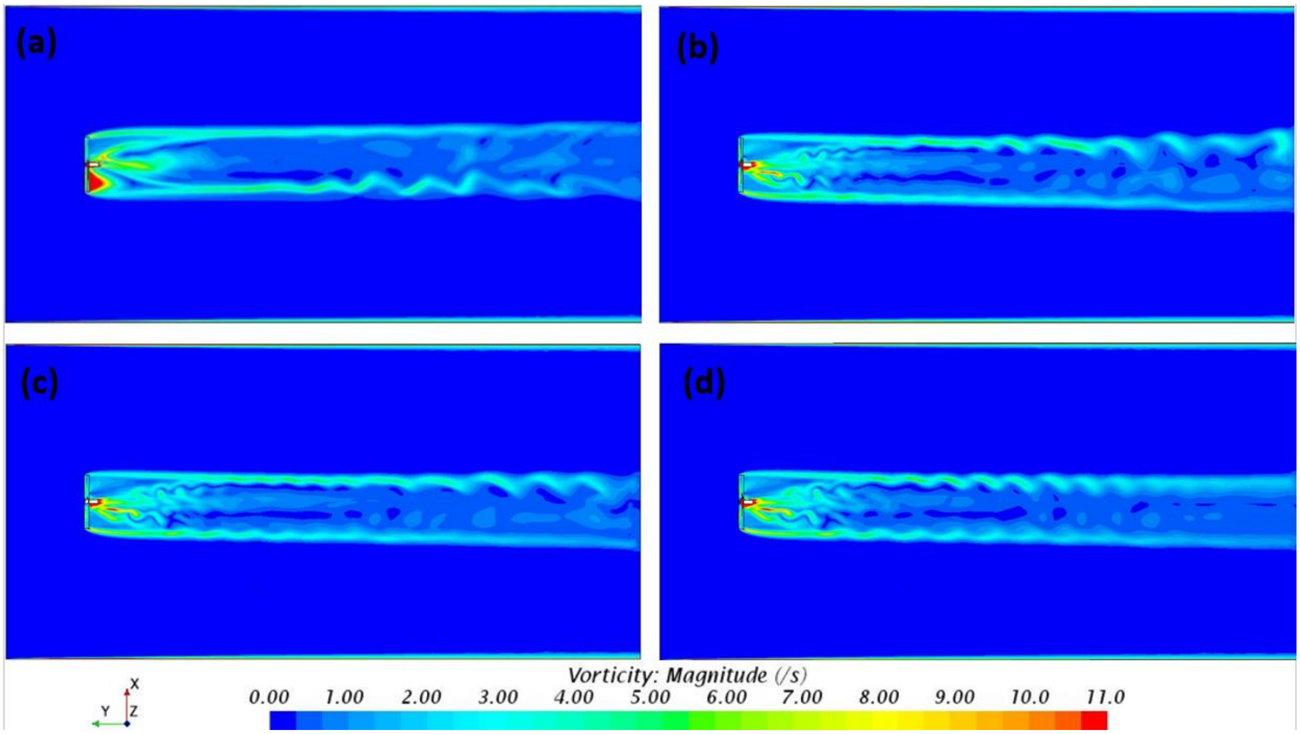

Figure 7-12: Vorticity magnitude contours over a horizontal plane that cuts the wake at hub height: (a) GOE 447 base design, (b) 30 degrees cant angle winglet, (c) 60 degrees cant angle winglet, (d) 90 degrees cant angle winglet

Figure 7-13 and **Figure** 7-14 shed light on the same previous phenomenon but from different perspective. They demonstrate the evolution of winglets' impact on the flow. The winglets effect is initiated at the blades tip and propagates downstream of the rotor.

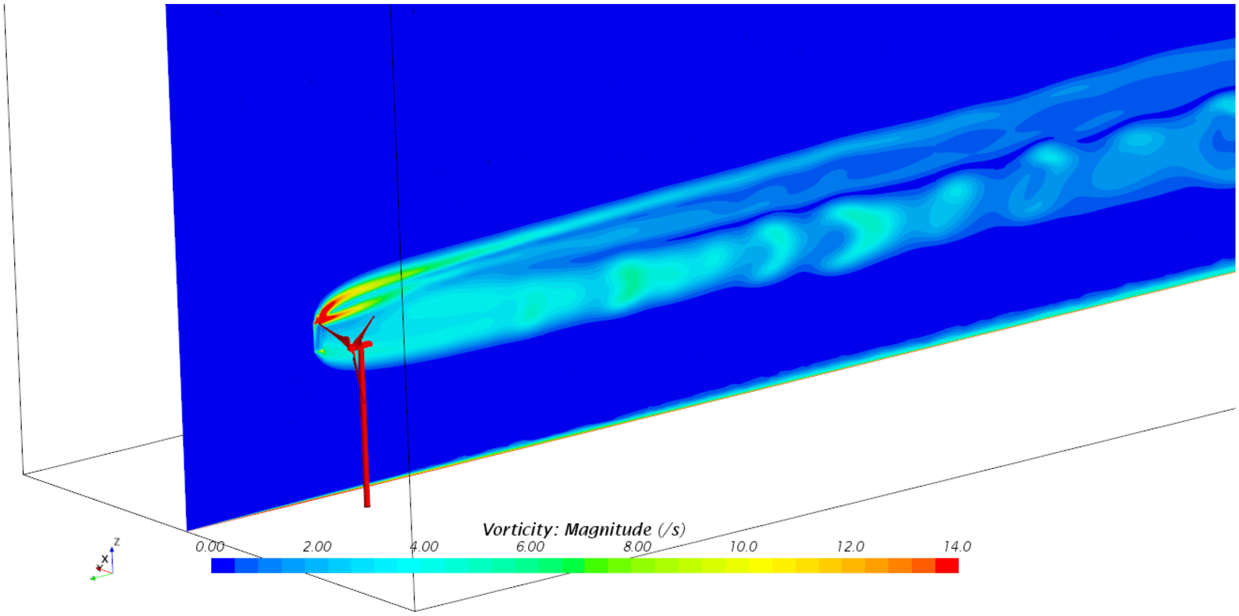

Figure 7-13: Representation of the longitudinal plane that cuts the blade at its tip

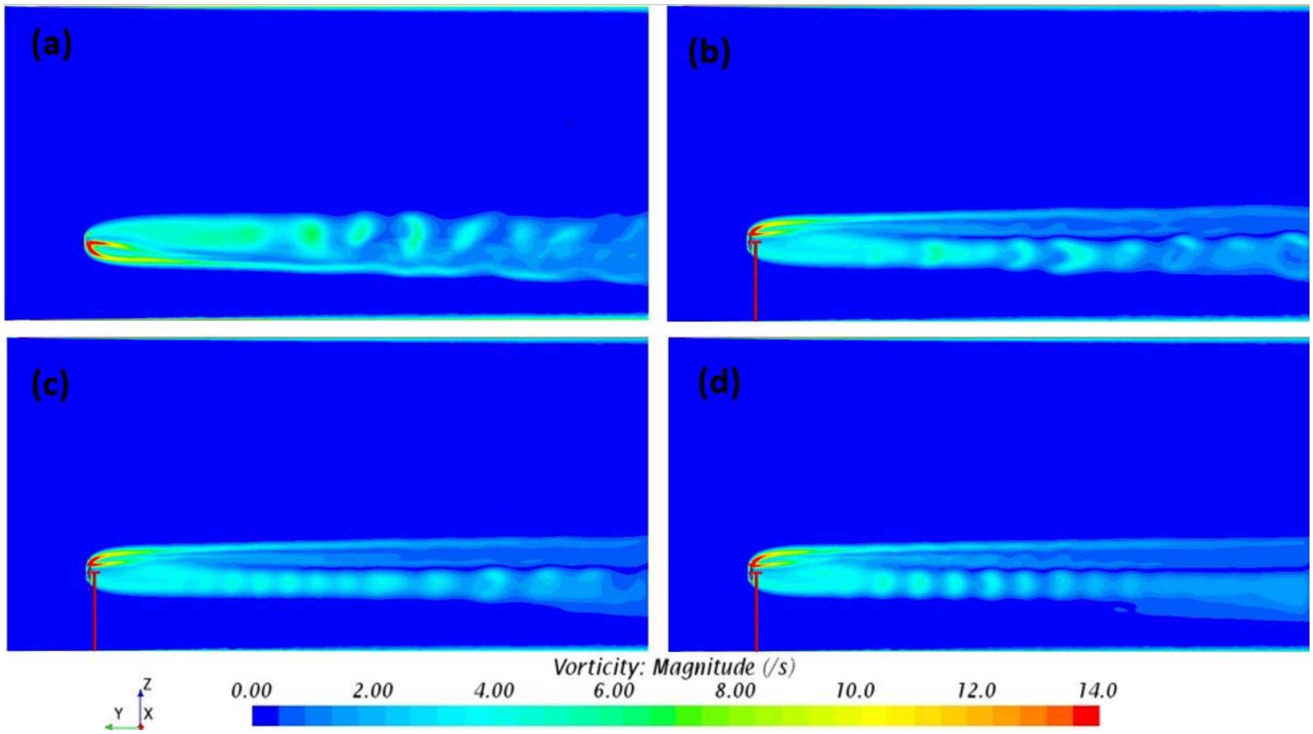

Figure 7-14: Vorticity magnitude contours over a longitudinal plane that cuts a blade at its tip: (a) GOE 447 base design, (b) 30 degrees cant angle winglet, (c) 60 degrees cant angle winglet, (d) 90 degrees cant angle winglet

In **Figure** 7-14 part (a), the turbine model is behind the display scene, while parts (b), (c) and (d) have the model in front of the display scene. The highest vorticity location in all parts is the tip, which is an indication of the location where the generated vortices detach from the blade in the wake downstream. In parts (c) and (d) winglets with 60^{o} and 90^{o} can't angles, the sheet of high vorticity can keep its form and strength until the end of the wake region, which entails the ability of the 60^{o} and 90^{o} can't angles to better guiding the tip vortices away from the rotor. Consequently, reduced induced drag and higher power are obtained.

7.3.3 Tubercles-Winglets Combination Analysis

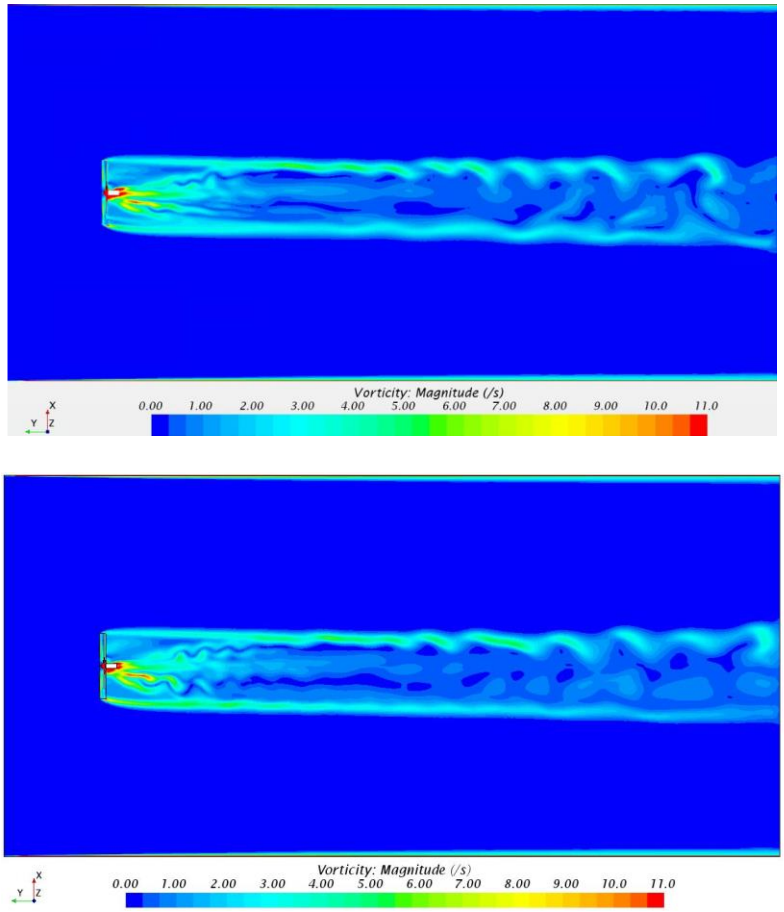

Figure 7-15: Contours of vorticity magnitude over a horizontal x-y plane that cuts the domain at hub height: (top) model with combined tubercle [c] and winglet 60, (bottom) model with combined tubercle [d] and winglet 60

In **Figure** 7-15, it is obvious that the leading-edge tubercles negatively influence the ability of the winglets to lead the tip vortices away from the rotor plane. Tubercles guide the flow in the chordwise direction. This action interferes with the structure of the spanwise flow. Subsequently, limiting the ability of winglets to efficiently diverge the tip vortex, which can be deduced from the disability of the high-vorticity sheet to keeping its strength far downstream, hence not reaching the optimum power increase.

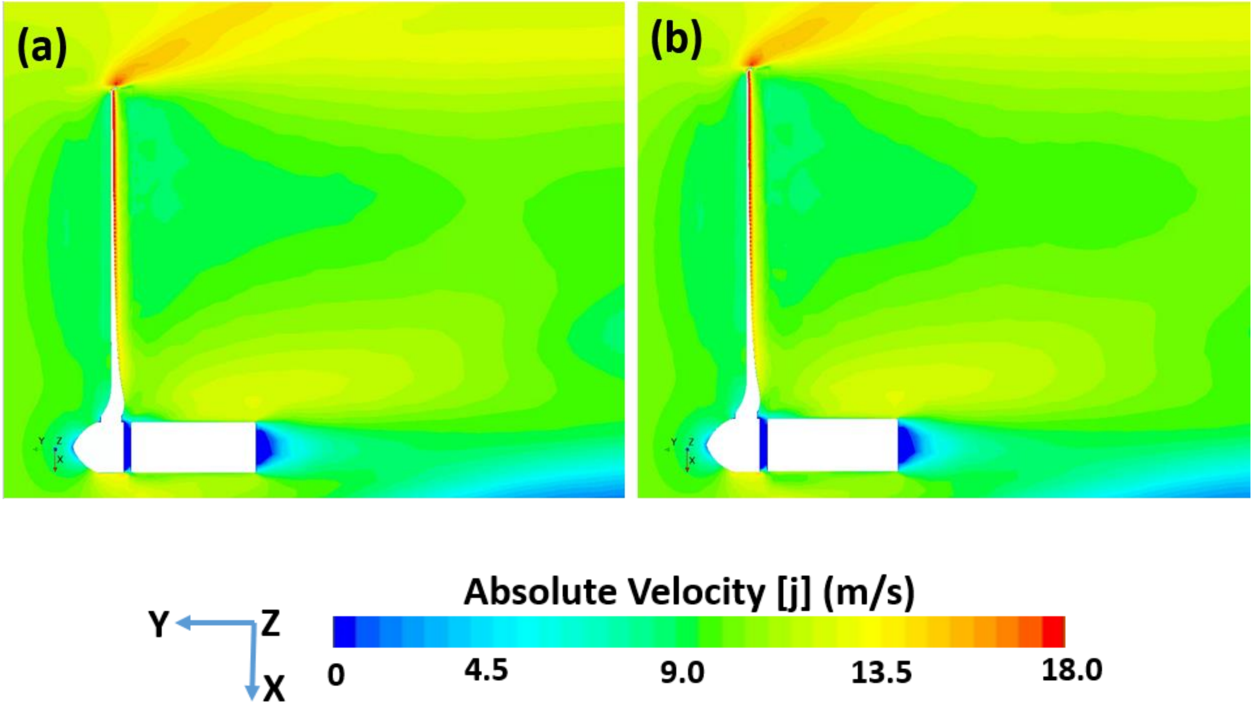

Figure 7-16: Absolute axial velocity contours over a tilted plane that cuts through one of the blades: (a) model with combined tubercle [c] and winglet 60, (b) model with combined tubercle [d] and winglet 60

Table 7-2 shows that combining different tubercle designs with all winglets leads to, unexpectedly, a reduction in power production (an average of 20% less power than the baseline design at rated wind speed) or negligible power improvement. The reason behind this observation can be explain by comparing part (c) of **Figure** 7-10 to both parts of **Figure** 7-16**.** When tubercles are incorporated with a winglet on the same blade, tubercles mechanism of enhancing the chordwise flow interferes with the ability of winglet to moving the tip vortex away from the rotor plane towards the wake's downstream direction. Hence inefficient reduction of induced drag on the blade. In both parts (a) and (b) of **Figure** 7-16, only 10 m/s of axial velocity obtained in the wake, which entails reduced rotor's ability to power extraction, compared to part (c) of **Figure** 7-10 where 6 m/s is obtained in downstream of the rotor.

7.4 Conclusions

Geometry parameters of leading-edge tubercles plays a key role in dictating chordwise flow structure around the turbine blade, hence power production. Four among the five tested designs are unable to increase power, except for one design characterized by low values of both amplitude and wavelength. Moreover, power improvement percentage using this technique is wind speed dependent and maximizes at rated speed (5.5%).

Winglets' ability to diverge tip vortex flow away from the rotor to reduce induced drag and produce more power are excellent for thin airfoils. The power improvement drops slightly at the rated wind speed for winglets with cant angles 30^o and 60^o However, power improvement gets higher as the wind speed goes higher for the wiglet with 90^o cant angle. For instance, a maximum of 10.5% power improvement is achieved by the 60^o winglet blade at 17.5 m/s wind speed.

The tubercles-winglets combination is found to produce less power than the baseline design in most of the cases, except for four cases. One case with a negligible increase at the rated wind speed. In addition to three cases at 17.5 m/s, achieving an average of 4% power improvement only. However, this power improvement is not more than what a single technique can achieve. Additionally, the 17.5 m/s wind speed is less likely to happen.

Chapter 8 : Future Work

8.1 Proposed Setup

It was planned to build a setup to measure the turbine mechanical power using a torque sensor shown in **Figure** 8-1. The idea is shown in **Figure** 8-2, where the torque sensor will be connected from its active end to the turbine rotor, instead of the motor demonstrated. Whereas the other end of the sensor will be connected to the eddy current brake or a generator. The output torque reading can be obtained by any of the three devices shown in (USB, handheld display or digital display).

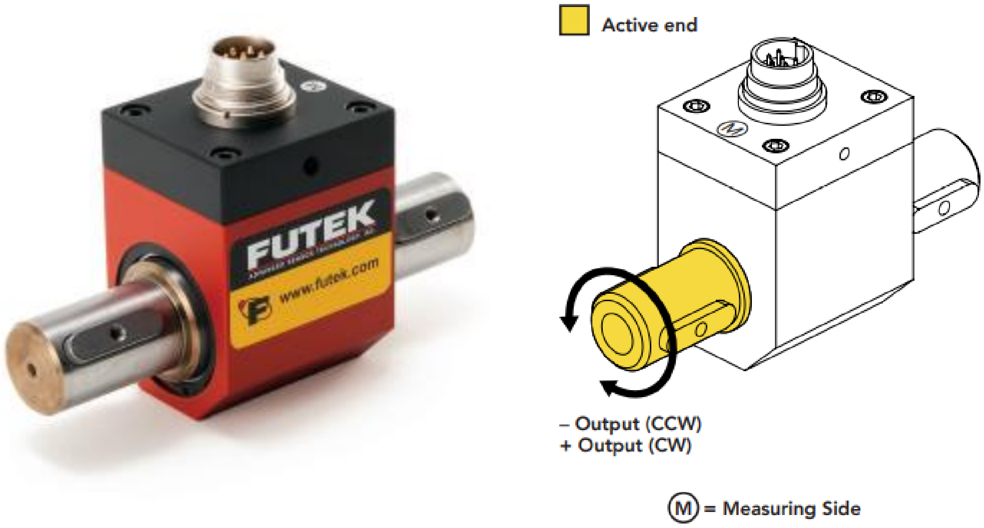

Figure 8-1: Torque meter

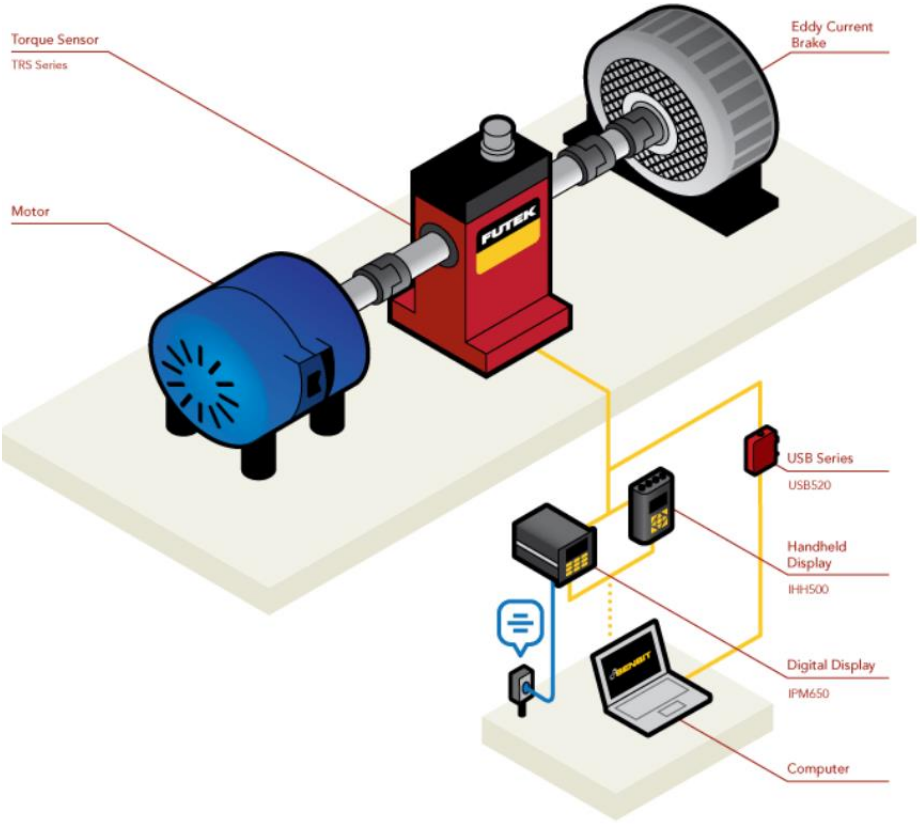

Figure 8-2: Proposed experimental setup. [91]

The decision was to go with the USB device shown in **Figure** 8-3. Since it eliminates the need for power supply and display equipment. The module is supplied by PC power through a USB Cable, providing excitation voltage for the sensor. The analog output voltage of the sensor is then digitized and processed by a microprocessor using the integrated high resolution (24 bits) analogue to digital converter (ADC). The on-board USB device allows the microprocessor to communicate with the PC by means of the USB link. [91]

Figure 8-3: USB digital device

8.2 Actual Built Setup

The left picture of **Figure** 8-4 shows the actual setup built for mechanical power measurement. The setup is going to be very useful platform to be utilized for future work in the wind tunnel lab. It is always essential to validate CFD models against experimental data to ensure the effectiveness of CFD models in predicting the flow parameters, In the past, wind tunnel lab researchers were only able to verify CFD velocity measurements versus experimental data, since the lab is equipped with HWA system. However, there was no setup to measure mechanical turbine power so that one has a reference to compare CFD calculated power to. Therefore, this setup will facilitate a lot of HAWTs research in the future.

The right picture of **Figure** 8-4 shows the straight blade turbine model ready for power measurement in the test section. It is a 60-cm rotor. It is worth noting that the attached hub and blades are replaceable so that any blade design can be 3D printed in the future and get tested in a very short time. Blades can be fixed in position with simple set screws

Figure 8-4: (left) the actual built power measurement setup details, (right) side view of the straight blade model.

Left picture of **Figure** 8-5 shows the turbine model with upstream winglets, while the right picture shows the blades with trailing edge tubercles.

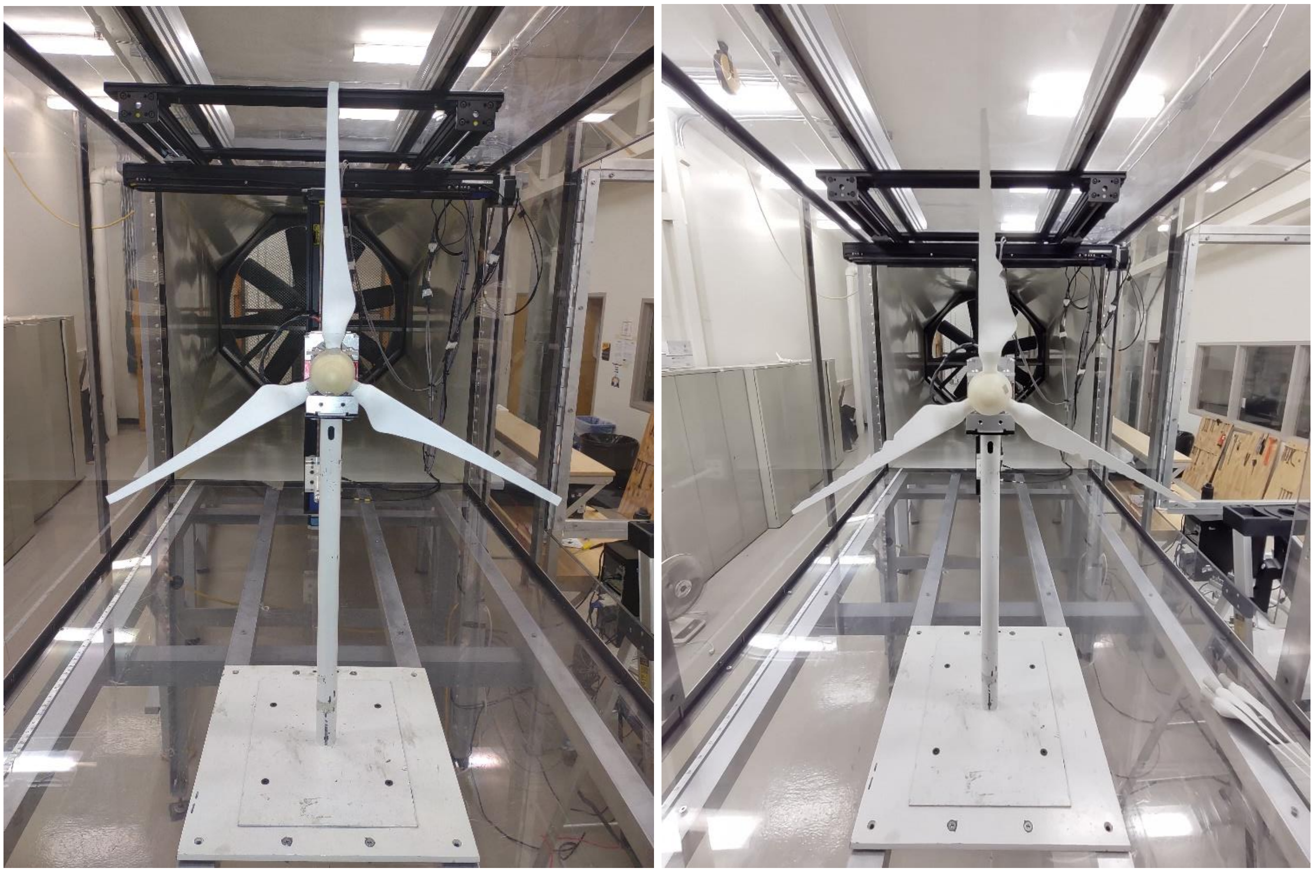

Figure 8-5: (left) front view of the upstream wingletted model, (right) front view of the trailing edge tubercles model

References

[1] G. Stein-Brzozowska, C. Bergins, A. Kukoski, S. Wu, M. Agraniotis and E. Kakaras , "The Current Trends in Conventional Power Plant Technology on Two Continents from the Perspective of Engineering, Procurement, and Construction Contractor and Original Equipment Manufacturer," *J. Energy Resour. Technol.*, vol. 138, no. 4, p. 044501, 2016.

[2] K. Vincent Wong, "Engineering Solutions to the Greenhouse Gases Generated by Hydroelectric Plants," *J. Energy Resour. Technol.*, vol. 136, no. 2, p. 024701, 2014.

[3] B. Prasad, "Energy Efficiency, Sources and Sustainability," *J. Energy Resour. Technol.*, vol. 132, no. 2, pp. 1-2, 2010.

[4] "Renewables 2019 Global Status Report," REN21 Secretariat, Paris, 2019.

[5] "Global Wind Report," Brussels, Belgium, 2018.

[6] A. Crespo, J. Hernandez and S. Frandsen , "Survey of modeling methods for wind turbines wakes and wind farms," *Wind Energy*, vol. 2, pp. 1-24, 1999.

[7] B. Sanderse, S. vand der Pijl and B. Koren, "Review of computational fluid dynamics for wind turbine wake aerodynamics," *Wind Energy*, vol. 14, pp. 799-819, 2011.

[8] J. Sumner, C. Watters and C. Masson, "CFD in Wind Energy: The Virtual Multiscale Wind Tunnel," *Energies,* vol. 3, pp. 989-1013, 2003.

[9] A. Miller, B. Chang, R. Issa and G. Chen, "Review of computer-aided numerical simulation in wind energy," *Renewable and Sustainable Energy Reviews,* vol. 25, pp. 122-134, 2013.

[10] G. Xiaoxia, Y. Hongxiang and L. Lin, "Optimization of wind turbine layout position in a wind farm using a newly-developed two-dimensional wake model," *Applied Energy,* vol. 174, pp. 192-200, 2016.

[11] N. O. Jensen, "A note on wing generator interaction," Riso National Laboratory, Roskilde, Denmark, 1983.

[12] R. S. Amano and P. M. Das, "Flow analysis of different turbine blades in both blade and wake region," in *Proceedings of the ASME Turbo Expo 2011*, Vancouver, British Columbia, Canada, 2012.

[13] X. Shen, X. Zhu and Z. Du, "Optimization of wind turbine blades using lifting surface method and genetic algorithm," in *Proceedings of the ASME Turbo Expo 2011*, Vancouver, British Columbia, Canada, 2011.

[14] F. De Bellis and L. Catalona, "Single and multi-objective CFD optimization of horizontal axis wind turbines," in *Proceedings of the ASME Turbo Expo 2011*, Vancouver, British Columbia, Canada, 2011.

[15] S. Beyhaghi and R. S. Amano, "Multivariable Analysis of Aerodynamic Forces on Slotted Airfoils for Wind Turbine Blades," *Journal of Energy Resources,* vol. 141, no. 3, p. 051214(10 pages), 2019.

[16] S. Beyhaghi and R. S. Amano, "Improvement of Aerodynamic Performance of Cambered Airfoils Using Leading-Edge Slots," *Journal of Energy Resources Technology,* vol. 139, no. 5, p. 051204, 2017.

[17] F. Kurtulmus and A. Izli, "Aerodynamic Analyses of Different Wind Turbine Blade Profiles," *Journal of Applied Science,* vol. 7, no. 5, pp. 663-670, 2007.

[18] F. Hsiao, C. Bai and W. Chong, "The Performance Test of Three Different Horizontal Axis Wind Turbine Blade Shapes using Experimental and Numerical Methods," *JEnergies,* vol. 6, no. 6, pp. 2784-2803, 2013.

[19] N. Tobin, A. Hamed and L. Chamorro, "An Experimental Study on the Effects of Winglets on the Wake and Performance of a Model Wind Turbine," *Energies,* vol. 8, pp. 11955-11972, 2015.

[20] M. Khaled , M. Ibrahim , H. AbdelHamed and A. AbdelGawad, "Investigation of a small horizontal axis wind turbine performance with and without winglet," *Energy,* vol. 187, p. 115921(14 pages), 2019.

[21] A. Farhan, A. Hassanpour, A. Burns and A. Motlaph, "Numerical study of the effect of winglet planform and airfoil on a horizontal axis wind turbine performance," *Renewable Energy,* vol. 131, pp. 1255-1273, 2019.

[22] M. G. Khalafallah, A. M. Ahmed and M. K. Emam, "The effect of using winglets to enhance the performance of swept blades of a horizontal axis wind turbine," *Advances in Mechanical Engineering*, vol. 11, no. 9, pp. 1-10, 2019.

[23] J. Johansen and N. Sorensen, "Aerodynamic Investigation of Winglets on Wind Turbine Bladesusing CFD," Riso National Laboratory, Roskilde, Denmark, 2006.

[24] F. Muhle, J. Bartl, T. Hasen, M. Adaramola and L. Saetran, "An experimental study on the effects of winglets on the tip vortex interaction in the near wake of a model wind turbine," *Wind Energy*, pp. 1-15, 2020.

[25] Y. Ostovan and O. Uzol, "Experimental study on the effects of winglets on the performance of two interacting horizontal axis model wind turbines," *Journal of Physics: Conference Series*, p. 022015 (9 pages), 2016.

[26] M. Ibrahim, A. Alsultan , S. Shen and R. S. Amano, "Advances in Horizontal Axis Wind Turbine Blade Designs: Introduction of Slots and Tubercle," *ASME Journal of Energy Resources Technology*, vol. 137, no. 5, p. 051205(6 pages), 2015.

[27] S. Kumar and R. Amano, "Wind turbine blade design and analysis with tubercle technology," in *Proceedings of ASME IDETC/CIE 2012*, Chicago, IL, 2012.

[28] G. Abate, D. Mavris and L. Sankar, "Performance Effects of Leading-Edge Tubercles on the NREL Phase VI Wind Turbine Blade," *Energy Resorces Technology*, vol. 141, no. 5, p. 051206 (9 pages), 2019.

[29] R. Amano, A. Alsultan, S. Kumar and A. Welsh, "Design and Analysis of Wind Turbine Blades-- Winglet, Tubercle, And Slotted," in *Proceedings of ASME 2013 Turbo Expo*, San Antonio, TX, 2013.

[30] G. Huang, Y. Shiah, C. Bai and W. Chong, "Experimental study of the protuberance effect on the blade performance of a small horizontal axis wind turbine," *Wind Egineering and Industrial Aerodynamics,* vol. 147, pp. 202-211, 2015.

[31] R. Zhang and J. Wu, "Aerodynamic characteristics of wind turbine blades with a sinusoidal leading edge," *Wind Energy,* vol. 15, pp. 407-424, 2012.

[32] R. Jackson and R. Amano, "Experimental Study and Simulation of a Small-Scale Horizontal-Axis Wind Turbine," *Energy Resources Technology,* vol. 139, no. 5, p. 051207 (19 pages), 2017.

[33] P. Ma, M. Li, J. Jilesen, F. Lien, E. Yee and H. Harrison, "A comparison of coarse-resolution numerical simulation with experimental measurements of wind turbine aerodynamic performance," *Procedia Engineering,* vol. 79, pp. 17-27, 2014.

[34] N. Choi, S. Nam, J. Jeong and K. Kim, "Numerical study on the horizontal axis turbines arrangement in a wind farm: Effect of separation distance on the turbine aerodynamic power output," *Wind Enginering and Industrial Aerodynamics,* vol. 117, pp. 11-17, 2013.

[35] *Probes for hot wire anemometry,* Skovlunde, Denmark: Dantec Dynamics, 2014.

[36] *Installation and user's guide for mini CTA 54T30,* Skovlunde, Denmark: Dantec Dynamics, 2004.

[37] *User's guide for hot wire calibrator 54H10*, Skovlunde, Denmark: Dantec Dynamics, 2003.

[38] R. Jackson, *Application of Reynolds Stress Model Using Direct Modeling and Actuator Disk Approaches for a Small-Scale Wind Turbine*, Milwaukee, WI: University of Wisconsin-Milwaukee, 2016.

[39] R. Howell, N. Qin, J. Edward and N. Durrani, "Wind tunnel and numerical study of a small vertical axis wind turbine," *Renewable Energy,* vol. 35, pp. 412-422, 2010.

[40] A. Crespo and R. Gomez-Elvira, "Effect of the proximity of land on wind farm performance for offshore flow," in *European Seminar OWEMES'97*, La Magdalena, Sardinia, 1997.

[41] Y. Zhiyin, "Large-eddy simulation: past, present and the future," *Chinese Journal of Aeronautics,* vol. 28, no. 1, pp. 11-24, 2015.

[42] C. Plengsaard, *Improved engine wall models for Large Eddy Simulation (LES)*, Madison, WI: University of Wisconsin-Madison, 2013.

[43] J. Manwell, J. Mcgoan and A. Rogers, Wind energy explained theory, design and application, Wiltshire: Great Britain, 2010.

[44] R. Mahu and F. Popescue, "NREL Phase VI Rotor Modeling and Simulation Using Ansys Fluent 12.1," *Mathematical Modeling in Civil Engineering,* no. 1/2, pp. 185-194, 2011.

[45] A. Aranake, V. Lakshminarayan and K. Duraisamy, "Assessment of Transition Model and CFD Methodology for Wind Turbine Flows," in *42nd AIAA Fluid Dynamics Conference and Exhibit*, New Orleans, Louisiana, 2012.

[46] H. Tennekes and J. Lumley, A first course in turbulence, Cabbridge, Massachusetts, USA nad London, England: The MIT Press, 1972.

[47] R. S. Amano, "Aerodynamic Behavior of Rear-Tubercle Horizontal Axis Wind Turbine Blade," in *Sustainable Development for Energy, Power, and Propulsion*, Springe, 2021, pp. 545-562.

[48] R. S. Amano and B. Sunden, Aerodynamics of Wind Turbine Blades--Emerging Topic, WIT Press, 2015.

[49] R. S. Amano, "Chapter 1: Introduction to Wind Energy," in *Aerodynamics of Wind Turbine Blades--Emerging Topics*, WIT Press, 2015, pp. 1-9.

[50] R. S. Amano and P. M. Mohan Das, "Chapter 2: Basic Theory for Wind Turbine Blade Aerodynamics," in *Aerodynamics of Wind Turbines--Emerging Topics*, WIT Press, 2015, pp. 11-22.

[51] R. Malloy and R. S. Amano, "Chapter 7: Structural Consideration for Wind Turbine Blades," in *Aerodynamics of Wind Turbine Blades--Emerging Topics,*, WIT Press, 2015, pp. 161-177.

[52] K. Anwar, S. Deshmukh and S. Rizvi, "Feasibility and Sensitivity Analysis of a Hybrid Photovoltaic/Wind/Biogas/Fuel-cell/Diesel/Battery System for Off-Grid Rural Electrification Using HOMER," *Journal of Energy Resources Technology,* vol. 142, no. 6, pp. 061307 (1-10), 2020.

[53] M. Qandil, A. Abbas, A. Salem, A. Abdelhadi, A. Hasan, F. Nourin, M. Abousabae, O. Selim, J. Espindola and R. Amano, "Net Zero Energy Model for Wastewater Treatment Plants," *Journal of Energy Resources Technology,* pp. 1-38, 2021.

[54] P. Laws, J. Saini, A. Kumar and S. Mitra, "Improvement in Savonius Wind Turbines Efficiency by Modification of Blade Designs-A Numerical Study," *Journal of Energy Resources Technology,* vol. 142, no. 6, pp. 061303 (1-12), 2020.

[55] R. Hassanzadeh, M. Mohammadnejad and S. Mostafavi, "Comparison of different blade profiles in a Two-Blade Conventional Savonius Wind Turbine," *Journal of Energy Resources Technology,* vol. 143, no. 2, p. 021301 (12 pages), 2021.

[56] N. Alom and U. Saha, "Examining the Aerodynamic Drag and Lift Characteristics of aewly Developed Elliptical-Bladed Savonius Rotor," *Journal of Energy Resources Technology,* vol. 141, no. 5, p. 051201 (12 pages), 2016.

[57] A. Hasan, R. Jackson and R. Amano, "Experimental Study of the Wake Regions in Wind Farms," *Journal of Energy Resources Technology,* vol. 141, no. 5, p. 051209 (12 pages), 2019.

[58] A. Hasan, T. ElGammal, R. Jackson and R. Amano, "Comparative Study of the Inline Configuration Wind Farm," *Journal of Energy Resources Technology,* vol. 142, no. 6, p. 061302 (10 pages), 2020.

[59] S. Addamane, M. Pandey, N. Sunil, N. Satish, V. Mugundhan and R. Velamati, "Numerical study of effect of pitch angle on performance characteristics of a HAWT," *Engineering Science and Technology, an International Journal,* vol. 19, no. 1, pp. 632-641, 2016.

[60] A. Muheisen, M. Yass and I. Irthiea, "Enhancement of horizontal wind turbine blade performance using multiple airfoils sections and fences," *Journal of King Saud University – Engineering Sciences,* p. In Press, 2021.

[61] A. Eltayesh, F. Castellani, M. Burlando, M. Hanna, A. Huzayyin, H. El-Batsh and M. Becchetti, "Experimental and numerical investigation of the effect of blade number on the aerodynamic performance of a small-scale horizontal axis wind turbine," *Alexandria Engineering Journal,* vol. 60, no. 4, pp. 3931-3944, 2021.

[62] M. Mohammadi and M. Maghrebi, "Improvement of wind turbine aerodynamic performance by vanquishing stall with active multi air jet blowing," *Energy,* vol. 224, p. 120176, 2021.

[63] A. Hasan, M. Abousabae, A. Salem and R. Amano, "Study of Aerodynamic Performance and Power Output for Residential-Scale Wind Turbines," *Journal of Energy Resources Technology,* vol. 143, no. 1, p. 011302 (10 pages), 2021.

[64] A. Hays and K. Treuren, "A Study of Power Production and Noise Generation of a Small Wind Turbine for an Urban Environment," *Journal of Energy Resources Technology,* vol. 141, no. 5, p. 051202 (10 pages), 2019.

[65] K. Qaissi, O. Elsayed, M. Faqir and E. Essadiqi, "Performance Enhancement Analysis of a Horizontal Axis Wind Turbine by Vortex Trapping Cavity," *ASME J. Energy Resour. Technol.,* vol. 144, no. 3, p. 031303, 2022.

[66] J. Johansen, N. Soerensen and F. Zahle, "Aerodynamic accessories," Riso National Lab, Roskilde, Denmark, 2004.

[67] N. Sørensen, F. Zahle, C. Bak and T. Vronsky, "Prediction of the Effect of Vortex Generators on Airfoil Performance," *Journal of Physics: Conference Series,* vol. 524, p. 12, 2014.

[68] I. Salviano, D. Dezan and J. Yanagihara, *International Journal of Heat and Mass,* vol. 82, pp. 373-387, 2015.

[69] S. Shun and N. Ahmed, "Wind turbine performance improvements using active flow control," *Procedia Engineering,* vol. 49, pp. 83-91, 2012.

[70] J. Chawla, S. Suryanarayanan, B. Puranik, J. Sheridan and B. Falzon, "Efficiency improvement study for small wind turbines through flow control," *Sustainable Energy Technologies,* vol. 7, pp. 195-208, 2014.

[71] G. Gyatt, "Development and Testing of Vortex Generators for Small Horizontal Axis Wind Turbines," NATIONAL AERONAUTICS AND SPACE ADMINISTRATION, Springfield, VA, 1986.

[72] H. Wang, B. Zhang, Q. Qin and X. Xu, "Flow Control on the NREL S809 Wind Turbine Airfoil Using Vortex Generators," *Energy,* vol. 118, no. 1, pp. 1210-1221, 2017.

[73] D. Astolfi, F. Castellani, M. Fravolini, S. Cascianelli and L. Terzi, "Precision Computation of Wind Turbine Power Upgrades: An Aerodynamic and Control Optimization Test Case," *J. Energy Resour. Technol.*, vol. 141, no. 5, p. 051205 (9 pages), 2019.

[74] The White House, 8 12 2021. [Online]. Available: https://www.whitehouse.gov/briefing-room/statements-releases/2021/12/08/fact-sheet-president-biden-signs-executive-order-catalyzing-americas-clean-energy-economy-through-federal-sustainability/. [Accessed 21 3 2022].

[75] L. Mishnaevsky, K. Branner, H. Petersen, J. Beauson, M. McGugan and B. Sorensen, "Materials for Wind Turbine Blades: An Overview," *Materials (Basel),* vol. 10, no. 11, p. 1285, 2017.

[76] R. Zhang and V. Wu, "Aerodynamic characteristics of wind turbine blades with a sinusoidal leading edge," *Wind Energy,* vol. 15, no. 3, pp. 407-424, 2012.

[77] N. Troldborg, F. Zahle and N. Sorensen, "Simulations of wind turbine rotor with vortex generators," *Journal of Physics: Conference Series,* vol. 753, no. 2, p. 9, 2016.

[78] H. Hu, X. Li and B. Gu, "Flow Characteristics Study of Wind Turbine Blade with Vortex Generators," *International Journal of Aerospace Engineering,* vol. 2016, p. 11, 2016.

[79] J. Johansen , N. Sorensen, M. Reck, M. Hansen, A. Stuermer, J. Ramboer, C. Hirsch, J. Ekaterinares, S. Voutsinas and Y. Perivolaris, "KNOW-BLADE Task-3.3 report; Rotor Blade Computations with 3D Vortex Generators," Riso National Laboratory, Roskilde, Denmark, 2005.

[80] G. Gyatt, "Development and Testing of Vortex Generators for Small Horizontal Axis Wind Turbine," National Technical Information service, Springfield, VA, 1986.

[81] N. Tobin, A. Hamid and L. Chamorro, "an Experimental Study on the Effects of Winglets on the Wake and Performance of a Model Wind Turbine," *Energies,* vol. 8, pp. 11955-11972, 2015.

[82] A. Johansen and A. Sorensen, "Aerodynamic Investigation of Winglets on Wind Turbine Blades Using CFD," Riso National Laboratory, Roskilde, Denmark, 2006.

[83] Y. Li, S. Mohammed, G. Nariman, N. Aljojo, A. Rezvani and S. Dadfar, "Energy Management of Microgrid Considering Renewable Energy Sources and Electric Vehicles Using the Backtracking Search Optimization Algorithm," *ASME. J. Energy Resour. Technol.,* vol. 142, no. 5, p. 052103, 2020.

[84] J. Ball, "A Review of Geothermal Technologies and Their Role in Reducing Greenhouse Gas Emissions in the USA," *ASME. J. Energy Resour. Technol.,* vol. 143, no. 1, p. 101903, 2021.

[85] J. Ball, "Macro Energy Trends and the Future of Geothermal Within the Low-Carbon Energy Portfolio," *ASME. J. Energy Resour. Technol.,* vol. 143, no. 1, p. 010904, 2020.

[86] A. Hasan, O. Selim, M. Abousabae, R. Amano and W. Otieno, "Economic, Exergy, and Environmental Analyses of the Energy Assessments for U.S. Industries.," *ASME. J. Energy Resour. Technol.,* vol. 143, no. 11, p. 112107, 2021.

[87] S. Al Hamad, O. Habash, A. Hasan and R. Amano, "Effect of the J-Shaped Wind Turbine Airfoil Opening Ratio and Thickness on the Performance of Symmetrical Airfoils," *ASME. J. Energy Resour. Technol.*, vol. 144, no. 5, p. 051303, 2022.

[88] O. Shah, M. Jamal, T. Khan and U. Qazi, "Experimental and Numerical Evaluation of Performance of a Variable Pitch Vertical-Axis Wind Turbine," *ASME. J. Energy Resour. Technol.*, vol. 144, no. 6, p. 061303, 2022.

[89] M. Jamal and O. Shah, "Performance Evaluation of a 1 kW Variable Pitch-Straight Blade Vertical Axis Wind Turbine.," *ASME. J. Energy Resour. Technol.* , vol. 142, no. 12, p. 121304, 2020.

[90] R. Amano, "Review of Wind Turbine Research in 21st Century," *ASME. J. Energy Resour. Technol.*, vol. 139, no. 5, p. 050801, 2017.

[91] [Online]. Available: https://www.futek.com/applications/Torque-Motor-Test-Stand. [Accessed 2 11 2020].

[92] [Online]. Available: https://arc.aiaa.org/doi/pdf/10.2514/1.C034845. [Accessed 2 11 2020].

[93] M. Mourad , I. Shahin, S. Ayad, O. Abdellatif and T. Mekhail, "Effect of winglet geometry on horizontal axis wind turbine performance," *Engineering Reports*, 2020.

[94] [Online]. Available: https://www.windpowerengineering.com/vortex-generators-boost-wind-turbine-performance-aep/. [Accessed 2 11 2020].